Sea ice thickness and iceberg distribution in the Southern Ocean

Thesis

Sea ice thickness and iceberg distribution in the Southern Ocean

A thesis submitted for the Degree of Doctor of

Philosophy

by

Christopher J. Banks, B.Sc. (Lancaster)

Department of Earth Sciences
The Open University
September 2006

PAGINATED
BLANK PAGES
ARE SCANNED AS
FOUND IN
ORIGINAL
THESIS

NO
INFORMATION
MISSING

Abstract

The sea ice thickness distribution, represented by the probability density function (PDF), is critical to Earth's climate system and knowledge of the distribution in the Antarctic is limited. A novel methodology, using an acoustic Doppler current profiler, was developed to measure sea ice draft based on measurements taken from Autosub (an autonomous underwater vehicle). The PDF has been derived for three missions undertaken in the eastern Amundsen Sea during March 2003. The PDFs for all missions were found to have a single mode although there is evidence for variability in mean thickness along the ice front, as the most western mission has a lower mean draft. Geostatistical analyses of the data have allowed the derivation of PDFs to account for the spatial sampling.

A factor on the thickness of ice measured is the presence of icebergs within a study region. This thesis reports on work carried out to investigate whether a correction to the sea ice thickness PDF can be made to account for icebergs and over what scale(s) this correction is valid. To answer this question data from Autosub and satellite images were used to investigate whether icebergs were randomly distributed both in open ocean and within sea ice. In conclusion, it was found that icebergs do cluster on the scale of typical Autosub missions (~few km). However, there are differences between icebergs in sea ice compared with open water. Therefore, icebergs should be accounted for in the sea ice thickness PDF.

The work in Chapter 7 has been partially reported in the following publication:

Banks, C.J., M.A. Brandon, and P.H. Garthwaite, Measurement of sea ice draft using an autonomous underwater vehicle, *Annals of Glaciology*, 44, In press.

For Judith

Contents

List of Figures

List of Tables

Acknowledgements

To adequately thank everyone involved in some way or another in the production of this thesis would double its length and so I will be brief. To my family and friends for their love and support, words can never express my gratitude.

Next I must thank Simon Cox for encouraging me to return to education even if he did not know he was doing so. I should also like to thank Simon for his assistance with some of the nasty maths.

I am grateful to the officers, crew and members of the scientific party of JR84 in particular those involved in collecting data from the ice floes. The snow depth measurements were entirely collected by Sarah Jenkins and Ziggy Pozzi Walker. The latter proved to be a most amiable cabin mate keeping the potential aroma from his feet under control, I hope I did likewise. I owe a large debt of thanks to the Autosub crew in particular Steve McPhail for showing great patience and for always answering my email. Dan Hayes has been an endless source of information and again was always willing to answer my emails even when he moved to Cyprus to get away from my questions. Others who aided with the processing of the AUI data were Kate Stansfield and Povl Abrahamsen. Thanks also to David Vaughan who helped me try and make sense of the multibeam data as well as contributing greatly to the work in Chapter 5.

On those rare days in Milton Keynes I was *entertained* by Sam Hammond, Wes Fraser and Dave Kemp (if he lowered his standards!). I should also like to thank those unsung heroes who work in the OU Library always ready to help despite on occasions my inability to use the alphabet.

This work was funded by the UK Natural Environment Research Council (NER/S/R/2001/06749).

Last, and by no means least, I must thank my supervisors Mark Brandon and Paul Garthwaite. Paul must be congratulated on always being right even if sometimes it took

me 12 months to agree! Mark showed great patience dealing with my constant stream of queries and empathy with the *joys* of completing a PhD.

... and finally to anyone else to whom I owe thanks and I have forgotten. Thanks!

Commonly used symbols (and units)

Symbol	Description
a_r	effective range of a semi-variogram
c	speed of sound in water (ms^{-1})
C_o	nugget variance
D	water depth (m)
d_{data}	mean of nearest neighbour distance for data (m)
d_n	mean of nearest neighbour distance for n^{th} simulation (m)
E(X)	expected value of X
e_x	distance travelled at end of an iceberg (m)
F_c	Modified Cressie goodness of fit
g_i, g_j	observed values of ice draft (m)
$\hat{G}$	estimated value of G function
h	lag between two points in a kriging analysis
H(x)	cumulative density function (CDF)
I_d	index of dispersion
k	number of quadrats in a study region
$\hat{K}$	estimated value of K function
m_x	midpoint of distance travelled along an iceberg (m)
N	number of cases
n	number of simulations
P	pressure (decibars unless stated)
p	probability
P_i	angle of pitch (°)
p_s	sill in a semi-variogram
R	angle of roll (°)
$r_{i,A}$	distance from i^{th} iceberg to nearest neighbour within area A (m)
S	salinity (psu)

s^2	sample variance
s_x	distance travelled at start of an iceberg (m)
T	temperature (°C)
t	test statistic
T*	value estimated by kriging
T_f	freezing point of water (°C)
w_1, w_2, w_n	kriging weights
x_z	standardised value of x
$\bar{x}$	sample mean
Y	angle of yaw (°)
z_d	sea ice draft (m)
z_f	sea ice freeboard (m)
z_i	sea ice thickness (m)
z_s	snow depth (cm unless stated)
z_t	value transformed by hyperbolic sine function
α	critical p value
γ	semi-variance
δ	constant
Δ	Kolmogorov distance
Δy	change in measured depth of Autosub ADCP caused by non-zero pitch (m)
θ	pitch of Autosub (°)
κ	test statistic
λ	intensity of a point process
μ	Poisson parameter
ρ_i	density of sea ice (kgm^{-3})
ρ_s	density of snow (kgm^{-3})
ρ_w	density of (sea) water (kgm^{-3})
σ_ε^2	kriging estimation variance

Chapter 1 Introduction

The area covered by and the thickness of Antarctic sea ice are critical variables in the understanding of Earth's climate. For example, the rejection of salt as winter sea ice forms is the primary cause of deep, cold water in the oceans (Budd, 1991). In addition, the amount of sea ice can be used as an indicator of climate change: in the simplest terms a higher volume of ice implies colder global temperature and vice versa. The sea ice-albedo feedback mechanism is where the presence of sea ice increases the amount of energy reflected from the surface and hence decreases the amount of energy input into the ocean. Conversely, during winter, sea ice decreases the loss of heat from ocean to atmosphere compared with the flux from open water.

Sea ice is formed when the temperature of the ocean falls sufficiently to allow the seawater to freeze. This is possible because of the unusual nature of water in that the solid phase is less dense than the liquid phase (i.e., ice floats on water). The presence of sea ice has a number of critical impacts on local and global climate including affecting the exchange of energy and matter between ocean and atmosphere, reducing the amount of light able to penetrate the surface layer and modifying seawater properties. The thickness of sea ice is also a critical variable and Thorndike (2000) points out the thickness of ice is variable in time and space and the way in which it varies is complex. To account for this variability, in climate models for example, the probability density function (PDF) of ice thickness is used. The ice thickness PDF is defined in Section 1.2.2 but is similar to a histogram describing the amount of ice of various thicknesses within a region.

Whilst there are a significant number of data, from satellites regarding the extent of Antarctic sea ice, there are fewer data available on its thickness and there are many more data regarding the sea ice thickness distribution in the Arctic, than relate to the Antarctic. The main reason for this is military although the need for data on pressure ridge impact on oil platforms and shipping are also of importance. Submarines have been operating under Arctic sea ice since the late 1940s and have made underway measurements of sea ice

thickness since the USS *Carp in* 1948 (Calvert, 1960). The development of nuclear powered submarines dramatically increased the operating range of submarines under ice and this was demonstrated in 1958 when the *USS Nautilus* completed the first under ice crossing of the Arctic. Numerous subsequent submarines equipped with upward-looking sonar (ULS) have provided the data used to derive PDFs of sea ice thickness. Using the results from these submarine missions over time, Rothrock *et al.* (1999) have shown a significant thinning of the Arctic ice cover since 1958. In contrast, most work in the Antarctic to date has relied on either synoptic scale satellite imagery concerning the extent/concentration of sea ice (e.g., Gloersen *et al.*, 1992) and thickness work based on drilling holes (e.g., Wadhams *et al.*, 1987).

A key component of the sea ice system is the overlying snow, which increases the overall thickness of the sea ice cover. The snow acts as an insulator and hence affects the thickness of the underlying sea ice as well as the energy exchange between ocean and atmosphere.

Acoustic, upward-looking methods of measuring sea ice draft may well result in the inclusion of the draft of icebergs in the sea ice draft datasets. Ideally, the unwanted signal from icebergs within the sea ice must be removed from the sea ice thickness PDF.

1.1 Importance of sea ice thickness

There are a number of physical quantities that are affected by the thickness of sea ice and in turn, through feedback, may themselves impact on the thickness. These factors include surface temperature of sea ice, turbulent and radiative heat exchange with the atmosphere, potential energy, salt content, compressive strength and ice growth rate (Thorndike *et al.*, 1975).

Radiation from the sun incident on the ocean surface or sea ice surface can either be reflected or absorbed. The amount of radiative energy absorbed is key to the energy balance as it impacts on the temperature of the ocean and hence influences the melting of sea ice. How much energy from the sun is absorbed is described using the albedo, which

is defined as the ratio of reflected radiation to the total incident radiation. The values of albedo for sea ice are highly variable depending on such factors as ice type, ice thickness, snow and water cover, topography and whether ice is melting or forming (Perovich, 1996). The variability of albedo values for different sea surface conditions given in Perovich (1996) is large with a minimum value of 0.05 for open water. The values of albedo for sea ice are given as between 0.4 and 0.7 depending on the ice type. In general, the presence of snow increases the albedo with a value of the albedo for new snow of 0.87 (seventeen times greater than that for open water). As can be seen by the large area of sea ice coverage (see below), the much higher albedo obviously has a significant impact on the Earth's radiation balance. Sea ice reflects much of the incident solar radiation and has a positive feedback effect as more ice reflects more radiation and *vice versa*. Conversely, because of the low thermal conductivity of sea ice as the thickness increases the heat exchange between the top and bottom surfaces is reduced.

As sea ice forms, salt is rejected and denser (i.e., higher salinity) water is formed. In winter, cooling alone is insufficient to cause mixing deeper than the 100-200m deep wind induced mixing (Budd, 1991). With the addition of dense water formed during sea ice formation there is deeper mixing. The more sea ice that is formed (i.e., the higher the thickness) the greater the volume of high salinity water produced. Conversely, in summer melting a higher thickness of ice results in the addition of an increased volume of cold, low salinity water that also impacts on the stability of the water column and the production of water masses.

1.2 Background to project

In Antarctica the paucity of ice thickness data means that the PDF of sea ice is poorly understood. This thesis is concerned with the production of PDFs for sea ice draft by developing a novel methodology using data collected from Autosub, an autonomous underwater vehicle (AUV), in the eastern Amundsen Sea. A photograph of the Autosub vehicle about to be deployed from *RRS James Clark Ross* is shown in Figure 1-1.

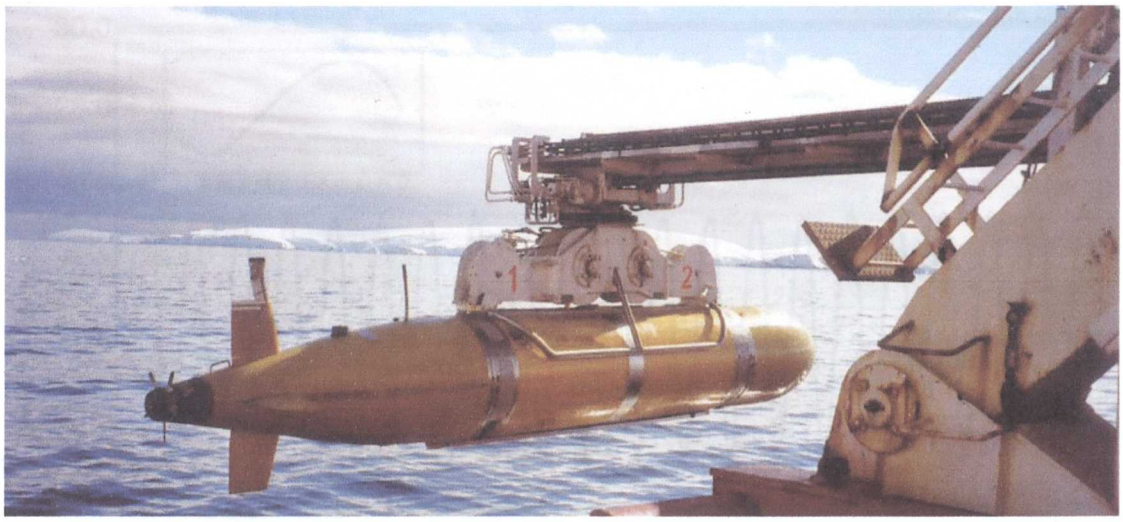

Figure 1-1 Autosub vehicle ready for launch from aft of *RRS James Clark Ross.*

1.2.1 Scale and seasonality of Antarctic sea ice cover

The seasonal variation in the amount of Antarctic sea ice is considerable; there is also a significant, but smaller, interannual variation. Zwally *et al.* (2002a) provides average values of sea ice extent from satellite measurements for a twenty-year period between 1978 and 1998, where sea ice extent is defined as those areas with greater than 15% of ice within a pixel. The variation of sea ice extent is shown in the time series of total Antarctic sea ice extent from Zwally *et al.* (2002a) in Figure 1-2 although the interannual differences are harder to observe in this representation than the seasonal fluctuations. Also shown in Figure 1-2 is the averaged monthly sea ice extent showing the averaged seasonal variability of sea ice extent. The mean winter (i.e., maximum) extent is given as 17.1 $x10^6$ km^2 with a maximum in September 1998 of 18.7 $x10^6$ km^2. The mean summer extent is less than a quarter of the winter value at 3.9 $x10^6$ km^2 with a minimum of 2.46 $x10^6$ km^2 in February 1993.

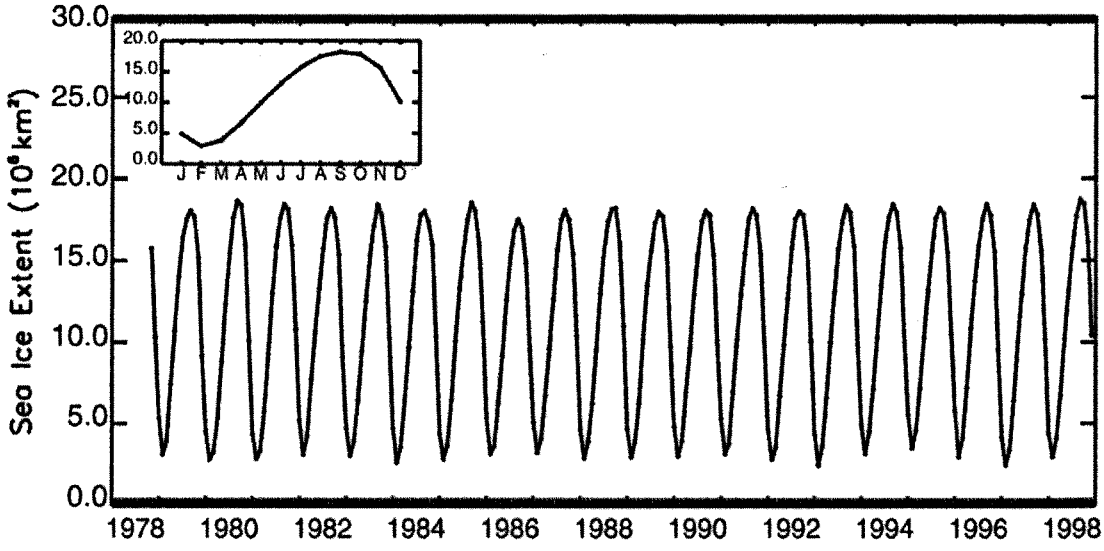

Figure 1-2 Time series of satellite derived monthly average Antarctic sea ice extent (10^6 km^2) from November 1978 through December 1998. Sea ice extent is defined as all pixels with greater than 15% of ice. Inset shows the seasonal cycle averaged over the 20-year period. Taken from Zwally *et al.* (2002a).

Whilst the overall sea ice extent may not show any significant variability, different regions can show noticeable variability in sea ice concentration as can be seen in Figure 1-3 taken from Gloersen *et al.* (1999). Figure 1-3 shows the decadal changes in sea ice concentration (based on an 18.2 year record) over the southern hemisphere demonstrating the high spatial variability of the concentration.

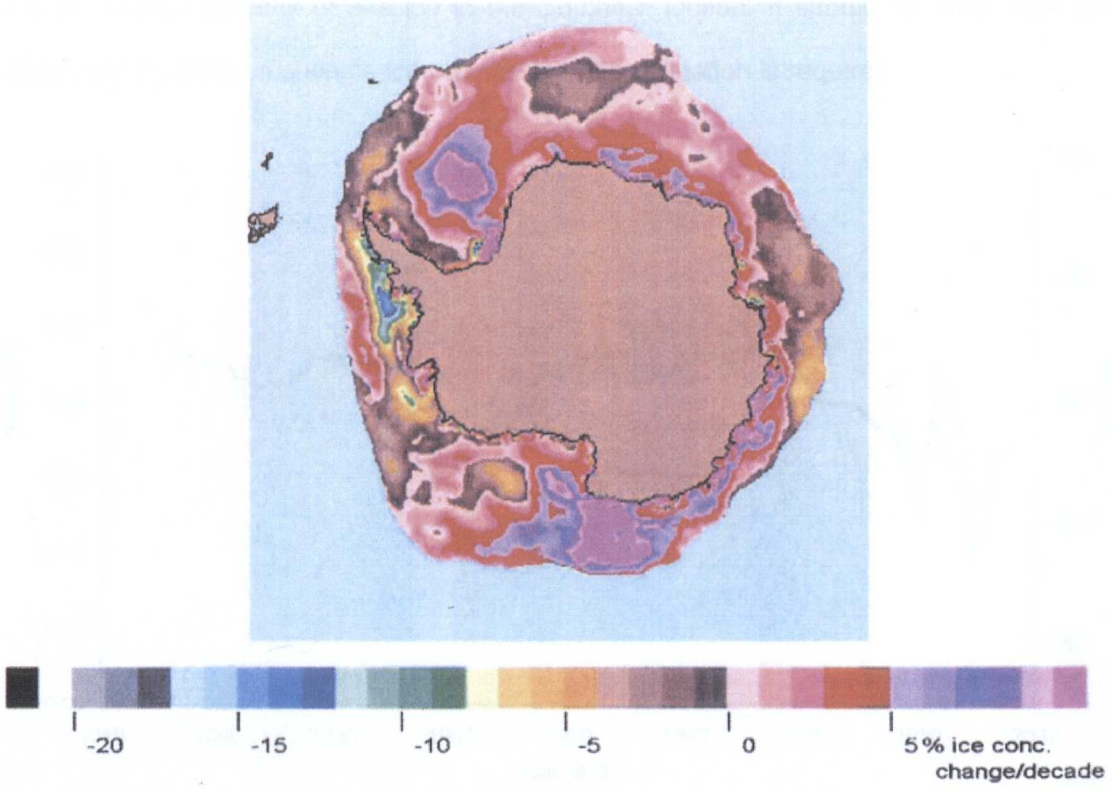

Figure 1-3 Satellite derived variations in the sea ice concentrations from Gloersen *et al.* (1999). The colour bar shows the decadal change in sea ice concentration.

Longer-term variability has been studied by using methanesulphonic acid (MSA) as a proxy. MSA is a product of biological activity and in the Southern Ocean MSA production is dominated by algae in sea ice covered areas (Curran *et al.*, 2003). Figure 1-4 is taken from Curran *et al.* (2003) and shows the relationship between the amount of MSA from a single ice core at Law Dome and the sea ice extent (as a latitude) in the region between 80°E to 140°E for the period between 1841 and 1995. The 20-year running mean (thick black line) indicates that within this sector the amount of MSA remained fairly constant up until about 1950 when it began to decline. During the overlapping periods (1974 to 1995) the satellite derived sea ice extent values for this region shown in Figure 1-4 (black line with open circles) correlate with the MSA concentration and hence MSA can be used as a proxy for the historical sea ice extent record. The conclusion of Curran *et al.* was that this decrease in MSA resulted from a corresponding decrease in sea ice extent within this sector. The study also indicated a significant correlation between the MSA concentration

and the overall quantity of sea ice in the Southern Ocean. It should be noted that the study only reported on a single ice core and further validation is required.

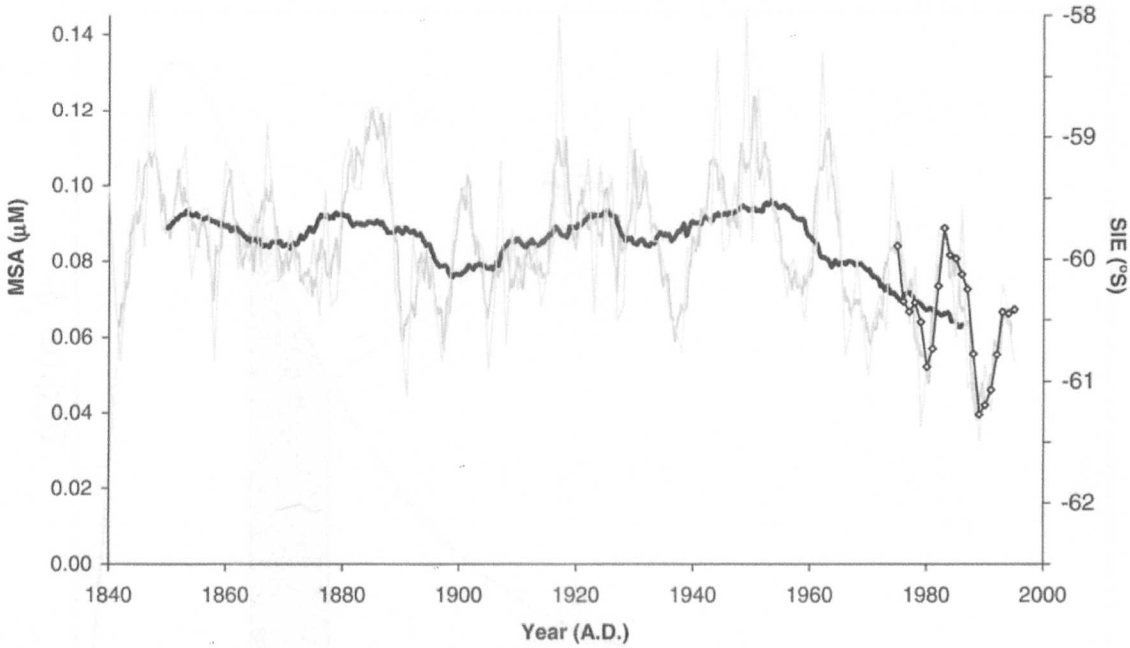

Figure 1-4 Law Dome annual MSA record (light grey) compared with maximum sea ice extent derived from satellite methods (1974 to 1995) from August, September and October (black line with open circles). Thick grey line is 3-year running mean of MSA and thick black line is 20-year running mean. Taken from Curran *et al.* (2003).

1.2.2 Thickness distribution

The aim of many studies of Antarctic sea ice draft or thickness, including this one, is to derive a probability density function (PDF) of the ice draft or thickness. A hypothetical PDF is shown in Figure 1-5. The sea ice draft distribution is defined (Thorndike *et al.*, 1975) for region **R** of area R containing an area of ice with draft between z_1 and z_2 of $A(z_1,z_2)$ then

$$\int_{z_1}^{z_2} g(z)\,dz = \frac{1}{R} A(z_1, z_2) \qquad (1.1).$$

If the units of ice draft are given in metres then the units for the PDF, g(z), are m^{-1} and the area under the curve is dimensionless. The total area under the curve in Figure 1-5 or

similar plots is always one. For any given value of z the equivalent value of g(z) indicates the relative amount of ice of that draft with the region.

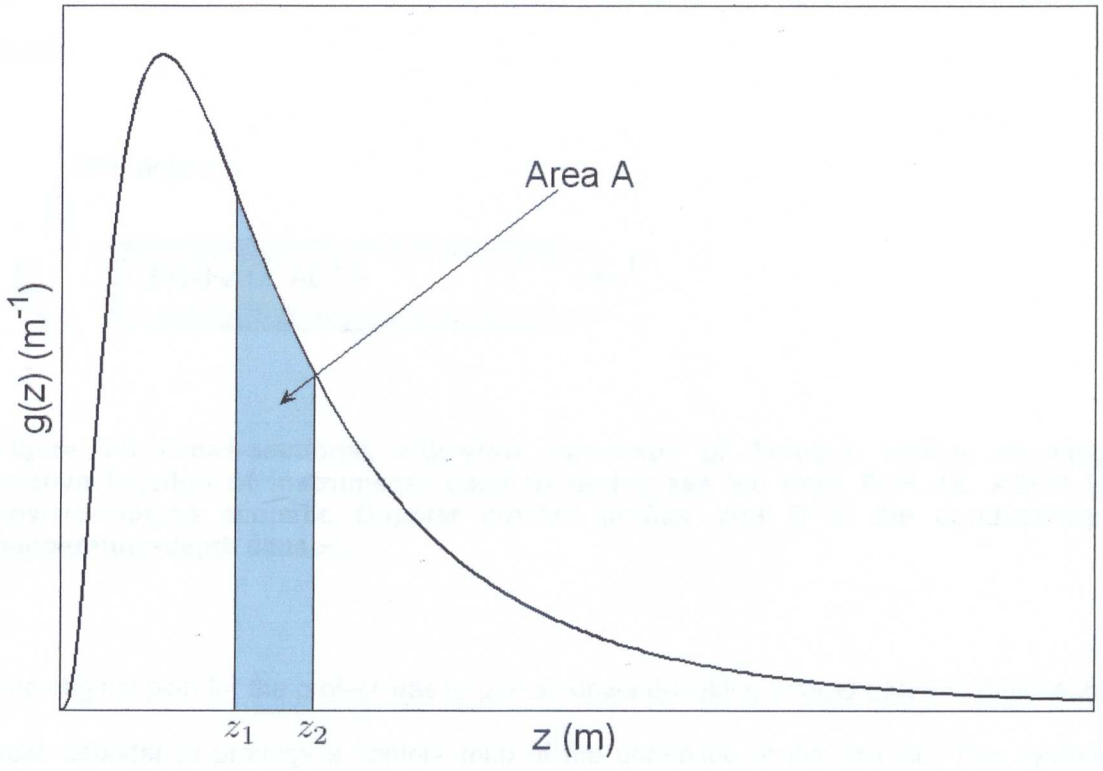

Figure 1-5 Theoretical PDF for sea ice draft for region of area R, showing shaded area A with sea ice draft between h_1 and h_2.

The shape of the PDF depends on a combination of thermodynamic and dynamic processes. Dynamic processes tend to redistribute the thickness of sea ice by creating pressure ridges whereas thermodynamics thickens (freezes) or thins (melts) sea ice. Further discussion of these processes is given in Chapter 2.

1.3 Autosub

The platform for the data collection for this thesis was the 7m long Autosub AUV that was designed, built and operated by the National Oceanography Centre, Southampton (see Millard *et al.*, (1998) for further details). Autosub was designed with a long-range capability ~hundreds of kilometres (up to 60 hours endurance) and has to date completed in excess of 350 scientific missions with the longest mission over 250km in length. With a

diameter of 0.9m Autosub carries a variable scientific payload (~1m^3 volume) according to mission requirements. A simple, schematic cross-sectional representation of Autosub is given in Figure 1-6 and shows the relative locations of all the instruments used within this thesis.

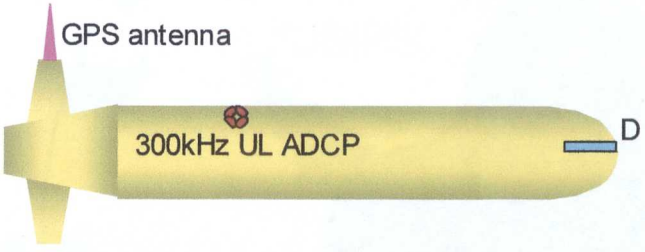

Figure 1-6 Cross-sectional, side-view schematic of Autosub vehicle showing relative location of instruments used to derive sea ice draft PDF. UL ADCP is upward-looking acoustic Doppler current profiler and D is the conductivity-temperature-depth sensor.

The original plan for the project was to use an upward-looking Simrad EM2000 multibeam echo sounder to produce a contour map of the underside of the sea ice. This system failed to provide any useful data and the reasons will be discussed in Chapter 7. Figure 1-7 shows an image of Antarctica and the Southern Ocean with the locations of the Autosub Under Ice (AUI) study region marked in red. The cruise track for each of the missions was originally designed to utilise the multibeam nature of the data and an example of the pattern design (for M324) is shown in Figure 1-8. The *lawnmower* pattern, as it was referred to because of the parallel transects, would have enabled readings based on pings from the port side to be compared with pings from the starboard side on the adjacent leg. The V-shaped track at the end of the mission over the studied region was to provide information on the impact of the vehicle's direction on the measurements.

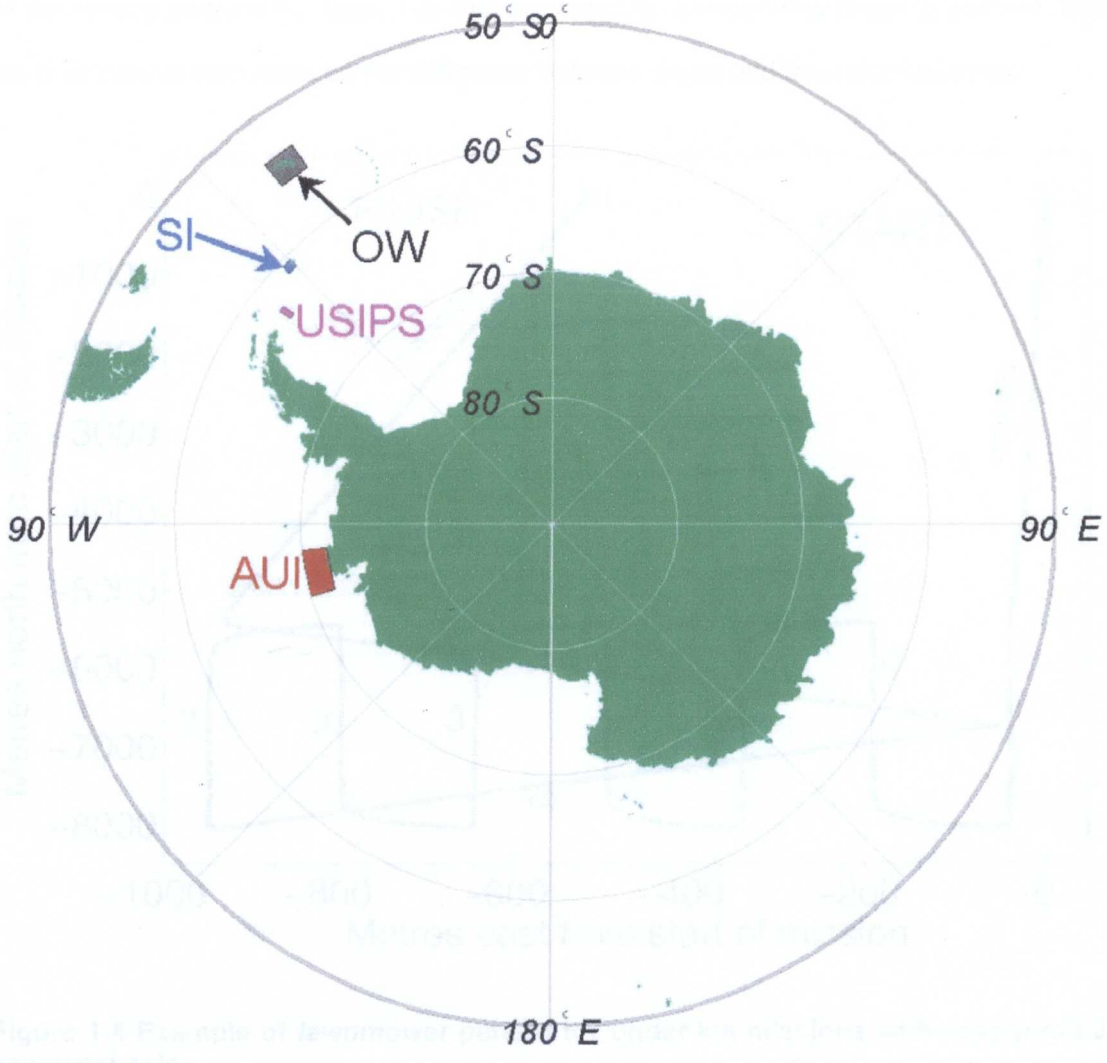

Figure 1-7 Map of Antarctica showing AUI (Autosub Under Ice) study region. Also shown are the USIPS (Under Sea Ice and Pelagic Surveys) study region to be used in Chapter 4 as well as the locations of the two satellite images used in Chapter 5 marked as SI and OW.

As the multibeam system could not provide useful data a new methodology described in this thesis is used to derive the sea ice draft PDF using the upward-looking acoustic Doppler current profiler (ADCP) mounted on Autosub (located as shown in Figure 1-6). The ADCP provides an estimate of range to surface for each of its four beams. These range values are normally used to establish the range over which currents can effectively be measured without interference from side-lobes from surface returns (RD Instruments, 1996). Autosub is also fitted with conductivity-temperature sensors (mounted in the nose

of the vehicle as seen in Figure 1-6) that are capable of measuring depth (pressure). Sea ice draft can be calculated as the difference between depth and the values of range.

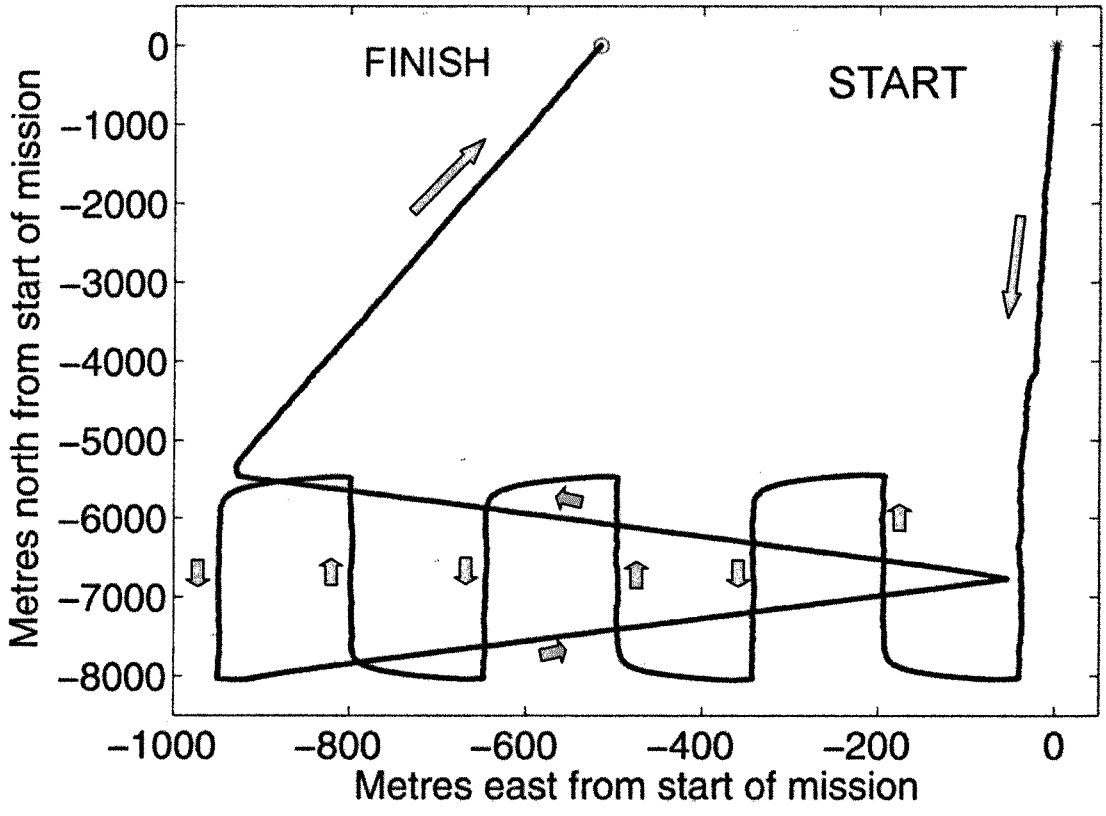

Figure 1-8 Example of *lawnmower* pattern for under ice missions with exaggerated east-west axis.

1.4 Use of ADCP under sea ice

The use of upward-looking ADCP to measure sea ice velocity from a moored buoy has been achieved (Belliveau *et al.*, 1990). These authors suggested that an ADCP could discriminate between open water and ice covered water and this has also since been achieved (Visbeck and Fischer, 1995). In this latter study, the range to surface was estimated using the local maximum of the backscattered signal. However, no high-precision depth sensor was available on the mooring and so no estimates of ice draft could be made. More recently, Shcherbina *et al.* (2005) reported on work using a moored upward–looking ADCP coupled with a high-precision depth sensor to measure the draft of

sea ice. A critical variable in calculating the range to the surface is the speed of sound between the sensor and the surface. The authors concluded that the unknown sound speed profile has a significant impact on the measured ice draft. Another critical variable identified by the authors is the variability of depth due to changes in atmospheric pressure. The work presented in this thesis allows these variables to be accounted for.

1.5 Research questions

Sea ice thickness is of such importance that data to establish the PDF is critical. However, there are few data on sea ice thickness in the Antarctic that do not come from ship-based observations, drilled point measurements or large-scale satellite measurements. The research questions this thesis aims to ask are given below along with a brief explanation of the importance of each.

1. Produce a series of PDFs and descriptive statistics for sea ice draft using measurements from Autosub. This is the key question within this thesis for the reasons above.

2. Provide a geostatistical analysis of the data from 1. This ensures that the spatial nature of the sampling is accounted for and provides revised PDFs.

3. Investigate the variability of snow depth on sampled floes because in order to convert sea ice draft to thickness knowledge of the snow depth is required.

4. Compare the distributions from 1 and 2 above with ship-based observations and direct measurements of snow and ice thickness. This question is concerned with validating the novel methodology described in this thesis.

5. Investigate the likely impact of the spatial distribution of icebergs (whether they cluster or not) on measurements of ice draft from ULS or similar methods (e.g., using Autosub as described in Research Question 1 above). Icebergs generally have a larger draft than sea ice and so a cluster of icebergs would

increase the average measured sea ice draft where no other means exist for discriminating between icebergs and sea ice.

1.6 Summary and thesis outline

This chapter has introduced the background for the topics to be considered in this thesis. In Chapter 2 I present the current state of knowledge of the formation of sea ice and icebergs as well as discussing some of the processes that impact on the shape of the thickness PDF. This is followed, in Chapter 3 by an introduction to the spatial statistical methods required.

From Chapter 4 onwards, I will answer the research questions posed above as follows. In Chapters 4 and 5, the spatial distribution of icebergs and the likely impact of this on the sea ice draft PDF is tested. Chapter 4 uses one-dimensional data collected using Autosub in 2001. Work on the same research question is extended to two-dimensional satellite images in Chapter 5. In Chapter 6 I report on work measuring sea ice thickness from drilling on a number of floes. In addition, I describe work on measuring the snow depth across the same floes. Chapter 7 provides details of the new methodology using Autosub to measure the draft of sea ice. The results of these data are reported as well as the impact of geostatistical analyses. Finally in Chapter 8, the results from all chapters are discussed in light of the questions posed in Section 1.5. Chapter 8 also reports my conclusions and my recommendations for further work.

Chapter 2 The nature of ice in the ocean

This thesis is designed to provide data on sea ice draft (and hence estimates of thickness) in the Antarctic. This chapter provides information on how sea ice forms, how the shape of the thickness distribution changes due to physical and thermodynamic processes and details of how previous measurements of ice thickness have been made. In addition, a review is made of the existing data on the sea ice thickness distribution in the Bellingshausen/Amundsen Seas. Icebergs obviously do exist within the sea ice zone and because of their possible impact on measurements of the sea ice draft PDF a brief explanation of their formation is included.

2.1 Sea ice formation

A common misunderstanding by the general public is that sea ice and icebergs are the same. However, the fundamental differences between the two are critical. Icebergs are glacial in origin and are originally formed on land. In contrast, sea ice is created when seawater freezes. The presence of salts in seawater depresses the freezing point below 0°C. The freezing point of water T_f in °C of salinity S (in practical salinity units - psu) and pressure P (in bars) is

$$T_f = aS + bS^{3/2} + cS^2 + dP \tag{2.1}$$

where a = -0.0575, b = 1.710523×10^{-3}, c = -2.154996×10^{-4} and d= -0.00753 (Apel, 1987). Using Equation (2.1), typical seawater (salinity 34 psu, standard atmospheric pressure 1013.25 millibars) would have a freezing point of -1.87°C.

The saline nature of seawater also affects the temperature of maximum seawater density. Above a salinity of 24.7 psu, as the temperature of the sea surface water cools, the density of the water increases and convection mixes the surface water to the depth of the pycnocline. Therefore for ice to form in the ocean the temperature of the water column from the surface down to the pycnocline must be at or below the freezing point.

An outline of the formation of the various sea ice types is given in Figure 2-1 based on standard nomenclature (WMO, 1970). This forms the basis of the following paragraphs. In Figure 2-1 the sun symbols are used to explain that *second-year* ice has survived a single summer of melting whereas *multi-year* ice has survived at least two summer melt seasons.

The initial appearance of sea ice is as small crystals called frazil. These frazil crystals form throughout the mixed surface layer including on the surface. As the number of crystals increases they begin to coalesce to form a grease ice slick (a mixture of seawater and frazil crystals) that results in the sea surface appearing dull as it reflects little light (WMO, 1970).

The next stage of development depends on the sea state – whether the sea is calm or disturbed. The surface may be calm because the area in which the ice is forming is deep within the pack so swell (in particular high frequency) has been attenuated (Squire and Moore, 1980) or, less likely in the Antarctic, because there is little wind or swell. If the surface is calm then the right-hand option in Figure 2-1 is followed and a thin flexible covering of nilas is formed. Nilas can be further sub-divided depending on the thickness into dark and light nilas and often *finger-rafts*. Finger-rafting is the process by which alternate floes are forced over and under each other to provide interlocking *fingers* of ice. Figure 2-2 shows an example of nilas formed on a calm surface deep within the pack ice in the Antarctic and also shows an example of finger-rafting.

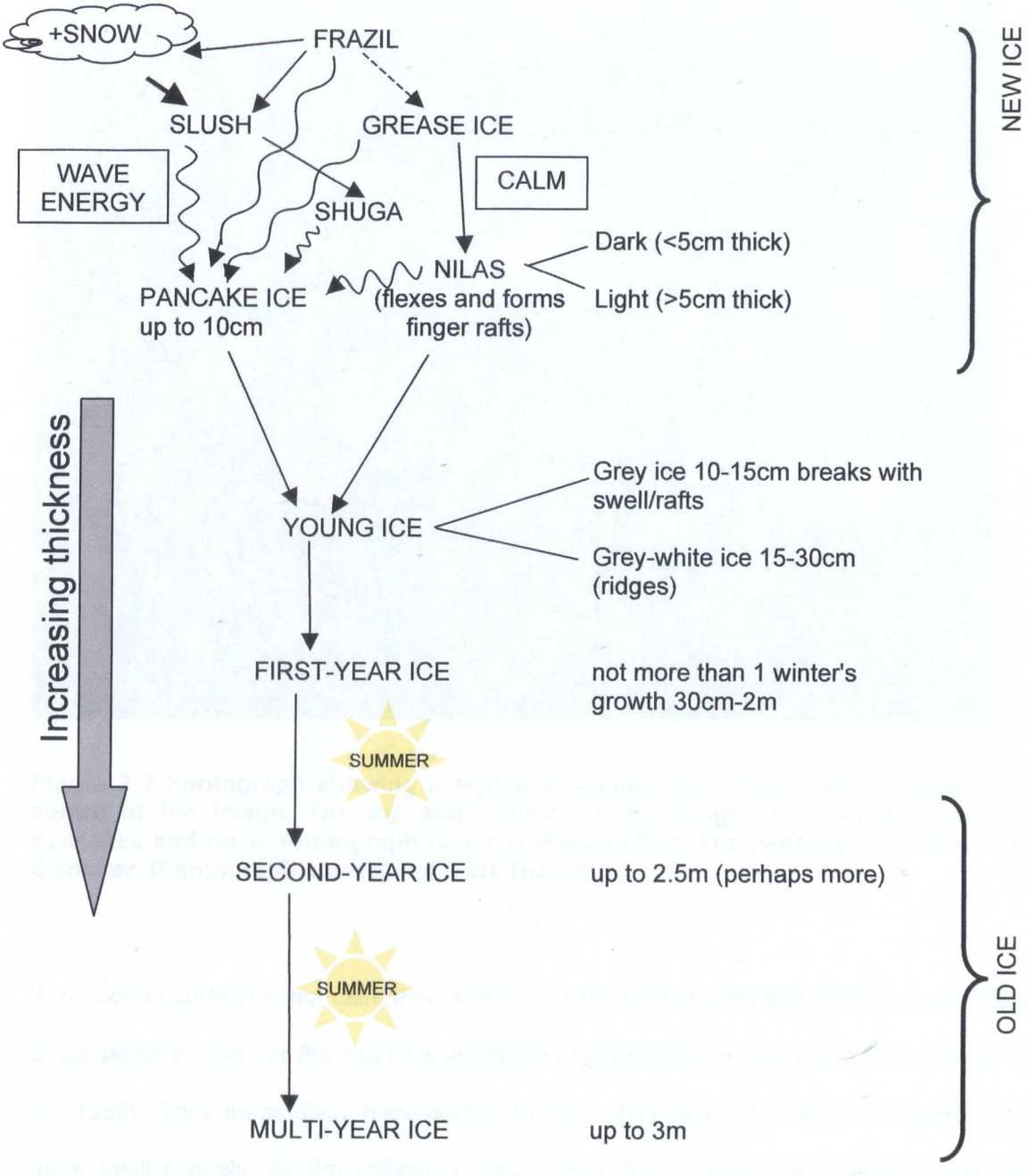

Figure 2-1 Formation of sea ice types based on WMO (1970). Wavy lines indicate ice type formed along that path through the action of waves/swell.

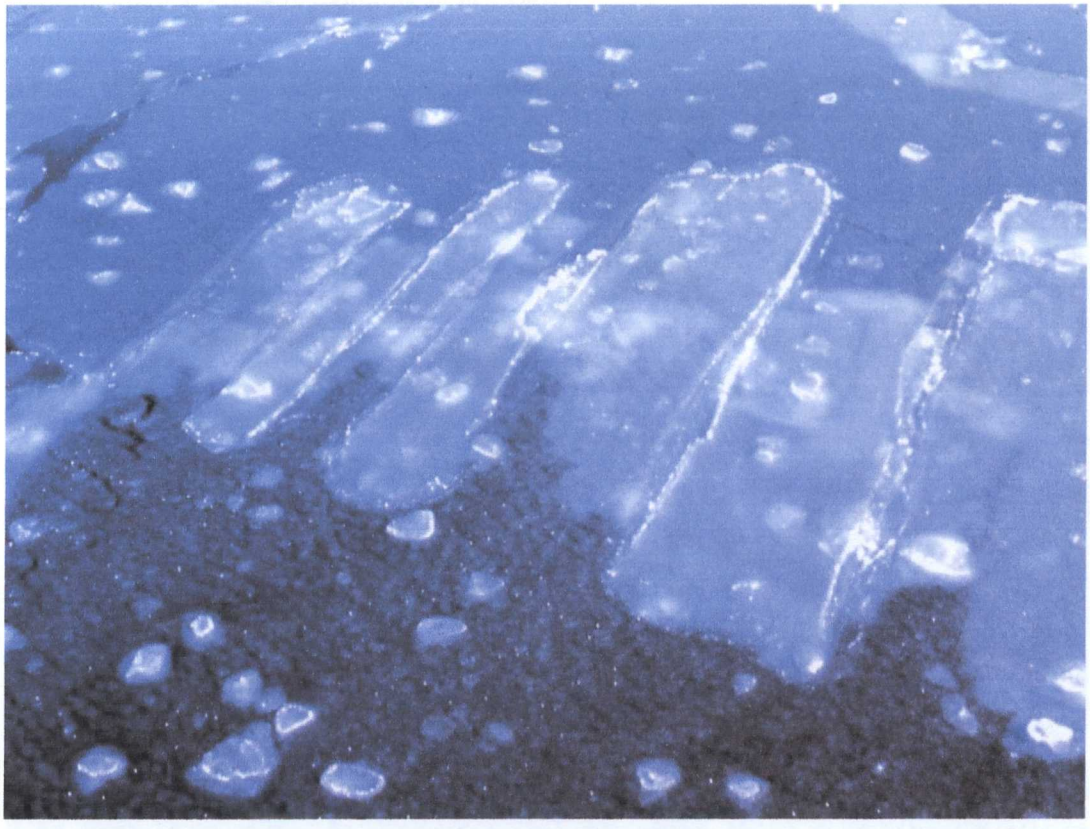

Figure 2-2 Photograph showing a region of young nilas finger rafting across the centre of the image. The top and bottom of the image show an amalgam of pancakes and frazil. Photograph taken in Weddell Sea. The pancakes are ~20cm in diameter. (Photograph courtesy of Mark Brandon).

If the ocean surface is not calm then sheets of nilas cannot form and instead small discs of ice begin to form as the frazil ice undergoes compression in the wave field (Lange *et al.*, 1989). Once these discs have started to form, they then grow with the accretion of more frazil crystals. As the individual discs collide frazil crystals are washed onto the edges and small rims begin to form and these discs with raised edges are known as pancake ice (WMO, 1970). Examples of pancakes are shown in Figure 2-3. Further from the ice edge as high frequency waves (i.e., shorter wavelength) are attenuated then the pancakes are able to grow in diameter and the pancakes coalesce into larger floes with frazil filling the gaps between floes (Wadhams *et al.*, 1987). Observations in the Weddell Sea suggest that at distances of above ~270km from the ice edge the pancakes start to

form a region of consolidated pancake ice (Wadhams, 2000) and that in midwinter this is the dominant ice type (Wadhams *et al.*, 1987).

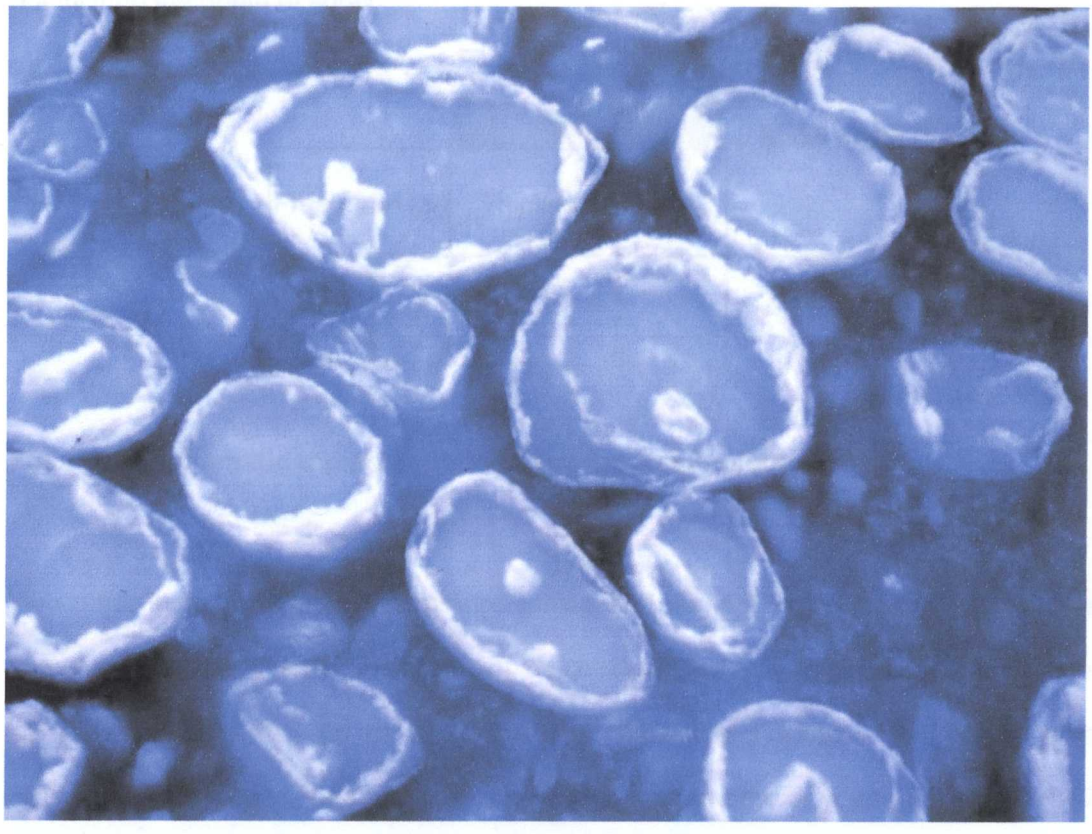

Figure 2-3 Photograph from the Greenland Sea showing a number of pancakes with the interstitial gaps filled with thinner frazil ice. Notice the raised ridges around the edges of the pancakes formed during collisions. The pancakes are ~50cm in diameter. (Photograph courtesy of Mark Brandon).

Once ice of any type has formed on the surface then water freezes on the underside and the ice grows downwards in a process known as congelation ice growth. In addition, snow falling on the surface of the ice can also contribute to the ice matrix and this will be discussed in Section 2.4.

2.2 Sea ice thickness terminology

Figure 2-4 shows how a variety of terms are defined relating to the thickness of sea ice and the location of the sea surface. To summarise, the total thickness of sea ice is the sum of the thickness of sea ice below local sea level (draft) and the thickness above sea

level (freeboard). Depending on the method used to measure the thickness of sea ice the snow depth (z_s) may or may not be included. Unless stated, thickness in this thesis does not include the depth of snow.

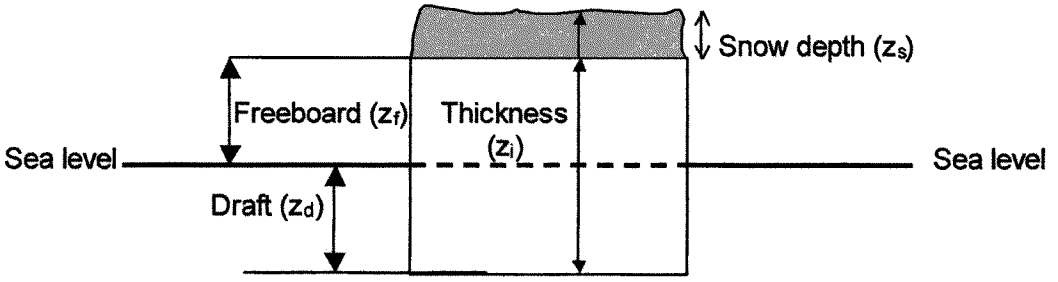

Figure 2-4 Schematic representation of sea ice terminology.

Two other important sea ice terms are rafting and ridging, which describe the different processes that result when two pieces of ice collide under pressure. In rafting one piece of ice is forced over the top of another so the new total thickness is the sum of the thicknesses of the two floes and this is most common in new or young ice (WMO, 1970) such as the finger-rafting shown in Figure 2-2. In contrast, ridging is a deformational process and is discussed in the following section.

2.3 Pressure ridges – an introduction

Sea ice is subject to wind and currents and hence drifts: different floes move differentially under the influence of the combined forces, either converging or diverging. The moving floes can collide and the resulting force can cause one or both of the floes to break. The blocks of the broken floe(s) are forced above and below the sea surface to form pressure ridges. Under divergence, floes move apart to create leads – regions of open water – that allow new ice to form, usually as nilas if deep within the pack ice, and are critical to the energy balance of the ocean-atmosphere system.

When a pressure ridge is formed the above sea level part is called a sail and that below is referred to as a keel. Pressure ridges are important when considering the thickness

distribution of Antarctic sea ice as their formation represents a method for generating much thicker ice than would be possible within the lifetime of the floe by thermodynamic processes alone. Pressure ridges represent the thickest ice in the seasonal Antarctic sea ice pack. An example of the sail from a pressure ridges is shown in the photograph in Figure 2-5.

Figure 2-5 Photograph showing a sail from a pressure ridge (on the central floe ~10m across). The collision of two floes labelled A and B resulted in the formation of a region of broken ice blocks that appear in a raised region above the floes' surfaces (maximum elevation ~1m). It is likely that there is a larger underwater keel. Photograph taken in northwestern Weddell Sea. (Photograph courtesy of Mark Brandon).

As with more general research on sea ice the majority of work to date has concentrated on Arctic sea ice rather than that in the Antarctic (in the Arctic the motion of pressure ridges is potentially hazardous to oil pipelines and platforms). Weeks *et al.* (1989) provide a basis for comparing a significant amount of data from the Ross Sea with sites in the Arctic and concluded that the likelihood of finding a ridge of a given size in the Arctic

regions studied was far greater than finding a comparable ridge in the Ross Sea and that ship reports suggested that the Ross Sea was representative of most Antarctic pack (excluding the western Weddell Sea). These results are not surprising given the differences in oceanographic conditions in the two regions and the residence times of sea ice of up to 5-7 years in the Arctic and the much shorter 1-2 years in the Antarctic (Dieckmann and Hellmer, 2003).

Understanding the processes underlying pressure ridge formation are an important consideration when studying the sea ice thickness distribution as it allows an assessment to be made of the likely numbers of pressure ridges within a region. Numerical models are used to model the formation of pressure ridges resulting from the collision of two floes. The factors that affect the shape of ridges include:

1. Friction between the two colliding floes: higher friction results in a smaller sail and a larger keel.
2. Whether there is initially a space between the two floes and whether this space is ice or water filled.
3. The size/thickness of the ice blocks/floes within the lead in 2 above.
4. The thickness of the two colliding floes: larger floes require more energy to be moved and a thinner floe will tend to fracture on collision with a thicker floe.
5. The strength of the two floes although this is clearly related to 4 above.

For further details of numerical modelling of the ridging process see Hopkins (1994) upon which the above list was based and from where Figure 2-6 was originally presented. In this study Hopkins looks at the energetics of ridge building when various parameters were changed, such as friction between blocks, speed of the collision, ice thickness and the elastic modulus of ice. It is clear from Figure 2-6 that the location of the keel and the associated sail are often not at the same location: the sail is to the right of the keel in Figure 2-6.

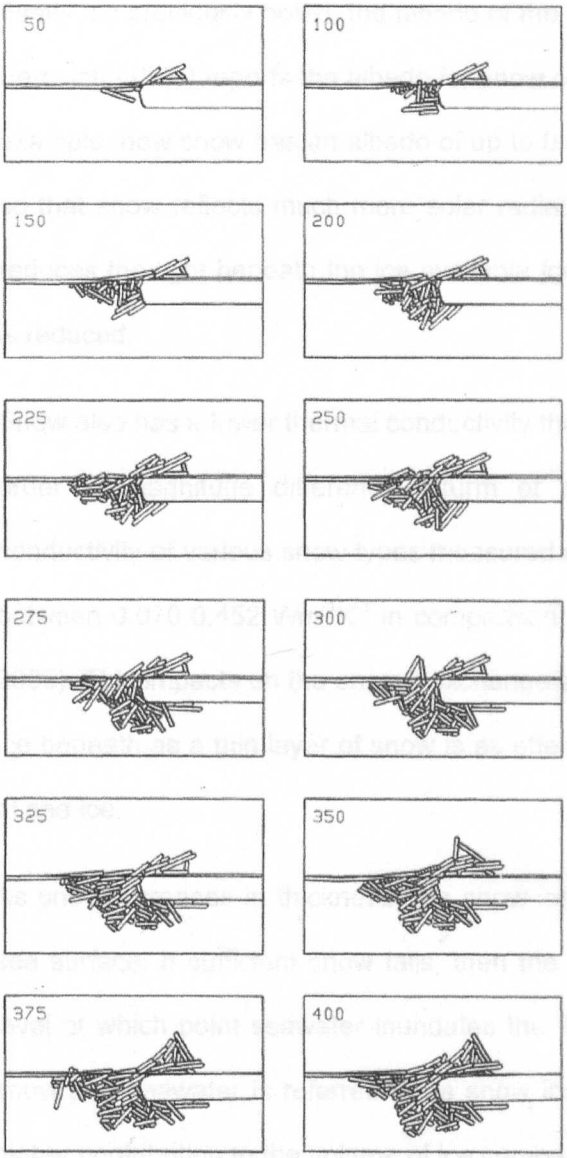

Figure 2-6 Sequential snapshots from a two-dimensional particle simulation model of sea ice ridging (Hopkins, 1994). An intact sheet of thin ice (thickness=30cm) is driven into a thicker sheet (thickness = 2m) with friction coefficients of 1.0 above water and 0.6 below water. The resulting forces cause the sea ice to break into blocks and ridges are formed from the blocks. Each frame is 12mx20m.

2.4 Snow on sea ice

Once sea ice has formed on the ocean surface then any subsequent snowfall will rest on the ice surface. This covering snow changes the characteristics of the sea ice layer in a number of ways and these in turn impact on the complexity of calculating sea ice thickness from values of sea ice draft.

Firstly, as previously noted, the albedo of the surface will increase when covered in snow. Perovich (1996) reports the albedo for snow covered ice as higher than that for sea ice for example, new snow has an albedo of up to 0.87 compared with bare first-year ice of 0.52, so that snow reflects much more solar radiation than sea ice. The reflected light energy reduces the light beneath the ice available for algal growth; hence such biological growth is reduced.

Snow also has a lower thermal conductivity than sea ice; Massom *et al.* (2001) suggest an order of magnitude difference. Sturm *et al.* (1998) provide values of the thermal conductivity of various snow types measured over a number of cruises and the values are between 0.070-0.452 $Wm^{-1}K^{-1}$ in comparison the value for sea ice is ~$2Wm^{-1}K^{-1}$ (Eicken, 2003). This impacts on the energy exchange and hence the formation and structure of the ice beneath as a thin layer of snow is as effective as an insulator as a much thicker layer of sea ice.

As snow increases in thickness, the snow-ice interface is depressed with respect to the sea surface. If sufficient snow falls, then the snow-ice interface is depressed below sea level at which point seawater inundates the floe and the resulting frozen combination of snow and seawater is referred to as snow ice. In the Antarctic snow ice makes a much higher contribution to the volume of ice compared to the Arctic (Jeffries, 1998).

Snow also impacts on the aerodynamic properties of sea ice floes. When wind speeds exceed ~6-$8ms^{-1}$ (at 5m above the surface) snow starts to be blown from snowdrifts that are at right angles to the wind direction (Andreas and Claffey, 1995). As the wind redistributes the snow on sea ice there is a tendency for the surface roughness to be lowered and in turn this reduces the aerodynamic drag of floes (Andreas *et al.*, 1993).

The amount of snow and snow ice as a proportion of the total ice in the ocean can be significant and has been found to be variable. For example, Eicken *et al.* (1994) reports that 4% of the total Weddell Sea ice volume is meteoric in origin. In addition, they suggest that 8% of the ice mass is composed of snow. In contrast, Worby and Massom (1995)

report that on average 18% of the total pack in East Antarctica is snow ice. These values are roughly in agreement with the limits of Lange *et al.* (1990) who suggested that in the Weddell Sea the amount of meteoric ice in the overall ice cover in Austral winter 1986 had a minimum value of 7.1±5.6%. The boundary between sea ice and snow ice is not necessarily easy to establish and can only be achieved with certainty using ice cores and more specifically use of oxygen isotope ratios (Lange *et al.*, 1990). As Massom *et al.* (2001) point out that many authors do not specify whether their results refer to percentages of total core length or composition of individual cores so direct comparisons are not possible.

Reported values for the density of snow vary greatly; Massom *et al.* (2001) summarise a number of studies where for the area of this study the range of snow densities is between 99 and 543kgm^{-3}. The mean values of snow density are less variable and the two relevant studies summarised in Massom *et al.* give a weighted mean of 351kgm^{-3}. Assuming typical values for seawater and sea ice density, a 1m thick sea ice floe would have a draft of ~0.9m without any snow cover; in contrast 50cm of snow on top of this ice would result in a draft of ~1.1m although this does not take into account the formation of snow ice. If the snow depresses the floe sufficiently to become flooded then this will result in the draft increasing as the water or the snow ice, if it forms, has a higher density compared to the snow. Snow is also less dense than glacial ice, Weeks and Mellor (1978) indicate that ~40m of snow depth is required to compact the snow to a similar density to that of glacial ice.

2.4.1 Snow depth distribution

The hydrostatic equilibrium of an ice floe, and hence its draft, depends (amongst other factors) on the weight of the floe including any overlying snow. The weight of the snow is clearly correlated with the thickness of the snow or more accurately with the thickness distribution of the snow. Knowledge of the distribution of snow in the survey region is therefore critical to be able to convert values of sea ice draft into sea ice thickness.

Previous studies of the depth of snow on sea ice in the Antarctic have provided variable results depending on the location of the floes and the season in which the measurements were made. For example, in the Weddell Sea in winter Eicken *et al.* (1994) reports mean snow depths from the Winter-Weddell-Gyre study varying between 0.12m and 0.79m depending on the underlying ice type. Massom *et al.* (2001) summarise a number of studies including some in the Bellingshausen/Amundsen Sea areas for which the snow depths in summer-autumn have a much smaller range with means between 0.29m and 0.49m with standard deviations between 0.15m and 0.30m. It is likely that that this deeper snow is a result of the high regional precipitation (Massom *et al.*, 2001). However, this must have seasonal variation as well because in the same region, for the winter-spring of 1993 Worby *et al.* (1996) provide a mean snow depth of 0.23m from direct measurements with a standard deviation of 0.16m with lower values from ship-based observations (between 0.12m and 0.23m increasing with distance from the ice edge). It should be noted that the direct measurements from Worby *et al* (1996) do not include thin, unconsolidated or thick, heavily ridged floes.

2.5 Conversion of ice draft to thickness

As stated at the beginning of this thesis, apart from sea ice extent the other critical factor relating sea ice and climate is the thickness of ice. Autosub and ULS measure sea ice draft; hence, a relationship is required to convert draft into thickness. An additional issue is the presence (or absence) of snow on the sea ice surface and hence increased variability in the density of the materials within the sea ice matrix. Only estimates of thickness can be made from values of draft (or freeboard) because the effective density of the floe varies according to the amount and type of sea ice, snow, snow ice and possibly water. In addition the densities of these various constituents are not well defined as they vary with such factors as porosity and whether the pore spaces are air or water filled. Bowen and Topham (1996) provide a useful summary of the range of values available for the porosity of Arctic ridges varying from 1% up to 40% for ridges and 30% to 43% for sails.

Whilst hydrostatic equilibrium is maintained over a floe or given region this is not necessarily the same on smaller scales. Melling *et al.* (1993) report that over a scale length of ~200-300m hydrostatic equilibrium is maintained whereas this is not the case on a shorter (~10m) scale. For this reason, making point estimates of ice thickness from ice draft are inappropriate whereas deriving overall regional estimates of thickness, such as those for Autosub missions, are more appropriate.

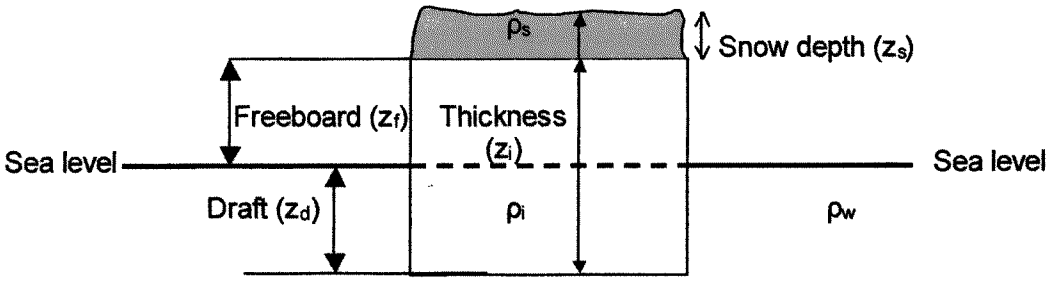

Figure 2-7 Schematic representation of sea ice terminology. ρ_i, ρ_s and ρ_w are the densities of ice, snow and water respectively.

As discussed in Section 2.4, in any one measurement of thickness there is variability in the proportions of how much of the various components of the sea ice matrix there are. In order for hydrostatic balance to be maintained in the situation shown in Figure 2-7 then the following relationship must hold

$$\rho_w z_d = \rho_i (z_d + z_f) + \rho_s z_s \qquad (2.2).$$

Using approximate values of density for seawater and sea ice (ρ_w and ρ_i) as 1027kg m^{-3} and 920 kg m^{-3} the latter as given by Eicken *et al.* (1994) and the late summer/autumnal mean density of snow (ρ_s) from Section 2.4 as 351 kg m^{-3} a relationship exists for the thickness of ice, z_i

$$z_i = z_d + z_f = \frac{\rho_w z_d - \rho_s z_s}{\rho_i}$$
$$z_i \approx \frac{1027 z_d - 351 z_s}{920} \text{ metres} \qquad (2.3).$$

For example, for sea ice with a draft of 1m and 25cm of overlying snow the ice thickness (z_f+z_d) is 1.02m (i.e., a freeboard of 2cm). If the late summer value of snow density of 391kgm^{-3} quoted in Massom *et al* (2001) from Hass *et al* (1996) is used then the ice thickness relating to the same draft is lower at 1.01m (i.e., ~1% reduction).

As discussed before, the equilibrium position can be altered if the snow thickness is sufficient to depress the floe below the sea surface. Sea water can flood the floe (or at a level over which waves can inundate the floe) and depress the floe as the density of the water/snow ice is greater than the density of the snow. Using the same values from Section 2.4 with a 1m depth of sea ice loaded with 50cm of snow resulting in a negative freeboard of ~10cm and allowing this region to flood would result in an additional ~10cm of negative freeboard.

2.5.1 Relationship between snow depth and ice thickness

At points for which both snow and ice thickness are measured there is evidence for an inverse relationship between the two variables suggesting that thinner snow is found on thicker ice. This is possible as wind action on loose snow tends to level the surface so that snow is blown off sails and piles up on the lee side (Worby *et al.*, 1996). In addition, snow retards thermodynamic growth as it is an effective insulator (Eicken *et al.*, 1994). For individual floes that are in hydrostatic equilibrium rather than points that are not the correlation between snow thickness and ice thickness is positive. Worby *et al.* (1996) give an approximation between snow thickness (z_s) and sea ice thickness (z_i) of

$$z_s \approx 0.3 z_i \qquad (2.4).$$

Worby *et al.* (1996) believe this relationship is maintained by additional snow ice being formed at the base of the snow layer when the floe is depressed as new snow falls onto the surface. This approximation was developed using data from late winter and so care must be taken when considering results from other seasons.

2.6 Importance of open water in sea ice

Regions of open water within the sea ice zone are important for a number of different reasons including the energy balance of the ocean/atmosphere and biological impacts. They are also used by ships to make easier passage.

The albedo of open water is low at 0.05 compared with that for ice/snow of 0.15-0.87 (Perovich, 1996) and as such patches of open water absorb far more solar energy than sea ice. This solar energy input through open water not only heats the upper ocean layer but also provides energy for summer melting of sea ice (Steele, 1992). Up to 80% of the thermal energy entering a lead is involved in melting ice and the remaining 20% is stored in the water column even when there is still ice present (i.e., it warms the water) (Steele, 1992). In terms of heat loss, open water is far more efficient at losing energy than sea ice; the sea ice is effectively a cap on the ocean. Using the results from Badgley (1966) it is estimated that heat losses through leads in the Arctic are two orders of magnitude greater than through sea ice (Thorndike *et al.,* 1975). Hence, in an area of sea ice with just 1% of the area as open water, half of the heat lost is through the small fraction of open water.

During winter months open water areas (i.e., leads and polynyas) are sometimes referred to as "ice factories". As regions of open water are exposed to the cold atmosphere sea ice starts to form. This sea ice readily forms ridges (see Figure 2.6) thus creating new, thicker sea ice. This process is often noticeable along the coasts where katabatic winds blow the sea ice offshore. Gill (1973) estimates that within 3km of the shore the amount of brine released is equivalent to 20m of sea ice within a six-month period compared with 6m of sea ice within 30km of the shore.

Finally, mammals (e.g., whales and seals) beneath the ice are dependent on open water patches to allow them to come to the surface to breathe. Many species use polynyas to provide access to open water during the winter although in the Antarctic most polynyas receive little sunlight and hence there is only a very limited source of food for mammals (Ainley *et al.*, 2003).

2.7 Sea ice thickness measurement techniques

A number of different techniques exist for measuring the thickness of sea ice. Most methods rely on inferring the thickness of the ice from measuring either the draft or the freeboard. Methods used in measuring the thickness of sea ice include; visual methods, drilling holes, acoustic systems, radar/laser altimetry and electromagnetic induction methods.

2.7.1 Underway estimates from ships and visual methods

Whilst unable to provide the accuracy of other methods, underway estimates of sea ice thickness are important as they allow relatively large areas to be covered. The method used in this thesis has been developed through the Antarctic Sea-Ice Processes and Climate project (ASPeCt) (Worby, 1999). The ASPeCt protocols allow simple observations from a ship to provide information about the state of sea ice in a region. The system requires a user to make estimates of features such as ice type, ice thickness, amount and scale of ridging as well as type and depth of snow cover. These approaches are most reliable in thinner, less-ridged ice, as differences in the thickness of deeper ice are harder to identify.

2.7.2 Drilling

Whilst drilling provides the most accurate estimate of ice thickness at a point (potentially it also allows differentiation between sea ice, snow and snow ice), it has a number of practical difficulties. Obviously the number of observation is limited by the availability of resources (personnel, equipment and ship time) in addition, drilling parties cannot readily measure the thickness of very thin ice.

In Antarctica most studies involve the drilling of holes not only as the primary data collection process (Ackley, 1979; Lange and Eicken, 1991; Worby *et al.,* 1996) but also for validating or calibrating other methods. For example, Haas (1998) used drilled holes to

evaluate a ship-based electromagnetic induction system and Wadhams *et al.* (1987) used drilling to groundtruth a helicopter-based radar.

2.7.3 Acoustic techniques

Underwater methods for measuring ice thickness normally rely on using sound to measure the distance from a transducer to the reflecting surface (i.e., underside of sea ice) with knowledge of the depth of the transducer. The distance is calculated based on halving the two-way travel time and knowing the speed of sound through which the signal and the echo have travelled. The difference between the depth and the distance to the reflecting surface is a measurement of the sea ice draft that can then be converted to a value for sea ice thickness. The development of the use of under ice sonar to measure ice draft reflects the development of sonar itself. Sonar was developed for military purposes (to detect submarines) and under ice usage was implemented for military purposes, as the Arctic became the front line in the Cold War.

Sonar has been used under Arctic ice since the early 1950s; however its use in Antarctica is more limited because no submarines are known to have operated underwater in the region until the development of Autosub and other AUVs. Autosub was the first moving vehicle to use sonar under ice in Antarctica as part of the Under Sea Ice and Pelagic Systems (USIPS) project (Brierley *et al.*, 2002, 2003).

A number of studies have utilised moored, upward looking sonar buoys but these only provide information about the ice passing over a fixed point. Whilst being an ideal approach to measuring the seasonal fluctuation of sea ice draft over a point, moored ULS do not readily provide any information on the (synoptic) spatial variability of ice draft. Using a number of ULS under certain circumstances Strass and Fahrbach (1998) show how ULS measurements can be used to provide spatial information. The circumstances are that the ice field is moving over the ULS at constant speed or that the ice draft is homogenous over the distance the sea ice moves between consecutive measurements.

To date the largest ULS dataset in the Antarctic was processed by Strass (1998) and provided data on the sea ice draft at a number of locations along either ends of a transect across the Weddell Sea at ~65°S as part of a larger scale oceanographic project investigating the Weddell Gyre (Fahrbach *et al.*, 1994). The other Antarctic ULS mooring study provided data on sea ice draft at a single mooring located off the continental shelf in East Antarctica (*Worby et al.*, 2001).

2.7.4 Electromagnetic induction

The basis of electromagnetic (EM) induction techniques is to use a primary electromagnetic field to induce a secondary electromagnetic field in a conductor. In applied geophysics, this conductor is frequently a shallow buried ore body or groundwater source within low conductivity rock. The strength of the secondary EM field can then be measured and from this the depth of the conductor can be calculated (Telford *et al.*, 1990). Sea ice has a low value of electrical conductivity (i.e., it is an electrical insulator) when compared with seawater which has a much higher conductivity, hence, a primary EM field will produce a secondary EM field in the seawater. Measuring this secondary field allows calculation of the distance from the instrument to the water surface.

The technique of EM induction has been used by placing the instrumentation directly on the ice surface (e.g., Kovacs and Morey, 1991; Kovacs *et al.*, 1996; Haas *et al.*, 1997; Worby *et al.*, 1999); using aircraft based surveys (e.g., Kovacs and Holladay, 1990) and also mounting the instrument on a ship (Haas, 1998). For the latter two approaches the distance from the instrument to the (snow) surface must be subtracted from the distance to the sea surface and this is usually achieved using a laser altimeter.

2.7.5 Satellite methods

For over 30 years, satellite imagery of the sea ice zones in both hemispheres has enabled detailed studies of sea ice extent (e.g., see Figure 1-2). Today, satellite derived monthly summaries of sea ice extent and concentration are readily available from the National

Snow and Ice Data Center website (http://nsidc.org) and the images for March 2003 are shown in Figure 2-8.

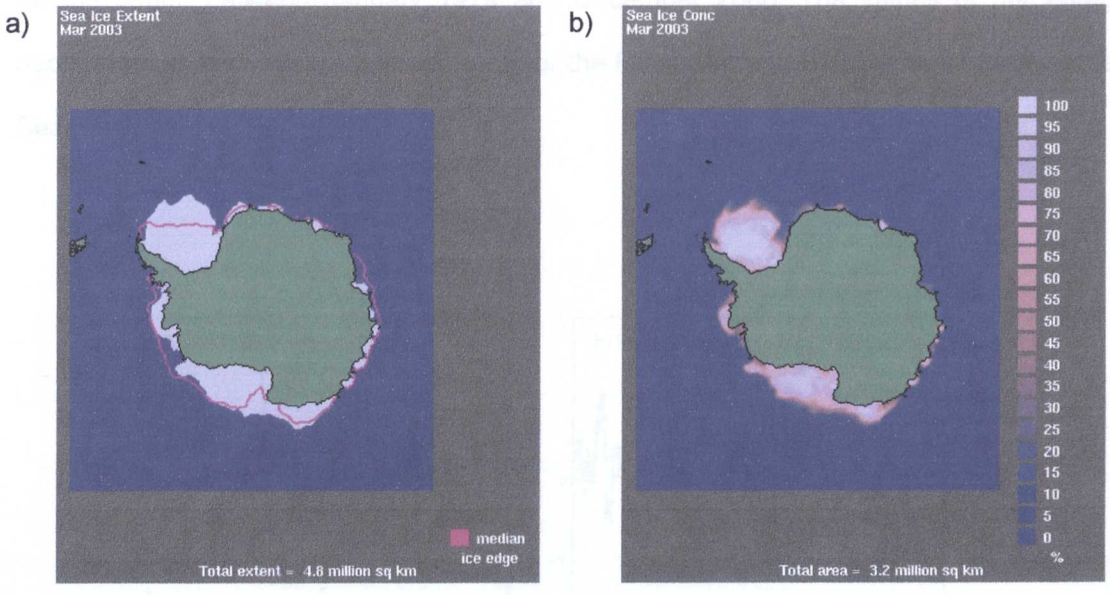

Figure 2-8 Images of the monthly sea ice index from Fetterer and Knowles (2002-updated 2004) for Antarctica in March 2003 for a) sea ice extent shown in pink (see text for explanation of median ice edge) and b) sea ice concentration in % using the colour bar.

The data in Figure 2-8a define sea ice extent using an arbitrary 15% concentration: pixels calculated to have areal sea ice concentration above this 15% cut-off are defined as sea ice and those pixels below 15% are taken to be open water. The median ice edge is based on all data for March between January 1979 and December 2000 where for each pixel the probability is above 0.5 that the sea ice concentration is above 15%.

Regression studies in the northern hemisphere suggest that overall the amount of ice (extent and area*) is declining (Comiso *et al.*, 2003). In the Antarctic there is a slight overall increase in sea ice extent and area although the number of data are limited and hence interpretation is more ambiguous (Comiso, 2003). However, on a regional scale in the southern hemisphere there are significant trends with extent and area increasing in

* Sea ice area is taken to be the extent weighted by the sea ice concentration.

the Ross Sea and decreasing in the Bellingshausen/Amundsen Seas (Comiso, 2003). Figure 2-9 shows the anomalies in sea ice extent for the Antarctic overall and by region for the period between January 1979 and December 2000. The values of percentage decadal trend in sea ice extent and area for the Ross Sea and Bellingshausen/Amundsen Seas are given in Table 2-1.

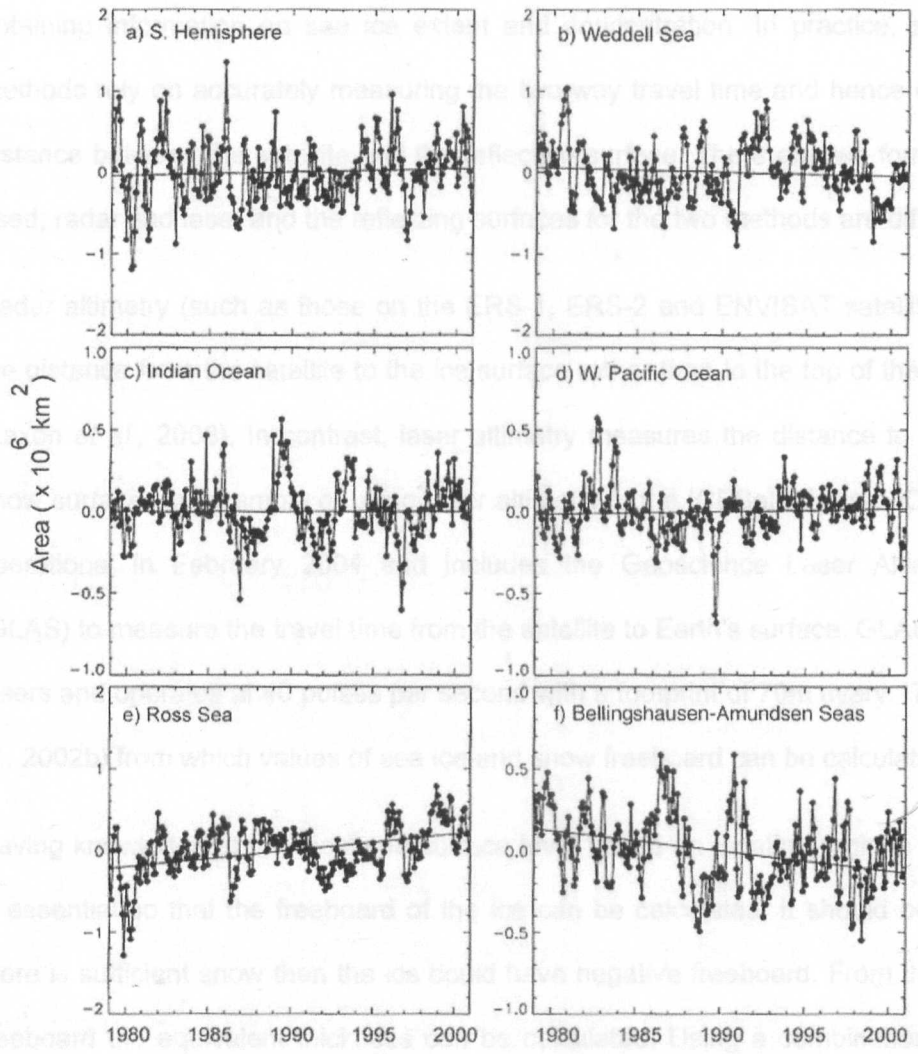

Figure 2-9 Monthly sea ice extent anomalies in the Antarctic and by sector taken from Comiso (2003). The anomalies are calculated as the difference between a value for a given month and the average value over the entire record period (January 1979 to December 2000).

Table 2-1 Trends in extent and area of sea ice for Ross Sea and Bellingshausen/Amundsen Seas based on Comiso (2003)

Region	Trend in extent ± error (% per decade)	Trend in area ± error (% per decade)
Ross Sea	+7.0 ±1.0	+8.7±1.0
Bellingshausen/Amundsen Seas	-8.1±1.4	-6.3±1.5

Using satellites, the derivation of a PDF for sea ice thickness is not as straightforward as obtaining information on sea ice extent and concentration. In practice, satellite based methods rely on accurately measuring the two-way travel time and hence calculating the distance between the satellite and the reflecting surface. There are two forms of altimetry used; radar and laser and the reflecting surfaces for the two methods are different.

Radar altimetry (such as those on the ERS-1, ERS-2 and ENVISAT satellites) measures the distance from the satellite to the ice surface rather than to the top of the snow surface (Laxon *et al.*, 2003). In contrast, laser altimetry measures the distance to the top of the snow surface. An example of using laser altimetry is the ICESat mission. ICESat became operational in February 2004 and includes the Geoscience Laser Altimeter System (GLAS) to measure the travel time from the satellite to Earth's surface. GLAS consists of 3 lasers and operates at 40 pulses per second with a footprint of 70m every 170m (Zwally *et al.*, 2002b) from which values of sea ice and snow freeboard can be calculated.

Having knowledge of the local sea surface level based on locating regions of open water is essential so that the freeboard of the ice can be calculated. It should be noted that if there is sufficient snow then the ice could have negative freeboard. From these values of freeboard the equivalent thickness can be calculated. Using a combination of laser and radar altimetry systems allows the thickness of sea ice and snow cover to be measured. Errors in freeboard measurements are magnified when used to calculate the sea ice thickness because only a small proportion of the ice is above the surface. According to Kwok *et al.* (2004) in the Arctic this proportion is 11% of the floating ice. The proportion in the Antarctic is less because of the higher proportion of snow (as discussed in Section

2.4). This implies that using measurements of freeboard, in particular satellite methods, has a higher error in the Antarctic compared with the Arctic.

In their study, Laxon *et al.* (2003) compared ERS radar measurements of sea ice thickness in the Arctic with "near-co-incident" submarine data (within 15 days and 100km) and obtained a significant relationship between the two estimates of sea ice thickness. They further used the satellite data to show the (inter- and intra- annual) variability of sea ice thickness and suggest that the mean Arctic ice thickness is heavily influenced by changes in the amount of summer melt.

Results from the Arctic from early in the ICESat mission (from March 2003) have also been reported (Kwok *et al.*, 2004). Whilst a precision over smooth ice of ~2cm is given the unknown variability of snow depth provides the largest source of uncertainty in the results. Using an average snow climatology ±10cm to account for the uncertainty Kwok *et al.* report the maximum variation in measured ice thickness was ~0.5m.

2.8 State of knowledge of sea ice thickness in Amundsen/Bellingshausen Seas area

There are limited sea ice draft/thickness data in the Amundsen and Bellingshausen Seas and the two published studies are summarised below.

Haas (1998) reported combined snow and ice thickness from February 1994 with a mean thickness of 3.12m and a mode between 2.7m and 3.1m determined with an electromagnetic sensor. The PDFs for the combined thickness of ice and snow reported in Haas are shown in Figure 2-10 for four profiles. Profiles 054 and 055 were located in the same region as the Autosub missions in this thesis and show that most values of combined ice and snow thickness are between zero and 6m.

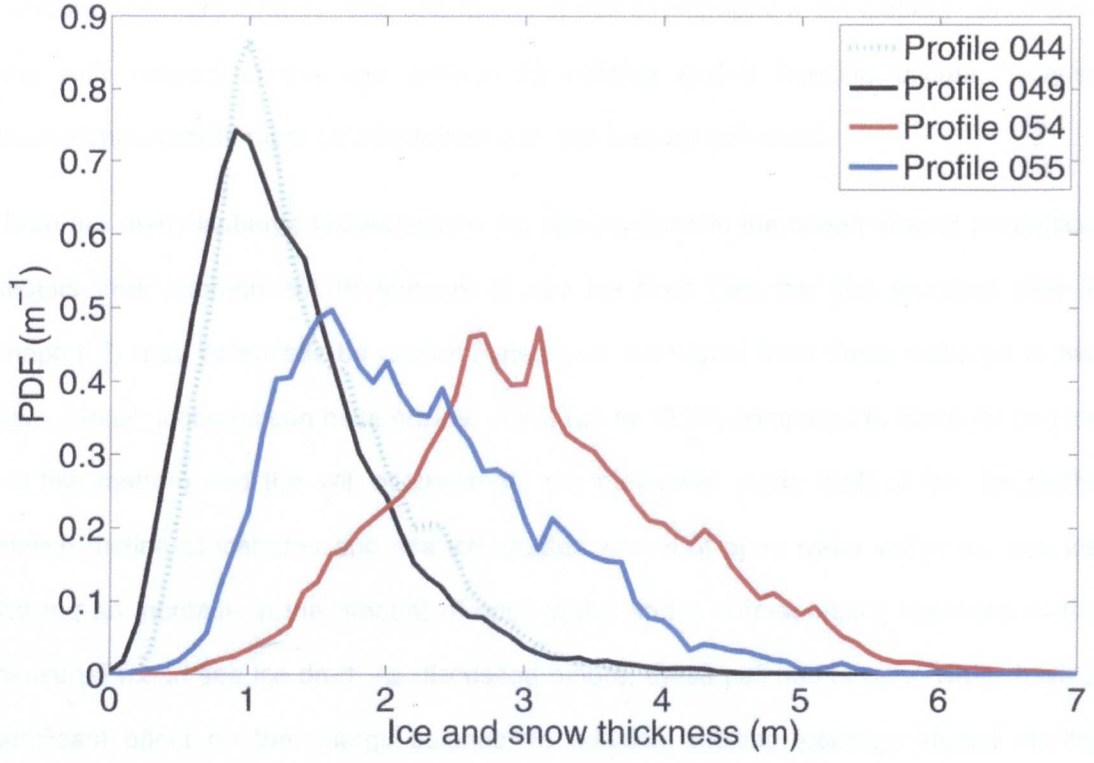

Figure 2-10 PDFs of combined sea ice and snow thickness from the four ship-based profiles reported in Haas (1998). Profiles 054 (red) and 055 (blue) are in the same region as the Autosub missions in this thesis.

Worby *et al.* (1996) used both drilling holes and ship-based observations of ice and snow thickness during late winter. The mean and standard deviation of ice thickness from the drilled measurements (set A) was found to be 0.90m and 0.64m respectively and the snow mean thickness was 0.23m (i.e., an average total thickness of 1.13m). The ship-based observations (set B) show an increase in ice thickness with distance from the ice edge from 0.45m to 0.65m in a similar manner to the mean values of snow depth discussed in Section 2.4.1.

2.9 Icebergs and their spatial distribution

When pieces of glaciers and ice shelves (glacier floating on the ocean) calve into the ocean the resulting floating pieces of ice are referred to as icebergs although strictly speaking an iceberg is calved glacial ice in the ocean with freeboard > 5m (WMO, 1970). Glaciers are formed on land by the accumulation of layers of precipitation (snow) and

therefore have stratigraphy. The orientation of this stratigraphy in an iceberg varies over time with respect to the sea surface as melting and/or freezing occurs because gravitational stability must be maintained (i.e., the iceberg rolls over).

There are many icebergs located within the sea ice zone in the ocean around Antarctica. Results from submarine/AUV surveys of sea ice draft (like the one reported later in Chapter 7) may potentially be contaminated with the signal from these icebergs in two ways. Firstly, icebergs can have greater drafts (up to 300m) compared to those for sea ice (~a few metres) and this will overestimate the measured mean draft of ice. Secondly, relative motion of icebergs and sea ice creates *wakes* of open water within the sea ice causing an increase in the amount of open water and a corresponding decrease in the measured mean sea ice draft. As discussed before, these patches of open water have a significant effect on the energy balance. In addition, melting icebergs impact on the stability of the water column (i.e., changes the density structure) by adding relatively low salinity, cold water into the ocean (Huppert and Josberger, 1980).

Figure 2-11 is an ASTER image clearly showing patches of open water within the sea ice region associated with the relative motion of icebergs and sea ice. Whilst very large values of ice draft (>~15m) in Antarctic data sets can be accounted for by icebergs; the cut-off value at which this occurs is not obvious. In addition, no account can be made of the open water wakes, compared to other causes of open water, when trying to establish the distribution of ice draft. As well as reporting on measurements of sea ice draft, this thesis (Chapters 4 and 5) also considers assessing the potential contamination of upward looking approaches of measuring sea ice draft from icebergs resulting from the spatial distribution of icebergs.

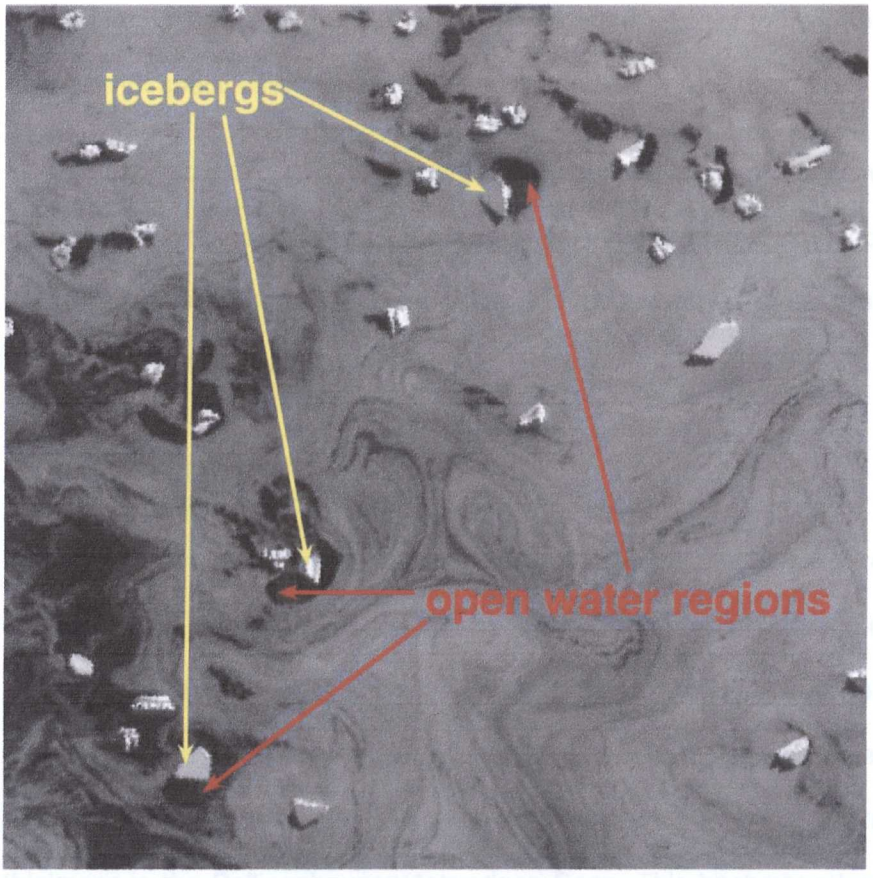

Figure 2-11 ASTER image of a number of icebergs (bright area) within a region of sea ice (grey) showing the 'wakes' (regions of open water – black) created by the relative motion of iceberg and sea ice. The scale is 6 km by 6 km. The image will be used and described in more detail in Chapter 5.

The spatial distribution of icebergs is dependent on their motion and icebergs move as a result of the total forces acting upon them (e.g., wind, currents, friction and whether the iceberg is grounded). The motion of icebergs in the Southern Ocean has been considered for large-scale studies of iceberg drift (Tchernia and Jeannin, 1984; Gladstone *et al.* 2001; Gladstone and Bigg, 2002) and also on smaller spatial scales (Madejski and Rakusa-Suszczewski, 1990). However these authors have not explicitly considered the spatial distribution of icebergs and the resulting impact on measurements of sea ice draft. For example, Gladstone and Bigg (2002) used satellite Synthetic Aperture Radar (SAR) imagery to identify what they classified as small to medium icebergs (0.2-5 km diameter), and presented iceberg concentration values within two regions of the Weddell Sea, but

apart from noting icebergs are obviously concentrated near to their source (i.e., the coast) they did not specifically consider spatial distribution.

The potential clustering of icebergs is an important issue not only within this thesis but from methodologies utilising ULS on other AUVs and submarines such as McLaren *et al.* (1984) for example or from pseudo-line transects such as those created from moorings (e.g., Strass, 1998; Worby *et al.*, 2001).

2.10 Summary

In this chapter I have provided a background to sea ice and iceberg formation. I have also outlined some key types of sea ice. I have discussed the importance of open water within sea ice and the impact of snow on sea ice. Basic formulae were introduced to convert snow depth or ice draft into ice thickness. Finally a discussion of existing methods for measuring sea ice thickness was given as well as a summary of the knowledge of sea ice thickness in the Bellingshausen/Amundsen Seas. This background will form the basis of all subsequent chapters.

Chapter 3 Statistical techniques

This thesis involves studying the spatial distribution of icebergs and requires the PDF of sea ice thickness to be corrected for the spatial sampling. This chapter concentrates on the theory and practice of using selected spatial statistical techniques to achieve these aims. There are a number of additional sections at the end of the chapter that deal with more general statistical approaches used within the rest of this thesis (e.g., analysis of variance and testing for normality).

3.1 Introduction to spatial statistics

Many commonly used statistical tests assume that observations are independent of each other, but over spatial and temporal domains this is clearly not true. For example, the close proximity of icebergs may be because they were formed by the break-up of a single larger iceberg and so the iceberg locations are not independent. There are two types of analysis discussed in this chapter:

A. Those relating to a point process, for example, the location of icebergs. In reality assumptions are made so that the data represent a point at some scale. Information is required on whether the points cluster together, are evenly spaced or are randomly positioned.

B. The distribution of a variable over a region, where the values of a variable at unobserved locations and the assignment of errors to the estimates are required. For example, the calculation of the ice thickness distribution over the surveyed area is an example of this type of procedure.

Analyses of the type described in A above are point process issues and are discussed in Section 3.2. Data analyses relating to B are known as geostatistical techniques and are discussed in Section 3.3.

3.2 Point processes

Some examples of the possible outcomes for point processes are shown in Figure 3-1. Figure 3-1a shows the process of inhibition or regularity where perhaps there is a controlling factor causing the points to repel each other. At the other extreme, Figure 3-1b shows clustering or aggregation where the points are located in the same region of the study area. Figure 3-1c shows simulated random point locations. The aim of this section is to explain the techniques required to test whether a region such as that in Figure 3-1c could be described as completely spatially random. However, the red box in Figure 3-1b indicates an alternative study region; within this smaller region it is not clear whether the points are clustered. The sensitivity of the statistics to the area selected is important as the measure of clustering can be altered by selecting large margins with no events (Bivand and Gebhardt, 2000), for example the whole study region in Figure 3-1b rather than just the area within the red box.

The techniques of analysing point processes require data that can be represented as precise locations on a map. For the purpose of this thesis and the techniques described here a process can be considered a *point process* if the scale of the area of interest is large compared to the scale of the feature of interest. For example, a 200m x 200m iceberg can be considered a point process on the scale of a 15km by 7.5km satellite image. The concept of complete spatial randomness (CSR) is frequently referred to in this thesis. CSR is defined as the situation where icebergs are independently and uniformly distributed over the study region (Cressie, 1991).

a) Inhibition

b) Clustering

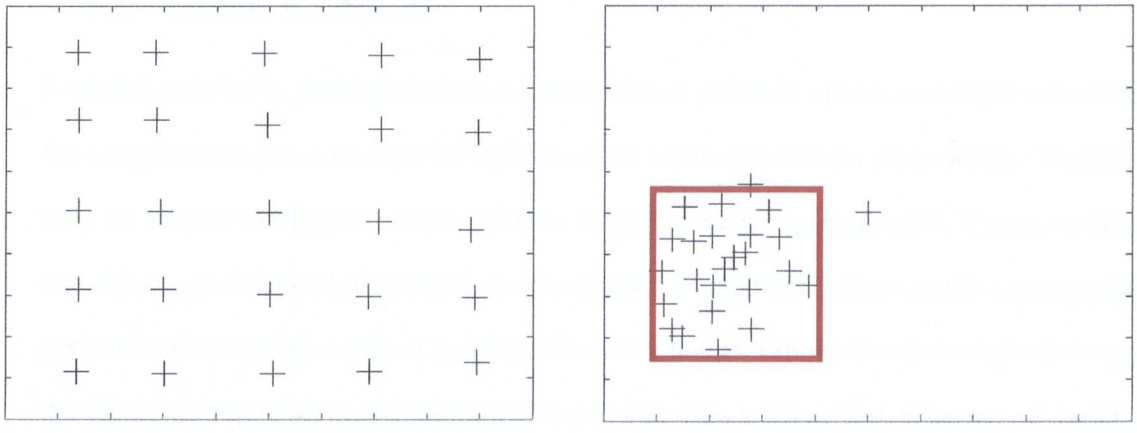

c) Random

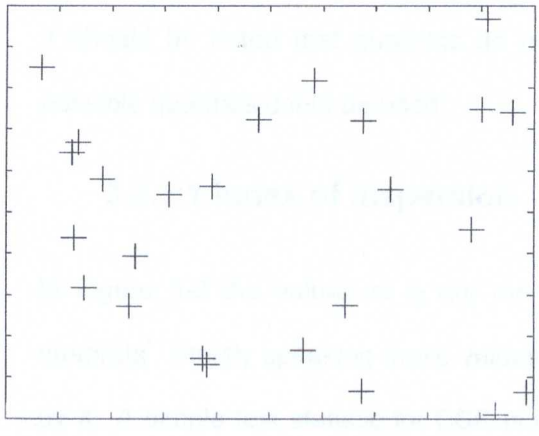

Figure 3-1 Examples for point processes showing a) regularity/inhibition b) clustering/aggregation and c) an example of CSR where visual examination is not conclusive.

Techniques using point processes have been used in a variety of backgrounds from such diverse fields as criminology, ecology, forestry, biology and geology and on different scales of the processes ranging from biological cells through to stars (Diggle, 2003). Within this thesis I consider the use of point process techniques on iceberg locations.

There are two main categories of tests for 2-dimensional point processes considered in this thesis: those relating to counts of icebergs within sub-regions and those using the x,y

coordinates of each iceberg. Another case where icebergs occur along a line (i.e., the 1-dimensional case) is considered separately in Chapter 4.

3.2.1 Quadrat counts

A simple method for testing whether a distribution of points in space is random is to divide the sample area into a number of regions of the same size known as quadrats. Tests can then be carried out based on the number of events within each quadrat. These methods can either use a limited number of randomly placed quadrats (often used in ecology field experiments) or utilise a grid of quadrats as in this thesis. From a theoretical point of view, the shape of a quadrat is unimportant and only the area is important. However, in practice it is likely to be far easier to use a regularly shaped quadrat. An example of a region split into quadrats is shown in Figure 3-2; the region is divided up into k quadrats of equal area. It should be noted that quadrats do not have to be adjacent as just a sample of the possible quadrats could be used.

3.2.1.1 Index of dispersion

In Figure 3-2 the values of x_i are the observed values of the count in each of the k quadrats*. Strictly speaking these values are realisations of the random variables denoted by X_i. A simple test statistic for CSR is the index of dispersion (I_d) given by Lewis (1988) as

$$I_d = \frac{V(X)}{E(X)} \tag{3.1}$$

where V(X) is the variance of the quadrat count and E(X) is the expected value for the quadrat count. If the icebergs are located following CSR then they follow a random/Poisson distribution. A Poisson distribution is represented by a single parameter (μ) where μ=V(X) = E(X), i.e., the variance equals the mean. Therefore under CSR using

---

* k is used rather than N because N is reserved to be the total number of icebergs

Equation (3.1) the value of $I_{d(Poisson)}=1$. Values of $I_d > 1$ (i.e., variance of the quadrat counts greater than the mean quadrat count) indicates clustering in the pattern. Conversely, for values of $I_d < 1$ (i.e., mean quadrat count greater than variance of quadrat counts) there is evidence for regularity in the pattern.

x_1	x_2	x_3
x_4	x_5	x_6
x_{k-2}	x_{k-1}	x_k

Figure 3-2 Example of grid of k quadrats where x_i is the value of the observed cell count.

E(X) and V(X) can be estimated using the sample mean ($\bar{x}$) and sample variance (s^2) respectively which are calculated using

$$\bar{x} = \frac{\sum_{i=1}^{k} x_i}{k} \tag{3.2}$$

$$\text{and } s^2 = \frac{\sum_{i=1}^{k} (x_i - \bar{x})^2}{k-1} \tag{3.3}.$$

Therefore an estimate of the index of dispersion is

$$\hat{I}_d = \frac{s^2}{\bar{x}} \tag{3.4}.$$

This value of $\hat{I}_d$ can be tested to see if it is significantly different from one, i.e., whether the difference can be explained by variability in sampling. In this thesis, from now on events are referred to as icebergs. In order to test the following hypothesis I use a chi-squared test:

H_0: icebergs are randomly distributed (following a Poisson distribution), i.e., $I_d = 1$. Test that $\Phi \sim \chi^2$ where $\Phi = (k-1)\hat{I}_d = \frac{k\sum_{i=1}^{k}(x_i - \bar{x})^2}{N}$ (Lewis, 1988) with (k-1) degrees of freedom and N icebergs in total

H_1: icebergs are not randomly distributed

H_0 is rejected if Φ exceeds the critical value of a chi-squared distribution with k-1 degrees of freedom for a chosen significance level. There are a variety of values for the minimum sample size and the minimum expected value in any quadrat. Here I follow the values suggested in Lewis (1988) of $N \geq 20$ and $\frac{N}{k} \geq 4$ where N is the total number of icebergs in the quadrats.

3.2.2 Nearest neighbour methods (G function)

One of the most popular methods of testing for CSR uses the distances to nearest neighbours and defines the function G(r) as the probability that the distance from a randomly chosen iceberg to the nearest iceberg is less than or equal to distance r (Cressie, 1991). There are various alternatives for estimating values of G from data denoted by $\hat{G}$. Define $J(\bullet) = \begin{cases} 1 \text{ if } (\bullet) \text{ is true} \\ 0 \text{ otherwise} \end{cases}$ and $\frac{0}{0} \equiv 0$. Then for N icebergs in a study region A, the estimate of G is given by

$$\hat{G}(r) \equiv \sum_{i=1}^{N} \frac{J(r_{i,A} \leq r)}{N} \tag{3.5}$$

where $r_{i,A}$ is the distance from the i^{th} iceberg to its nearest neighbour within area A (Cressie, 1991).

The format of $\hat{G}$ in Equation (3.5) above does not take into account cases where the nearest neighbour is located outside the study region and there are a number of ways of dealing with the need for an adjustment for this effect known as edge corrections.

The first edge correction option is to use a guard area by identifying icebergs in the area outside of the study region but not considering these icebergs as part of the sample studied, but using them to measure distances to icebergs in the sample. Secondly, by means of a toroidal correction, that is repeating the study region on all four sides so that points on opposite sides of the region are considered to be close together. Thirdly, and the method employed here, is to take account of the distance to the edge using the (Ripley) edge correction in Cressie (1991). Equation (3.5) becomes

$$\hat{G}(r) = \frac{\sum_{i=1}^{N} J(r_{i,A} \le r, d_i > r)}{\sum_{i=1}^{N} J(d_i > r)} \tag{3.6}$$

where r>0 and d_i is the distance from the i^{th} iceberg to the nearest edge of the study region A. Cressie (1991) provides an estimate for the theoretical values of G(r) for CSR (i.e., for a Poisson process) as

$$G(r) = 1 - \exp\left(-\frac{N}{A}\pi r^2\right) \tag{3.7}.$$

$\frac{N}{A}$ is an estimate of the intensity for the study region and it is sometimes referred to as $\hat{\lambda}$.

In an idealised situation, under CSR the values of the estimates in Equations (3.6) and (3.7) are equal so a plot of $\hat{G}(r)$ on the y-axis against G(r) would then produce a straight line. In order to test whether any differences are significantly different, simulated data are used to provide confidence intervals for the relationship (see Section 3.2.4).

As alternatives to measuring the distance between an iceberg and its nearest neighbour it is also possible to measure the distance between a random point and the nearest iceberg or to find the closest iceberg to a random sample point and then measuring the distance from this iceberg to its nearest neighbour. Most of these latter methods were developed for the forestry industry and were not designed for studies where all cases are mapped, such as for the iceberg locations in this thesis.

3.2.3 K Function

The G function described above only depends upon the separation of pairs of icebergs. To extend the test to incorporate all icebergs in the study region the K function is introduced. This is defined in Cressie (1991) as follows

$$K(r) \equiv \lambda^{-1} E(\text{number of icebergs within distance r of an arbitrary iceberg}) \quad (3.8)$$

where λ is the intensity and is estimated by $\hat{\lambda}$ $(=\frac{N}{A})$. The value of $\hat{K}(r)$, an estimated value of K(r), including the edge-correction (as discussed in Section 3.2.2 for the G function) is given by Diggle (2003) as

$$\hat{K}(r) = \frac{A}{N(N-1)} \sum_{i=1}^{N} \sum_{\substack{j=1 \\ i \neq j}}^{N} \frac{M_r(u_{ij})}{w_{ij}} \quad (3.9)$$

The term M_r is defined using

$$M_r(u_{ij}) = \begin{cases} 1 \text{ if } u_{ij} \leq r \\ 0 \text{ if } u_{ij} > r \end{cases} \quad (3.10).$$

w_{ij} is the proportion of the circumference of the circle centred on the i^{th} iceberg that passes through iceberg j and is contained within the study region as shown in Figure 3-3. Also shown in Figure 3-3 is the definition of u_{ij} as the distance between iceberg i and iceberg j.

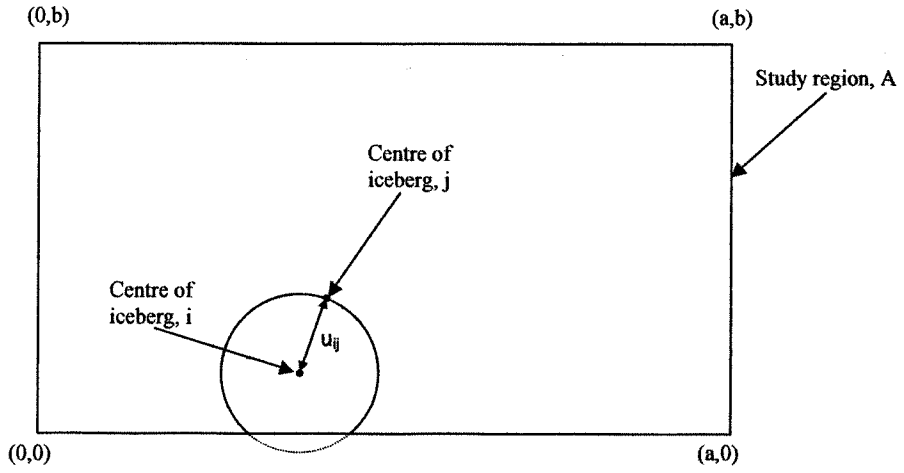

Figure 3-3 Representation of terms used in estimating K(r) in a region of area A with dimensions a and b: u_{ij} is the distance between iceberg i and iceberg j and w_{ij} is the proportion of the circle circumference that is marked as solid. The circle is centred on iceberg i and passes through iceberg j.

With reference to Figure 3-3, for a point with coordinates (x,y), let $d_1 = \min(x,a-x)$ (i.e., the distance to the nearest non-horizontal edge) and let $d_2 = \min(y, b-y)$ (i.e., the distance to the nearest horizontal edge). If $u_{ij} < \frac{1}{2}\min(a,b)$* then the algorithm for calculating w_{ij} is as follows

1. If $u_{ij}^2 \le d_1^2 + d_2^2$, put

$$w_{ij} = 1 - \frac{\cos^{-1}\left(\min(d_1,u_{ij})/u_{ij}\right) + \cos^{-1}\left(\min(d_2,u_{ij})/u_{ij}\right)}{\pi} \qquad (3.11)$$

or

---

* Different authors suggest different maximum values of the maximum distance over which K is calculated (not necessarily just for calculating values of w_{ij}). I use the value given in Diggle (2003) of half the minimum dimension (i.e., ½ of the length of the shorter of a and b).

2. if $u_{ij}^2 > d_1^2 + d_2^2$, put

$$w_{ij}=0.75-\frac{\cos^{-1}\left(d_1/u_{ij}\right)+\cos^{-1}\left(d_2/u_{ij}\right)}{2\pi} \quad (3.12).$$

After calculating the values of $\hat{K}(r)$ using Equation (3.9), a plot can be produced with distance (r) on the x-axis against $\hat{K}(r)$ on the y-axis. However, interpretation of this plot is not simple. A simpler way of visualising the results from $\hat{K}(r)$ is to use a transformation of $\hat{K}(r)$, denoted by $\hat{L}(r)$, where

$$\hat{L}(r)=\sqrt{\frac{\hat{K}(r)}{\pi}}-r \quad (3.13).$$

A plot of $\hat{L}(r)$ against distance r is much easier to interpret as values of $\hat{L}(r)$ above zero indicate clustering/aggregation (Figure 3-1b) whereas values below zero suggest regularity/inhibition (Figure 3-1a). CSR (Figure 3-1c) is represented by $\hat{L}(r)$ being zero. As with the G function, simulations of the data are used to provide confidence intervals for the results. This is considered in the next section.

3.2.4 Simulation

Although the methodologies described for the G and K functions provide a basis for testing for CSR, they do not enable a confidence level to be established. In order to establish a more rigorous framework I have used simulations of the icebergs within the study region and calculated values of G and K for these simulated study regions. Using a random number generating function, the locations of the icebergs in the simulations are randomly positioned throughout the simulated study region.

For the G function, the values of $\hat{G}$ are obtained for all possible values of distance for every simulation. Similarly, values of $\hat{K}$ are calculated for all values of distance for each

simulation. For every value of r, the values of $\hat{G}$ and $\hat{K}$ are rank ordered and the 5th and 95th percentile values are taken as the lower and upper 90% confidence intervals.

3.3 Geostatistics and kriging

The second type of spatial analysis in this thesis relates to the mapping of a variable onto a surface. This is given the general name of geostatistics but here I primarily consider the technique of ordinary kriging. Most estimates of the mean assume that the observations are independent, but in spatial analyses this is not true. Points that are close together are more strongly correlated than points further apart (e.g., in the case of sea ice draft measurements two points on a pressure ridge) and the concentration of observations is also critical. For these reasons location must be taken into account when deriving the PDF for sea ice draft. In this description of kriging I refer to ice draft but it could be any other variable such as snow depth (to be discussed in Chapter 6).

3.3.1 The semi-variogram

Consider two points in space separated by distance h (known here as the lag), with observations of ice draft of g_i and g_j, following the notation of Clark and Harper (2000). The differences between all pairs of observations separated by lag h can be used to obtain the following as the variance of the differences

$$s_h^2 = \frac{1}{N_h}\sum_h (g_i - g_j)^2 \tag{3.14}$$

where N_h is the number of pairs of values. Most texts follow the notation of Matheron (e.g., Cressie (1991) and Clark and Harper (2000)) who suggested adjusting Equation (3.14) by a factor of ½, thus the semi-variance, denoted by γ, can be readily calculated as

$$\gamma(h) = \frac{s_h^2}{2} = \frac{1}{2N_h}\sum_h (g_i - g_j)^2 \tag{3.15}.$$

Once the values for the experimental semi-variogram have been calculated (i.e., from the observations) the next stage is to model a semi-variogram that best represents the data.

There are many different models for the semi-variogram all of which share a common set of terminology. A sample semi-variogram is shown in Figure 3-4 and the various features to be modelled are shown. Of the numerous different models for the semi-variogram in this thesis I use three - linear, spherical and exponential.

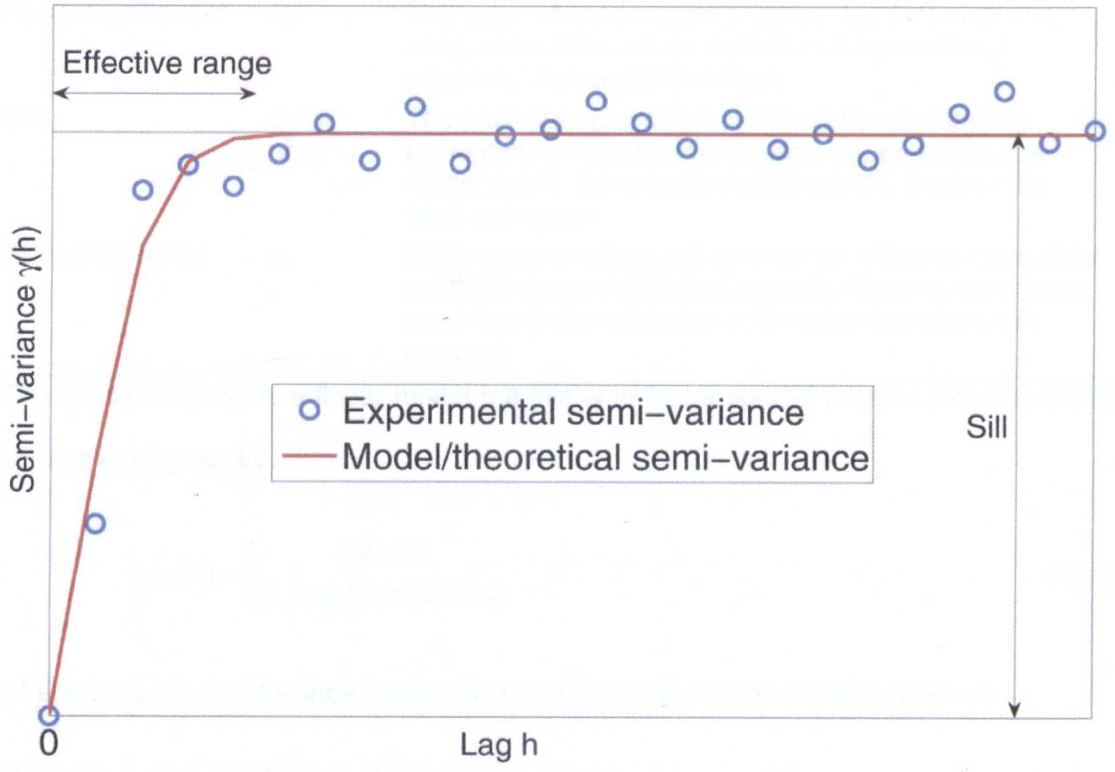

Figure 3-4 Sample semi-variogram showing the various features with zero nugget variance (i.e., C_0 =0).

Some common nomenclature used is summarised in Table 3-1. The term nugget variance indicates the origins of kriging theory in the gold-mining industry and relates to the finite size of gold nuggets.

Table 3-1 Common nomenclature of terms used for semi-variogram models.

Term	Symbol	Explanation
Lag	h	Distance between a pair of samples
Semi-variance	γ	See text
Nugget (variance)	C_0	The value of semi-variance at zero lag (intercept on γ axis), often taken as an indicator of experimental accuracy/ instrument precision.
Sill	$C+C_0$ or p_s	The maximum (asymptotic) value of semi-variance (Sometimes there are more terms depending on the model used). For a linear model it is the slope of the semi-variogram.
(Effective) range	a_r	Distance over which points exert an influence over other points for some (spherical) models. Name is commonly used for other models but alternative definitions are required.

The simplest model is a linear model but this is in fact a special case of the generalised linear model given by

$$\gamma_{glm}(h) = \begin{cases} 0 \text{ if } h=0 \\ C_o + p_s h^{\omega} \text{ otherwise} \end{cases} \quad (3.16)$$

where $0< \omega <2$. For the linear model $\omega=1$ and hence the linear model is given as

$$\gamma_{linear}(h) = \begin{cases} 0 \text{ if } h=0 \\ C_o + p_s h \text{ otherwise} \end{cases} \quad (3.17).$$

Hence, for the linear model the sill, p_s, is the slope of the semi-variogram as can be seen in Equation (3.17).

The spherical model is given for the various possible ranges of h as

$$\gamma_{spherical}(h) = \begin{cases} 0 \text{ if } h=0 \\ C_0 + C\left(\frac{3h}{2a_r} - \frac{h^3}{2a_r^3}\right) \text{ if } 0<h<a_r \\ C_0 + C \text{ if } h>a_r \end{cases} \quad (3.18).$$

For the spherical model, if the lag is greater than the effective range (a) then the semi-variance is a constant (=the sill).

Finally the exponential model given by

$$\gamma_{exponential}(h) = \begin{cases} 0 \text{ if } h=0 \\ C_0 + C\left(1 - \exp\left(-\frac{h}{a_r}\right)\right) \text{ if } h>0 \end{cases} \quad (3.19).$$

3.3.2 Normality of data

Many texts, including Clark and Harper (2000) and Webster and Oliver (2001) recommend that the data used for kriging are normally distributed or are transformed to be normal as using normal data results in greater stability of the semi-variance estimates. For this reason, the first step in a kriging analysis before even fitting the semi-variogram model is to transform the data so that the sample values used are normal. A simple approach is to use the square roots of the data values in the analysis. Another common approach is to take the (natural) logarithms of the measurements (and optionally adding a constant before taking logarithms), if these values are normally distributed then the data are said to be lognormal.

One property of the lognormal distribution is that the variance is related to the mean. The implication of this is that converting the kriged values back to the original scale cannot be achieved by simply taking anti-logs; see Clark and Harper (2000) for further details.

3.3.3 Fitting a semi-variogram model

Many texts and software packages consider the fitting of semi-variograms to be a visual exercise or at least a combination of "art and science". The process of fitting semi-variograms – whether manually, automatically or as a combination of both – is a much-debated process and regular discussions on the issue can be found on the ai-geostats newsgroup.

3.3.4 Kriging

Once the model semi-variogram has been established the next stage is to use this to interpolate the values using kriging. There are a number of different kriging techniques;

here the method considered is ordinary kriging. The value estimated at any point is dependent on weighted values of all other values such that the estimated value at a point, denoted by T*, is given by (Clark and Harper, 2000)

$$T^* = w_1 g_1 + w_2 g_2 + w_2 g_2 + \ldots\ldots w_m g_m \tag{3.20}$$

where g_i is the value of ice draft at point i and w_i is the weight attached to this value in the estimation. In order to produce an unbiased value the restriction is introduced that $\sum_{i=1}^{m} w_i = 1$. If the nugget variance is taken as zero (i.e., $\gamma(0)=0$), as I do throughout this thesis, then the variance of the estimation error is given by

$$\sigma_\varepsilon^2 = 2\sum_{i=1}^{m} w_i \gamma(g_i, z_i) - \sum_{i=1}^{m}\sum_{j=1}^{m} w_i w_j \gamma(g_i, g_j) \tag{3.21}$$

where $\gamma(g_i, z_i)$ is the semi-variance between sample i and the point for which ice draft (z_i) is to be estimated. Since there is a model for the values of $\gamma(g_i, z_i)$ and $\gamma(g_i, g_j)$ this can be substituted into Equation (3.21) and using Lagrange multipliers the series of equations can be solved. In practice this stage of the analysis is performed using appropriate software.

To summarise, for any point the value of ice draft can be estimated as T* and the variance of that estimate (the kriging variance) as σ_ε^2. The values of the kriging variance can be used to calculate a standard error and 90% confidence intervals. The standard error is given by

$$1.645\sqrt{\sigma_\varepsilon^2} \tag{3.22}$$

where the value of 1.645 is the 5% critical value of the standard normal distribution.

3.3.5 Use of EasyKrig Toolbox

The Matlab toolbox used in this thesis for semi-variogram modelling and kriging is EasyKrig Version 3 (Chu, 2004). Whilst not having the advanced functionality to be found in some of the other available packages it is easy to use and has an informative graphical interface. Data are entered as text files and the location of the coordinates and variable values can be defined (as either X-Y or longitude-latitude). Values of the kriged variable are calculated for all nodes of a grid that is either user-defined or where the user sets both the resolution of the grid in the x and y directions and the co-ordinates of the outer edges of the grid.

A measure of fit of the model semi-variogram compared with the experimental semi-variogram is not available in the EasyKrig package that has been used. Clark and Harper (2000) suggest a modified version of the Cressie goodness of fit, F_c, as follows

$$F_c = \frac{1}{\sum_h N_h} \sum_h N_h \left(\frac{\gamma^*(h) - \gamma(h)}{\gamma(h)} \right)^2 \tag{3.23}$$

where $\gamma^*(h)$ and $\gamma(h)$ are the estimated (experimental) semi-variance and theoretical (modelled) semi-variance respectively and N_h is the number of pairs of points with separation h. The smaller the value of this fit the better is the agreement between the experimental and model semi-variograms. The value of F_c can be compared with successive models with the aim of minimising its value.

3.3.5.1.1 Kriging parameters

The region over which a kriged estimate is made is sometimes referred to as the *neighbourhood*. The choice of the neighbourhood in terms of its diameter and the number of data points it contains are controlled by four numeric parameters. The choice of their values within this thesis is partly influenced by a set of guidelines given in Webster and Oliver (2001), partly by the requirement to ensure that the kriged values reflect the full

range of the raw data and partly by the functionality available within EasyKrig. Webster and Oliver report that if defining a neighbourhood based on the number of observations then between about 7 and 20 observations are usually sufficient to define the neighbourhood and produce satisfactory results. They also suggest that the radius of the neighbourhood can be defined by the effective range. If the EasyKrig algorithm does not identify sufficient observations within the search radius then it increases the search radius until sufficient observations are found.

3.4 Isotropy and stationarity

It is possible that the semi-variance is dependent upon the direction in which the lag is measured. For example, the semi-variance will be greater across a series of pressure ridges than along a ridge. A variable that has the same semi-variance in any direction is said to be isotropic and, conversely, it is anisotropic when the semi-variance depends on direction. It should be noted that the semi-variances are calculated over all pairs of points and so it is the mean over all pairs that is of importance rather than individual cases.

Another consideration is that there is no drift in the mean value over the region of interest. If there is a drift then this trend must be removed first and the underlying variability modelled and then the drift added back in. The methodology for this process is known as universal kriging.

Neither anisotropy nor a drift have been found in any of the semi-variograms in this thesis or at least not over the scales for which the semi-variogram holds.

3.5 Other statistical methodologies

The following sections introduce a number of other statistical techniques that will be used in later chapters of this thesis.

3.5.1 Testing for normality

As has already been mentioned some texts recommend that data in a kriging analysis are normally distributed. In order to test whether data are normally distributed the Lilliefors test has been used. A function for the Lilliefors test for normality is available in Matlab called *lillietest* (The Mathworks, 2004). This function allows the user to specify a significance level and I have used a value of 0.01. A value of zero or one is returned depending on whether the data are normal or not-normal at the given significance level.

3.5.2 Alternative transformation to normality

Section 3.3.2 describes standard procedures for converting non-normal data to normal data. An alternative transformation used in the course of this thesis is

$$z_t = \sinh\left(\delta \sinh^{-1}\left(x_z\right)\right) = \frac{1}{2}\left(\left(x_z + \sqrt{1+x_z^2}\right)^{\delta} - \frac{1}{\left(x_z + \sqrt{1+x_z^2}\right)^{\delta}}\right) \quad (3.24)$$

(Jones and McConway, In preparation) where x_z represents the standardised values given by

$$x_z = \frac{x - \bar{x}}{s} \quad (3.25)$$

where x is the measured value, $\bar{x}$ is the mean of the observed values and s is the standard deviation. δ is a constant to be found and δ is less than one to correct for cases where the tails are heavier than normal and δ is greater than one to account for lighter tails than normal (δ=1 is normal). There is no relationship between the transformed mean and standard deviation. Therefore after kriging the values of z_t, the results represented by x_{kriged} can be back-transformed using

$$x_{kriged} = \sinh\left(\frac{\sinh^{-1} z_t}{\delta}\right) \quad (3.26).$$

The values of x_{kriged} can subsequently be converted back onto the original scale by re-arranging the relationship in (3.25) to be

$$\text{Kriged values on original scale} = \bar{x} + s^2 x_{kriged} \quad (3.27).$$

3.5.3 Analysis of variance

In order to test whether there are significant differences in the means of either snow depth on a number of floes or ice draft between Autosub missions, analysis of variance (ANOVA) techniques can be used. ANOVA methods partition the variance into *between* and *within* groups and then assess the relative importance of these to test whether there are significant differences between any of the floes/missions. *Between groups* measures the variation of the group means about the overall mean and *within groups* represents the variation within the groups around their group means. The ratio of these two values is compared to an F distribution (with number of missions/floes minus one degrees of freedom) and the subsequent significance value tests whether there is at least one group that differs from at least one other group. If the significance is less than 0.05 then there is evidence of group differences and to find out which groups are different *post hoc* tests are required.

3.5.3.1 *Post hoc* tests

Two *post hoc* tests were used in this thesis in order to examine pairwise differences between groups (i.e., either floes or missions). The first test is the least-significant difference (LSD) test, which is a liberal test and hence the most appropriate for showing no significant difference between groups. Second, the Scheffé test, which is a conservative test and hence appropriate for showing that there is a significant difference.

3.5.4 The Kolmogorov-Smirnov test

The Kolmogorov-Smirnov test (KST) is used to test whether two population distributions are significantly different based on the distributions of two samples (Kanji, 1993). The first step in the KST is to produce cumulative distribution functions (or cumulative probability

functions – CDFs) for the two samples. Two sample distributions $H_1(x)$ and $H_2(x)$ with sample sizes of n_1 and n_2 respectively have their CDFs plotted in Figure 3-5. The differences between these two distributions are found for all values of x (where x is, for example, snow depth) and the test is based on the largest difference, i.e., the maximum value of Δ where

$$\Delta = \left| H_1(x) - H_2(x) \right| \tag{3.28}.$$

The value of Δ in Equation (3.28) is sometimes referred to as the Kolmogorov distance and is compared with a critical value from tables. Here this is achieved using the *kstest2* function in Matlab (The Mathworks, 2004) with the null hypothesis that the two distributions are the same. If the value of Δ is greater than a critical value then the null hypothesis that the two distributions are the same can be rejected, conversely if Δ is less than the critical value then there is not enough evidence to reject the null hypothesis.

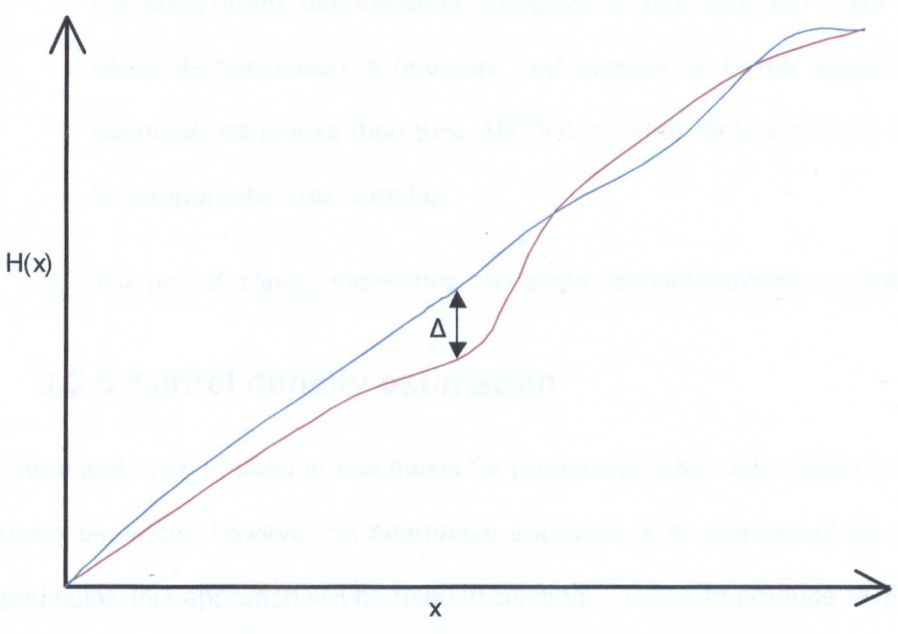

Figure 3-5 Diagrammatic representation of the Kolmogorov-Smirnov test showing the cumulative distributions of two samples ($H_1(x)$ in red and $H_2(x)$ in blue) and the Kolmogorov distance, Δ.

3.5.5 Comparing distributions with spatial component

The methods above (Section 3.5.3 to 3.5.4) for comparing the means/distributions assume that there is no correlation within each group, i.e., that the data represent a random sample of points and there is no autocorrelation. In space this is not necessarily true, as points close to each other will tend to be correlated. In practice what this implies, for ANOVA for example, is that if a particular value of α is set as the critical p value (e.g., $\alpha = 0.05$) then the null hypothesis (that the groups are the same) may be rejected but the true value of the equivalent p value is in fact higher and hence the null hypothesis should not have been rejected.

Statistical methods for investigating such models are beyond the scope of this thesis and will not be discussed further except to note some possible solutions. These solutions could include, amongst other methodologies:

1. For each group, use the semi-variogram to determine the maximum distance over which its correlation is non-zero and remove all cases where the separation of observations is less than this. ANOVA or other methods could then be employed to compare the sub-samples.
2. The use of a linear model that takes into account correlation within groups.

3.5.6 Kernel density estimation

The usual method used in this thesis for producing PDFs is to obtain a histogram using a given bin width, however an alternative approach is to use kernel density estimation. In particular, this approach will be used in Section 7.10.3.4 to produce PDFs for sea ice draft from the kriging results and incorporate the values of kriging error by using the kriging error as the bandwidth.

If there are N estimates of ice draft, with (mean) values of μ_i and an error value of σ_i then the estimate of the PDF at any ice draft (x) is given by

$$PDF_x = \frac{1}{N}\sum_{i=1,N} f(x) \tag{3.29}$$

where $f(x)$ is the value of the normal PDF at x for estimate i defined using

$$f(x) = \frac{1}{\sigma_i\sqrt{2\pi}}\exp\left(-\frac{1}{2}\left(\frac{x-\mu_i}{\sigma_i}\right)^2\right) \tag{3.30}$$

from Daly *et al.* (1995).

3.5.7 Transforming PDF variables

It is sometimes preferable to transform the original observations (for example taking logarithms of data that are lognormal) and provide a PDF based on the transformation. The PDF of the transformed variable can then be used to calculate the PDF of the original (untransformed) variable using the Jacobian. If a variable x has a PDF defined by $f(x)$ and a relationship exists between x and y where the PDF of y is given by $f(y)$ then

$$f(x) = f(y)\left|\frac{dy}{dx}\right| \tag{3.31}$$

where $\left|\frac{dy}{dx}\right|$ is the absolute value of the Jacobian (Hogg and Tanis, 1977).

For example, if

$$y = \ln(x+1) \tag{3.32}$$

then it is possible to calculate the derivative from Equation (3.31) by rewriting Equation (3.32) as

$$x = e^y - 1 \tag{3.33}$$

so that

$$\left|\frac{dx}{dy}\right| = e^{y} \Rightarrow \left|\frac{dy}{dx}\right| = e^{-y} \tag{3.34}$$

If the values of $f(y)$ are then calculated for a series of sample values the PDF of x (the untransformed values) can be rewritten using Equation (3.31) as

$$f(x) = f(y)e^{-y} \tag{3.35}.$$

3.6 Summary

In this chapter I have introduced a number of techniques that will subsequently be used in the following chapters of this thesis. In particular, the point process methods will be used in Chapter 5 and the geostatistical/kriging approaches will be used in Chapter 6 and Chapter 7.

Chapter 4 USIPS iceberg distribution

4.1 Introduction

This chapter is concerned with the spatial distribution of icebergs within the length-scale of Autosub missions (~ few km). The presence of icebergs within the sea ice zone will tend to over-estimate the measured sea ice draft as well as potentially increasing the proportion of open water as discussed in Section 2.9. If icebergs are spatially random over the length of an Autosub mission, the choice of study location will not be as critical. If icebergs are not randomly distributed then the study region chosen may have a distinctly higher or lesser concentration of icebergs than expected (c.f. the mean). In turn, this could result either in an over or under estimate of the draft of ice within the entire region as well as a change in the proportion of the amount of open water when compared to the average.

The work in this chapter will show that iceberg concentration between missions cannot be assumed to be random and therefore must be considered in the estimation of sea ice draft. I will also show that within an individual mission the icebergs are not necessarily randomly located and this too must be taken into account when deriving PDFs for sea ice draft.

In January/February 2001, as part of British Antarctic Survey Cruise JR58 (Under Sea Ice and Pelagic Surveys), the Autosub vehicle was deployed in the Weddell Sea as shown in Figure 4-1. Analyses of the data from these missions have already been used to study whether krill avoid ship-based surveys (Brierley *et al.*, 2002; *Brierley et al.*, 2003) and sea ice thickness (Brandon *et al.*, Submitted). In this chapter, I use data from four USIPS missions (M247, M248, M252 and M253). For these missions Autosub was deployed north of the sea ice zone and was programmed to follow 'U' shaped transects into the sea ice zone as shown in Figure 4-1. Each mission consisted of three legs: the first leg into the ice, the second leg at 90° to the first and the third leg out from the ice, parallel to the first

leg. For each of these missions, an upward-looking, single-beam echo-sounder mounted on Autosub was used to detect the locations of icebergs along the mission tracks. Simulations of the locations of these icebergs along Autosub's track within each mission have been used to establish whether icebergs are spatially random in one dimension (i.e., along the vehicle track).

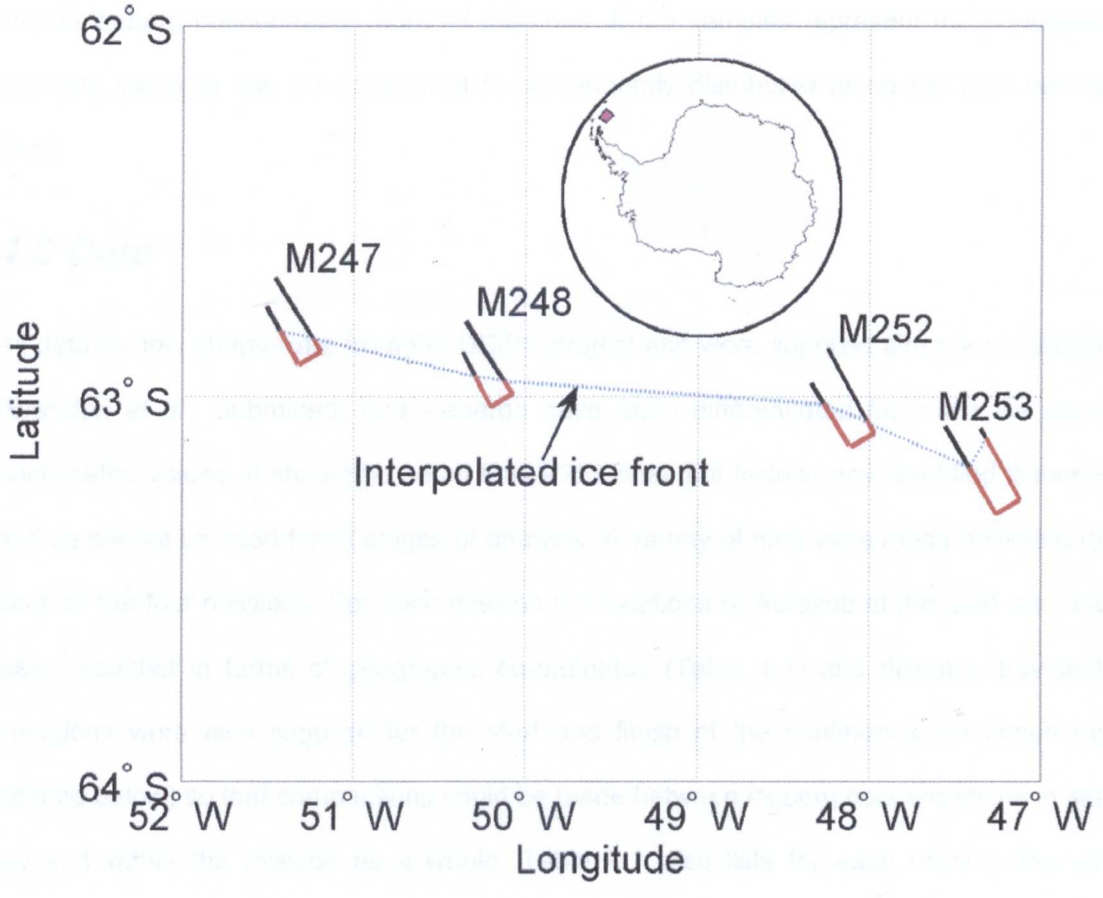

Figure 4-1 Location of relevant USIPS missions identified by Autosub cruise tracks and (inset) location of study region to the east of the Antarctic Peninsula. Sections identified as under sea ice are shown in red and under open water as black. The dotted blue line is the interpolated ice front found by joining the locations of the ice front from each of the relevant Autosub mission legs.

For each mission, a nearest neighbour methodology has been used to test whether the icebergs along the vehicle track are clustered. By comparing the mean separations of the icebergs from their nearest neighbours within the data with the distributions of the mean minimum separations from the simulations, conclusions can be made on whether the icebergs are clustered. Although two-dimensional locations for the icebergs are available,

these are only the icebergs along the vehicle's track and do not necessarily represent all icebergs within the region. Information was also provided on the start and finish of the continuous ice cover so that comparisons are made on the whole mission and just within the sea ice zone.

A chi-squared method is used to test whether the missions (samples) represent the overall iceberg concentration from all missions. If the samples represent the population then the icebergs can be considered to be randomly distributed along the total vehicle track.

4.2 Data

All data for this chapter are from the USIPS project and were supplied already processed (Brandon *et al.*, Submitted) and icebergs have been differentiated from sea ice using backscatter values. It should be noted that M253 does not include any identified icebergs and so cannot be used for all stages of analysis. A variety of data were made available for each of the four missions. For each mission the locations of Autosub at the start and end were provided in terms of geographic co-ordinates (Table 4-1) and distance travelled. Locations were also supplied for the start and finish of the continuous ice zones (as defined below) so that comparisons could be made between iceberg concentrations in sea ice and within the mission as a whole. Table 4-1 also lists for each mission the co-ordinates of the start and end of the ice zone and the locations of the ends of the first and second legs.

Table 4-1 Location of Autosub at start and end of USIPS missions; co-ordinates of start and end of ice zone (see text for definition) and locations of the ends of the first two legs.

	M247	M248	M252	M253
Location at deployment	-62.7617 S -51.509 W	-62.8823 S -50.3661 W	-62.9643 S -48.3371 W	-63.0832 S -47.353 W
Location at recovery	-62.6836 S -51.4593 W	-62.801 S -50.3446 W	-62.8716 S -48.238 W	-63.077 S -47.5548 W
Start of ice zone	-62.8269 S -51.4307 W	-62.9455 S -50.2952 W	-63.0185 S -48.2642 W	-63.1087 S -47.3214 W
Leg 1 ended	-62.9141 S -51.3264 W	-63.0265 S -50.2042 W	-63.1265 S -48.1186 W	-63.2685 S -47.1227 W
Leg 2 ended	-62.8813 S -51.1938 W	-62.9922 S -50.0763 W	-63.0959 S -47.9716 W	-63.3058 S -47.2581 W
End of ice zone	-62.8456 S -51.2381 W	-62.958 S -50.1229 W	-63.0627 S -48.0093 W	-63.1855 S -47.4155 W

For each iceberg the drafts were provided as well as the distance Autosub had travelled since the start of the mission. The latitude and longitude for the position of each iceberg draft were also provided.

The sea ice regions were identified within the data and they are defined as regions in which ice was continuous rather than in bands of ice and open water. For the rest of this chapter open water refers to regions of unconsolidated sea ice as well as areas of open water.

Using the location of the ice edge and the positions of the icebergs it is apparent which icebergs are within the sea ice zone. For each mission, the total number of icebergs and the number within the sea ice zone are given in Table 4-2.

Table 4-2 Number of icebergs in each mission and the number within the sea ice zone

Mission	Number of icebergs	Number of icebergs within sea ice zone
M247	8	6
M248	3	0
M252	11	10
M253	0	0

4.3 Method

4.3.1 Mission descriptions

For each mission (excluding M253) the length of each iceberg was derived. A number of values were calculated to provide an idea of the scale of each of the icebergs, as well as the supplied values of draft. Firstly, the average (mean) ice draft was found for each iceberg. Secondly, to take into account the overall scale of the iceberg, the area of the icebergs along the Autosub track was calculated as the product of the iceberg length and its mean ice draft. These latter values are only an indicator of iceberg size as they represent the part of the iceberg below which Autosub travelled, and this may not be the deepest part of the iceberg and Autosub's path may not have been along the longest axis (e.g., Autosub may just have passed beneath a corner).

4.3.2 Nearest neighbour method

The nearest neighbour approach treated each mission (M247, M248 and M252) as a separate analysis. The statistical tests used assume that the icebergs are points; this assumption is considered adequate given that

i) even the largest iceberg only accounts for a small proportion of the length of the total mission

ii) the total length of all icebergs << the total mission length.

Hence, I derived a midpoint of each iceberg to represent the location for the point process analyses; more precisely the midpoint of the iceberg encountered along the track was identified (i.e., in one dimension). If the distance travelled at the start of iceberg x was s_x and the distance travelled at the end of iceberg x was e_x then the midpoint (m_x) is given by

$$m_x = s_x + \frac{(e_x - s_x)}{2} \qquad (4.1).$$

The distances between each iceberg midpoint and its two neighbouring icebergs along the mission track (i.e., in one dimension) were found and the minimum of these two was taken as the nearest neighbour distance. As an indicator of the clustering/inhibition of icebergs on each mission, the means of all these nearest neighbour distances were calculated (referred to as d_{data}).

For missions with icebergs under sea ice (M247 and M252) the method was repeated for the length of track within the continuous ice region. For M248, where all the icebergs were in open water, the process was repeated for just the open water section.

In order to test whether the values of d_{data} are significantly different from what would be expected if the icebergs were spatially random I use a simulation methodology. Excluding M253, which contains no icebergs, the lengths and numbers of icebergs presented in the previous section were used to create simulated copies of the missions (i.e., M247, M248 and M252) with 'icebergs' randomly located along the tracks. As before, for each of the missions the analysis is two stage, firstly the entire mission and secondly either just the section under sea ice or, for M248, just the region under open water.

For each simulation, randomly generated midpoints were used to locate icebergs along a track of the same length. These icebergs are of the same length as those in the original data and are located with the additional requirement that no icebergs could overlap. The process of measuring the mean of the nearest neighbour distances was repeated for each simulation. The simulation was repeated n times for each mission and the mean nearest

neighbour distance (d_n) was calculated for all n simulations. Comparison of the value of d_{data} with the distribution of the values of d_n indicates the tendency of the icebergs to cluster or to be inhibited. The number of simulations (n) was 40,000 and the p value is defined as the proportion of simulations that have d_n less than d_{data}. A small p value (<0.05) suggests that the icebergs cluster compared with the random simulations. Conversely a large p value (>0.95) suggests the opposite, that the icebergs are regularly located. The number of simulations could have been reduced as the statistics converge using less than 40,000 simulations but this is still readily achieved using a desktop PC.

4.3.3 Chi-squared approach

A second test was used to compare the number of icebergs encountered on each mission and, taking into account the variable length of the missions, whether the number of icebergs on each mission would be expected given spatial randomness. The methodology is based on testing the number of icebergs in each mission given that the missions can be considered as samples. As with the simulations above the analysis is in two stages, firstly using the lengths of the whole missions and secondly using just the sections under sea ice. The methodology explained here is appropriate to both of these cases.

The length of the AUV track and number of icebergs are summed over all four missions and the overall number of icebergs per kilometre is then calculated. For each mission the estimated number of icebergs is calculated as the mission length multiplied by the overall number of icebergs per kilometre and this is the expected number of icebergs. The differences between the observed (obs) and expected (exp) number of icebergs for each mission are then calculated. Whether these samples come from the same population is then tested using a chi-squared test. M253 is included within this analysis because it contains data about the number of icebergs within the entire study region.

The null hypothesis being tested is:

H_0: the icebergs are randomly distributed between the n=4 missions. Test that $\kappa \sim \chi^2$

where with n-1 degrees of freedom, $\kappa = \sum_{i=1}^{n} \frac{(obs_i - exp_i)^2}{exp_i}$ (4.2)

H_1: icebergs are not randomly distributed between the four missions.

There are (n-1) degrees of freedom because the parameter of the overall number of icebergs per kilometre was estimated from the data. From the obtained values of chi-squared, the p values are found for (n-1) degrees of freedom. If the p value is less than 0.05 then the null hypothesis can be rejected and there is evidence that the icebergs are not randomly distributed between the missions. An additional requirement of the chi-squared distribution is that no expected value should be too small. A common rule-of-thumb is that no expected value should be less than five (e.g., Daly *et al.*, 1995).

4.4 Results - mission descriptions

There were no icebergs identified along the track of M253 so this mission cannot be used in the simulation process. However, in order to test the hypothesis that icebergs are randomly located throughout all missions (Section 4.3.3) M253 must be included.

4.4.1 Mission 247

Eight icebergs were identified in M247 and the positions of the centres of the icebergs, as defined by their midpoints along the vehicle's track, are shown in Figure 4-2. The solid red line in Figure 4-2 represents the continuous sea ice zone whereas the dotted black line indicates open water (or unconsolidated ice).

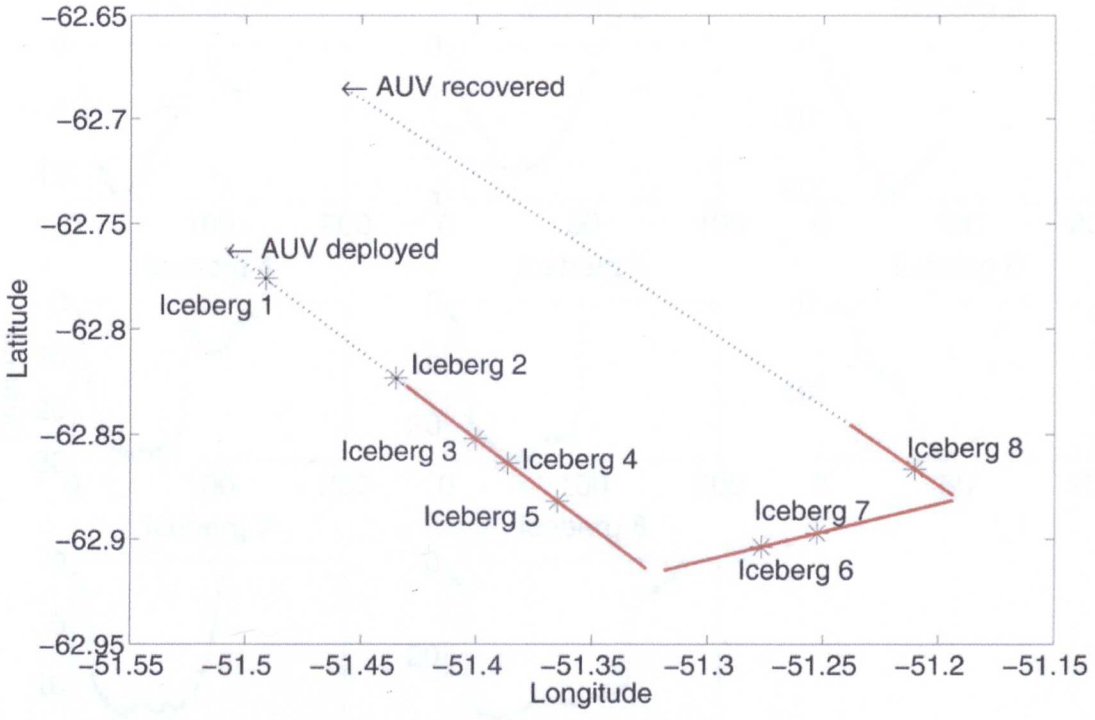

Figure 4-2 Location of mission track, iceberg midpoints and location of ice edge for M247. Solid red line shows track identified as under sea ice whereas dotted black line is track under open water. No data are available for the sections during which Autosub is turning and changing depth; hence the breaks on the two corners.

It is not obvious, by observation alone, whether the locations of the icebergs in Figure 4-2 are clustered or inhibited. To consider this objectively the methodology in Section 4.3.2 is used.

Figure 4-3 shows profiles of the icebergs along the vehicle's path; notice that the draft scales are variable and the horizontal scale for icebergs 2 and 6 are different from the others. The dimensions of the icebergs in M247 are tabulated in Table 4-3.

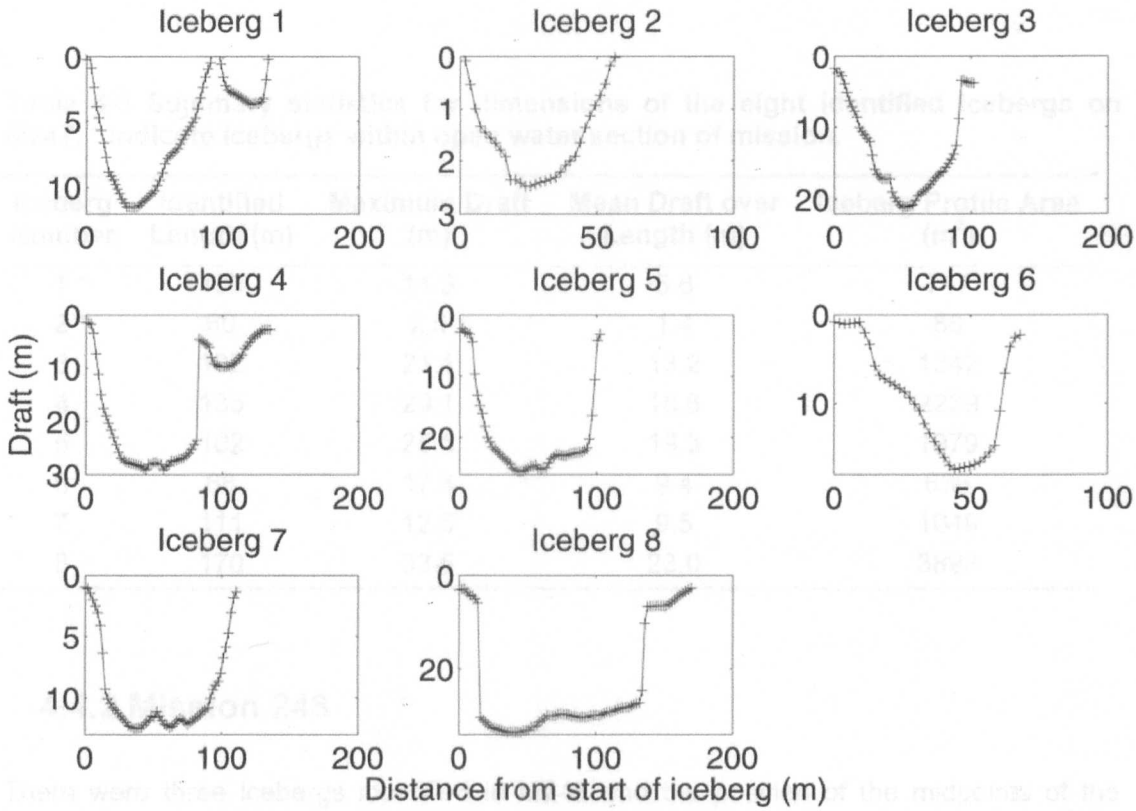

Figure 4-3 Profiles of identified icebergs from M247, note that vertical scales (for draft) are different for each iceberg and the horizontal scales for icebergs 2 and 6 are not the same as the other icebergs.

Iceberg 8 is the largest iceberg along the track with maximum draft of 33.5m and a length of the order of 170m. Iceberg 2 is the smallest iceberg with a mean draft of only 1.4m averaged over the entire length, but it is not a pressure ridge or rubble pile (as defined in Tin and Jeffries (2003)) as it exists in open water and is identified as glacial based on backscatter values (Mark Brandon, Personal Communication).

Table 4-3 Summary statistics for dimensions of the eight identified icebergs on M247. * indicate icebergs within open water section of mission.

Iceberg Number	Identified Length (m)	Maximum Draft (m)	Mean Draft over Length (m)	Iceberg Profile Area (m^2)
1 *	133	11.5	5.6	747
2 *	60	2.5	1.4	86
3	102	21.1	13.2	1342
4	135	29.1	16.6	2239
5	102	25.5	19.3	1979
6	68	17.4	9.4	636
7	111	12.5	9.5	1049
8	170	33.5	23.0	3893

4.4.2 Mission 248

There were three icebergs identified in M248 and the position of the midpoints of the icebergs along the vehicle's track, are shown in Figure 4-4. Profiles of the icebergs are shown in Figure 4-5 (which unlike Figure 4-3 has all the icebergs on the same scales) and their dimensions along Autosub's track are given in Table 4-4. Careful examination shows that, unlike M247, all of the icebergs are outside of the sea ice zone identified as the solid red line in Figure 4-4. For this reason only the first simulation described in Section 4.3.2 was applied to M248 (i.e., using the whole mission data and not the under ice section) although a second simulation was carried out using just the open water data.

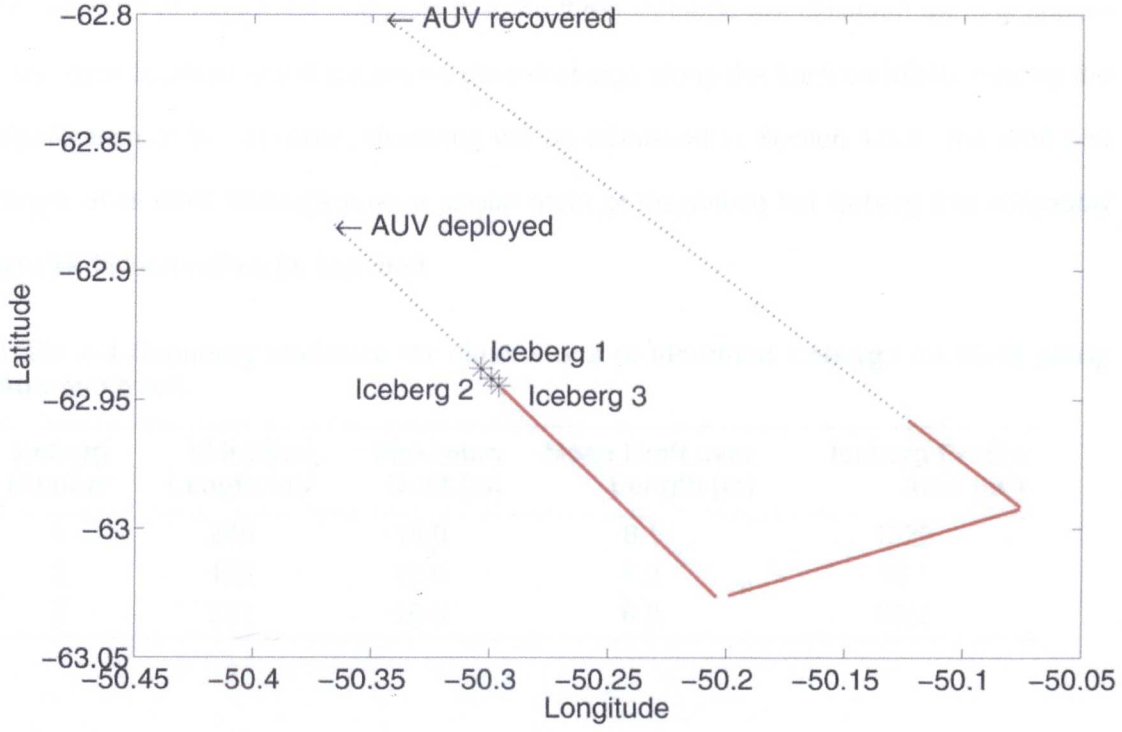

Figure 4-4 Location of mission track, iceberg midpoints and location of ice edge for M248. Solid red line shows track identified as under sea ice whereas dotted line is track under open water. No data are available for the sections during which Autosub is turning and changing depth.

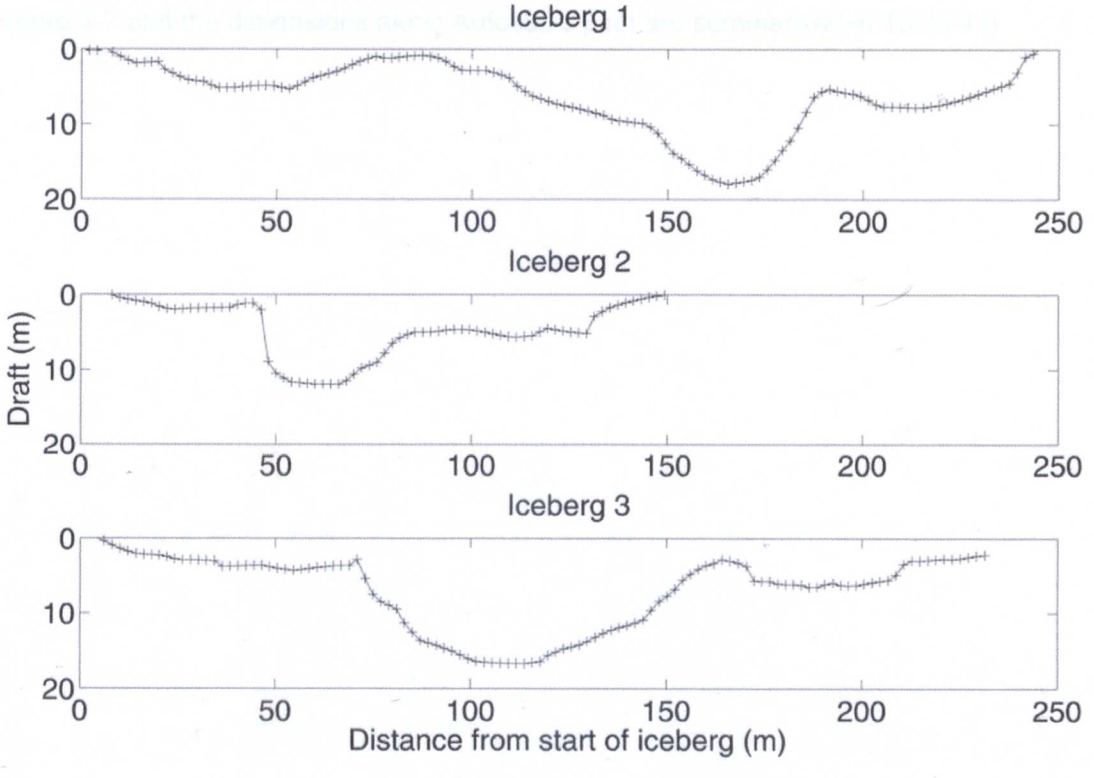

Figure 4-5 Profiles of identified icebergs from M248 plotted using the same vertical and horizontal scales.

Observation of Figure 4-4 suggests that the three icebergs are clustered as they appear very close together and there are no other icebergs along the track for M248. Testing the significance of this apparent clustering will be discussed in Section 4.5.2. The draft and length of all three icebergs have a similar order of magnitude but Iceberg 2 is noticeably smaller in terms of length and draft.

Table 4-4 Summary statistics for dimensions of identified icebergs on M248 along Autosub track.

Iceberg Number	Identified Length (m)	Maximum Draft (m)	Mean Draft over Length (m)	Iceberg Profile Area (m^2)
1	249	18.0	6.1	1526
2	159	12.0	4.2	667
3	231	16.6	6.0	1602

4.4.3 Mission 252

Eleven icebergs were found in M252 and the position of the midpoints of these icebergs along the vehicle's track, are shown in Figure 4-6. Profiles of the icebergs are shown in Figure 4-7 and the dimensions along Autosub's path are summarised in Table 4-5.

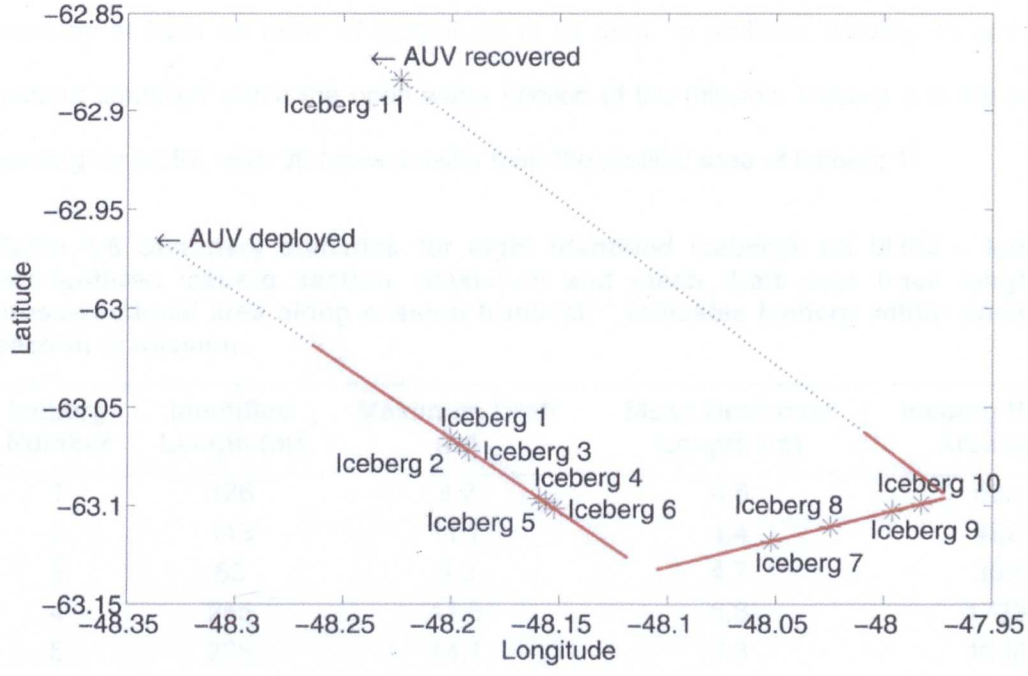

Figure 4-6 Location of mission track, iceberg midpoints and location of ice edge for M252. Solid red line shows track identified as under sea ice whereas the dotted black line is track under open water. No data are available for the sections during which Autosub is turning and changing depth.

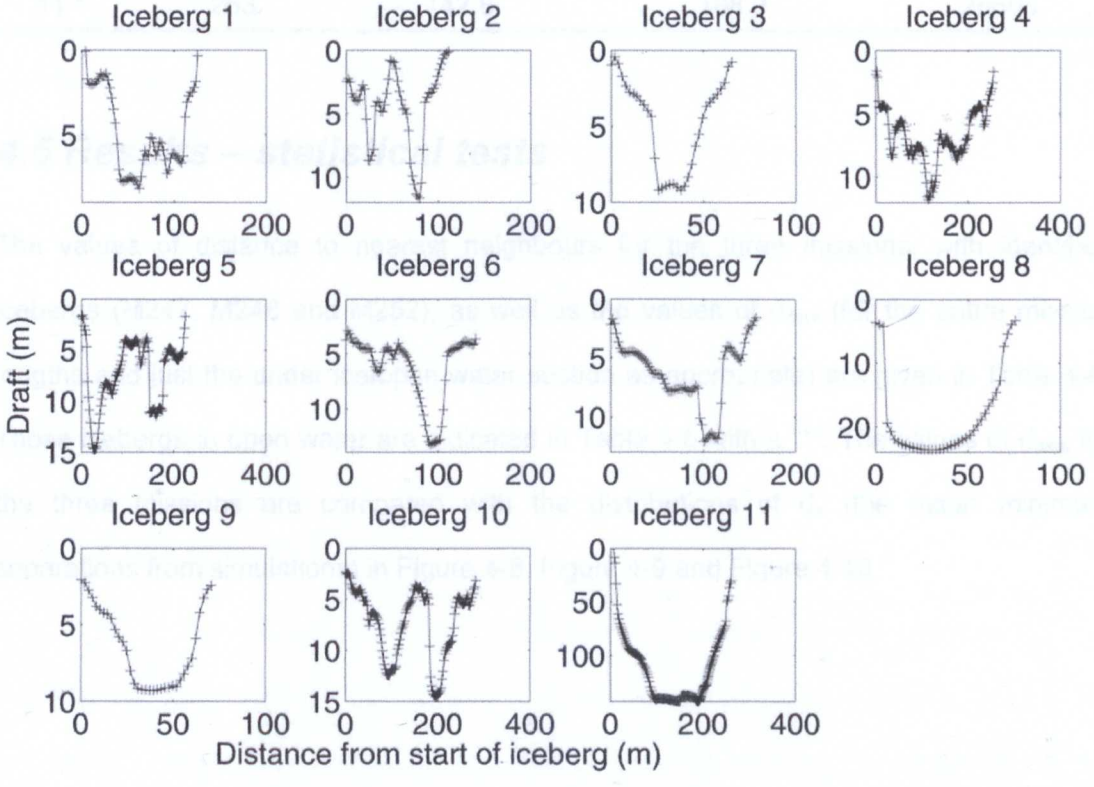

Figure 4-7 Profiles of identified icebergs from M252. Note different scales for vertical (ice draft) and horizontal axes in particular for Iceberg 11.

Iceberg 11 has a distinct profile compared to the other much smaller icebergs along this track by at least an order of magnitude in its draft. In addition, Iceberg 11 is the only iceberg identified within the open water section of the mission. Iceberg 3 is the smallest iceberg on M252, over 90 times smaller than the profiled area of Iceberg 11.

Table 4-5 Summary statistics for eight identified icebergs on M252 – length of encountered iceberg section, maximum and mean draft over track length and cross-sectional area along mission transect. * indicates iceberg within open water section of mission.

Iceberg Number	Identified Length (m)	Maximum Draft (m)	Mean Draft over Length (m)	Iceberg Profile Area (m^2)
1	126	8.2	4.6	584
2	113	11.7	4.4	492
3	65	9.2	4.7	309
4	255	11.8	6.8	1723
5	226	14.7	7.3	1638
6	141	13.3	6.2	879
7	157	12.1	6.2	982
8	76	23.6	18.2	1374
9	71	9.3	6.4	450
10	282	14.5	7.3	2058
11 *	263	142.8	108.9	28605

4.5 Results – statistical tests

The values of distance to nearest neighbours for the three missions, with identified icebergs (M247, M248 and M252), as well as the values of d_{data} (for the entire mission lengths and just the under ice/open water section as appropriate) are given in Table 4-6. Those icebergs in open water are indicated in Table 4-6 with a "*". The values of d_{data} for the three missions are compared with the distributions of d_n (the mean minimum separations from simulations) in Figure 4-8, Figure 4-9 and Figure 4-10.

Table 4-6 Distances to nearest neighbours for icebergs in M247, M248 and M252. A * indicates an iceberg within the open water section of a mission.

	Mean Distance (m)		
Iceberg	**M247**	**M248**	**M252**
1	6008*	480*	406
2	3660*	364*	406
3	1492	364*	425
4	1492	-	287
5	2286	-	287
6	1425	-	388
7	1425	-	1612
8	5438	-	1612
9	-	-	787
10	-	-	787
11	-	-	27599*
d_{data} (whole mission)	2903	403	3145
d_{data} (under ice)	2260	-	700
d_{data} (open water)	-	403	-

The most striking point about Table 4-6 is Iceberg 11 from M252 being the furthest away from its nearest neighbour by an order of magnitude compared with any other iceberg. Also of note is that, on average, the icebergs in M248 appear much closer together than those from the other two missions.

4.5.1 Mission 247

The results of the simulations for M247 are shown in Figure 4-8 and summarised in Table 4-7, showing the results for the whole mission and for just the six icebergs within the sea ice region. The p values calculated from the simulations are 0.25 for the whole mission and 0.52 for the under ice section. Hence, there is insufficient evidence to suggest that the icebergs cluster or are inhibited and I conclude that the icebergs are randomly located

along the whole mission length. For the same reasons I also conclude that the icebergs are randomly located along the section within the sea ice zone.

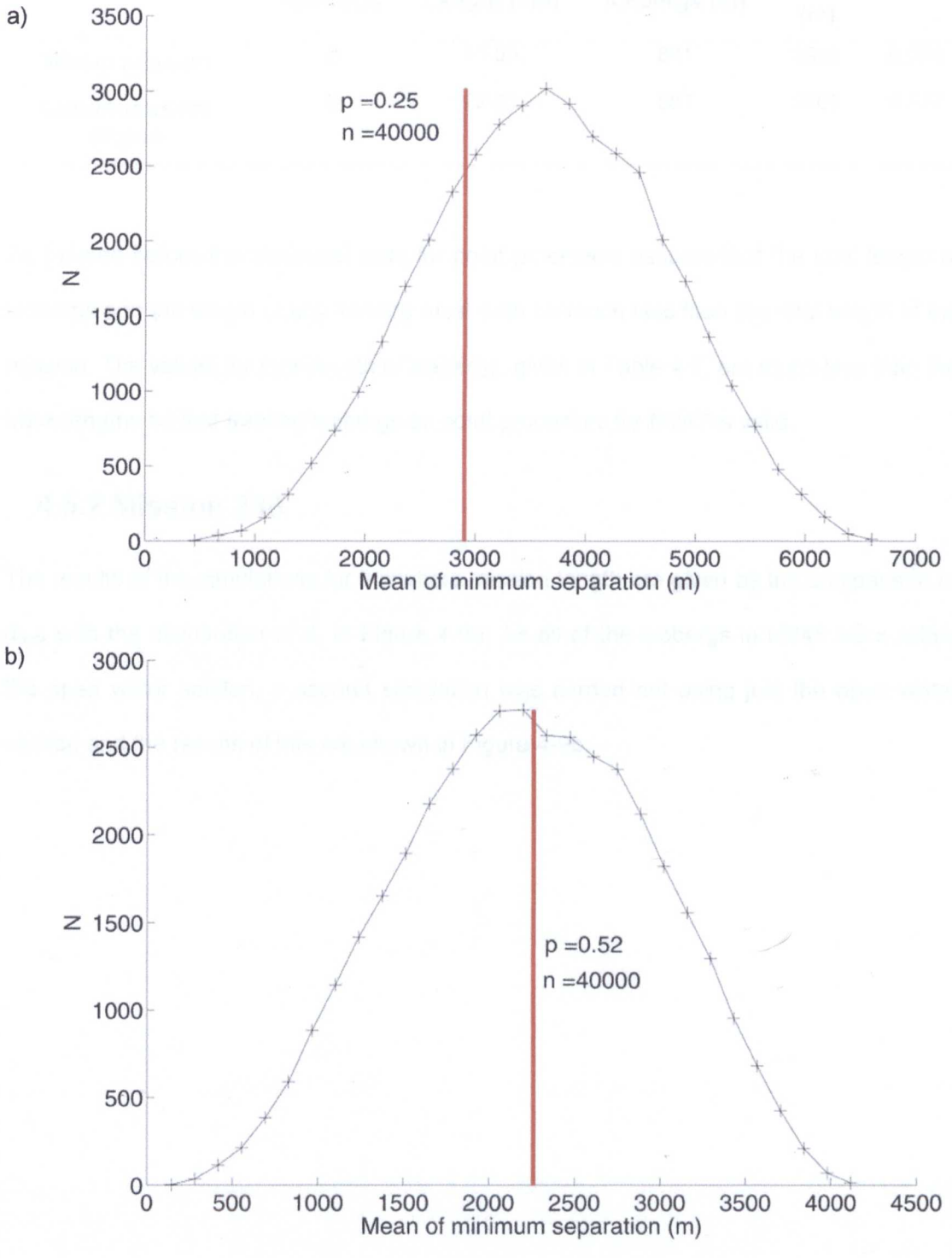

Figure 4-8 M247 simulated distribution (d_n) and actual value of the mean nearest neighbour distance for the 8 icebergs (d_{data}) a) along whole mission and b) for section under sea ice. N is the number of simulations for a given mean minimum separation.

Table 4-7 Summary of simulations for M247.

Stage	Number of icebergs	Track Length (km)	Total Length of Icebergs (m)	d_{data} (m)	p value
Whole mission	8	51.55	881	2903	0.254
Continuous ice region	6	22.81	687	2260	0.522

As I stated before the statistical tests for point processes assume that the total length of icebergs and the length of any iceberg must both be much less than the total length of the mission. The values for total length of icebergs, given in Table 4-7, are much less than the track lengths so that treating icebergs as point processes for M247 is valid.

4.5.2 Mission 248

The results of the simulations for the whole mission length are given by the comparison of d_{data} with the distribution of d_n in Figure 4-9a. As all of the icebergs in M248 were within the open water section, a second simulation was carried out using just the open water section and the results of this are shown in Figure 4-9b.

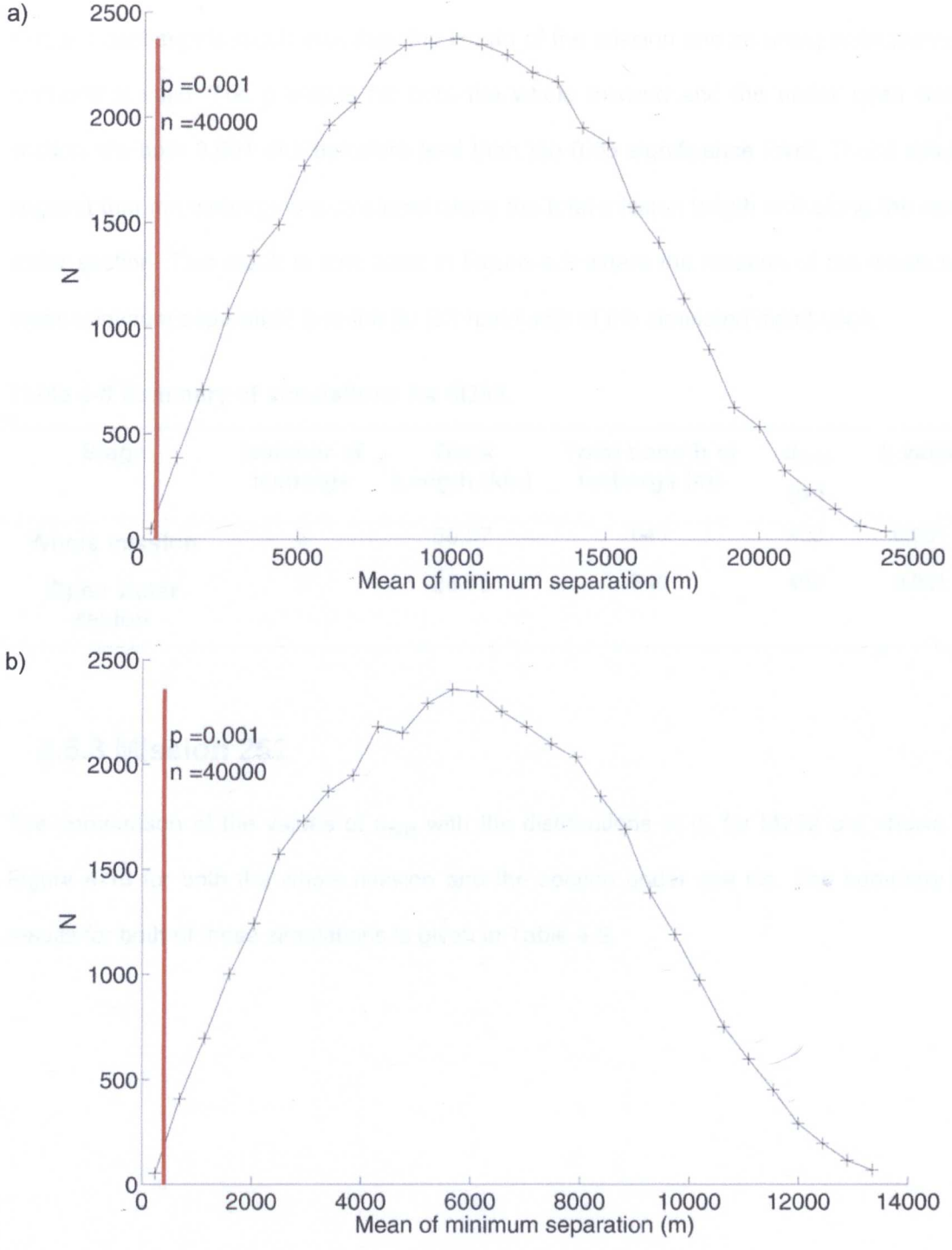

Figure 4-9 M248 simulated distribution (d_n) and actual value (vertical red line) of the mean nearest neighbour distance for the 3 icebergs (d_{data}) for a) whole mission and b) under open water section. N is the number of simulations for a given mean minimum separation.

As with M247, the values given in the summary table (Table 4-8) indicate that the overall length of icebergs is much less than the length of the mission and so using point process methods is valid. The p values for both the whole mission and the under open water section are both 0.001 and therefore less than the 0.05 significance level. These values suggest that the icebergs are clustered along the total mission length and along the open water section. This result is also clear in Figure 4-9 where the location of the measured mean minimum separation is to the far left-hand side of the simulated distribution.

Table 4-8 Summary of simulations for M248.

Stage	Number of icebergs	Track Length (km)	Total Length of Icebergs (m)	d_{data} (m)	p value
Whole mission	3	50.57	640	403	0.001
Open water region	3	28.73	640	403	0.001

4.5.3 Mission 252

The comparison of the values of d_{data} with the distributions of d_n for M252 are shown in Figure 4-10 for both the whole mission and the section under sea ice. The summary of results for both of these simulations is given in Table 4-9.

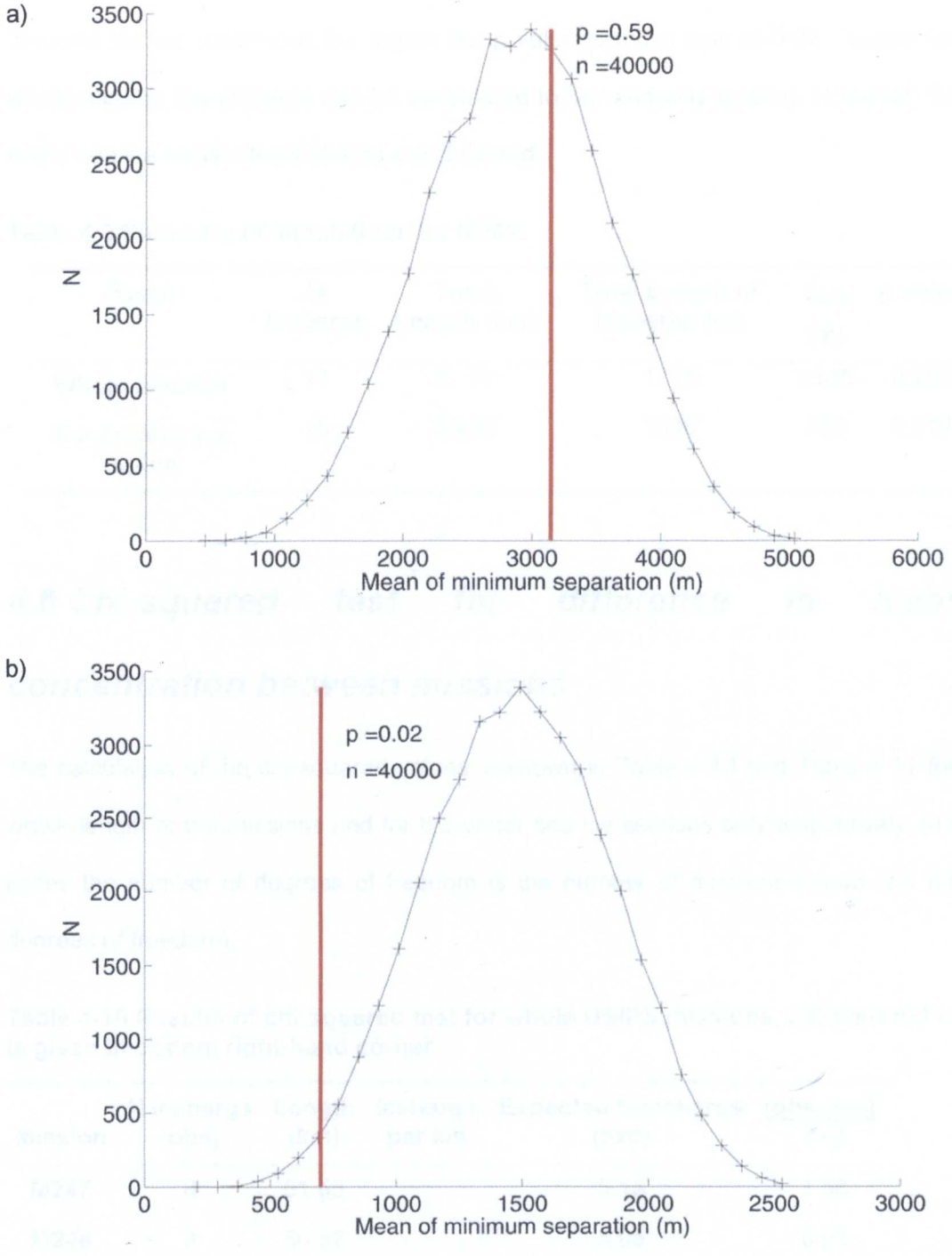

Figure 4-10 M252 simulated distribution (d_n) and actual value (vertical red line) of the mean nearest neighbour distance (d_{data}) for the a) 11 icebergs along whole mission and b) for the 10 icebergs under sea ice. N is the number of simulations for a given mean minimum separation.

Even with the larger number of identified icebergs for M252 (compared to the other missions) the total length of icebergs is much less than the overall track length so point

process methods are still valid. In Table 4-9 the p value for the whole mission is 0.59 whereas for the continuous ice region the p value is much less at 0.02. Hence, for the whole mission the icebergs can be considered to be randomly located. However, for the under sea ice section the icebergs are clustered.

Table 4-9 Summary of simulations for M252.

Stage	N icebergs	Track Length (km)	Total Length of Icebergs (m)	d_{data} (m)	p value
Whole mission	11	57.27	1775	3145	0.591
Continuous ice region	10	25.92	1536	700	0.017

4.6 Chi-squared test for difference in iceberg concentration between missions

The calculation of the chi-squared values is shown in Table 4-10 and Table 4-11 for the whole length of the missions and for the under sea ice sections only respectively. In both cases the number of degrees of freedom is the number of missions minus one (i.e., 3 degrees of freedom).

Table 4-10 Results of chi-squared test for whole USIPS missions, chi-squared value is given in bottom right-hand corner.

Mission	N icebergs (obs)	Length (km)	Icebergs per km	Expected N icebergs (exp)	$\frac{(obs-exp)^2}{exp}$
M247	8	51.55		5.15	1.58
M248	3	50.57		5.05	0.83
M252	11	57.27		5.72	4.88
M253	0	60.97		6.09	6.09
Overall	22	220.36	0.10	22	κ =13.4

Table 4-11 Results of chi-squared test for under sea ice sections of USIPS missions, chi-squared value is given in bottom right-hand corner.

Mission	N icebergs (obs)	Length (km)	Icebergs per km	Expected N icebergs (exp)	$\frac{(obs-exp)^2}{exp}$
M247	6	22.81		3.19	2.47
M248	0	21.84		3.06	3.06
M252	10	25.92		3.63	11.19
M253	0	43.72		6.12	6.12
Overall	16	114.29	0.14	16	κ =22.84

The chi-squared value for the combined lengths of all four USIPS missions is found to be 13.4 with three degrees of freedom. The under sea ice sections of the four USIPS missions give a chi-squared value of 22.84 again with three degrees of freedom. The equivalent one tail p value for the entire length of all missions is 0.004. The under ice sections have $p<0.001$. The chi-squared test may not be completely appropriate for the under sea ice section because the expected values for all but M253 are less than five (c.f. Section 4.3.3). At the same time though, the expected values all exceed three, so they are not very small, and the p value is very near zero. Hence, it is unlikely that the icebergs distribute randomly in the sections under sea ice.

4.7 Discussion and Conclusions

4.7.1 Simulations

The results from M247 in Figure 4-8a suggest that there is insufficient evidence not to accept that icebergs are randomly located along the whole mission transect ($p = 0.254$, $n = 40,000$). Similarly, the icebergs in M247 are randomly located within the under ice section ($p = 0.522$, $n = 40,000$) as can be seen in Figure 4-8b.

For M248 the three icebergs are all located within the open water section so the p values have been calculated based on the whole mission length and the open water section only.

In both cases p = 0.001 and n= 40,000 (Figure 4-9). These low p values suggest that the icebergs are clustered, i.e., the icebergs are close to each other (Figure 4-4). The length and depth of Iceberg 1 and Iceberg 3 are very similar (Figure 4-5) and it is possible that they were once part of the same iceberg but Iceberg 1 has rotated 180°, see Figure 4-5 or Figure 4-11a. It is also possible that Iceberg 2 was part of the same larger iceberg (or section of ice shelf). A possible explanation of these similarities is shown in Figure 4-11b. where as the icebergs drift they rotate and perhaps Iceberg 1 has rotated ~180°.

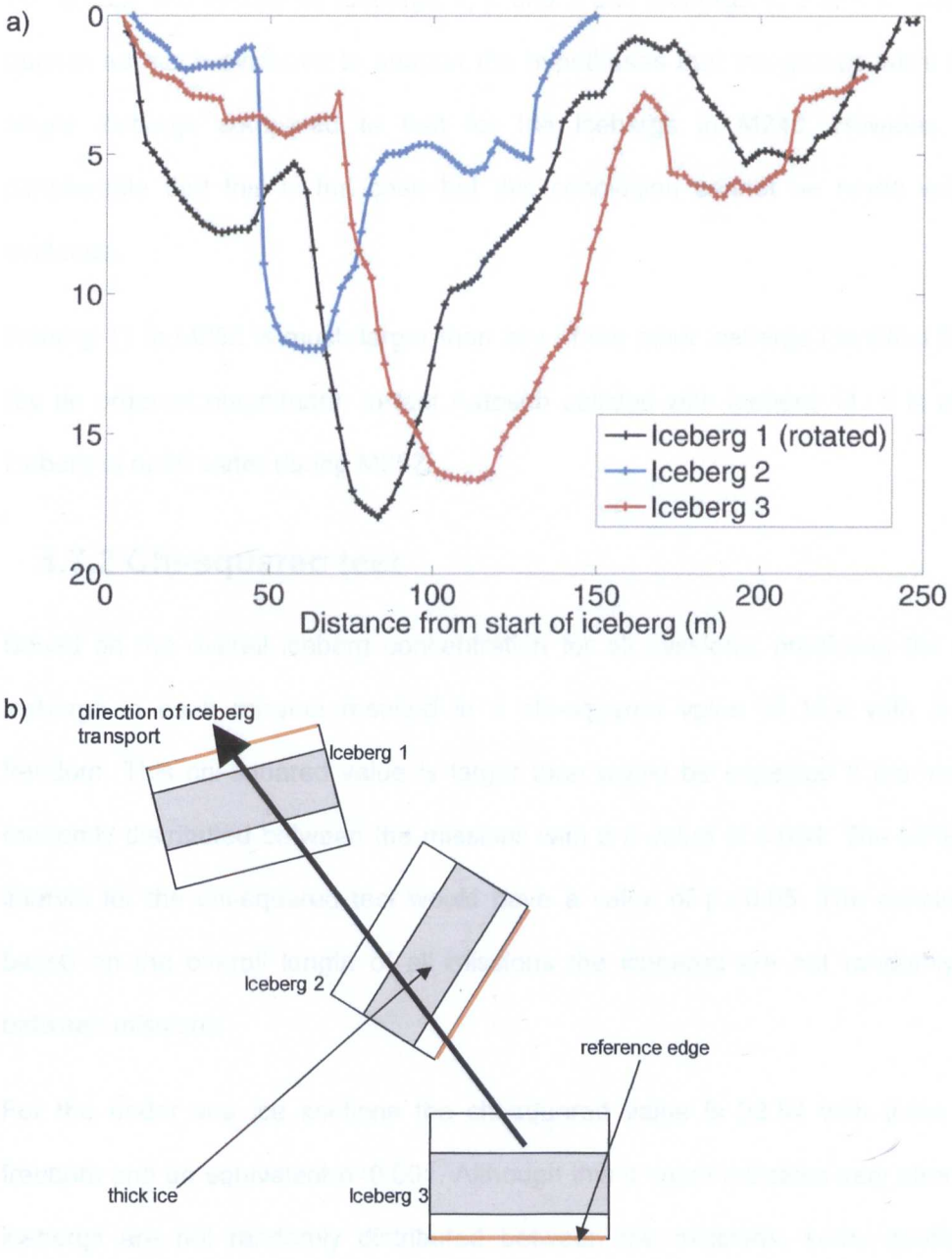

Figure 4-11 a) Iceberg profiles for M248 with the direction of Iceberg 1 reversed compared with Figure 4-5 and b) Schematic representation of a possible cause of similar profiles for M248 icebergs.

For M252 the p value from the simulations is 0.591 (Figure 4-10) indicating that the icebergs can be considered randomly distributed along the whole mission track. However, for the under sea ice section of M252 the p value is 0.017 (n=40,000) suggesting that the icebergs are clustered within this section of the mission. Inspection of Figure 4-6 shows

that there are two distinct clusters of icebergs along the first leg of the vehicle track. The two groups are formed by icebergs 1, 2 and 3 and icebergs 4, 5 and 6. There does not appear as much evidence to support the hypotheses that the groups were formed from single icebergs compared to that for the icebergs in M248. However, it is quite conceivable that this is the case but this conclusion cannot be made without further evidence.

Iceberg 11 in M252 is much larger than any of the other icebergs identified for this study (by an order of magnitude); in fact Autosub collided with Iceberg 11. It is also the only iceberg in open water during M252.

4.7.2 Chi-squared test

Based on the overall iceberg concentration for all missions, predicting the numbers of icebergs in each mission resulted in a chi-squared value of 13.4 with 3 degrees of freedom. This chi-squared value is larger than would be expected if the icebergs were randomly distributed between the missions with a p value of 0.004. The 95% confidence interval for the chi-squared test would have a value of $p \geq 0.05$. The conclusion is that based on the overall length of all missions the icebergs are not randomly distributed between missions.

For the under sea ice sections the chi-squared value is 22.84 with three degrees of freedom and an equivalent $p<0.001$. Although this p value indicates very strongly that the icebergs are not randomly distributed between the missions, some caution must be exercised in drawing conclusions, as the conditions for the chi-squared test to be fully applicable are not satisfied as a number of the expected values (see Table 4-11) are less than five. Overall, I conclude that it is unlikely that the icebergs are randomly located within the sections of mission track under sea ice.

4.7.3 Summary

The aims of this chapter were to examine the spatial distribution of icebergs along one-dimensional Autosub tracks to investigate whether:

a. the icebergs along the tracks were clustered within each mission

b. the icebergs found within the sea ice sections of these missions were clustered

c. to establish if there was a difference in the distributions in a and b above

There is no overall, clear pattern in whether icebergs are clustered within a given mission either for the whole track-length or just the section under sea ice. Between missions the icebergs are seen to cluster more than would be expected by the random variability of the number of icebergs in each mission. This latter statement holds for both the entire track-lengths and for just the under sea ice sections.

From these results, it can be concluded that iceberg concentration between missions cannot be assumed to be random and this must be considered when using Autosub to estimate sea ice draft. Similarly, within a mission it is not possible to generalise whether icebergs are distributed randomly in space and therefore it is important to consider icebergs when producing the PDF for sea ice draft.

To examine these matters further requires data on a larger region from which samples can be taken to test the hypothesis that icebergs are completely spatially random. This work can be found in the following chapter.

Chapter 5 Satellite imagery of iceberg spatial distribution

5.1 Introduction

This chapter is an extension to the methodology developed in the previous chapter to investigate the issue of whether icebergs are randomly distributed in space. The research questions considered relate to icebergs identified within 2-dimensional satellite images rather than the 1-dimensional case considered in Chapter 4. The specific questions investigated are:

1. Do icebergs cluster or are they inhibited in space within sea ice (on the scale of a typical Autosub mission)?
2. Do icebergs cluster or are they inhibited in space within the open ocean (on the scale of a typical Autosub mission)?
3. Is there a difference between the results of 1 and 2 above?

As discussed in Section 2.9, these research questions are aimed at assessing the spatial distribution of icebergs on the scale of typical Autosub missions and hence the biasing of the sea ice draft given iceberg clustering/inhibition.

Preliminary work using the data presented in Chapter 4 suggested that icebergs were clustered in the edge of the sea ice region and that there were very few icebergs in the adjacent open water regions. The data in this current chapter are insufficient to investigate if this is the case as no image was readily available showing a region of contiguous sea ice and open water.

A number of statistical tests are used to determine whether the icebergs can be considered to be completely spatially random. The first methodology divides the study regions into quadrats and compares the counts in these quadrats with the expected

values if the icebergs are spatially random. The other two methods (G and K functions) rely on knowing the separation of the icebergs either from all other icebergs or just the nearest neighbour and graphically comparing the values from the data with simulations of the images. The theory for these tests was introduced in Section 3.2. Under complete spatial randomness (CSR), for the G function a plot of the measured values of G against the theoretical values of G is a straight line. Whereas for the K function, zero values of L indicate CSR.

The three methodologies above investigate the CSR hypothesis based on different levels of detail about the spatial distributions of the icebergs, i.e.,

1. the distribution of the number of icebergs within quadrats
2. the distances between an iceberg and its nearest neighbour
3. the distances between an iceberg and all other icebergs.

As #2 above does not account for the separations between all icebergs within a study region, the results of #1 and #3 should be given precedence as they do account for the separations between all icebergs.

5.2 Data

The data for this chapter were selected from two satellite images from the southern hemisphere both with a pixel resolution of 15m. The locations of the image scenes are shown in Figure 5-1 and were chosen so that one included icebergs within open water and the other showed icebergs within sea ice. These two images could then be used to establish if there is a difference in the clustering of icebergs between open water and sea ice as suggested by the preliminary conclusions from Chapter 4 that icebergs cluster on the edge of the sea ice zone. A study region was chosen from each of the two images based on a number of criteria:

1. The study region had an area of similar magnitude to that covered by an Autosub mission.

2. That an iceberg can occur within any area of the study region, this was achieved using visual assessment of possible study regions (see Section 3.2).

3. So that the area of the study region (i.e., number of pixels) was manageable by a desktop PC.

The area chosen for each study region was 15km by 7.5km (1000 by 500 pixels). The north/south alignment of the two study regions is different as can be seen in Figure 5-2 and Figure 5-3. A summary of the two images is given in Table 5-1 and they are discussed further in the following sections.

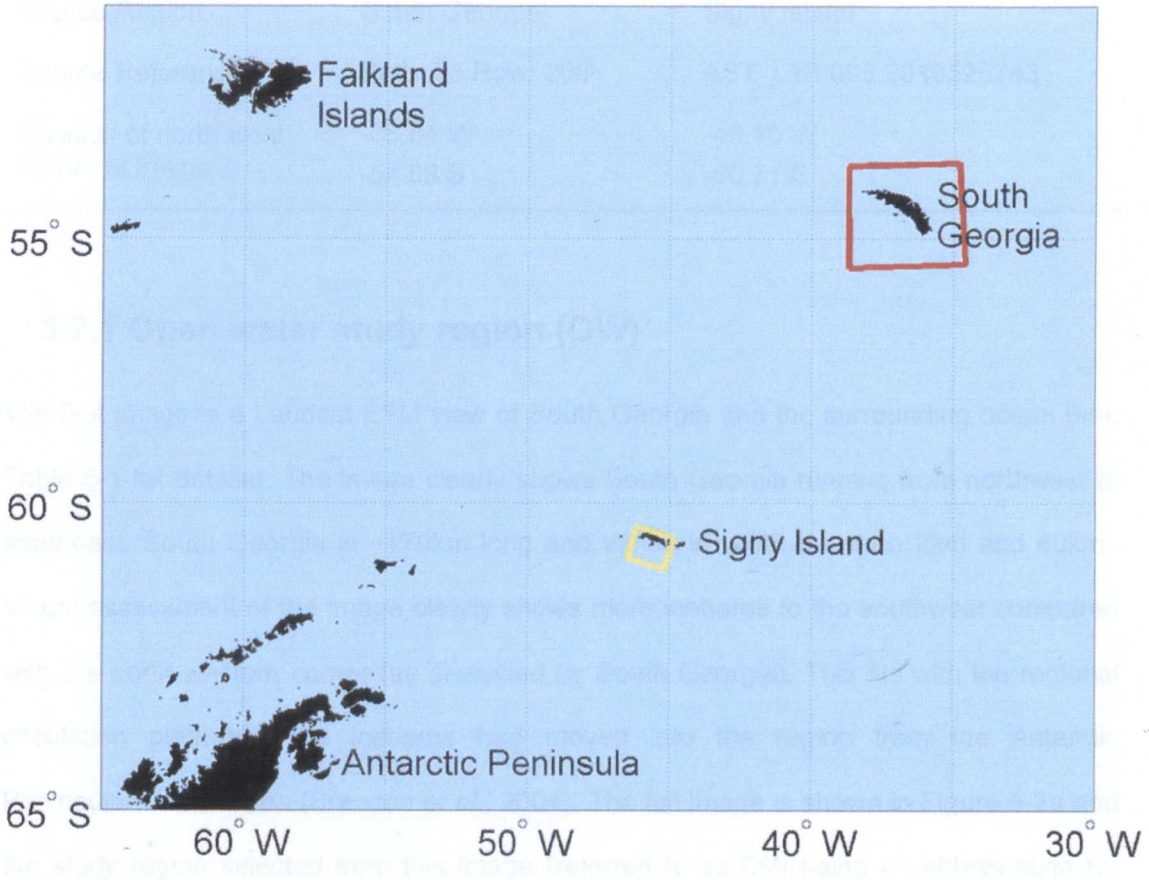

Figure 5-1 Location of two satellite images for iceberg spatial distribution analysis – SI ( ) and OW ( ) both located northeast of the Antarctic Peninsula.

Table 5-1 Summary information for two satellite images used.

Attribute	OW	SI
Sea state	Open water	Sea ice
Satellite/Sensor	Landsat Enhanced Thematic Mapper (ETM)	Advanced Spaceborne Thermal Emission & Reflection Radiometer (ASTER)
Band	8	3 band in visible near-infrared (VNIR)
Source Acquisition Date	7 February 2003	18 September 2001
Source Region	South Georgia	Signy Island
Source Reference	Path: 98 Row: 206	AST_L1B.003.2018526743
Position of north west corner of image	-36.84 W -54.68 S	-46.10 W -60.71 S

5.2.1 Open water study region (OW)

The first image is a Landsat ETM view of South Georgia and the surrounding ocean (see Table 5-1 for details). The image clearly shows South Georgia running from northwest to southeast. South Georgia is ~170km long and varies in width between 2km and 40km*. Visual assessment of the image clearly shows more icebergs to the southwest compared with the north-western corner (as dissected by South Georgia). This fits with the regional circulation pattern if the icebergs had moved into the region from the Antarctic Peninsula/Weddell Sea (Brandon *et al.*, 2004). The full image is shown in Figure 5-2a and the study region selected from this image (referred to as OW being an abbreviation for open water) is shown in Figure 5-2b. The study region was chosen visually so that the three criteria in Section 5.2 were met. Particularly important is the second criterion that icebergs occurred throughout the chosen study region.

* from http://www.sgisland.org/pages/main/island.htm

a)

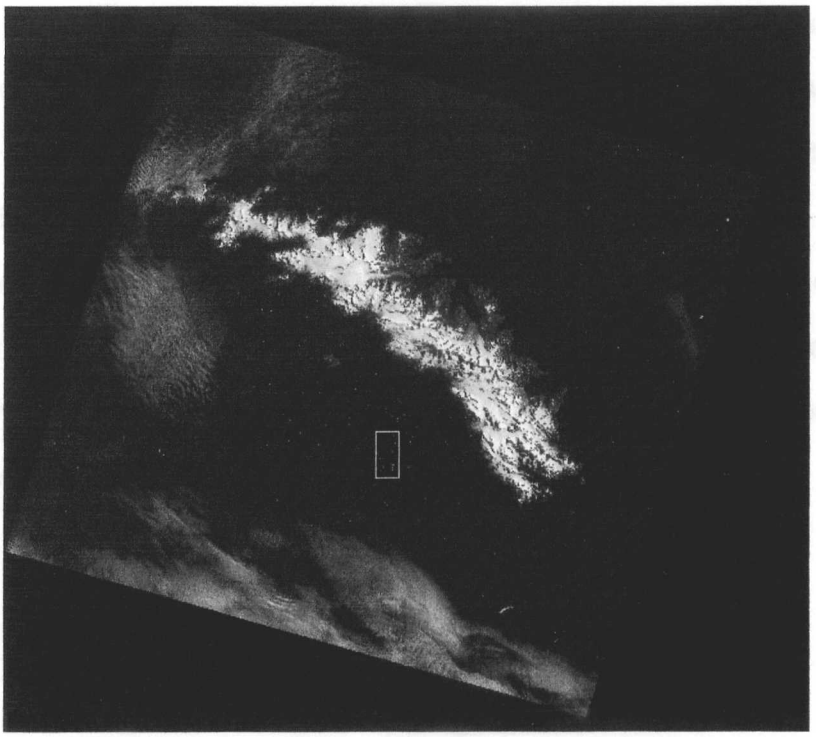

b)

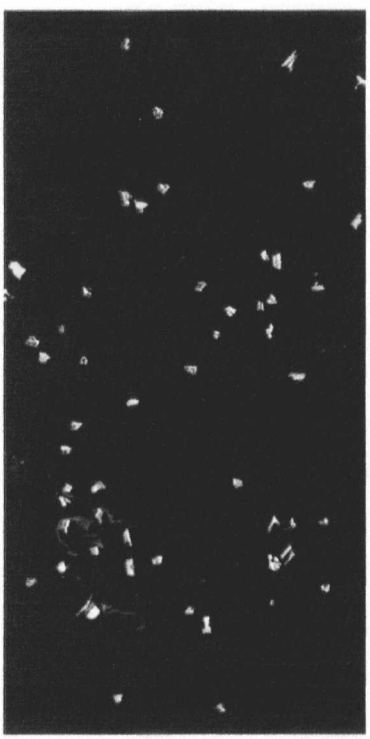

Figure 5-2 Landsat image for iceberg identification (see Table 5-1 for details) a) whole scene with study region marked by white box and b) OW study region (open water).

5.2.2 Sea ice study region (SI)

The second image was an Advanced Spaceborne Thermal Emission and Reflection Radiometer (ASTER) image utilising three bands in the visible and near-infrared (VNIR) (with wavelengths of 0.52-0.60μm, 0.63-0.69μm and 0.78-0.86μm) (Abrams et al., 2002). The image was acquired on 18th September 2001 (see Table 5-1 for further details) and shows part of Signy Island in the South Orkney Islands. The image shows icebergs within an area of extensive sea ice concentrated in the western half of the image and is shown in Figure 5-3a. This second study region is referred to as SI (abbreviation of sea ice) and is shown in Figure 5-3b.

a)

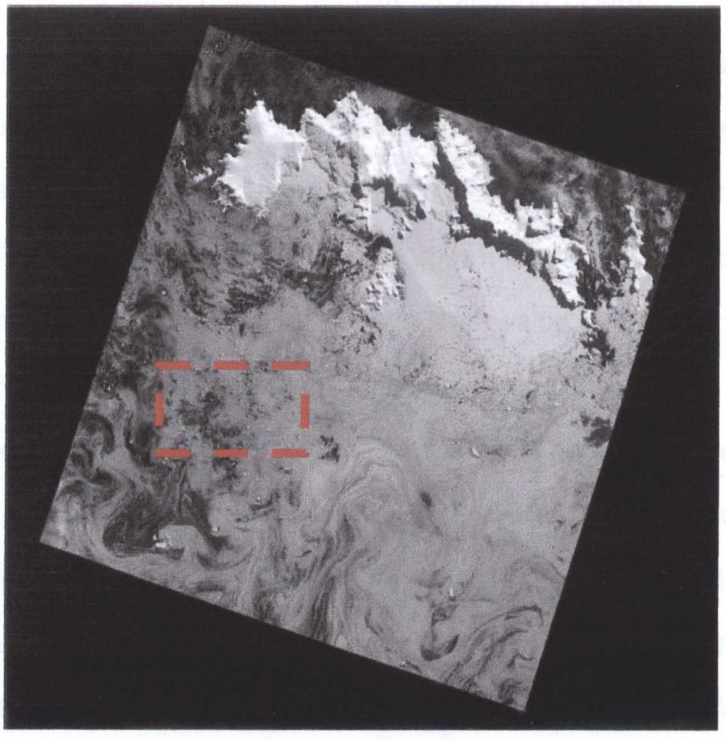

b)

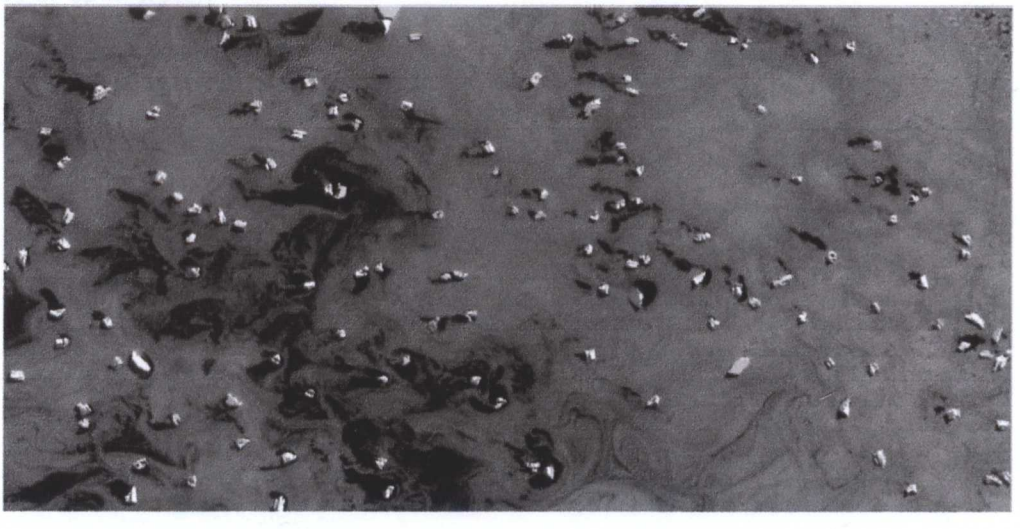

Figure 5-3 ASTER image for iceberg identification (see Table 5-1 for details) a) whole scene with study region marked by red box and b) SI study region (sea ice).

5.3 Processing images

The processing of both study regions followed a common methodology and used Matlab® and, in particular, its associated Image Processing Toolbox (The Mathworks, 2004). The first step was to identify icebergs and separate them from the rest of the study region. This was done using a threshold value based on the intensities of the pixels. The intensity

values for icebergs are greater than those for open water or for sea ice, allowing us to threshold the study regions (as can be seen in Figure 5-2 and Figure 5-3). For SI the normalised threshold value was chosen as 0.8, i.e., values above 0.8 times the maximum value of intensity (which is 255) in the study region are classified as icebergs (glacial) and values below are sea ice or open water. Figure 5-4 shows the histogram for pixel intensity for SI with the threshold value of 0.8 shown as the vertical red line. It would appear that the threshold could have been set at a lower value, at a value of ~0.51 (130 in Figure 5-4) say However, visual inspection of the thresholded image would show that some regions of sea ice were still included. The reason for this is because of the relatively bright (i.e., high pixel intensity) snow on top of sea ice. For OW the threshold value was estimated at 0.41, because the difference between the intensity of icebergs and the surrounding ocean is greater than that between icebergs and sea ice. These threshold values were found by trial and error, as visually the icebergs are clearly discernible from either the surrounding sea ice or open water.

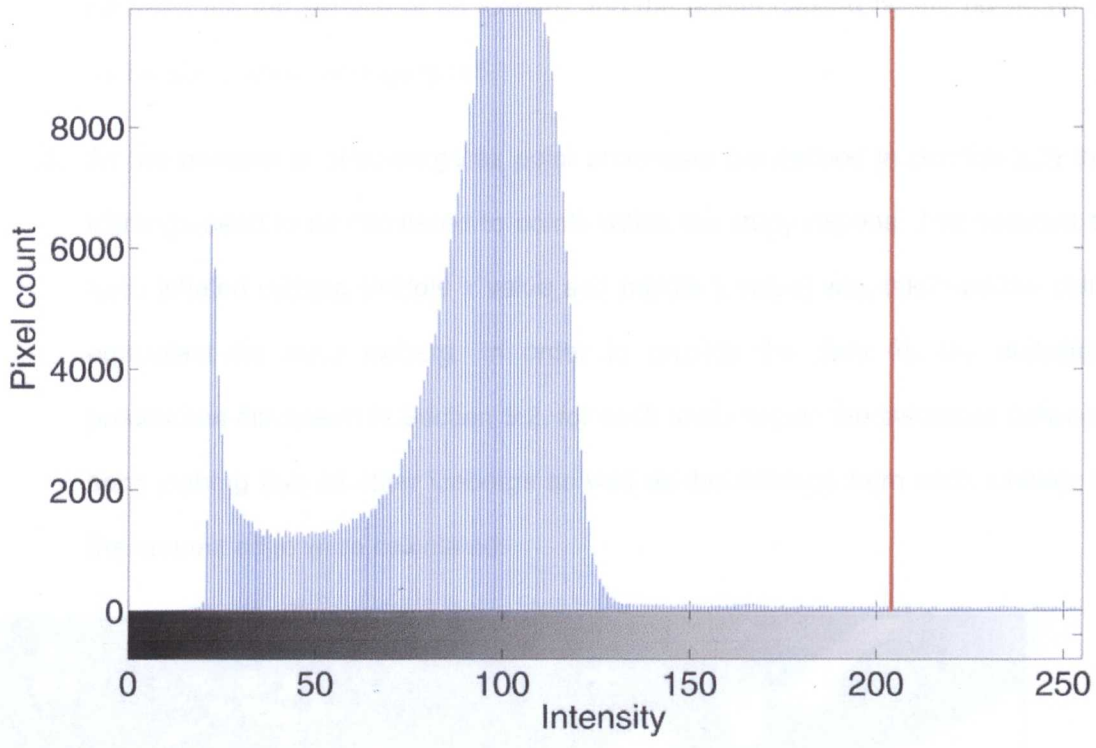

Figure 5-4 Histogram of pixel intensity for SI. The vertical red line is the chosen threshold of 0.8 (204 on the intensity scale) and the intensity of the pixels are shown on the scalebar beneath the plot.

After producing thresholded (binary) images where every pixel is either identified as 'iceberg' or 'not iceberg' the following steps were followed:

1. In order to reduce the effects of noise only those icebergs that consisted of at least three pixels were identified for use in the subsequent analysis. This step implies that for this study an iceberg must have an approximate minimum area of 675m^2. At this stage information on the number and size distribution of the icebergs was recorded (see Section 5.4.1 below).

2. The identified icebergs were inflated so that the edges moved one pixel outwards. This had the effect of reducing the number of icebergs as any icebergs that were close to each other were treated as a single iceberg. The reason for this stage in the analysis was to ensure that icebergs partially covered by seawater or meltwater are not treated as separate icebergs. An example of the lower contrast

between the top surface of an iceberg and the ocean caused by the presence of meltwater is shown in Figure 5-5.

3. As the analysis is of icebergs as point processes (as defined in Section 3.2) the icebergs need to be converted to points within the study regions. The midpoint of each inflated iceberg (middle x value and middle y value) was taken as the point equivalent for each iceberg. In order to provide the data for the statistical procedures discussed in Section 3.2, for each study region the distances between each iceberg and all other icebergs as well as the distance from each iceberg to the nearest edge were calculated.

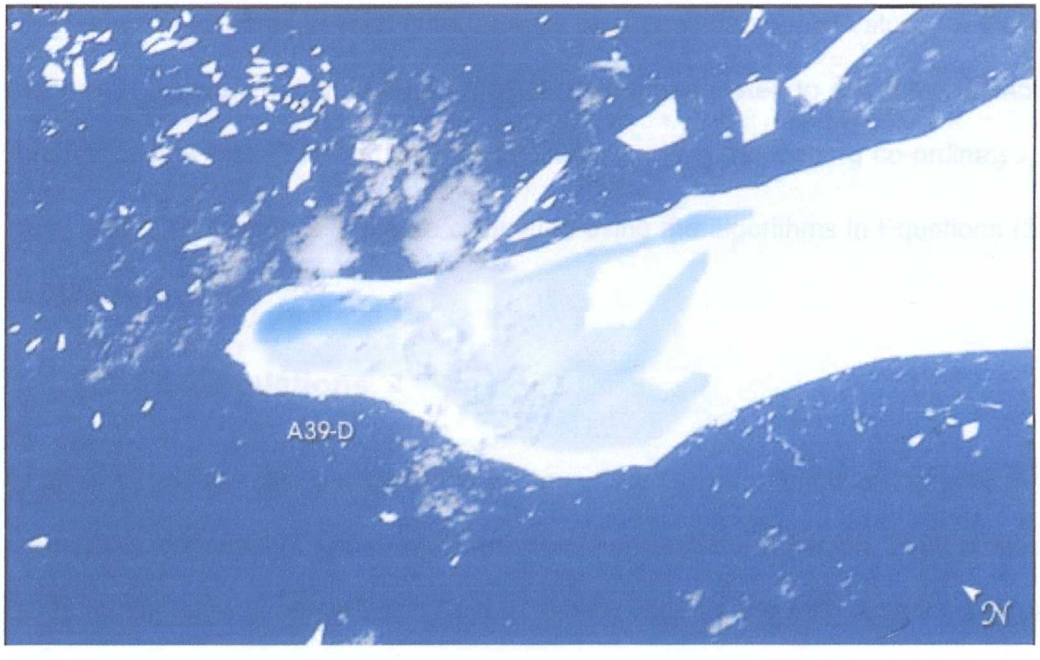

Figure 5-5 Photograph from International Space Station showing meltwater on an iceberg (A39-D) near to South Georgia*. The meltwater on the iceberg reduces the contrast between the flooded region (left-hand end) and the surrounding ocean potentially this could allow misclassification of this region of the iceberg.

* Taken from http://earthobservatory.nasa.gov/Newsroom/NewImages/images.php3?img_id=16484

5.3.1 Method of analysis

The quadrat count methodology (see Section 3.2.1) requires study regions to be divided into a number of equal-sized sub-areas and the numbers of icebergs in each of these quadrats counted. The initial method tests if the index of dispersion (I_d) is close to unity. There are a number of criteria that must be met in order that the chi-squared test (see Section 3.2.1.1) is valid. These criteria have been taken into account in the selection of the number of grids used. For ease of processing rectangular quadrats have been used. As there are more icebergs in SI compared with OW there are fewer quadrats used for OW (allowing for the restrictions on numbers of icebergs per grid).

The counts of icebergs in each quadrat were calculated and hence values for the index of dispersion (I_d) were obtained. The value of I_d was then tested to see if the distribution of quadrat counts was Poisson distributed. Similarly, using the iceberg co-ordinates, values of $\hat{G}$ and $\hat{K}$ (and hence $\hat{L}$) were calculated using the algorithms in Equations (3.6) and (3.9) respectively.

5.3.1.1 Simulations

In order to test the significance of the values of the G and L functions, simulations of the icebergs in both study regions were required. For each study region, 2000 copies of the study region were generated and random points used as the midpoints for the icebergs. This number of simulations was sufficient for the statistics to converge and was within the capability of a desktop PC. For each iceberg the size and orientation is maintained from the original data and if a simulated iceberg overlaps with an existing simulated iceberg then a new location for the midpoint is generated. This results in simulations that closely represent the original data in all respects except for the locations of the icebergs. For each study region and each simulation the locations of the iceberg midpoints were noted and from these the inter-iceberg distances and distances to closest edge of the study region were recorded. Using these values of simulated distance, estimates were made of G and L for every simulation. As discussed in Section 3.2.4, the values of G and L for every

value of distance are rank-ordered and the 5th and 95th percentile values are taken as the (90%) confidence intervals.

5.4 Results

5.4.1 Summary of iceberg numbers and sizes

Table 5-2 shows the summary statistics for the sizes and numbers of icebergs for both study regions. The size distributions for the icebergs are shown in Figure 5-6 and Figure 5-7 for the open water and sea ice study regions respectively. It is clear from these data that the icebergs in study region SI are more numerous and smaller than the icebergs in OW.

The variability in iceberg size is also larger in OW, which is not surprising given that the icebergs tend to be larger. The coefficient of variation, however, indicates that after taking into account the larger size of icebergs in OW the relative sizes of the standard deviations are similar.

Table 5-2 also shows the percentage of the study region covered in icebergs and the percentage of the study region covered by the largest iceberg. From these values I conclude that an assumption of treating icebergs as point processes is valid because the size of the study regions is much larger than the size of the icebergs.

Table 5-2 Summary of iceberg sizes in OW and SI expressed in number of pixels (1 pixel ≈ 225m^2).

	OW	SI
Number of icebergs	58	127
Mean	96.84	20.52
Median	90.00	15.00
Mode	77	7
Std. Deviation	59.245	17.011
Skewness	1.237	3.012
Std. Error of Skewness	.314	.215
Kurtosis	2.555	15.422
Std. Error of Kurtosis	.618	.427
Range	298	130
Minimum	6	4
Maximum	304	134
Coefficient of variation (SD/mean)	0.61	0.83
Percentage of study region identified as iceberg covered	1.12	0.52
Percentage of study region covered by largest iceberg	0.06	0.03

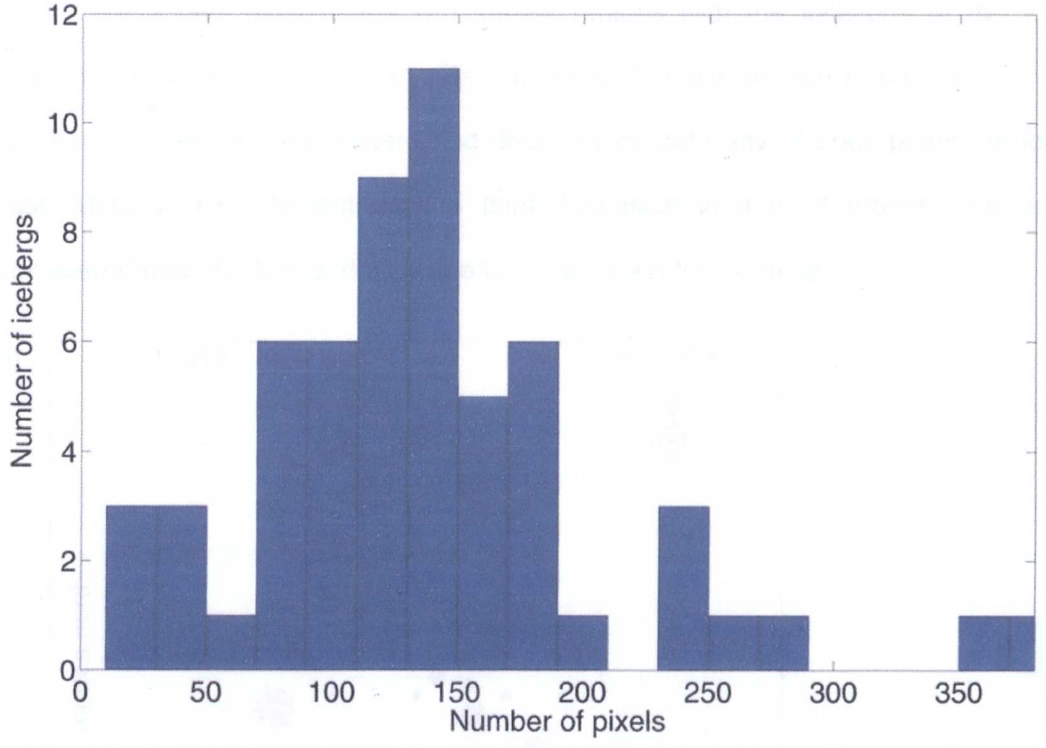

Figure 5-6 Histogram of iceberg size (in pixels) for OW (1 pixel ≈ 225m^2).

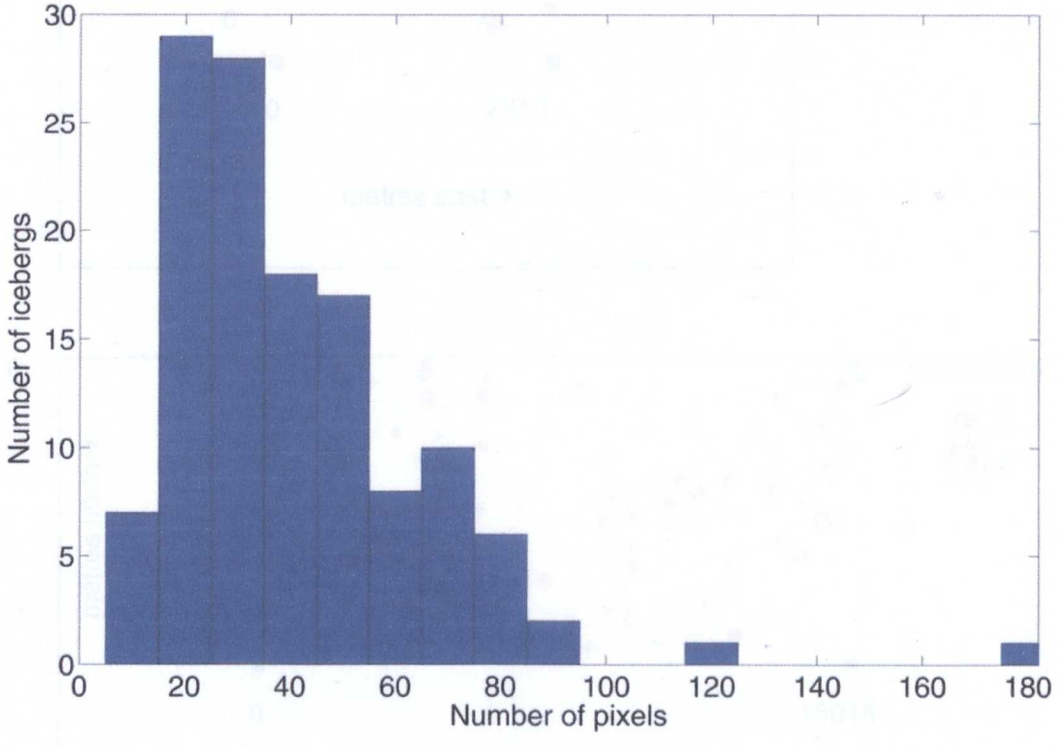

Figure 5-7 Histogram of iceberg size (in pixels) for SI (1 pixel ≈ 225m^2).

Figure 5-8 shows plots of the two survey regions with the locations of the iceberg midpoints marked by bubbles of different sizes. The bubble size is proportional to the number of pixels in each iceberg and does not indicate any obvious pattern in iceberg size. Methods exist to test such a third dimension in a point process but are not considered here, for further details see Cressie (1991) for example.

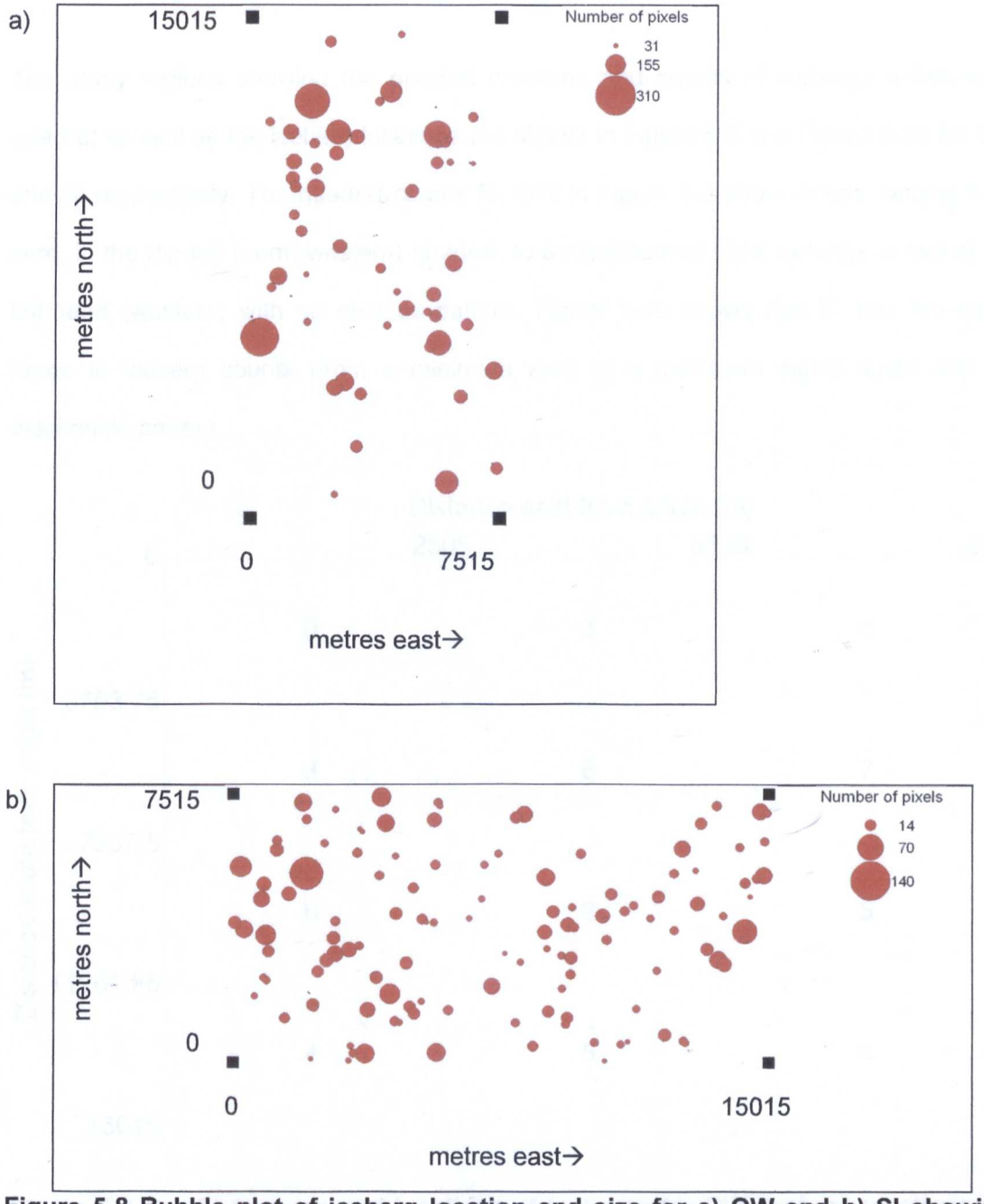

Figure 5-8 Bubble plot of iceberg location and size for a) OW and b) SI showing location of icebergs and distribution of iceberg size over study region. (1 pixel ≈ 225m^2). The solid black squares mark the corners of the study regions.

5.4.2 Analysis using quadrat counts

Using the nomenclature from Section 3.2.1.1, the study regions were each divided into k quadrats with N icebergs in each study region. Testing of the assumptions on the numbers of icebergs and quadrats introduced in Section 3.2.1.1 from Lewis (1988), that i) $N \geq 20$ and ii) $\frac{N}{k} \geq 4$, are tabulated in Table 5-3.

The study regions showing the quadrat locations and counts of icebergs within each quadrat as well as the iceberg locations are shown in Figure 5-9 and Figure 5-10 for OW and SI respectively. The quadrat counts for OW in Figure 5-9 show values ranging from zero, in the top-left (north-western) quadrat, to a maximum of eight icebergs in two of the left-hand (western) with no obvious pattern. Figure 5-10 shows that SI has the same range in iceberg counts (from a minimum zero to a maximum eight) again with no discernible pattern.

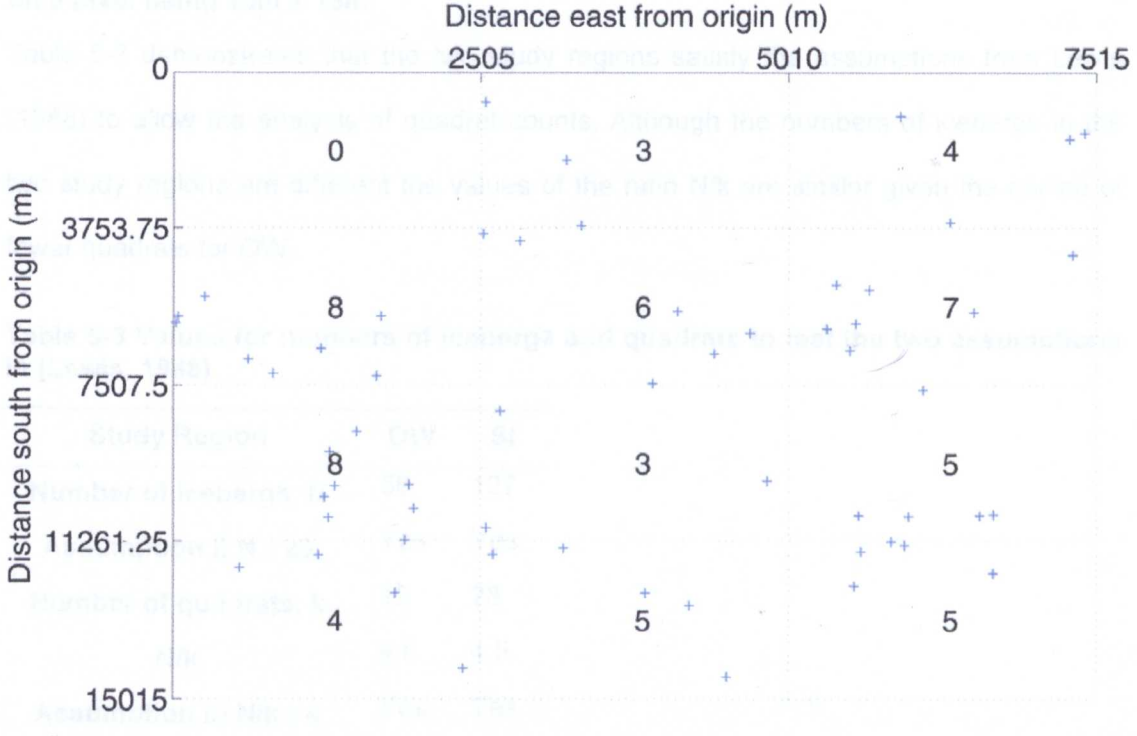

Figure 5-9 Quadrat counts and locations of icebergs for OW. Iceberg locations are marked by blue crosses (+). Quadrats are marked by dotted lines with the iceberg count for each quadrat stated in the middle of each quadrat. Distances are based on a pixel being 15m x 15m.

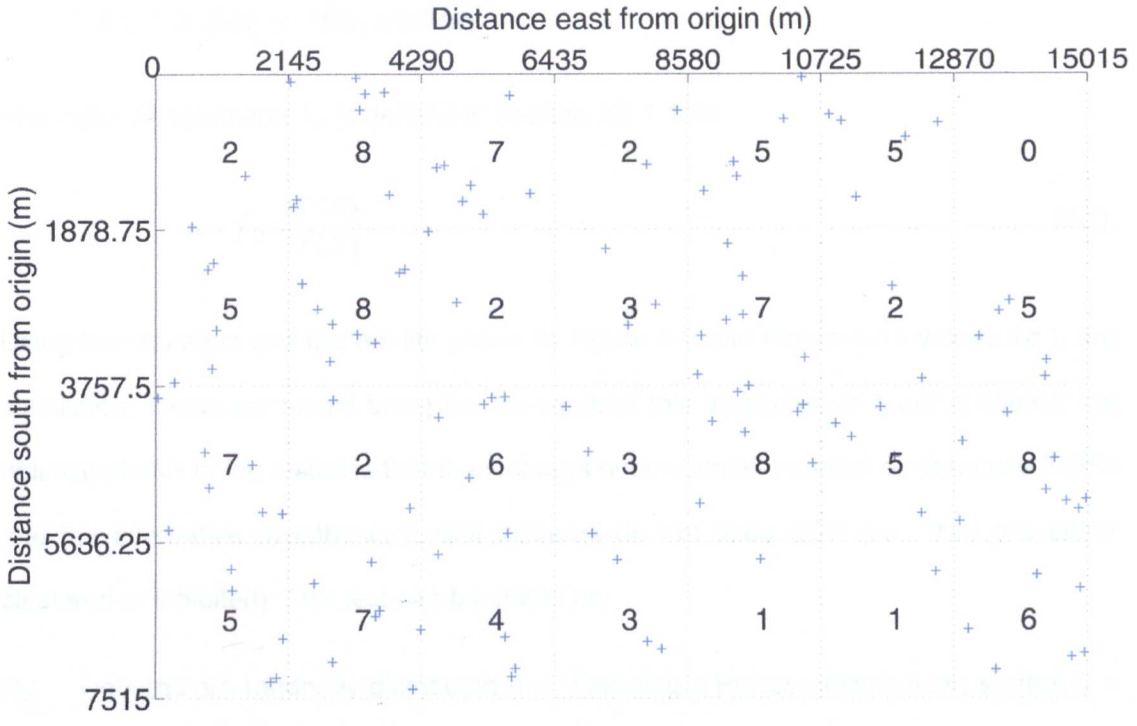

Figure 5-10 Quadrat counts and locations of icebergs for SI. Iceberg locations are marked by blue crosses (+). Quadrats are marked by dotted lines with the iceberg count for each quadrat stated in the middle of each quadrat. Distances are based on a pixel being 15m x 15m.

Table 5-3 demonstrates that the two study regions satisfy the assumptions from Lewis (1988) to allow the analysis of quadrat counts. Although the numbers of icebergs in the two study regions are different the values of the ratio N/k are similar given the choice of fewer quadrats for OW.

Table 5-3 Values for numbers of icebergs and quadrats to test the two assumptions in (Lewis, 1988).

Study Region	OW	SI
Number of icebergs, N	58	127
Assumption i) $N \geq 20$	Yes	Yes
Number of quadrats, k	12	28
N/k	4.8	4.5
Assumption ii) $N/k \geq 4$	Yes	Yes
Criteria i and ii satisfied?	Yes	Yes

5.4.2.1 Index of dispersion

The index of dispersion, I_d, is defined in Section 3.2.1.1 as

$$I_d = \frac{V(X)}{E(X)} \qquad (3.1).$$

Using this equation and the results shown in Figure 5-9 and Figure 5-10 values for I_d are calculated. These are tested using the chi-squared test as applied to quadrat counts: the null hypothesis being tested is that the icebergs obey complete spatial randomness (CSR) and the alternative hypothesis is that icebergs do not obey CSR (i.e., they are either clustered or inhibited). This test can be stated as:

H_0: icebergs are randomly distributed (i.e., following a Poisson distribution) so that I_d =

1. Test that $\Phi \sim \chi^2$ where $\Phi = (k-1)\hat{I}_d = \frac{k\sum_{i=1}^{k}(x_i - \bar{x})^2}{N}$ with k-1 degrees of freedom

and the alternative hypothesis is

H_1: icebergs are not randomly distributed

For the two grids shown in Figure 5-9 and Figure 5-10, the expected count for each cell is calculated as the number of icebergs divided by the number of quadrats used (i.e., the mean number of icebergs per quadrat).

Table 5-4 Critical values for calculating chi-squared for two study regions.

Study region	OW	SI
Number icebergs	58	127
Number quadrats	12	28
Estimate of expected cell count ($\bar{x} = \frac{N}{k}$)	4.83	4.54
Estimate of variance $\left(s^2 = \frac{\sum_{i=1}^{k} (x_i - \bar{x})^2}{k-1} \right)$	5.24	6.04
Estimate of I_d	1.08	1.33
$\Phi(=(k-1)\hat{I}_d)$	11.93	35.93
Degrees of freedom	11	27
p value	0.369	0.117

H_0 is rejected if Φ exceeds the critical value of a chi-squared distribution with k-1 degrees of freedom for a chosen significance level. Using a value of α=0.05, I conclude to accept the null hypothesis that the icebergs are completely spatially random in both study regions based on testing the index of dispersion.

5.4.3 G function

As discussed in Section 3.2.2 the G function is a measure of whether there is another iceberg within a given distance (r) of a selected iceberg, summed over all icebergs. Figure 5-11 and Figure 5-12 show the results of the analysis of the study regions using the G function. The x-axes are the theoretical values of G (labelled as G(r)) based on a Poisson random distribution (using Equation (3.7)). The y-axes show the estimated values of the G function for the same values of distance (r) labelled as $\hat{G}(r)$ for the data and for the simulations. Values for the data are plotted in black and the confidence intervals (α=0.05) are shown in red. The extreme values for each distance (i.e., value of r) from the

simulations are plotted in yellow. Under CSR the values of $\hat{G}(r)$ would be the same as the values of the theoretical values of G(r) and hence would produce a straight line. The simulations allow the deviation from this straight line to be assessed visually – if the line falls within the 90% confidence interval (red lines) then there is insufficient evidence to reject CSR.

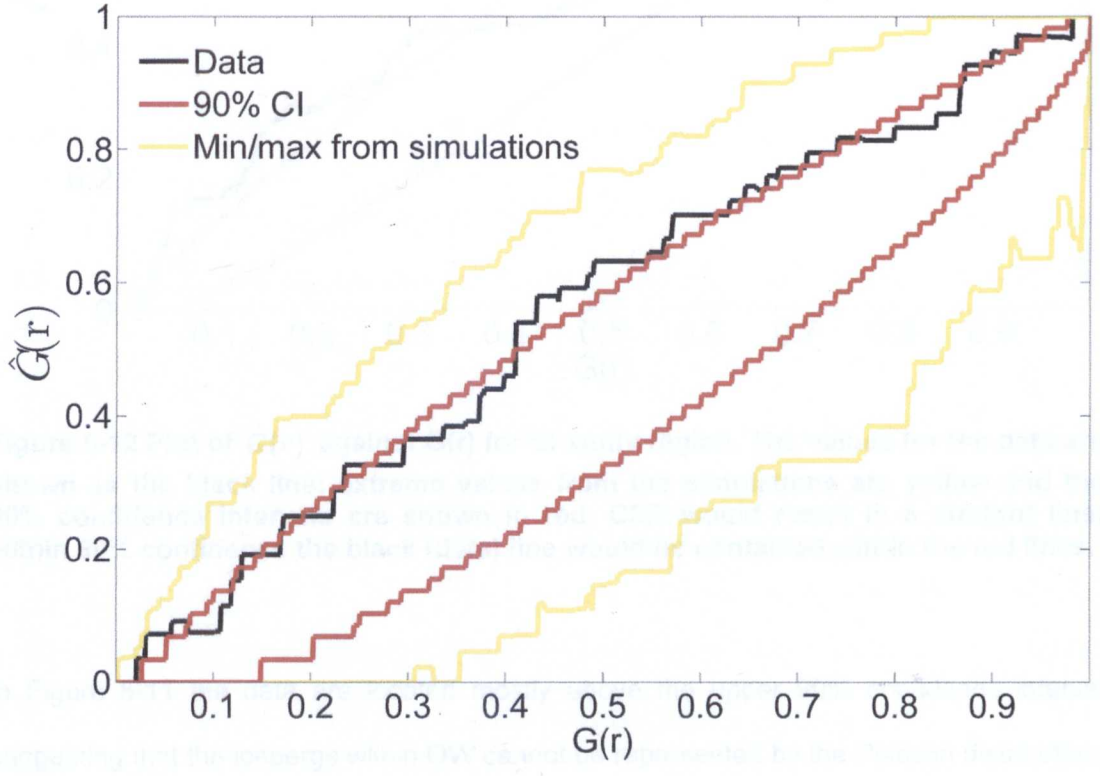

Figure 5-11 Plot of $\hat{G}(r)$ against G(r) for OW study region. The values for the data are shown as the black line; extreme values from the simulations are yellow and the 90% confidence intervals are shown in red. CSR would result in a straight line; within 90% confidence the black (data) line would be contained within the red lines.

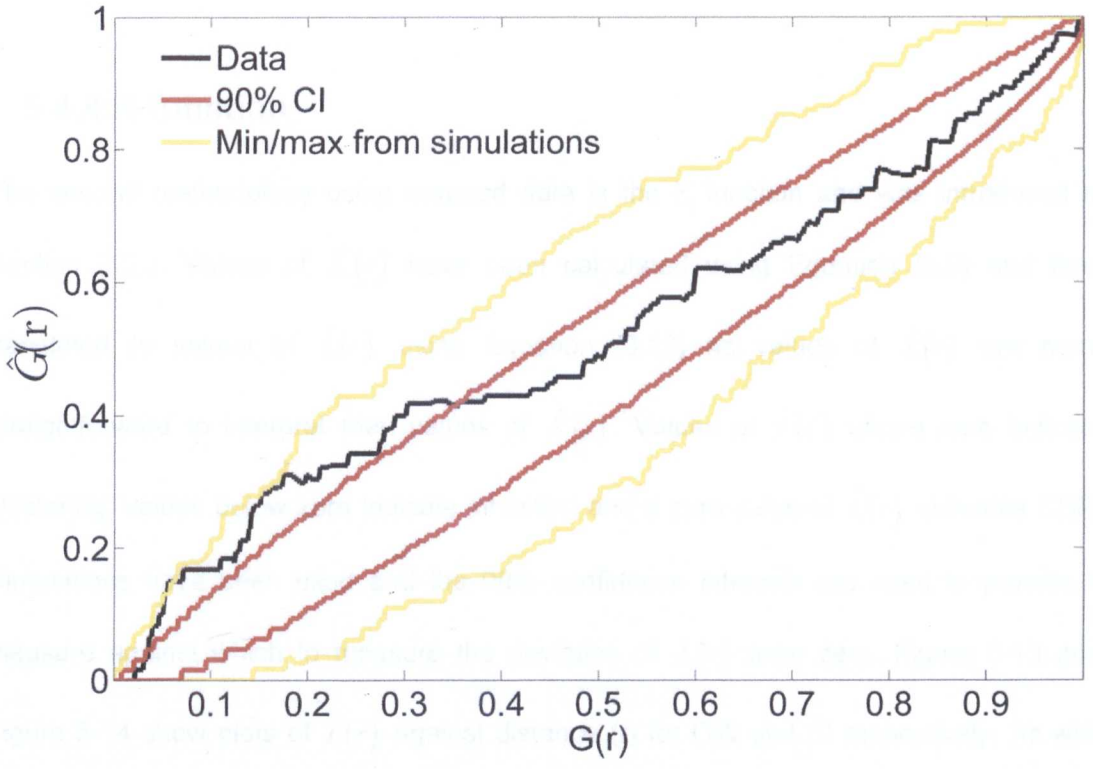

Figure 5-12 Plot of $\hat{G}(r)$ against G(r) for SI study region. The values for the data are shown as the black line; extreme values from the simulations are yellow and the 90% confidence intervals are shown in red. CSR would result in a straight line; within 90% confidence the black (data) line would be contained within the red lines.

In Figure 5-11 the data are located mostly above the upper 90% confidence interval suggesting that the icebergs within OW cannot be represented by the Poisson distribution, i.e., the icebergs within OW are clustered. Figure 5-12 shows a similar pattern for SI although at larger values the data are contained by the confidence interval. Data for both OW and SI lie within the maximum and minimum values from the simulations suggesting that a less strict confidence interval may produce a different conclusion. Overall I conclude, from the G function, that the icebergs within both study regions are not completely spatially random. However, it should be noted that the G function only relates to pairs of nearest neighbours to consider separations of all icebergs I use the K function.

5.4.4 K function

The second methodology using mapped data is the K function and was introduced in Section 3.2.3. Values of $\hat{K}(r)$ have been calculated using Equation (3.9) and then translated to values of $\hat{L}(r)$ using Equation (3.13) as values of $\hat{L}(r)$ are more straightforward to interpret then values of $\hat{K}(r)$. Values of $\hat{L}(r)$ above zero indicate clustering, values below zero indicate inhibition and a zero value of $\hat{L}(r)$ indicates CSR. Simulations have been used and the 90% confidence intervals are used to provide a measure against which to measure the deviation of $\hat{L}(r)$ from zero. Figure 5-13 and Figure 5-14 show plots of $\hat{L}(r)$ against distance (r) for OW and SI respectively. As with the plots for the G function in Section 5.4.3, the data are shown as black lines and from the simulations the extreme values are yellow and the 5th and 95th percentiles are plotted in red.

Different authors suggest different maximum values for distance; here I use the value of half minimum dimension of the study region as suggested in (Diggle, 2003) (i.e., ½ x 7.5km = 3.75km).

In both Figure 5-13 and Figure 5-14 the data lie above the zero line indicating a tendency to cluster although the confidence intervals need to be taken into account to consider the significance of this. The plot for OW shows that, apart from at larger distances (>~2.5 km) the data lies outside of the 90% confidence intervals. Figure 5-13 also shows how that at some points (~1.6 km) the data is outside of the limit established from the maximum value from the simulations. In contrast, the data in the plot for SI are mostly within the 90% confidence interval.

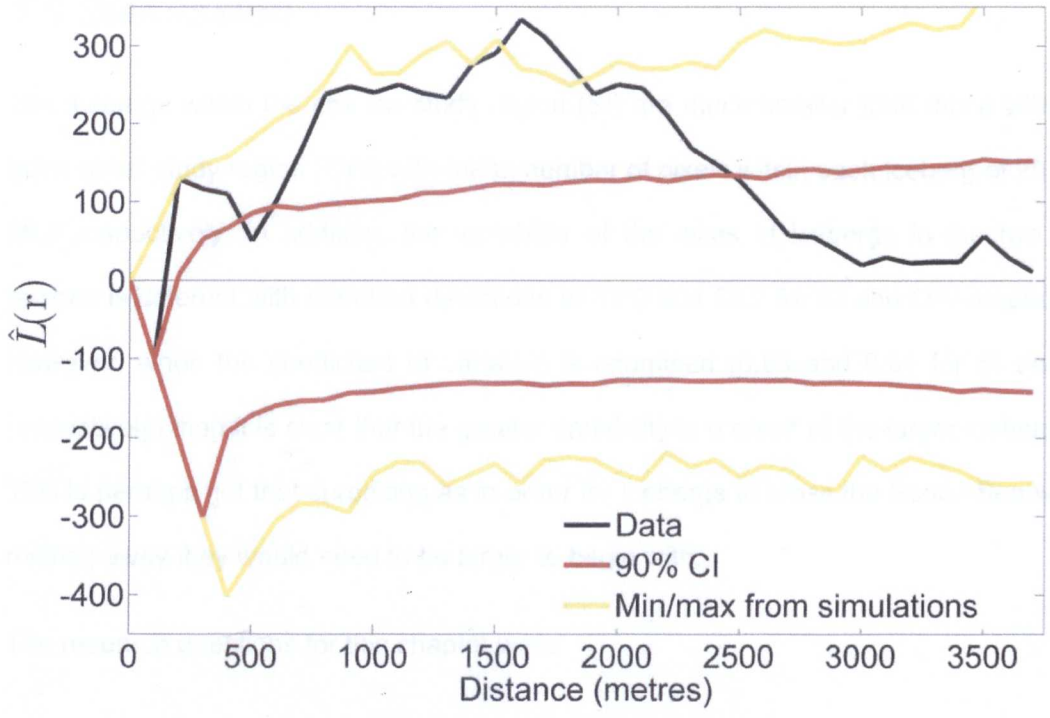

Figure 5-13 Plot of $\hat{L}(r)$ against r for OW study region. The values for the data are shown as the black line; extreme values from the simulations are yellow and the 90% confidence intervals are shown in red. CSR is a value of zero for $\hat{L}(r)$; within 90% confidence the black (data) line would be contained within the red lines.

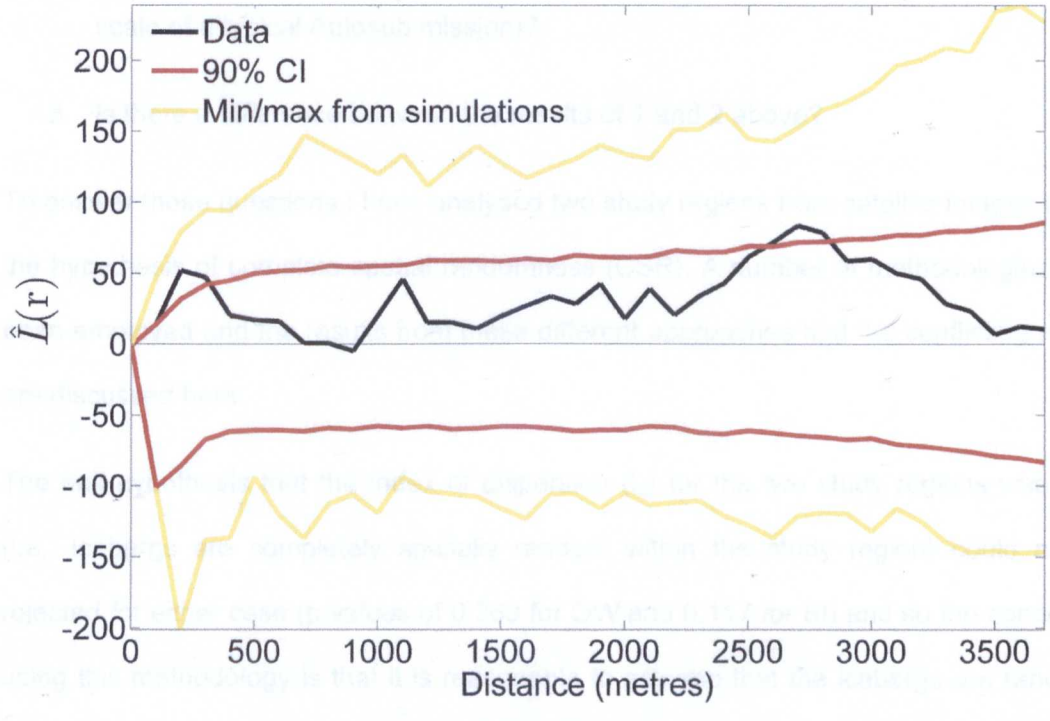

Figure 5-14 Plot of $\hat{L}(r)$ against r for SI study region. The values for the data are shown as the black line; extreme values from the simulations are yellow and the 90% confidence intervals are shown in red. CSR is a value of zero for $\hat{L}(r)$; within 90% confidence the black (data) line would be contained within the red lines.

5.5 Discussion

The icebergs within the sea ice study region (SI) are much smaller than those within the open water study region (OW) with mean number of pixels within each iceberg of 20.5 and 96.8 respectively. In addition, the variability of the sizes of icebergs in the two study regions is different with standard deviations of 17.0 and 59.2 for SI and OW respectively. However, when the coefficient of variation is examined (0.83 and 0.61 for SI and OW respectively) then it is clear that the greater variability is a result of the larger iceberg size. This is perhaps not that surprising as in order for icebergs to cross the Scotia Sea without melting away they would need to be larger to begin with.

The research questions for this chapter were:

1. Do icebergs cluster or are they inhibited in space within sea ice (on the scale of a typical Autosub mission)?
2. Do icebergs cluster or are they inhibited in space within the open ocean (on the scale of a typical Autosub mission)?
3. Is there a difference between the results of 1 and 2 above?

To answer these questions I have analysed two study regions from satellite images to test the hypothesis of complete spatial randomness (CSR). A number of methodologies have been employed and the results from these different approaches and the conflicting results are discussed here.

The null hypothesis that the index of dispersion (I_d) for the two study regions was unity (i.e., icebergs are completely spatially random within the study region) could not be rejected for either case (p values of 0.369 for OW and 0.117 for SI) and so the conclusion using this methodology is that it is reasonable to assume that the icebergs are randomly distributed within both study regions.

The next approach uses the G function nearest neighbour approach. Examining Figure 5-11 and Figure 5-12, which show the 90% confidence intervals, the values of G for the

data do not fall entirely within these confidence intervals. The values of the G function therefore suggest that the hypothesis of CSR should be rejected in both cases and that the icebergs cluster.

The third methodology used is the K function and the results of the modified K values (referred to as L) are shown in Figure 5-13 and Figure 5-14. Using this approach, there is a clear difference between the two study regions over the range of distances for which the values of L have been calculated. The plot for OW (Figure 5-13) indicates that at distances less than 2.5km the icebergs cluster, as the values of L are significantly greater than zero. Values of L for distances above 2.5km suggest complete spatial randomness. Overall the CSR hypothesis for OW is rejected using the K function approach. In contrast, using the K function for SI, the values of L (Figure 5-14) are contained within the confidence intervals apart from a few outlying values and so we cannot reject the CSR hypothesis for SI.

These different approaches result in different conclusions. The index of dispersion, I_d, utilises information on *all icebergs*. Ripley's K uses information on the separations of all possible iceberg pairs. The G function only considers pairs of icebergs (as discussed at the end of Section 5.1). For SI the hypothesis of CSR is rejected using the results of the G function whereas the other two methodologies (which use all icebergs) accept the hypothesis of CSR. More specifically, the values of L for SI indicate that icebergs are completely spatially random on scales up to 3.75km, this will be important in considering how to treat icebergs within Autosub missions.

The CSR hypothesis is rejected for OW using all but the I_d approach and overall I conclude that the hypothesis of CSR is rejected at all scales for this study region.

It is not clear from this study whether the differences in spatial randomness between sea ice and open water are a result of the sea state or other factors. Other relevant factors that could influence this result include:

1. **The difference in location of the two study regions.**

Ideally a region of sea ice contiguous to a region of open water with icebergs throughout should be used to test whether there is a difference between the two states (sea ice/open water). Hopefully this would also remove the concern about the different mean size of the icebergs discussed below.

2. **Size of icebergs and bathymetry**

The icebergs in OW are larger than those in SI and given the same water depth would, therefore, be more likely to be grounded. If icebergs grounded at a particular region of shallow water then it would not be hard to envisage a tendency for icebergs of similar draft to cluster. No investigations have been made to examine the bathymetry of the ocean in either region and so I cannot comment on the likely size of an iceberg that would be seen to be grounded at any point in either image.

3. **Study regions are not representative**

This is a small-scale study and as such has only included two study regions that were chosen from images that were readily available. To verify that the hypothesis of CSR is true for sea ice and can be rejected for open water more study sites are required from a variety of areas across the regions in which large numbers of icebergs are located.

5.6 Summary

The results of this chapter suggest that large icebergs (>~675m^2) cluster within open water and are completely spatially random within the sea ice zone on scales up to 3.75km. This would suggest that on similar scale lengths to these (i.e., Autosub missions) icebergs can be considered as spatially random within sea ice, i.e., no additional compensation is necessary to provide sea ice thickness PDF to account for iceberg clustering.

Chapter 6 Snow and sea ice thickness from direct measurement

6.1 Introduction

This chapter details work designed to provide ground truth data for the subsequent Autosub missions and also to investigate the spatial variability of the snow cover on sampled floes. As discussed in Chapter 2 drilling sea ice is frequently used as groundtruth data for remotely sensed data and it was for this reason that is was envisaged that drilling should be carried out on a number of floes prior to and during Autosub missions.

Section 2.4 described how an important element of the sea ice system is the overlying snow, not only because of the effects on energy exchange but also because the weight of the snow impacts on the draft. The weight of snow is highly correlated with the thickness of snow and therefore a knowledge of the snow thickness was required to be able to convert sea ice draft into thickness. Hence, on all the sampled floes systematic measurements were made of the snow depth and in turn these have been geostatistically analysed to provide the mean snow depth on each floe. The advantage of using a geostatistical approach is that values of snow depth can be interpolated across the whole floe, based on the sample points, and for each interpolated value there is a corresponding estimate of the error. Using the obtained mean snow depth values from each floe approximations of the floe thicknesses have been made.

6.2 Floe sites

Three ice floes were sampled over two days (8th and 9th March 2003 local time) for both the thickness of sea ice and the snow depth. Table 6-1 gives the location of the *RRS James Clark Ross*, which was moored alongside the floe of interest as can be seen, for example, in Figure 6-1. The choice of floes was primarily guided by safety policy and hence were not random. The sampled floes were large in area (~tens of metres squared)

and were required to be judged, when viewed from the ship, as able to support the weight of a small scientific party.

Table 6-1 Date and time of occupation of three studied floes and location of *RRS James Clark Ross*.

Floe Label	Start time/Date (GMT)	End time/Date (GMT)	Longitude	Latitude
FS1	00:00 9/3/03	00:50 9/3/03	101°09.76'	70°58.84'
FS2	17:30 9/3/03	18:40 9/3/03	102°00.0'	70°51.35'
FS3	20:15 9/3/03	21:18 9/3/03	102°21.4'	70°53.0'

An example of the floe type is given in the photograph in Figure 6-1, which shows members of the scientific party on FS3. No attempt was made to measure directly the thickness of thinner, more broken ice (as can be seen for example towards the bottom of Figure 6-1), estimates of this ice thickness and amounts were obtained using ship-based observations (see Section 7.2).

Figure 6-1 View from *RRS James Clark Ross* of members of the scientific party on floe station FS3 on 9th March 2003. Region A is discussed in Section 6.7. x and y show the approximate orientation of the grid used for snow depth measurements. (Photograph courtesy of Prof. David Vaughan).

The floe parties consisted of three teams, with one team concerned with snow, another with ice thickness and the third responsible for deploying a satellite buoy. An additional member, not involved in any of these activities, was charged with being responsible for the safety of the party and staying in contact with the ship via radio. For each floe, one team drilled holes in order to measure the thickness of the sea ice whilst another team collected data on the snow thickness across the floe.

The drill-sites on each floe were chosen to represent the thickness of level ice (as viewed from the surface) rather than either a systematic survey or to acquire maximum values by drilling through sails. Also, as will be seen in Section 7.3, due to technical problems with Autosub there were no under ice missions in the region until 22 March (~13 days later). As such, this chapter concentrates on the values of snow depth because of their importance

for calculating the values of sea ice thickness from studies of ice draft. I examine the distribution of snow depth from the three floes and also look at the impact of a geostatistical study on the results. No information was gathered on the texture, salinity or isotopic nature of the ice/snow layers within the floes.

6.3 Method

6.3.1 Sea ice drilling

All the holes drilled used the same methodology, starting with a pit being dug through the snow to allow the two person drilling team access to the ice. The depth of the snow at the locations of the drill holes was measured once the drilling was complete. A variety of drills and augers were used to drill through until seawater flooded the drill hole. A weighted cord was lowered into the hole (see Figure 6-2) with the trigger cord pulled taut until the weight reached below the expected bottom of the ice, when the trigger cord was relaxed and the bar fell into the horizontal position. The bar was then hooked onto the underside of the ice and the length of cord was measured and that value was taken as the thickness of the ice.

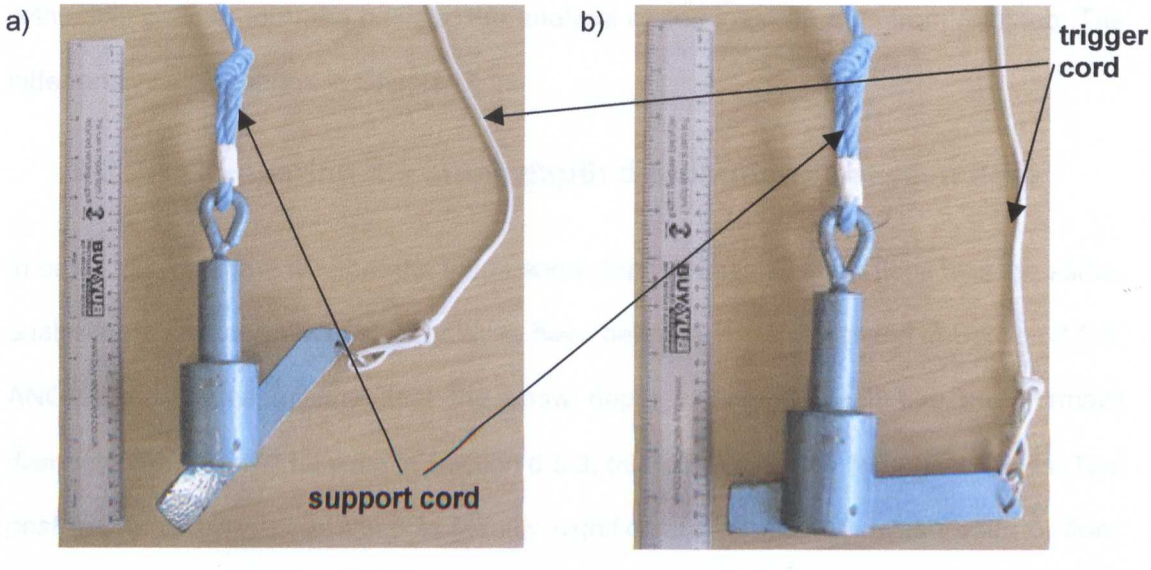

Figure 6-2 Device for locating bottom of ice floe shown with a) bar partially open and b) bar in fully opened position. The bar is kept from falling into the horizontal position by keeping the trigger cord taut, when the water surface is reached the trigger cord is released and the horizontal bar is hooked under the edge of the sea ice.

6.3.2 Snow depth measurements

As discussed in Section 2.4, snow on sea ice is a critical component in the thermal and total ice thickness properties of the sea ice system. This project used direct measurements to obtain data on the snow thickness distribution. Knowledge of the snow depth is required to convert values of sea ice draft into thickness (see Section 2.5). In addition, the mean thickness of snow on a floe can be used to approximate the total mean thickness using Equation (2.4).

A heavy metal bar was forcefully thrust into the snow surface and the depth that the bar penetrated was taken as the depth of snow (measured to the nearest cm). Readings were ideally made along transects at one metre intervals within the confines of the safe working limit of each floe and also within the time constraints allowed. No records were taken of floe orientation or of the orientation of the snow measurement grids. Values could be derived for orientation from digital photographs given the known position and orientation of the ship. However, this has not been done.

The statistical methodologies for dealing with the values of snow depth that are developed within this chapter form the basis of the analysis of sea ice draft data from Autosub. The latter analysis is reported in Chapter 7.

6.3.2.1 Comparing the snow depth distributions between floes

In order to investigate whether the mean snow depth across all three floes was the same, analysis of variance (ANOVA) techniques have been used, as discussed in Section 3.5.3. ANOVA techniques assume that the snow depth values for each floe are normally distributed and, as will be seen in Section 6.5.3, this is not the case for all three floes. Two *post hoc* tests have been used to identify significant differences between pairs of floes and are the least squared difference (LSD) and Scheffé tests as discussed in Section 3.5.3.1.

An alternative test for such a situation is the (non-parametric) Kruskal-Wallis (KW) test that tests whether the medians are the same. The values of the medians are ranked for each floe and then compared with rankings from another floe. A simple interpretation is that if the rankings are similar then the medians are the same. A more objective approach is to perform a chi-squared test and if the significance is less than a critical value (i.e., $\alpha = 0.05$) then the distributions are considered different. I have also used an independent samples *t* test between the two floes with normally distributed snow depth values to further validate the hypothesis that they have the same mean.

In order to test that the various combinations of pairs of floes had significantly different distributions (rather than just different average values), the Kolmogorov-Smirnov test has been used. For each floe the cumulative distribution function has been calculated and these have been used as the basis for the Matlab *kstest2* function (The Mathworks, 2004). This test indicates whether to reject the null hypothesis that the floes are from the same distribution or whether there is insufficient evidence to reject this hypothesis.

6.4 Kriging of snow depth measurements

As discussed in Section 3.3 spatial data are not independent measurements and therefore kriging techniques are used to provide estimates of the mean snow depths on a grid across the floes. The first stage in processing the data is to test whether the values are normally distributed (see Section 3.3.2) or whether they can be transformed to a normal distribution.

A Lilliefors test was used to test the snow depth values for normality with a significance level of 0.01. If the values of snow depth were found to be neither normal nor lognormal (with either 1- or 2-parameters) then the hyperbolic-sine transformation (Jones and McConway, In preparation) given in Equation (3.24) was used to transform the data. Data transformed using this function can readily be back-transformed to the original scale as shown in Equation (3.26).

6.5 Results

6.5.1 Ice drilling

The ice drilling program during JR84 was limited in terms of personnel and time so a limited numbers of holes were drilled on the three floes. On FS1 only one drill hole was started. This found that its ice thickness was greater than 1m but the drilling was not complete. The drilling program on FS2 was completed with one drill-site that gave a thickness of 1.91m but no details of the snow depth at that point were taken.

Two drill sites were completed on FS3 with depths of 2.43m and 2.66m and snow depths of 27cm and 34cm respectively, giving combined ice and snow thicknesses of 2.70m and 3.00m. A third drill-site on FS3 was found to have ice in excess of 2.7m but there was insufficient time to finish drilling at this sample point.

6.5.2 Snow depth measurements

6.5.2.1 Raw data

Figure 6-3 to Figure 6-5 show the locations of the sample points on floes FS1, FS2 and FS3. The colour of the marker in these plots indicates the depth measured. Hence, these figures show the spatial variability of snow over the three sampled floes. The x and y-axes were defined during the survey and do not represent alignment to the ship or the compass. Whilst most adjacent values of snow depth varied by only a few cm it was not unusual for changes of 50cm to occur over the 1m spacing. For an example of such a large change in snow depth see the points on FS2 in Figure 6-4 at (1,3) and (1,4). As an aid to interpretation, Figure 6-6 shows the interpolated values for snow depths on the three floes using the Matlab *contour* function (The Mathworks, 2004). Areas of thicker snow are clearly visible in all three floes – in the top left hand corner of FS1, the bottom right hand corner of FS2 and away from the top left corner of FS3.

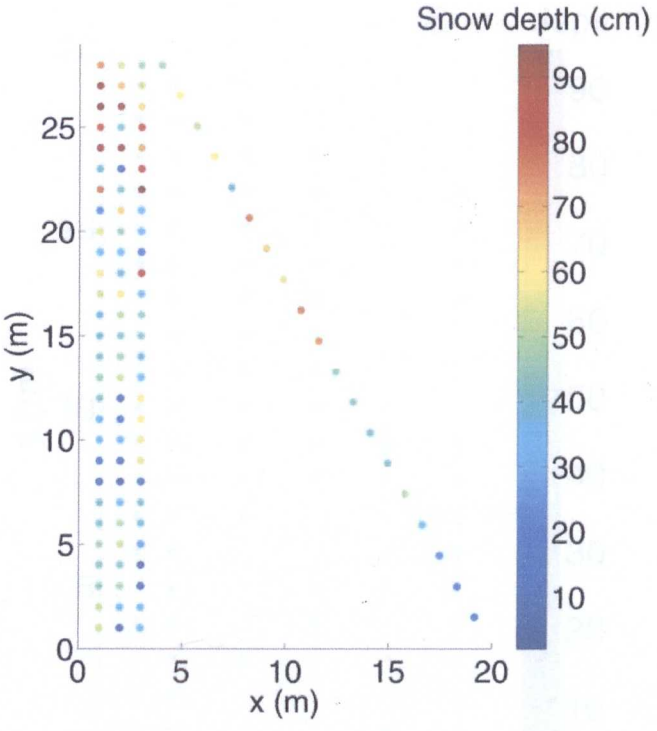

Figure 6-3 Scatter plot of snow depth measurements (in cm) across FS1.

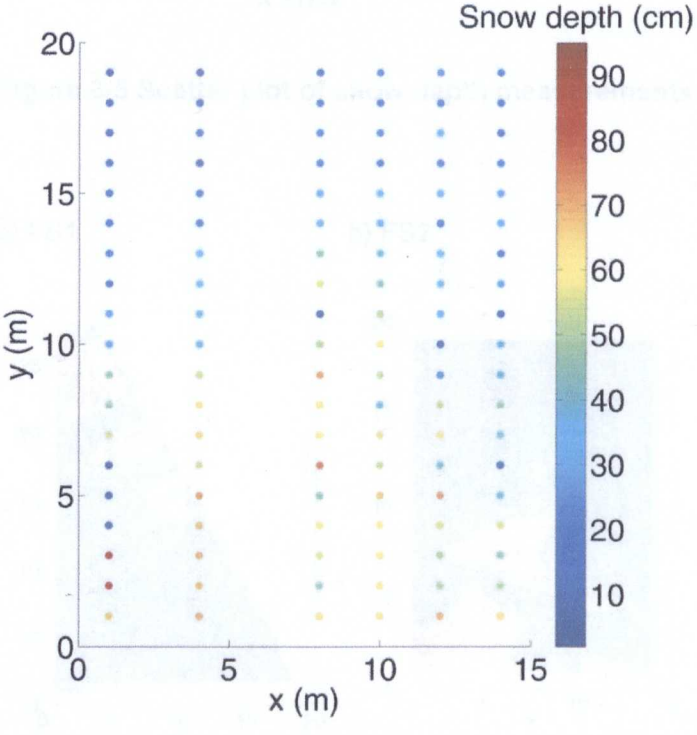

Figure 6-4 Scatter plot of snow depth measurements (in cm) across FS2.

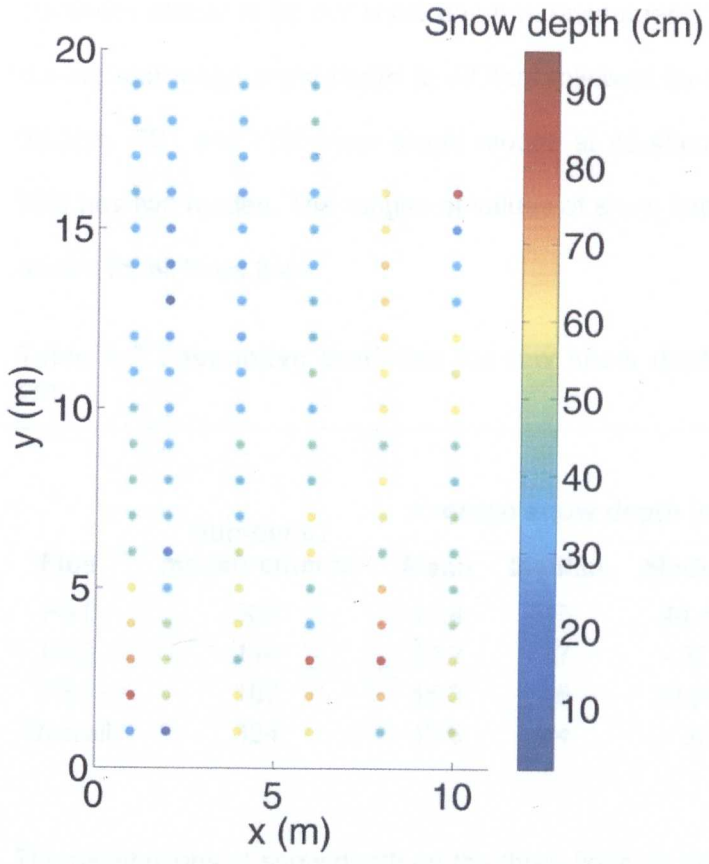

Figure 6-5 Scatter plot of snow depth measurements (in cm) across FS3.

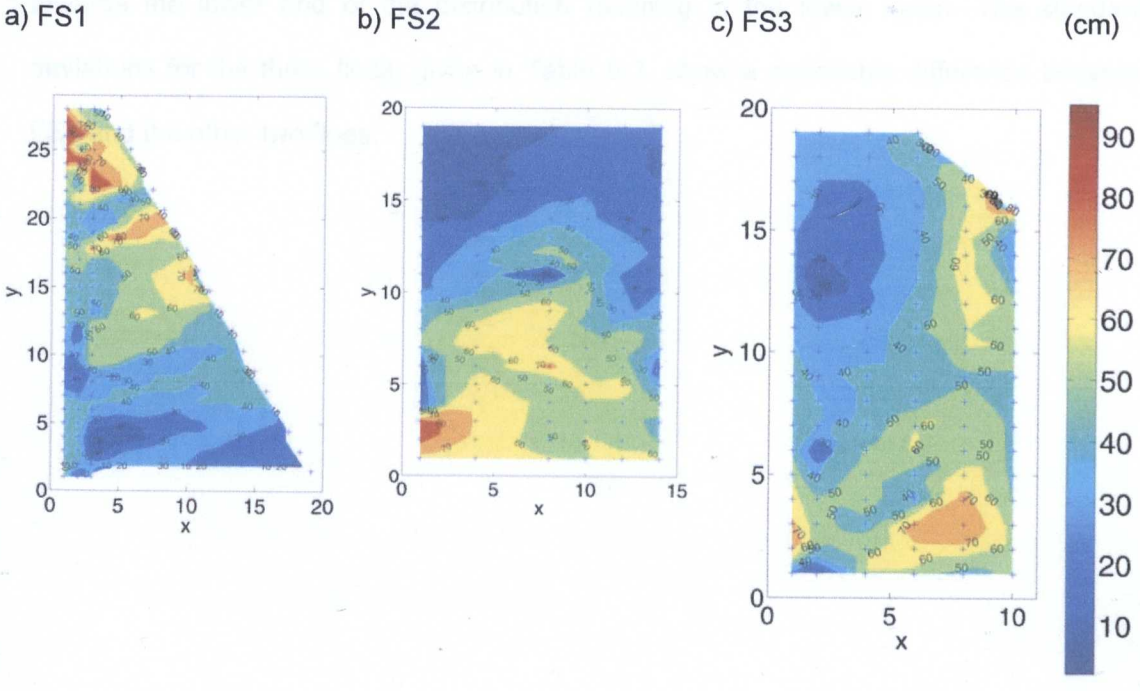

Figure 6-6 Interpolated snow depth values (in cm) across a) FS1 b) FS2 and c) FS3.

Summary statistics for the snow depth measurements are shown in Table 6-2. FS1 has the highest mean snow depth at 47.4cm followed by FS3 at 45.3cm and finally FS2 at 39.2cm. FS1 and FS2 have single modes at 44-45cm and 37cm respectively whereas FS3 has two modes. The ranges of values of snow depth (overall from 2cm to 95cm) are similar for all three floes.

Table 6-2 Descriptive Statistics for raw snow depth measurements all values are cm.

Floe	Number of measurements	Average snow depth (cm)			SD (cm)	Min. snow depth (cm)	Max. snow depth (cm)
		Mean	Median	Mode(s)			
FS1	103	47.4	45	44-45	21.1	6	95
FS2	114	39.2	37	37	20.3	5	88
FS3	107	45.3	45	30 (46)	15.6	2	86
Overall	324	43.8	44	37	19.4	2	95

The distributions of snow depth on the three floes do not have the same shape as can be seen in the PDFs in Figure 6-7 For this figure a 10cm bin width was used otherwise the results are too noisy. FS2 is distinct from the other two floes in that it has more data towards the lower end of the distribution resulting in the lower mean. The standard deviations for the three floes, given in Table 6-2, show a noticeable difference between FS3 and the other two floes.

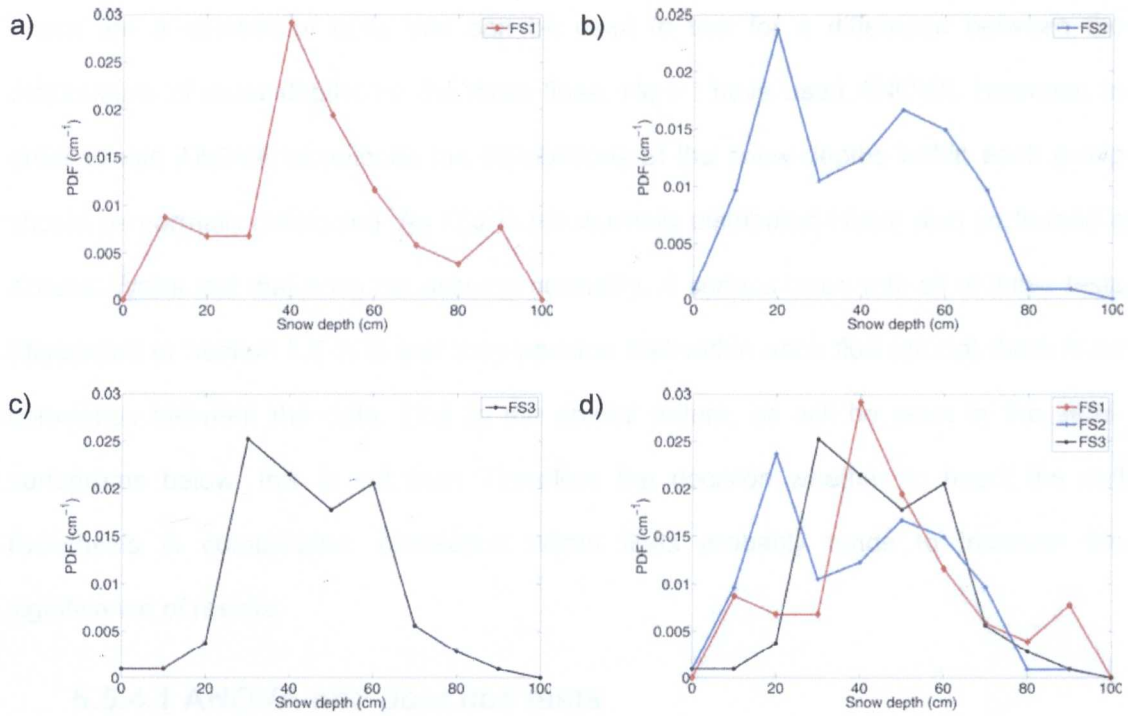

Figure 6-7 PDFs for snow depth thickness on a) FS1, b) FS2, c) FS3 and d) floes FS1, FS2 and FS3 (using 10cm bin widths).

6.5.3 Results of testing for normality

As discussed before, an assumption required for ANOVA is that data are normally distributed; this is also preferable for kriging. Using the Lilliefors test, FS1 and FS3 were accepted as normally distributed, as the level of significance of the hypothesis that they were not normally distributed was less than 0.01. FS2 was neither normal nor lognormal (with either 1 or 2 parameters) and so the hyperbolic-sine based transformation given in Section 3.5.2 was used to transform the data in floe 2. The value of δ in Equation (3.24) for FS2 was established by experimentation and was estimated as 1.9. The results of this testing are borne in mind during the following analyses and the transformed values for FS2 are used in the geostatistical analyses.

6.5.4 Comparison of snow depth values between the three floes

There are a number of tests that can be used to test for a difference between the distributions of snow depths on the three floes. Here I have used ANOVA. However, in order to use ANOVA techniques the distributions of the snow depths within each group should be normally distributed. As FS2 is not normally distributed I have also performed a Kruskal-Wallis test that does not assume normality. A serious issue with all of these tests (discussed in Section 3.5.5) is that they assume that within each floe (group) there is no correlation between the data. Due to the spatial nature, as will be seen in the semi-variograms below, this is not true. Therefore the decision whether to reject the null hypothesis is complicated: correlation within floes probably tends to increase the significance of results.

6.5.4.1 ANOVA and *post hoc* tests

The results of the ANOVA test on the snow depth values between the three floes are given in Table 6-3. The value of significance of 0.005 is well below the 0.05 critical value, indicating that there is evidence of a difference between the snow depth distributions in at least one pair of floes.

Table 6-3 ANOVA on snow depth measurements with floe station as the factor.

	Sum of Squares	df	Mean Square	F	Sig.
Between Groups	3964.5	2	1982.2	5.4	.005
Within Groups	118014.5	321	367.6		
Total	121979.0	323			

In order to establish which pair(s) of floes differ I used the LSD and Scheffé tests as discussed in Section 3.5.3.1. The LSD test is a liberal test and is most appropriate for testing that there is no difference within pairs (i.e., between FS1 and FS3). Conversely, the Scheffé test is conservative and is appropriate for showing that there is a significant difference within a pair (i.e., FS2 and the other two floes). The results of these *post hoc*

tests on the snow depth distributions from the three floes are shown in Table 6-4. The *post hoc* tests are testing the null hypothesis (H_0) that there is no difference between the mean snow depths from the two floes, i.e.,

H_o: No difference in the mean snow depths on Floe M and Floe N

H_1: Mean snow depths on Floe M and Floe N are not the same.

If the significance level of the test (labeled as *Sig.* in Table 6-4) is less than 0.05 then there is evidence that the two floes do not have the same mean snow depth. Conversely, if *Sig.*>0.05 then there is insufficient evidence to conclude that the two means are different. The *95% confidence interval* in Table 6-4 is the confidence interval of the differences in means between snow depth on Floe M and Floe N. To assist with the interpretation of Table 6-4 shading has been used to show for which pairings each test should be used.

Table 6-4 Results of *post hoc* tests on snow depth (in cm) from pairings of FS1, FS2 and FS3. Mean Difference is the difference in mean snow depth between the measurements from Floe M and Floe N, * next to the Mean Difference indicates a significance level less than 0.05. Shaded boxes for the Scheffé test indicate that a difference between groups is being tested whereas shaded boxes for the LSD test indicate testing for no difference.

						95% confidence interval	
	Floe M	Floe N	Mean Difference (N-M)	Std. Error	Sig.	Lower	Upper
Scheffé (Difference between distributions)	FS1	FS2	-8.18 *	2.61	0.008	-14.59	-1.77
	FS1	FS3	-2.11	2.65	0.728	-8.62	4.40
	FS2	FS3	6.07	2.58	0.064	-0.28	12.42
LSD (No difference between distributions)	FS1	FS2	-8.18 *	2.61	0.002	-13.31	-3.05
	FS1	FS3	-2.11	2.65	0.426	-7.32	3.10
	FS2	FS3	6.07 *	2.58	0.019	0.99	11.15

6.5.4.2 Kruskal-Wallis test

The Kruskal-Wallis test was used to test whether the distributions of snow depth on the three floes differ: the results are shown below in Table 6-5. The resulting chi-squared test has a value of 8.31 and this has a significance of 0.016 with 2 degrees of freedom (number of floes minus one), suggesting that the three floes do not have the same average snow depth.

Table 6-5 Kruskal-Wallis test on snow depth values between FS1, FS2 and FS3.

Floe	N	Mean Rank
FS1	103	177.08
FS2	114	142.55
FS3	107	169.72
Total	324	

6.5.4.3 Independent samples *t* test

To further test whether the means of the snow depth values from FS1 and FS3 differ, I have used an independent samples *t* test. The results are given in Table 6-6. In order to establish whether to use the "Equal variances assumed" or "Equal variances not assumed" category, Levene's test for equality of variances is used. If the significance of the Levene test is greater than 0.05 then one can assume equal variances for both groups. Here the F value of 4.4 with a significance of 0.037 suggests that the "Equal variances not assumed" option should be used. However, as can be seen from the values in Table 6-6 whether or not equal variances are assumed makes little difference to the results.

Table 6-6 Independent t test for equality of means between snow depths on FS1 and FS3, significance is 2 tailed, DF is degrees of freedom and a value of Sig. less than 0.05 indicates a significant difference between the snow depths on the two floes.

	t	DF	Sig.	Mean Difference	Std. Error Difference	95% Confidence Interval of the Difference	
						Lower	Upper
Equal variances assumed	0.82	208	0.41	2.11	2.56	-2.94	7.15
Equal variances not assumed	0.82	187.7	0.41	2.11	2.57	-2.97	7.19

The results in Table 6-6 suggest no difference between the snow depth measurements on FS1 and FS3.

6.5.4.4 Kolmogorov-Smirnov test

In order to test whether the distributions (rather than just the means or the variances) are the same the Kolmogorov-Smirnov test has been used to compare the three possible pairings of the three floes. The results are given below in Figure 6-8 to Figure 6-10. Each plot concerns a single pair of floes and shows the two empirical cumulative distribution functions (CDFs), results from using the *kstest2* function in Matlab (The Mathworks, 2004) and the *p* value indicates the significance of the Kolmogorov distance (the maximum difference in the two CDFs, see Section 3.5.4).

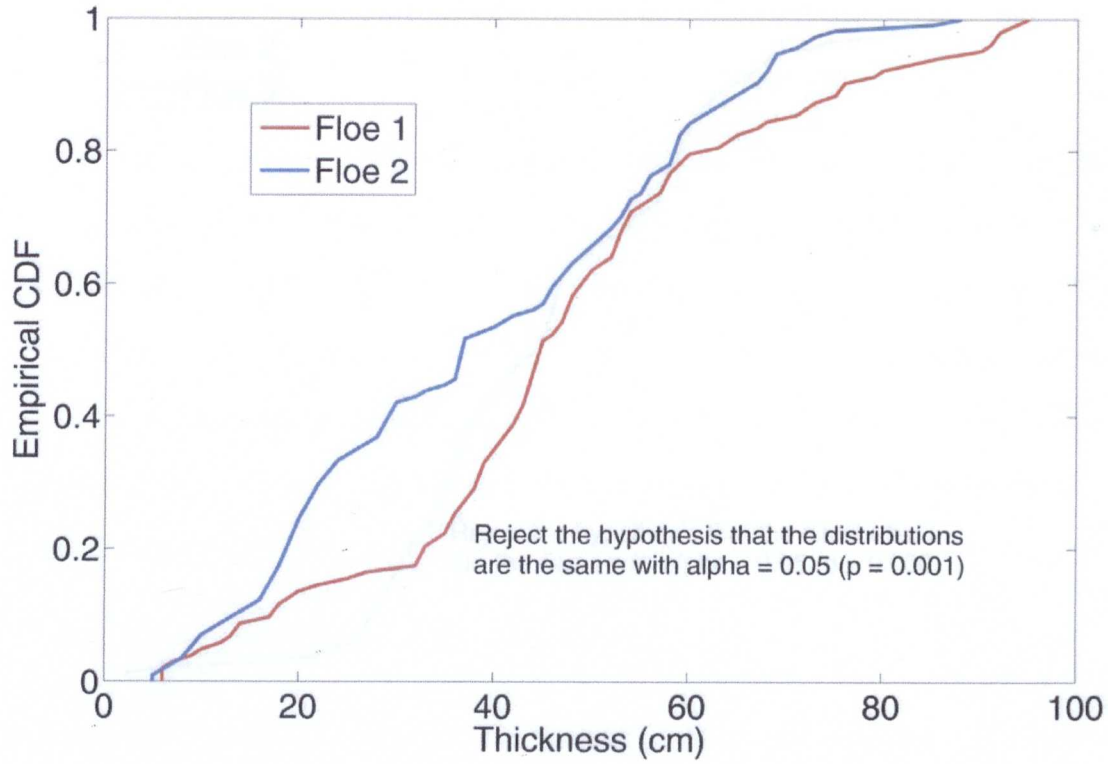

Figure 6-8 Two-Sample Kolmogorov-Smirnov Test FS1 and FS2.

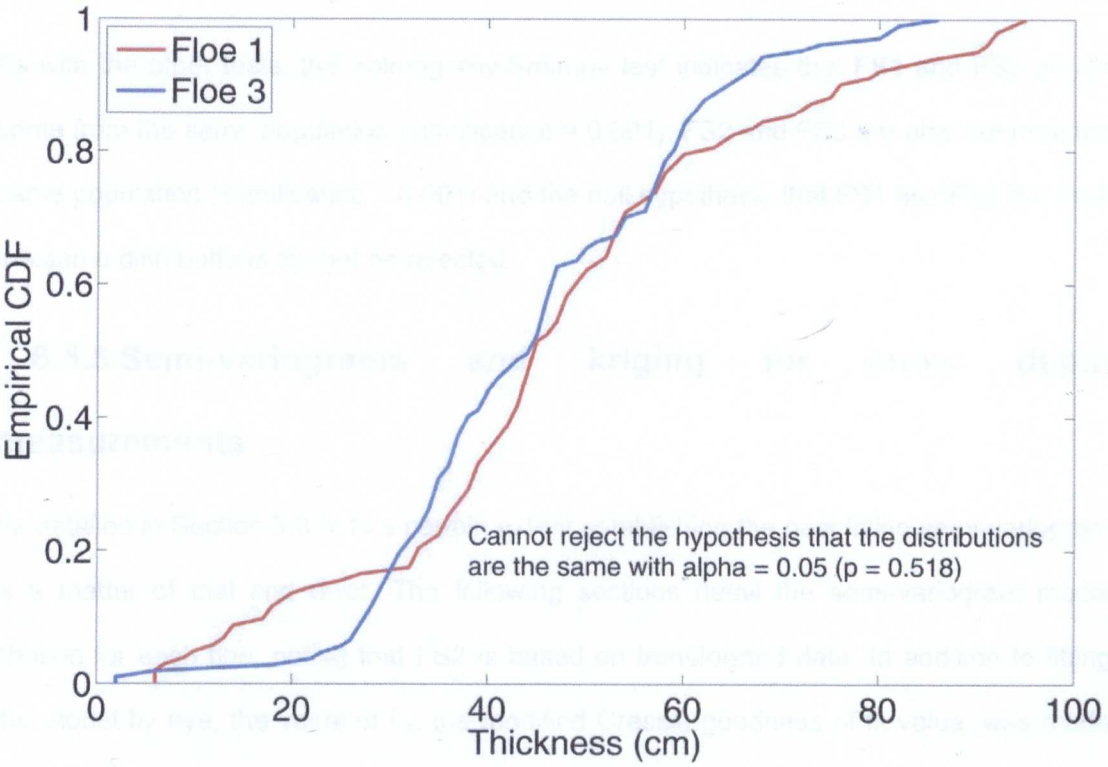

Figure 6-9 Two-Sample Kolmogorov-Smirnov Test FS1 and FS3.

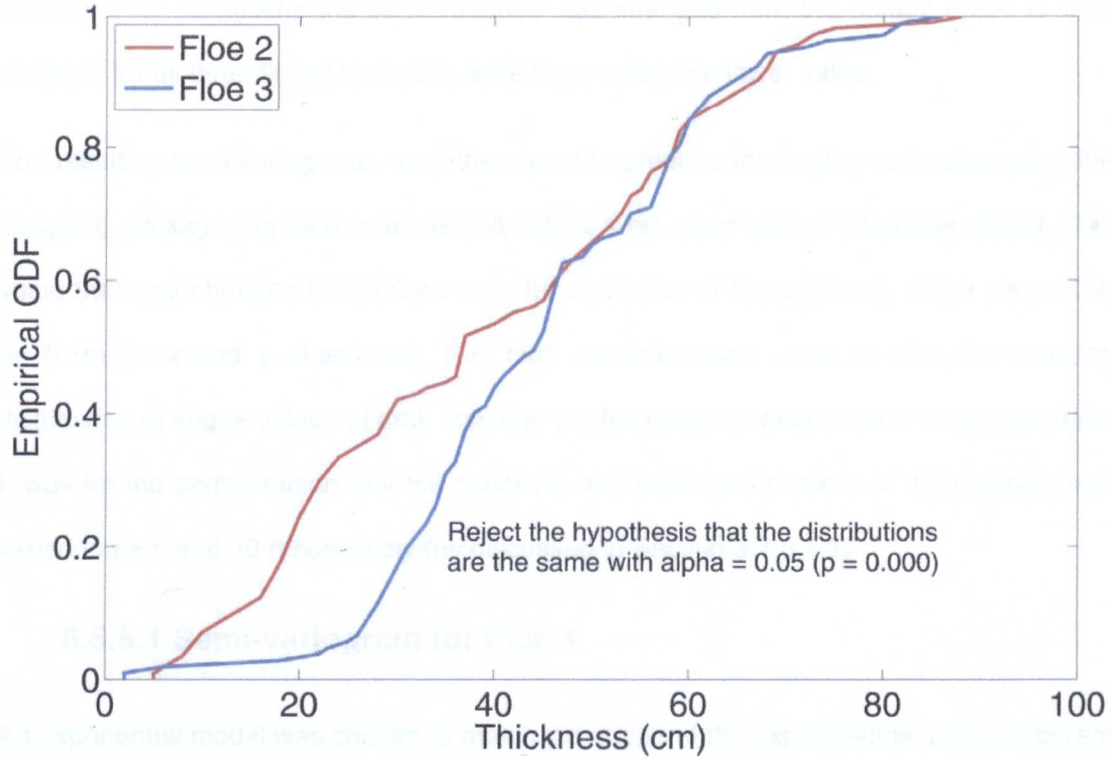

Figure 6-10 Two-Sample Kolmogorov-Smirnov Test FS2 and FS3.

As with the other tests, the Kolmogorov-Smirnov test indicates that FS1 and FS2 do not come from the same population (significance = 0.001). FS2 and FS3 are also not from the same population (significance < 0.001) and the null hypothesis that FS1 and FS3 are from the same distributions cannot be rejected.

6.5.5 Semi-variograms and kriging for snow depth measurements

As detailed in Section 3.3.3, to a certain extent establishing the best fitting semi-variogram is a matter of trial and error. The following sections detail the semi-variogram model chosen for each floe, noting that FS2 is based on transformed data. In addition to fitting the model by eye, the value of F_c, the modified Cressie goodness of fit value, was made as small as possible. Unless otherwise stated the default values for EasyKrig were kept, if default values were changed then the reason is explained in the subsequent text. The

resolution for calculating the semi-variance was changed from the default 0.025 to 0.05 because for all three floes the results were noisy using the lower value.

The resulting semi-variograms were then used to produce the kriging estimates using the EasyKrig package. As before, all default values were used unless otherwise stated. One value that was changed for all floes was the resolution of the grid size, which was set to be 0.1m (in x and y directions). This high resolution was used so that the resulting distribution of kriged values of draft included the full range of values found in the raw data. It was for the same reason that the minimum and maximum number of data points were varied to be 5 and 20 respectively (as discussed in Section 3.3.5.1.1) .

6.5.5.1 Semi-variogram for Floe 1

An exponential model was chosen to match the shape of the experimental semi-variogram and the parameters that specify this model are shown in Table 6-7. The semi-variogram for the data from FS1 is shown in Figure 6-11 and has a F_c value of 0.002.

Table 6-7 Parameter values for exponential model of semi-variogram for FS1, values are proportional to the total length scale (metres in parenthesis).

Parameter	Value
Sill	0.82
Length	0.04
Effective range	0.54 (=17.6m)
Nugget (semi-variance)	0
F_c	0.002
Resolution	0.05

The full range of values for the lag has not been used for the semi-variogram modelling. Higher values of semi-variance relating to lag above about 17m have been ignored. This is not an unusual case in modelling semi-variograms and represents a trend in the values of snow depth across the floe as can be seen in Figure 6-6a where the snow is deeper in the top left hand corner. Provided that the resulting semi-variogram is restricted to within the critical 17m then this is acceptable and the resultant parabolic nature of the semi-

variogram can be considered to be acceptable (see Example 9.3.1 in Clark and Harper (2000)). The effective range of the semi-variogram used for kriging FS1 was set at 17.6m.

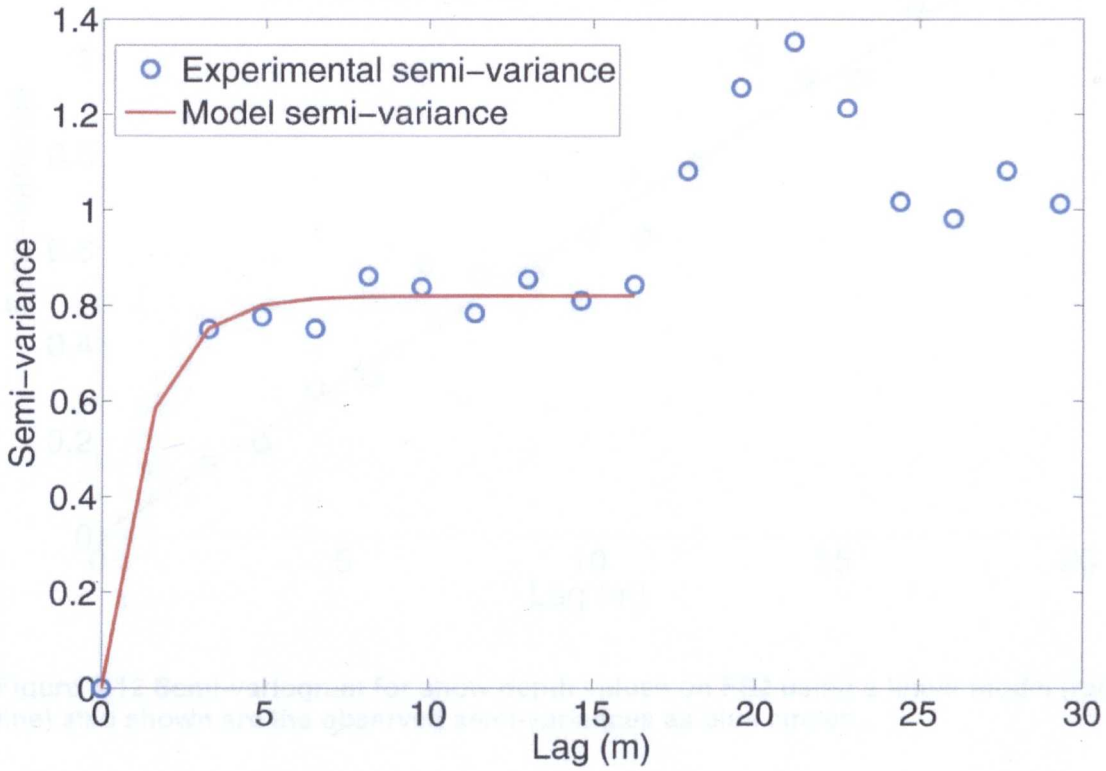

Figure 6-11 Semi-variogram of snow depth values from FS1, data are shown as blue circles and the (exponential) model semi-variogram is the red line.

6.5.5.2 Semi-variogram for Floe 2

As noted above, regarding the normality of the data in the three floes, FS2 is different from the other two floes. Semi-variogram modelling and kriging were carried out using transformed data (using the hyperbolic-sine transformation in Equation (3.24)), these data being transformed back once the kriging process was complete. A linear model was chosen to represent the semi-variance as shown in Figure 6-12.

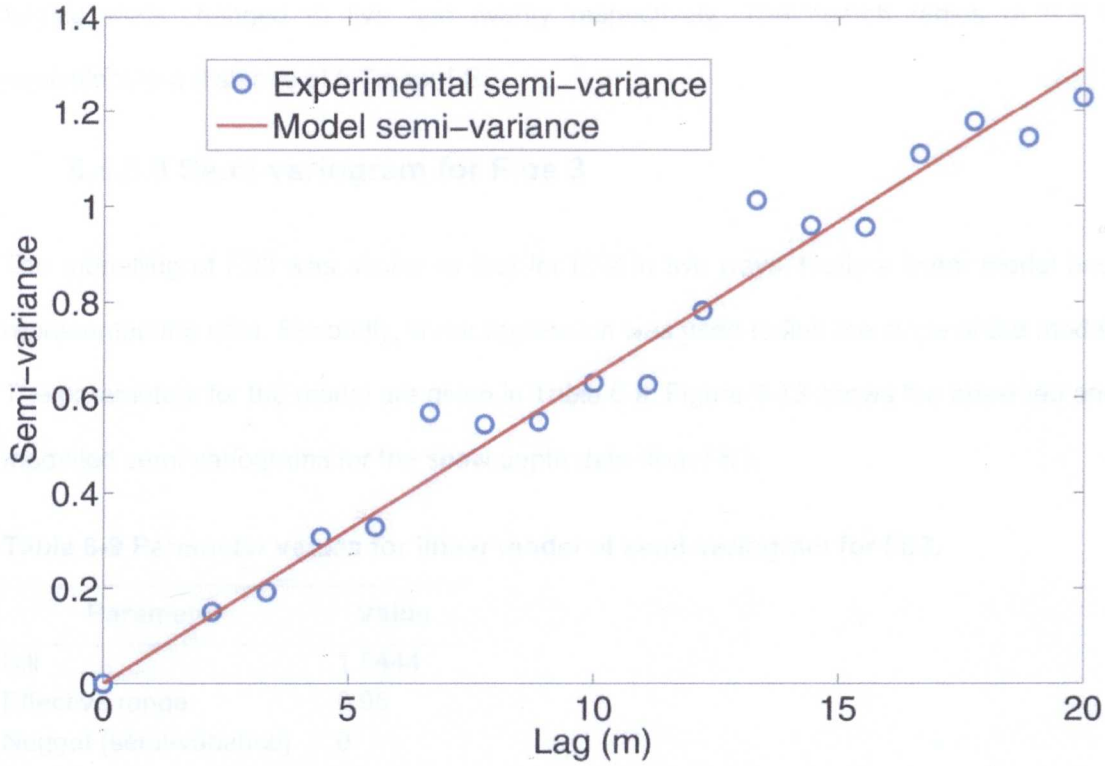

Figure 6-12 Semi-variogram for snow depth values on FS2 using a linear model (red line) also shown are the observed semi-variances as blue circles.

Linear regression was used to obtain the value of the slope of the relationship shown in Figure 6-12 with the intercept on the semi-variance axis set to be at zero (i.e., the nugget is zero). The resulting parameters that specify the model for the semi-variogram are listed in Table 6-8.

Table 6-8 Parameter values for linear model of semi-variogram for FS2.

Parameter	Value
Sill	1.432
Effective range	0.95
Nugget (semi-variance)	0
F_c	0.011
Resolution	0.05

As with FS1, the defaults for the kriging were changed in order that the kriging reflected the range of values in the raw data: the minimum and maximum number of points for

kriging were changed to five and twenty respectively. The search radius of 0.3 is equivalent to a distance of 6.7m for FS2.

6.5.5.3 Semi-variogram for Floe 3

The modelling of FS3 was similar to that for FS2 in two ways, firstly a linear model best represented the data. Secondly, linear regression was used to find the slope of the model. The parameters for the model are given in Table 6-9. Figure 6-13 shows the observed and modelled semi-variograms for the snow depth data from FS3.

Table 6-9 Parameter values for linear model of semi-variogram for FS3.

Parameter	Value
Sill	1.5444
Effective range	0.95
Nugget (semi-variance)	0
F_c	0.074
Resolution	0.05

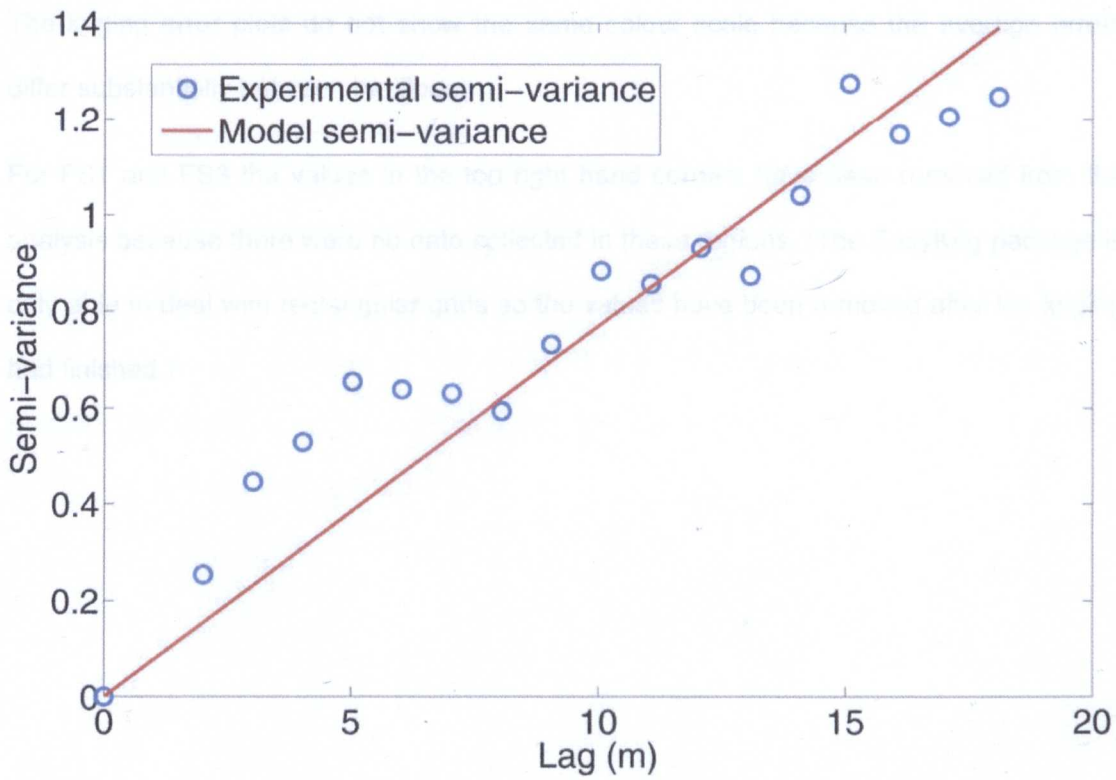

Figure 6-13 Semi-variogram for snow depth values on floe 3 showing observed semi-variance as blue circles and modelled linear semi-variogram as red line.

The semi-variogram shown in Figure 6-13 was used in the subsequent kriging to produce a 0.1m resolution grid of snow depth values. The search radius of 0.3 for FS3 equates to a distance of 6.0m.

6.5.6 Results of kriging for snow depth measurements

The semi-variograms produced above were used to krige the data, still using the EasyKrig package. For FS2, once the data were processed the values were back-transformed to account for the earlier process (using Equation (3.26)). The kriged values of snow draft for FS1, FS2 and FS3 are shown in Figure 6-14 to Figure 6-16.

The figures also show the interpolated 90% kriging standard error surface of the snow depth values. This error is calculated using Equation (3.22) and is the error associated with the kriging process at each of the nodes and does not reflect the experimental uncertainties in measurement.

For snow depth values the colour scale is the same for all three floes to allow comparison. The kriging error plots do not show the same colour scale because the average errors differ substantially between the floes.

For FS1 and FS3 the values in the top right hand corners have been removed from the analysis because there were no data collected in these regions. (The EasyKrig package is only able to deal with rectangular grids so the values have been removed after the kriging had finished.)

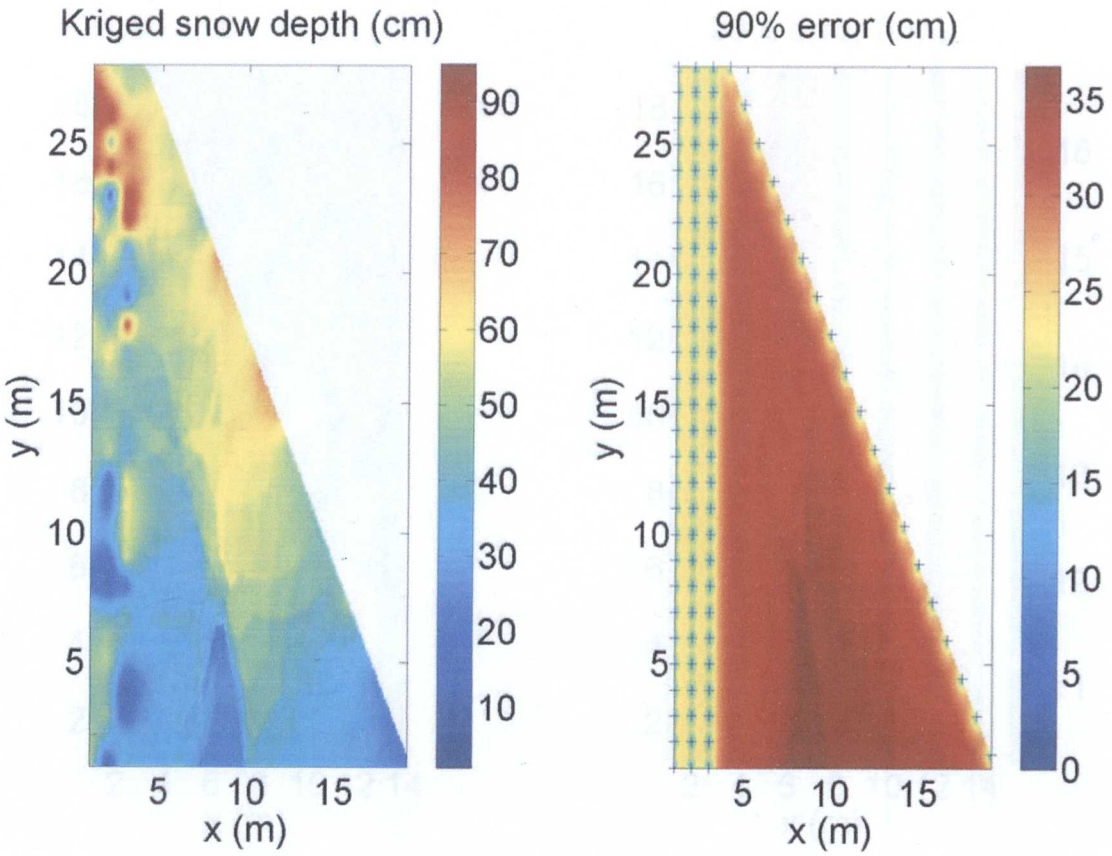

Figure 6-14 Contour plots (in cm) of kriged snow draft for FS1 and the associated estimation error showing the sample points as +.

Figure 6-14 shows the trend in deeper snow (red) towards the top of FS1 compared with the shallower (blue) snow depth at the bottom of the plot. This trend is most likely the cause of the parabolic nature of the associated semi-variogram (Section 6.5.5.1). The kriging error plot shows the relationship between the increasing kriging error and the greater spatial distance from sample data. The lower the kriging error the greater the confidence in the associated snow depth.

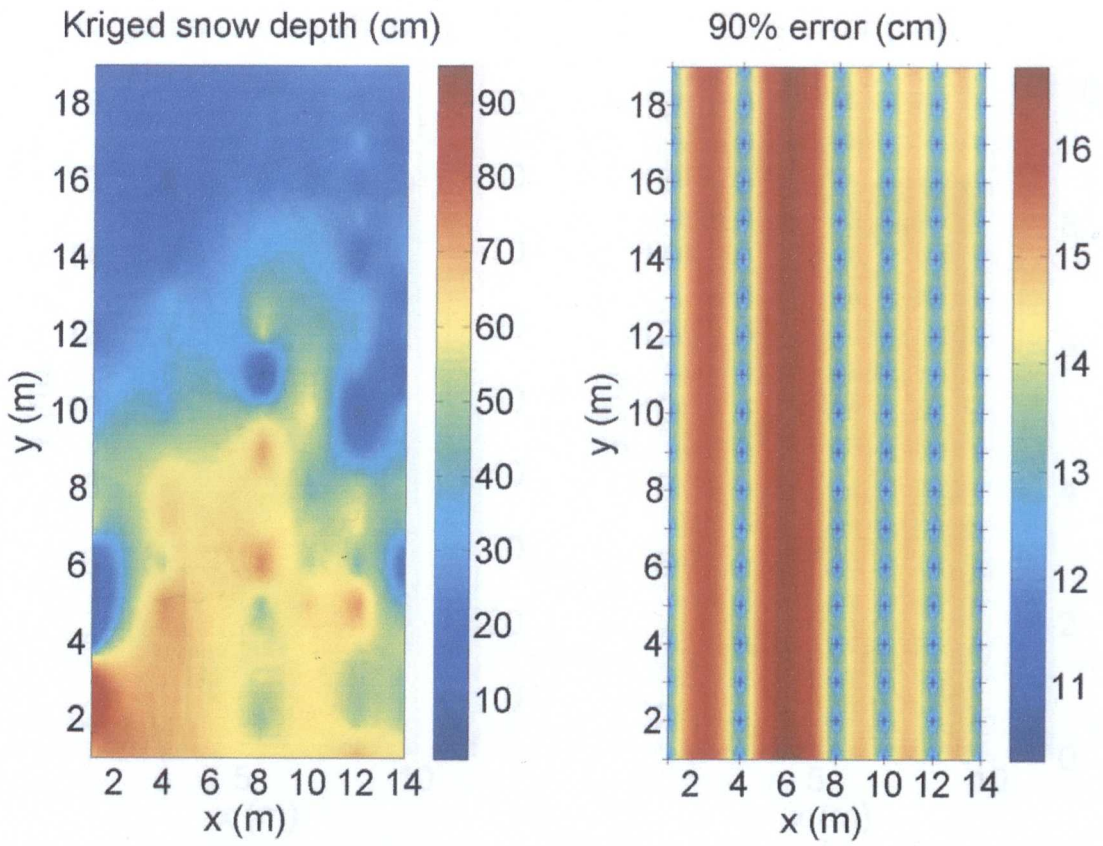

Figure 6-15 Contour plots (in cm) of kriged snow draft for FS2 and the associated estimation error showing the sample points as +.

The kriged values of snow depth for FS2 are shown along with the associated kriging errors in Figure 6-15. Notice how the larger separations of sample points result in higher kriging error values, in this case giving a striped pattern. The top of the floe has a thinner snow cover compared with the bottom end, in particular the thick snow (~80 cm) in the bottom left-hand corner.

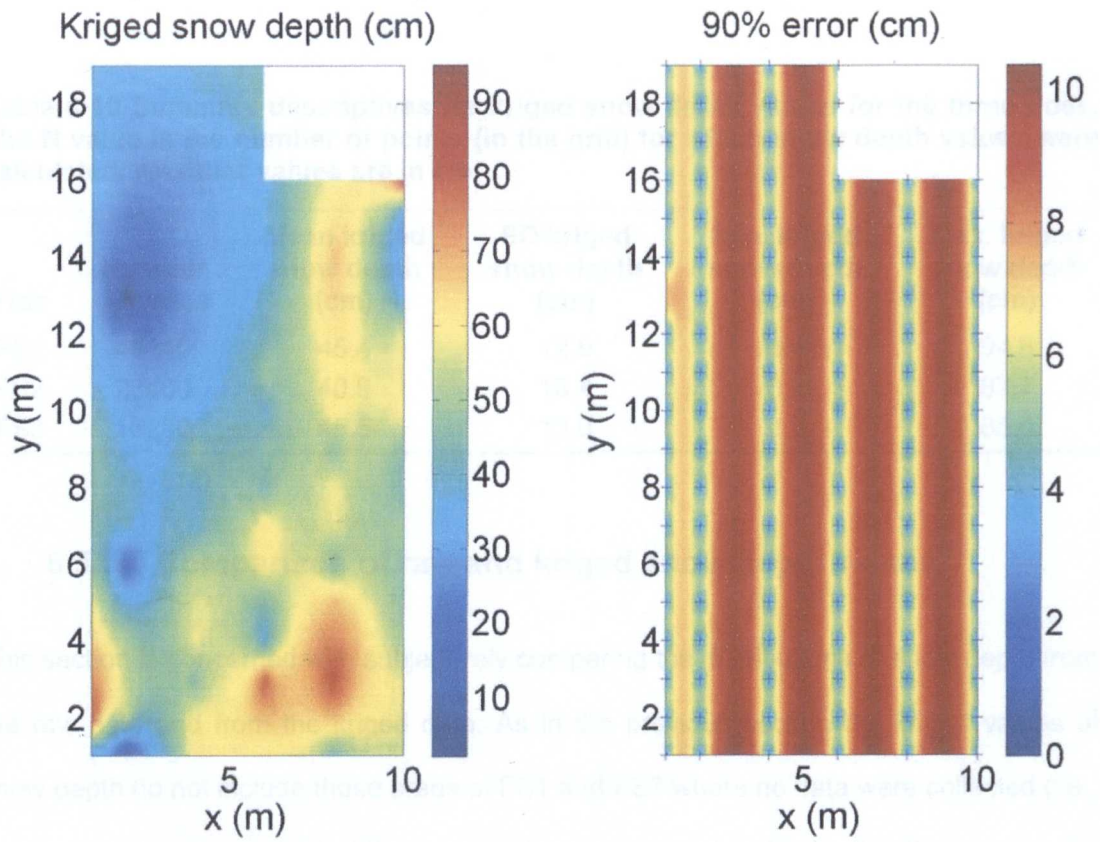

Figure 6-16 Contour plot (in cm) of kriged snow draft for FS3 and the associated estimation error showing the sample points as +.

Figure 6-16 shows the kriged snow depth values over the sampled area of FS3 and the associated kriging errors. The gap in the top right hand corner is where there are no sample points. As with Figure 6-15, the values of kriging error in Figure 6-16 show a striped pattern due to the systematic grid of sample points.

The summary statistics for the kriged values of snow depth from the three floes are given in Table 6-10 below. The mean kriged value of snow depth on FS1 was found to be 45.5cm with a standard deviation of 12.9cm. For FS2 the mean and standard deviation of kriged snow depth were 40.9cm and 18.4cm respectively. With a mean of 45.5cm and a standard deviation of 13.0cm the kriged values of snow depth on FS3 are very similar to those for FS1. The value of *N* in Table 6-10 is the number of nodes for which the value of snow depth has been calculated using the EasyKrig toolbox.

Table 6-10 Summary descriptives for kriged snow depth values for the three floes. The N value is the number of points (in the grid) for which snow depth values were calculated. All other values are in cm.

Floe	Number of nodes	Mean kriged snow depth (cm)	SD kriged snow depth (cm)	Min. kriged snow depth (cm)	Max. kriged snow depth (cm)
FS1	49140	45.4	12.9	6.4	94.8
FS2	23400	40.9	18.4	6.2	87.7
FS3	16200	45.5	13.0	2.9	85.0

6.5.6.1 Comparison of raw and kriged snow depth values

This section is concerned with subjectively comparing the distributions of snow depth from the raw data and from the kriged data. As in the previous section the kriged values of snow depth do not include those areas of FS1 and FS3 where no data were collected (i.e., the top right hand corners) but this is desirable, in order to be able to directly compare the same regions. The PDFs for the three snow thickness distributions are shown below in Figure 6-17 to Figure 6-19 for both the raw and kriged data. In general, the shapes of the PDFs for the raw snow depth values are similar to the PDFs for the kriged snow depth values.

Observing Figure 6-17, the kriged data has far fewer values at the extremes of snow depths compared to the raw data. To balance this the central peak of kriged snow depth values is wider.

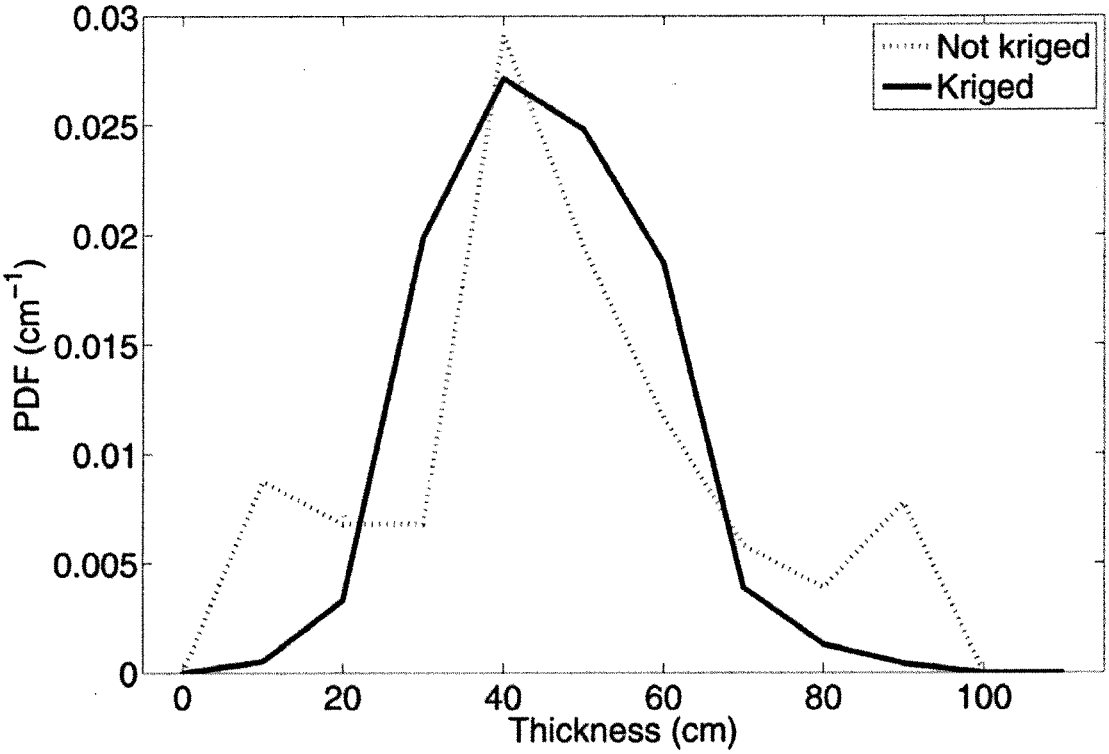

Figure 6-17 Comparison of PDFs for snow thickness measurements on FS1 for kriged and raw values with a bin width of 10 cm.

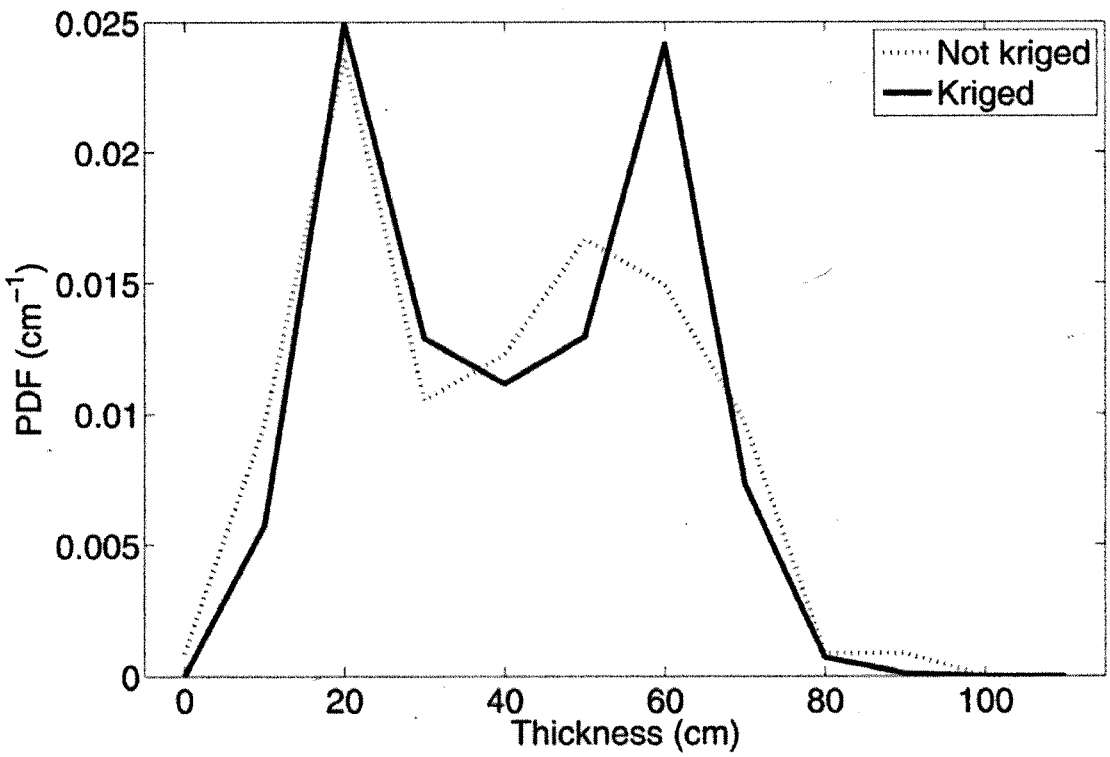

Figure 6-18 Comparison of PDFs for snow thickness measurements on FS2 for kriged and raw values with a bin width of 10 cm.

The kriged snow depth distribution for FS2, shown in Figure 6-18, also has fewer values at the extremes compared to the raw data. The distributions are both bimodal and the locations of the modes are similar although the raw data has a wider peak at the higher mode compared to the kriged data.

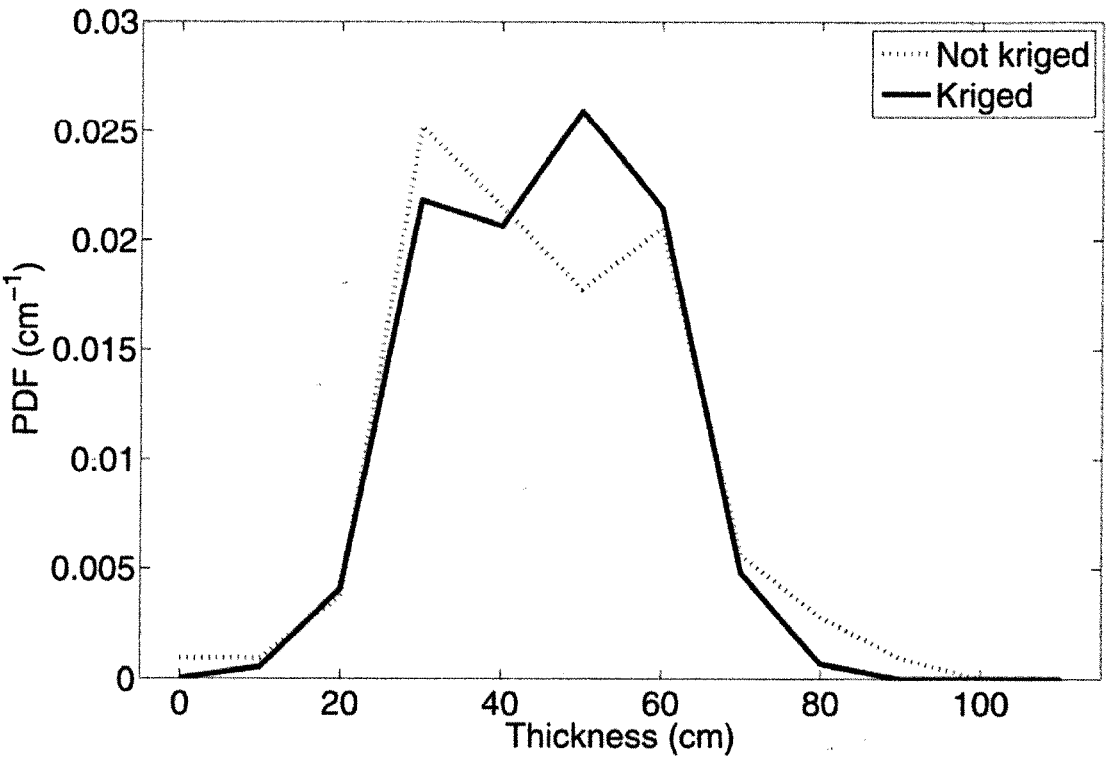

Figure 6-19 Comparison of PDFs for snow thickness measurements on FS3 for kriged and raw values with a bin width of 10 cm.

For FS3, the distribution of kriged snow depth values shown in Figure 6-19 is bimodal as is the distribution of raw values. This bimodality is perhaps not surprising when Figure 6-5 is studied; the figure shows the snow depth values are lower in the upper left corner and higher in the lower right corner. What is perhaps surprising is that this result is smoothed out in the distribution for the raw data.

The descriptive statistics for the raw and kriged snow depth data (taken from Table 6-2 and Table 6-10) are summarised in Table 6-11. The standard deviations from all three floes are smaller after kriging compared to the raw data although the ranges of snow depth values encountered before and after kriging are similar. This is not surprising as the

grid resolution and kriging parameters for EasyKrig were edited in order to ensure this (see Section 6.5.5). The mean snow depth for FS1 is smaller after kriging while the other two floes have larger means after kriging, although the increase in FS3 is small (0.2cm).

Using the approximation from Worby *et al.* (1996) between mean snow depth and mean ice thickness (Equation (2.4)), the mean depth of ice on a floe (z_i) is related to the mean thickness of snow (z_s) as

$$z_i \approx \frac{z_s}{0.3} \tag{6.1}.$$

Using this relationship Table 6-11 shows, for both raw and kriged values of mean snow depths, the estimates of ice thickness for the three floes. Using these results indicates total mean ice and snow thickness of 1.96m, 1.77m and 1.98m for FS1, FS2 and FS3 respectively based on the results of kriging the snow depth values (using the raw values would produce similar results). There may be a range of ice thickness values in Table 6-11 if flooding has occurred on any floes. However, there was no evidence for flooding on the drilled floes.

Table 6-11 Comparison of summary statistics for raw and kriged snow depth values from the three sampled floes measurements are all given in cm. See text for details of Predicted ice thickness.

Floe		N	Mean snow depth (cm)	SD snow depth (cm)	Min-Max snow depth (cm)	Predicted ice thickness (m)
FS1	Raw	103	47.4	21.1	6-95	1.58
	Kriged	49140	45.4	12.9	6.4-94.8	1.51
FS2	Raw	114	39.2	20.3	5-88	1.31
	Kriged	23400	40.9	18.4	6.2-87.7	1.36
FS3	Raw	107	45.3	15.6	2-86	1.51
	Kriged	16200	45.5	13.0	2.9-85.0	1.52
Overall	Raw	324	43.8	-	2-95	1.46
	Kriged	88740	44.2	-	2.9-94.8	1.47

6.6 Conclusions

6.6.1 Sea ice drilling

Comparing the locations of the floe stations with the locations of Autosub under sea ice missions (Figure 7-1) shows they are within the same region. However, there is a time difference of nearly two weeks between the last drill site and the first under sea ice mission. The sea ice drilling provides minimum values of sea ice thickness from the three floes but due to the limited nature of the drilling all that can be said is that the ice thickness of the sampled floes was ~2-3m.

6.6.2 Snow depth values

The mean measured snow depth across the three floes varied between 39.2cm and 47.4cm. The mean kriged values of snow depth were of a smaller range, between 40.9cm and 45.5cm. The mean kriged snow depth value for FS2 also shows how FS2 is distinct from the other two floes as it is lower by ~5cm. Using the kriged values for snow depth across the three floes FS1 and FS3 have lower standard deviations than FS2 indicating that their snow depths are more homogeneous compared to the snow depth of FS2.

The associated kriging errors are a maximum for FS1 and this is expected because the distance between sample points is also the maximum. Conversely, the finer grid structure of the FS3 sampling results in the smallest (on average) kriging errors and the same would have been the case for FS2 if there were not two missing transects (between x=0-5m and 5-10m as can be seen in Figure 6-4).

The sampling strategy on FS1 (see Figure 6-3) was unsatisfactory as it resulted in large gaps between sample points. The results of the sampling are clearly visible in the kriging error plot shown in Figure 6-14 as the large error values. It may be more appropriate for FS1 to use just the region where x<4m for the kriging analysis. However, the semi-variogram in Figure 6-11 suggests there is correlation in snow depth between locations separated by ~15m.

6.6.2.1 Comparing distributions and means of snow depth

I have used a variety of statistical tests to compare the means and distributions of snow depth from the three floes. ANOVA techniques have shown that at least one floe has a mean snow depth that is different from another floe. Evidence from *post hoc* tests suggests that FS1 and FS3 have the same mean. There is little evidence to indicate that the mean of FS2 compared with the means from the other two floes is the same. In order to test further the null hypothesis that the means of FS1 and FS3 are the same I performed a *t* test that suggested there was insufficient evidence for this hypothesis to be rejected.

ANOVA assumes that the measurements from the three floes are normally distributed and FS2 is not normal, so I have used a Kruskal-Wallis test that does not assume normality. The Kruskal-Wallis test ranks the values of snow depth for each floe. A chi-squared test on the rankings indicated that the three floes did not have the same average and this is in agreement with the results from ANOVA.

All of the methods for comparing the snow depth distributions/means assume that there is no correlation within the values for each floe. As discussed in Section 3.5.5, this is not the case with spatial data and there is the potential to incorrectly reject the null hypothesis that the groups are the same. From observation of the data from the three floes – averages, standard deviations and PDFs – it seems that the snow depths on FS2 are distinct from those on the other two floes.

6.6.2.2 Predicting ice thickness from snow depth

Values of total ice and snow thickness have been estimated from the kriged value of snow depth using Equation (6.1) and produce values of 1.96m, 1.77m and 1.98m for FS1, FS2 and FS3 respectively. A weighted average of the raw snow depth values from all three floes would give a mean ice thickness of the three floes of 1.46m and hence a combined snow and ice thickness of 1.90m. These values are lower than those expected from the drilling even though the drill-sites were chosen to represent the modal sea ice thickness.

6.7 Summary

Although it is unlikely that the ice draft would have increased substantially in the two week period between the ice drilling and the Autosub under ice missions, no substantive conclusions can be drawn from the sea ice drilling as there are too few measurements. However, it is worth noting the potential significant differences in sea ice thickness over relatively short distances (of the order of a few metres) between the drilling stations on FS3. In addition, the value of 2-3m thickness for ice and snow will form a useful value for comparing with Autosub measurements although this does represent the thickness of pancake, frazil and other thinner ice types within the region (such as bottom right of Figure 6-1). However, it is worth noting that these drilled values probably reflect the modal sea ice thickness as measured by Autosub. It is critical for future Autosub under sea ice missions to collect a large dataset of drilled groundtruth in order to further validate its use.

The depth of snow over a small area, of the order of a few hundred m^2, (see Table 6-2 and Figure 6-6) is clearly highly variable and over the three sampled floes the measured snow depth varied between 2cm and 95cm. Despite the complication in comparing the distributions of the snow depth because of correlations in space between values of depth I conclude that the distributions and means of FS1 and FS3 are different from those for FS2. However, the means of the kriged snow depths are more similar (only ~6cm difference). It is unlikely that the differences in snow depth suggest anything more than a different underlying structure of the sea ice, for example the deeper snow in FS3 (at about x=8m,y=3m in Figure 6-5) is caused by wind blown drifts as can be seen in Figure 6-1 as region A.

The mean values of snow depth reported here are in general agreement with those summarised in Massom *et al.* (2001) of between 29cm and 49cm for late summer 1994 for a similar longitude. The standard deviations of raw snow depth in this study (15.6cm to 21.1cm) are also similar to the values summarised in Massom *et al.* who reported values of between 15cm to 30cm.

The mean kriged snow depth of 44.2cm can be used to estimate the mean sea ice thickness of the three sampled floes to be 1.47m (using Equation (6.1)). This value of sea ice thickness can be used as an additional groundtruth value although it is lower than the values obtained from drilling.

Chapter 7 Sea ice draft measurements during AUI missions

This chapter is concerned with the interpretation of data concerning the sea ice draft in the AUI survey region to the north of Thurston Island (see Figure 1-7 for location). Details of a new methodology for obtaining sea ice draft from Autosub will be presented as well as geostatistical analyses to provide probability density functions (PDFs) of sea ice draft within the study region. I will show the PDFs for three missions incorporating the error associated with the spatial sampling of the data and compare these results with a series of observations made from the *RRS James Clark Ross*. In addition, statistical tests are used to compare the means and distributions of the ice draft between missions.

7.1 Introduction

The initial project plan was designed to use a multibeam echo sounder system, mounted in Autosub, to profile the underside of sea ice. However, technical difficulties during the cruise rendered that impossible for all but one of the missions (M321), see Section 7.1.1 for further details. Data for M321 only provides values of draft above a certain threshold and so I have designed an alternative methodology that allows data for all under sea ice missions to be used.

This alternative methodology requires knowledge of the vehicle depth and the values of range to surface returned by the upward-looking acoustic Doppler current profiler (ADCP). The data from Autosub can be compared with sea ice observations made using the methodology described in Section 7.2. Further comparisons will be made with other data sources in Chapter 8.

7.1.1 Problems with multibeam echo sounder

The EM2000 system multibeam echo sounder mounted on Autosub is designed for ease of use and as such, much of the processing of data can be considered to be "black box".

Critically, an example of this is that the travel times for the beams are not stored only the calculated distances from the vehicle to the surface. Any values of distance that exceeded the notional preset depth (as defined by the internal systems of the echo-sounder) of the vehicle based on the depth of the vehicle and the preset sound speed are treated as erroneous and stored as missing data. In order to correct for this a depth-offset correction (DSO) was applied with the aim of removing this additional "depth" at the processing stage.

In the case of M321, the DSO was set at 5m and for subsequent missions it was set at 15m. However, it appears that M321 only provided data on values of draft for ice greater than 3m and observations in the area suggest the presence of thinner ice. For the remaining under sea ice missions (M322, M323 and M324), a connector problem within the vehicle resulted in loss of all swath data (McPhail, 2003b). For these reasons the data from the EM2000 are unsuitable for the purposes of studying sea ice draft in this thesis although it is worth noting that the data for M321 may yet provide some limited information.

7.2 Sea ice observations

As an approach to groundtruthing, routine sea ice observations were made using the ASPeCt methodology as introduced in Section 2.7.1. These data can be summarised, using the software available (Worby, 1999) to provide estimates of albedo and average ice thickness. The ice thickness values are based on calculations using the observations of ice thicknesses as well as the type and proportion of ridges, see Worby and Allison (1999) for further details.

Whilst the *RRS James Clark Ross* was moving within the sea ice zone, sea ice observations were normally made at hourly intervals but sometimes more frequently to a minimum interval of 15 minutes. The sea ice observations were made from the same two locations on the *RRS James Clark Ross* (the port and starboard bridge wings) and were limited to ice within a 1km radius.

7.2.1 Sea ice observation method

Each observation required the documentation of ship position, date, time and an estimate of the total sea ice cover expressed in terms of the number of tenths of ice. The three dominant ice types were identified, provided there were that many types and the thickest ice type was labelled as primary, the next thickest as secondary and the thinnest as tertiary. The coverage of each ice type was also estimated as the number of tenths. For each of the ice types a series of coded values were recorded concerning the ice type, the diameters and thickness of the floes, the heights and aereal coverage of sails as well as the type and thickness of any snow. As discussed before (Chapter 2) the type of snow is important, as whether the snow is new or old or if it is cold or melting affects the albedo. The natures of regions of open water were noted, ranging from 0 ("No openings") through 4 ("Very Wide Breaks > 500 m") to 9 ("Open Sea").

Meteorological variables were noted from the ship's instruments and included air temperature, water temperature and wind speed. In addition, a number of meteorological observations were made and these were the proportion of cloud cover (in oktas), a code for the limit of visibility and a code representing a description of the weather. The forms used also allowed for any further relevant comments. For more details see Worby (1999). Simultaneously to each set of observations a video camera was used to film the sea ice, images from this were then used to verify the "live" sea ice observations.

7.2.2 Sea ice observation results

The statistics derived from the ASPeCt observations/software (Worby, 1999), for the area shown in Figure 7-1 (i.e., between –72°S and –70°S; between –107°W and -96°W) and for the time-period of the Autosub missions are given in Table 7-1. The observations were mostly made in the locations to the north of the Autosub missions as they were taken as the *RRS James Clark Ross* travelled through the sea ice to verify there were no large icebergs in the under-ice study region rather than throughout the whole selected region.

More specific questions on the ASPeCt sea ice observations will be made in Section 7.11.5 to establish the proportion of open water.

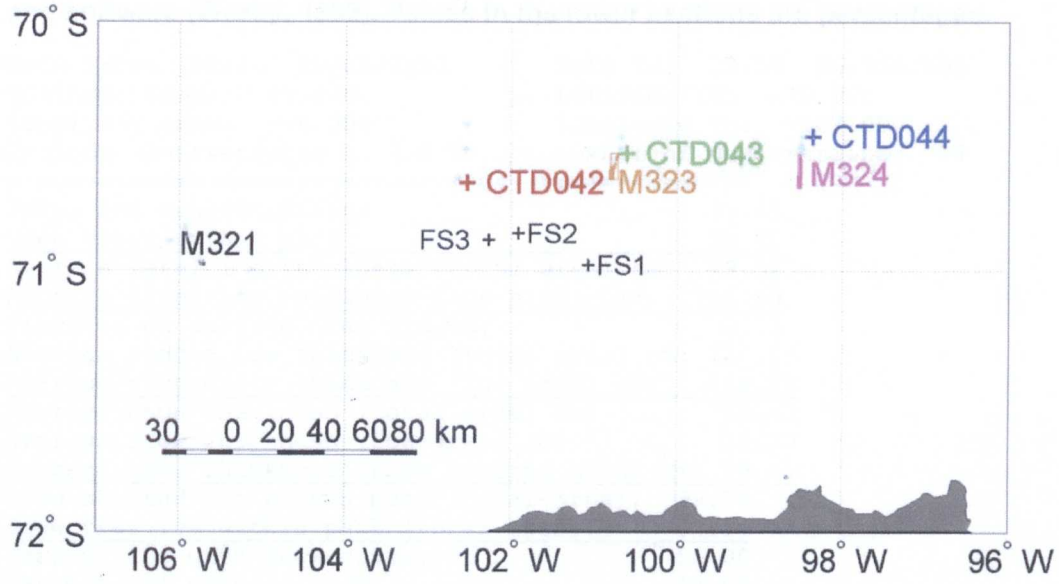

Figure 7-1 Positions of sea ice missions (Mnnn) used, floe stations (FSn), sea ice observation stations (+) and relevant CTD stations (CTDnnn).

The area averaged ice thickness was found to be just under 80cm although this value takes into account 28.6% of open water. Similarly, the area averaged snow thickness was calculated at 19.4cm, this value takes into account the areas of open water and ice with no snow cover. The mean ice thickness was found to be 1.1m and the mean snow thickness was 27cm giving an overall mean total thickness of 1.4m. The average ridged ice thickness was found to be 1.69m and assuming all this to be snow covered would give a combined snow and sea ice thickness of 2.2m. All these values assume that the observations from the 14 widely spaced stations reflect the nature of the ice in the region.

As discussed in Chapter 2, flooding of floes and the formation of snow ice can affect the measured sea ice draft. However, no evidence for flooding or snow ice formation was seen during either the sea ice observations or the sea ice drilling programmes.

Table 7-1 Summary statistics from sea ice observations for area shown in Figure 7-1 and for period 21st to 26th March 2003. Produced using the ASPeCt protocols and software (Worby, 1999). Values in the lower sections are percentages.

Date From:	00:00 21/03/2003	Date To:	23:59 26/03/2003
Latitude From:	-72.000	Latitude To:	-70.000
Longitude From:	-96.000	Longitude To:	-107.000
Exclude observations: <	2.0 Km	number of observations:	14

Total ice concentration:	71.43
Open water within pack:	28.57
Average level ice thickness (total area) cm:	79.92
Average level ice thickness (ice area) cm:	111.89
Fraction of surface area ridged:	0.13
Average ridged ice thickness (total area) cm:	120.52
Average ridged ice thickness (ice area) cm:	168.73
Average snow thickness (total area) cm:	19.43
Average snow thickness (ice area) cm:	27.20
Average snow thickness (snow covered area) cm:	49.45
Snow covered ice within pack (total area):	39.29
Snow free ice within pack (total area):	32.14
Percent ice with snow cover:	55.00
Percent ice with no snow:	45.00
Average albedo (total area):	**0.47**

Level Ice:

snow cover	0cm	0-3cm	>3cm
Water	28.57	0.00	0.00
New Ice (=<10cm)	7.14	0.00	0.00
Nilas (=<10 cm	0.00	0.00	0.00
Grey Ice (10-15cm)	7.14	0.00	0.00
Grey-White Ice(15-30cm)	0.00	0.00	0.00
1st Year(30-70cm)	0.00	0.00	0.00
1st Year (70-120cm)	0.00	0.00	4.29
1st Year (> 120cm)	0.00	0.00	10.00
Multiyear Ice	0.00	0.00	25.00
Brash	17.86	0.00	0.00
Fast Ice	0.00	0.00	0.00

Ridged Ice:

snow cover	0cm	0-3cm:	>3cm:
Water	28.57	0.00	0.00
New Ice (=<10cm)	7.14	0.00	0.00
Nilas (=<10 cm)	0.00	0.00	0.00
Grey Ice (10-15cm)	7.14	0.00	0.00
Grey-White Ice (15-30cm)	0.00	0.00	0.00
1st Year (30-70cm)	0.00	0.00	0.00
1st Year (70-120cm)	0.00	0.00	0.00
1st Year (> 120cm)	0.00	0.00	14.29
Multiyear Ice	0.00	0.00	25.00
Brash	17.86	0.00	0.00
Fast Ice	0.00	0.00	0.00

7.3 Autosub under ice missions

Autosub successfully completed four under sea ice missions during the course of JR84, numbered M321, M322, M323 and M324. Table 7-2 shows for each of these missions the date, time, length and the positions of Autosub at deployment and recovery. The positions of the Autosub missions are shown in Figure 7-1 as well as the locations of the sea ice observation stations and the location of the relevant CTD profiles. Table 7-2 also details M318, which was a mission within open water but is used extensively in my analysis.

Table 7-2 Locations and times of Autosub missions used in this study.

Mission Number	Date & Time (GMT) of Deployment and Recovery	Duration (hours)	Length (km)	At Deployment At Recovery Longitude	Latitude
M321	17:15, 22/3/03 TO 23:30 22/3/03	6¼	28	-105°44.3' TO -105°55.83'	-70°58.5' TO -70°49.77'
M322	18:12, 23/3/03 TO 03:40, 24/3/03	9½	44	-102°40.178' TO -102°24.01'	-70°38.841' TO -70°21.37'
M323	16:47, 24/3/03 TO 02:30, 25/3/03	9¾	45	-100°42.44' TO -100°41.27'	-70°32.1' TO -70°29.67'
M324	15:32, 25/3/03 TO 07:00, 26/3/03	15½	72	-98°29.7' TO -98°16.01'	-70°24.95' TO -70°22.84'
M318	00:00 18/3/03 TO 01:49 18/3/03	1¾	3	113°58.2' TO -113°58.8'	-71°17.4' TO -71°17.4'

7.3.1 Navigation and ADCP

The missions were designed so that they represented a series of parallel transects often referred to as the *lawnmower* patterns (examples can be seen as the red line in Figure 7-2

or in Figure 7-20). For M324 (Figure 7-2) the lawnmower pattern was overlaid with an additional V-shape designed to ensure that measurements of ice draft were not related to the direction in which readings were obtained (i.e., parallel transects may potentially follow similar alignments to those within the ice). Prior to each mission Autosub is programmed with a series of waypoints; onboard systems (detailed below) navigate the vehicle so that it passes through all these waypoints. These waypoints also include a depth component, so that at the start of each mission Autosub descends to the required mission depth. At the end of a mission Autosub maintains a holding pattern at a safe depth until contact is made with the ship via an acoustic beacon and the instructions are transmitted of where and when to surface.

Navigation for Autosub, and other submarine vehicles, whilst submerged is more complex than surface navigation because standard GPS techniques are not available underwater. Surface GPS fixes can provide a framework for Autosub operations but other methods are required when the vehicle is submerged.

One approach is to use dead reckoning whereby the AUV's velocity (i.e., speed and direction) is monitored relative to the water in order to estimate the distance travelled and in which direction. An alternative, and more accurate, approach is to measure the velocity of the vehicle with reference to a fixed surface such as the ocean floor (or potentially the underside of an ice shelf). The advantage of not using dead reckoning is that the effect of ocean currents can be removed. The problem with the latter method is that the fixed surface must be within range of the instrument being used.

For JR84, Autosub was fitted with an upward looking 300kHz RD Instruments (RDI) ADCP and a downward looking RDI 150kHz ADCP (McPhail, 2003a). Instrumentation on the vehicle is controlled centrally and both ADCPs are set to operate on a 2-second cycle. Within each 2-second period, the ADCP system produces one measurement of the range to surface for each of the four beams.

Navigation for Autosub is achieved using a combination of GPS fixes and a coupled system formed between either the upward or downward looking ADCP and an IXSEA PHINS Fibre Optic Gyro based inertial navigation system (INS) (see McPhail, 2003a). In water depths to about 400m below the vehicle, the downward looking ADCP is normally used to provide a value of velocity with respect to the ocean floor. This process is known as bottom tracking. If bottom tracking (or surface tracking using an ice shelf and the upward-looking ADCP) is not available then the relative vehicle speed is calculated using the closest velocity bin to the vehicle (i.e., within ~8m of Autosub). McPhail (2003a) reports that the accuracy of the system when using bottom track is 0.2% of distance travelled. Clearly, with appreciable currents and no bottom (or surface) tracking the accuracy of navigation is reduced as only the relative velocity to the water is obtained. For all missions presented here the navigation was initially derived in the latter manner, as the depth of water below Autosub was in excess of 400m. Post-mission, positions were corrected by measuring the difference between simultaneous values from a GPS fix and the ADCP/INS value of location and then interpolating all intermediate values assuming constant drift.

The above represents the standard processing of Autosub navigation data. However, there are problems with the four missions using this process (Daniel Hayes, Personal Communication). There are inexplicable spikes in the data for the values in the closest ADCP bin to Autosub and so the second bin down has been used. This bin represents the currents ~15m below Autosub. The re-processed values of vehicle position were supplied by Daniel Hayes and have been used in this thesis. For M321 and M323 the reprocessed data make little difference to Autosub's location. However, for M324 there is a marked difference between the positions from the traditional (first bin) approach and the reprocessed (second bin) method. The differences for M324 are shown in Figure 7-2, notice how the designed overlap of the V-pattern and the lawnmower pattern are offset due to the post-mission processing based on the GPS fixes and the different bins used for the calculations. Clearly, throughout M324 there was a strong current to the east.

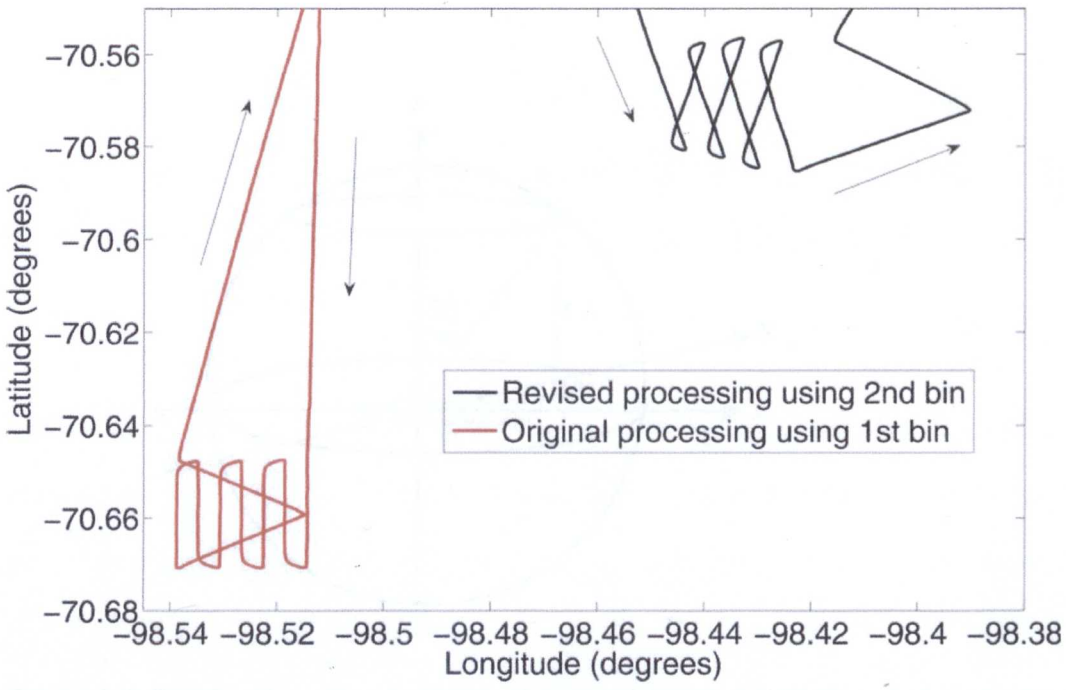

Figure 7-2 M324 Autosub locations as derived from original (first bin) method and reprocessed (second bin) approach, see text for further explanation of two methodologies.

7.3.2 ADCP setup

The RD Instrument acoustic Doppler current profiler (ADCP) consists of an array of four beams. The system is configured so that the axes of all four beams are pointing 30° from the vertical axis towards the surface as shown in Figure 7-3. In the horizontal plane, the beams are at right angles to each other as shown in Figure 7-4. The ADCP system was mounted on the vehicle so that beam 3 (see Figure 7-3 and Figure 7-4) is aligned at 45° to port (optimised for the on-board navigation system). Whilst there are internal attitude sensors within the ADCP they have not been used as the AUV's sensors are more accurate (Stephen McPhail, Personal Communication) and so they are used as an input.

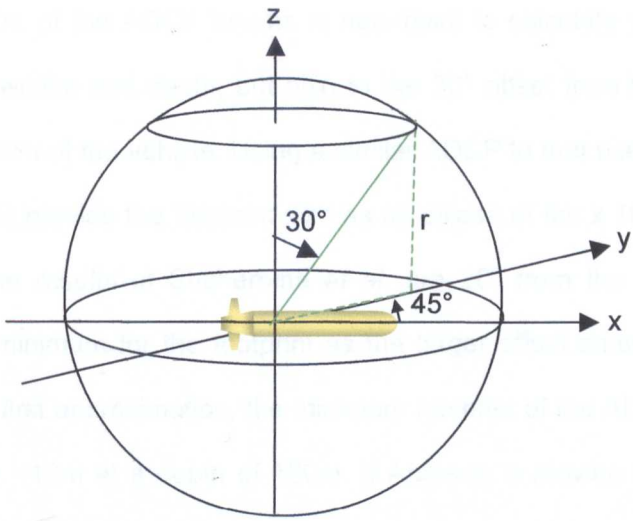

Figure 7-3 Schematic representation of upward looking ADCP on Autosub showing orientation of beam 3, the axes show Autosub's frame of reference. r is the vertical range to surface (as returned by the ADCP).

Each beam of the ADCP enables a value of range to surface (r in Figure 7-3) to be stored within the ADCP system giving four ranges for each ping. These values of range are based on converting the two-way travel time to the surface into a value of distance based on the sound speed within the ADCP unit.

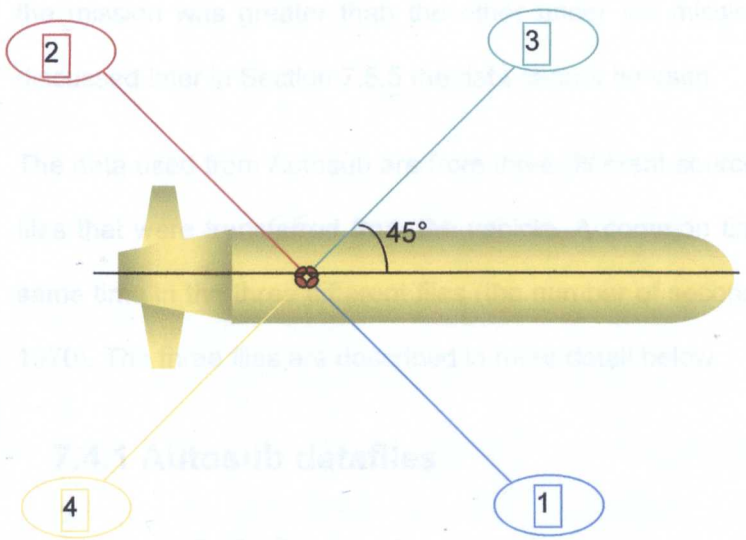

Figure 7-4 Plan view of Autosub ADCP setup (looking down) showing the beam numbers.

The footprint of the ADCP beams is non-trivial to calculate as it relates not only to the beam half-widths and depth, but also to the 30° offset from the vertical and, to a lesser extent, motion of the vehicle. Using a similar ADCP to that used for this thesis Shcherbina *et al.* (2005) provide the footprint size as an ellipse of 8m x 10m at a depth of 100m. The offset in the results of Shcherbina *et al.* are 20° from the vertical and therefore they provide a minimum for the footprint as the larger offset smears the signal over a larger area. As a first approximation, the minimum footprint of the ADCP in this thesis is taken to be ~10m x ~10m at a depth of 100m. If Autosub is moving between 1.5ms^{-1} and 2ms^{-1} with the ADCP pinging once every two seconds then each point on the surface is insonified between three and four times. This last calculation assumes that consecutive readings are obtained and implies that each point on the surface contributes more than once to the measured sea ice draft.

7.4 Data

Three under sea ice missions (M321, M323 and M324) were analysed using a standardised procedure to allow comparisons between missions. For M322 the depth of the mission was greater than the other under ice missions at ~200m and for reasons discussed later in Section 7.5.5 the data cannot be used.

The data used from Autosub are from three different sources and stored in three separate files that were transferred from the vehicle. A common timeline was used to identify the same time in the three different files (the number of seconds since midnight on 1 January 1970). The three files are described in more detail below.

7.4.1 Autosub datafiles

7.4.1.1 BNV files and navigation

The first file format is identified by the extension BNV short for Best Navigation Variables (e.g., m321.bnv). These files contain data on the status of the vehicle's position and

navigation system from the method described in Section 7.3.1. As discussed before, the navigation data contained in the BNV file is based on the first ADCP bin and for the purposes of this thesis has been replaced by the navigation derived using the second bin. The revised navigation data (using the second ADCP bin as detailed above) were combined to form an integral part of the BNV files.

7.4.1.2 LS2 files

The LS2 file contains data related to the upward looking and downward looking ADCP systems on-board Autosub as well as many other variables. The contents are transformed from the RD Instruments' format before the data are transmitted from Autosub. The data include the ranges to surface of the ADCP and the values of sound speed used. There is one record for each 2-second operating cycle.

7.4.1.3 CTD files

The third file type used has the extension CTD and contains data from the on-board Autosub Sea-Bird 9plus conductivity-temperature-depth (CTD) sensors. These sensors provide information on salinity and temperature and are recorded at 24Hz although for this thesis the two second averaged values are used. In order to compare CTD values with data from BNV and LS2 files the time codes for the CTD records were updated based on the time at the start of the mission. Autosub has a primary and a secondary CTD sensor and the values used in this thesis represent the mean values from both sensors over this period.

The difference between these two sensors is small (e.g., for M321 the maximum difference is ~0.1°C) except at the start of missions before both sensors are primed with seawater. The latter cases are treated as missing and few data are lost as the periods relate to the vehicle being on the surface or on-board the *RRS James Clark Ross*.

7.4.2 CTD data from RRS James Clark Ross

During Autosub's deployment under ice, three full water column conductivity-temperature-depth (CTD) stations collected data on water temperature and salinity (named CTD042, CTD043 and CTD044). The CTD sensor used for the profiles was a SeaBird 911 Plus operating at 24 Hz. The data used in this thesis are processed values showing the average values over 2 decibar bins see *Brandon et al.* (2003) for further details. The locations of these three CTD stations are shown in Figure 7-1 and are detailed in Table 7-3.

Table 7-3 Location of relevant CTD stations taken from *RRS James Clark Ross*.

CTD	Date	Longitude	Latitude	Notes
042	23/3/03	-102.6363	-70.6548	Simultaneous to M322
043	24/3/04	-100.7157	-70.5355	Simultaneous to M323
044	25/3/03	-98.4754	-70.4689	Simultaneous to M324

7.5 Pre-processing issues

In order to calculate the ice draft a number of issues that impact on values of the variables must be considered. The issues are depth of vehicle, the speed of sound in water, removal of surface pressure trends and offset of ADCP and CTD sensors. These are detailed in the sections below.

7.5.1 Vehicle depth

There are a number of different algorithms used to convert pressure into depth, the method used here is from Leroy and Parthiot (1998) and for depth D in metres then

$$D = \frac{9.72659\times10^{2}P - 2.512\times10^{-1}P^{2} + 2.279\times10^{-4}P^{3} - 1.82\times10^{-7}P^{4}}{g(\phi) + 1.092\times10^{-4}P} + \delta f_i(P) \quad (7.1)$$

where P is the pressure (in decibars), for Circumpolar Antarctic waters

$$\delta f_i(P) = 4\times10^{-2}P - 2\times10^{-4}P^{2} \quad (7.2)$$

and the correction for latitude ($g(\phi)$) is given by

$$g(\phi) = 9.780318\left(1 + 5.2788\times10^{-3}\sin^2\phi - 2.36\times10^{-5}\sin^4\phi\right) \quad (7.3).$$

This algorithm has a reported accuracy of 0.1m in the calculated depth.

7.5.2 Sound speed

A critical factor in calculating the range to the surface is the speed of sound in water (referred to from now on as sound speed). If no value of sound speed is input to the ADCP unit at the time of data collection then it defaults to 1500ms^{-1} (RD Instruments, 1998). The values of sound speed, c in ms^{-1}, used in this thesis are defined using the following equation

$$\begin{aligned} c = {} & 1492.9 + 3(T-10) - 6\times10^{-3}(T-10)^2 - 4\times10^{-2}(T-18)^2 + \\ & 1.2(S-35) - 10^{-2}(T-18)(S-35) + \frac{D}{61} \end{aligned} \quad (7.4)$$

where S is salinity in practical salinity units (psu), T is temperature in °C and D is depth in metres (Leroy, 1969).

Using Equation (7.4) with salinity as 34.06, temperature –1.53°C (the values from CTD042 for 100m depth) and depth 100m the sound speed is 1440.9ms^{-1} whereas the ADCP algorithm would calculate sound speed as 1442.4ms^{-1}. The one-way travel time measured by the ADCP would be the same in both cases so the ratio of distance travelled relative to sound speed would be

$$\frac{s_1}{u_1} = \frac{s_2}{u_2} \quad (7.5)$$

where s_1 = 100m, u_1 = 1440.9ms^{-1} and u_2 = 1442.4ms^{-1}. This results in a value of s_2 of 100.1m, i.e., an error of 10cm in the calculated range.

A further complicating issue is that both the above algorithms still assume that sound speed is constant throughout the water column. In order to calculate travel distances from travel time, knowledge is required of the sound speed profile from the surface to the vehicle and this is considered in the next sections.

7.5.2.1 Sound speed profiles from *RRS James Clark Ross*

For the three CTD profiles from *RRS James Clark Ross*, values of temperature, salinity and depth were, as previously stated in Section 7.4.2, averaged over two decibar bins. The temperature and salinity profiles for the top 200 decibars of these three CTD stations are shown in Figure 7-5.

For each of these 2 decibars bins the sound speed was calculated (using Equation (7.4)) and then for each bin the average sound speed was calculated for all bins from the surface down to that depth. Although the average does not represent the actual values of sound speed that would be experienced by the beam, it is accurate enough (calculated to be within ~2mm over 100m). Figure 7-6 shows the means of sound speed for the top 200 decibars based on the three CTD profiles.

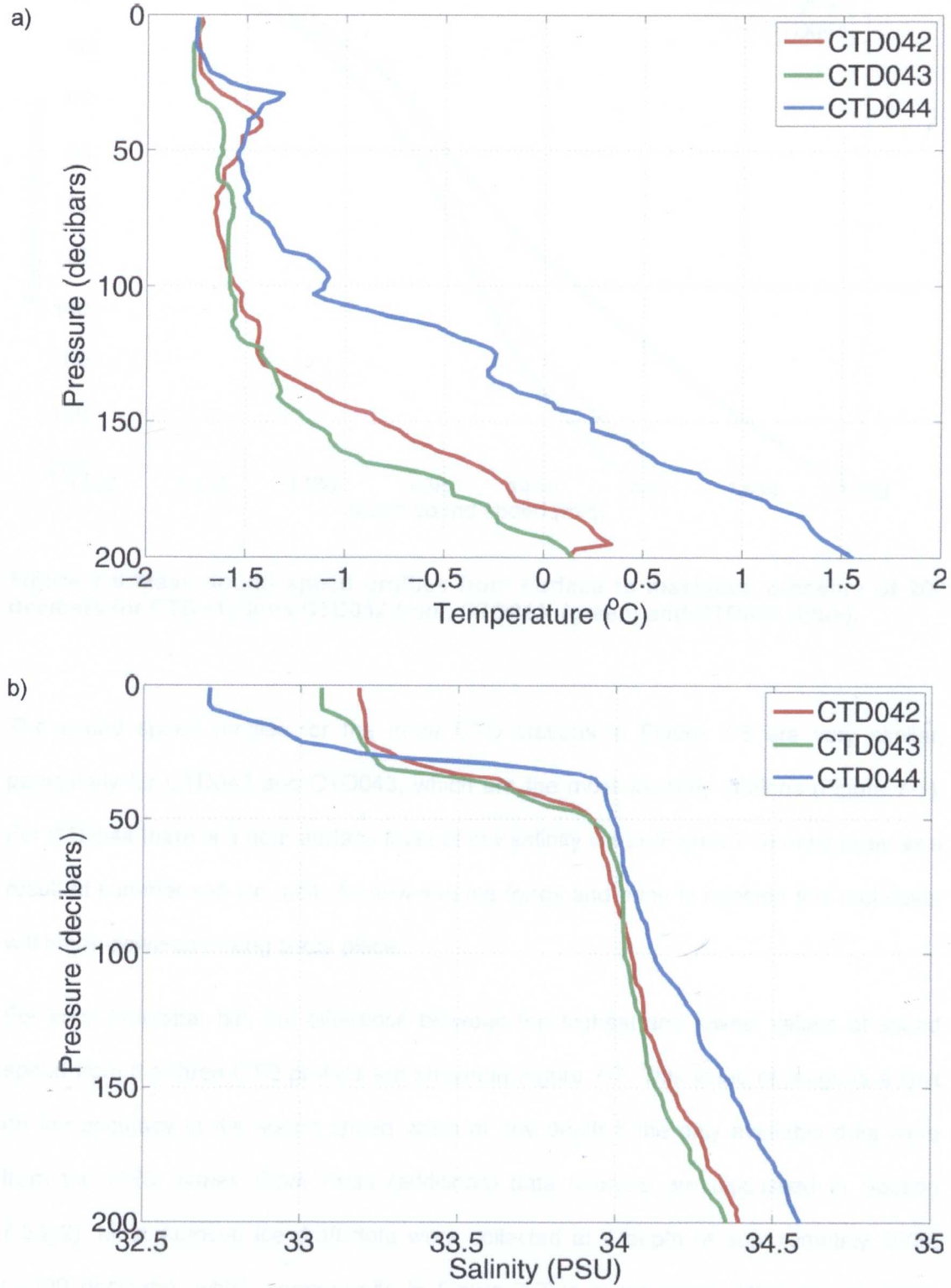

Figure 7-5 Profiles from surface to maximum pressure of 200 decibars for CTD stations CTD042 (red), CTD043 (green) and CTD044 (blue) for a) temperature in °C and b) salinity (psu).

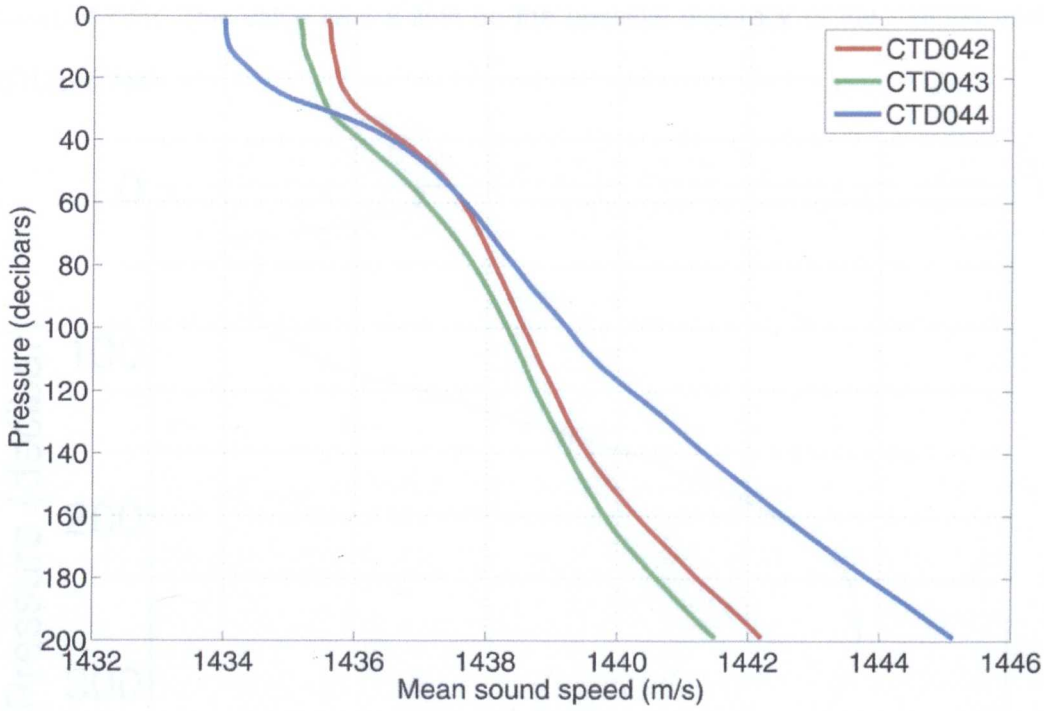

Figure 7-6 Mean sound speed profiles from surface to maximum pressure of 200 decibars for CTD stations CTD042 (red), CTD043 (green) and CTD044 (blue).

The sound speed profiles for the three CTD stations in Figure 7-6 are very similar, particularly for CTD042 and CTD043, which are the most westerly stations (Figure 7-1). For CTD044 there is a near-surface layer of low salinity water (Figure 7-5) most likely as a result of summer sea ice melt. As new sea ice forms and brine is rejected this melt-layer will break-down as mixing takes place.

For each 2-decibar bin, the difference between the highest and lowest values of sound speed from the three CTD profiles are shown in Figure 7-7. This value of range is a limit on the accuracy of the sound speed value at any depth if the only available data were from the *RRS James Clark Ross* (additional data sources are discussed in Section 7.5.2.2). Most Autosub ice draft data were collected at a depth of approximately 100m ($\approx$100 decibars), which corresponds in Figure 7-7 to a maximum difference in sound speed between the three CTD profiles of ~0.9ms^{-1}. At a depth of 100m this difference in sound speed is equivalent to a difference in measured depth and hence ice draft of the

order of 6cm. This value sets a limit on the possible accuracy of the method using the CTD profiles.

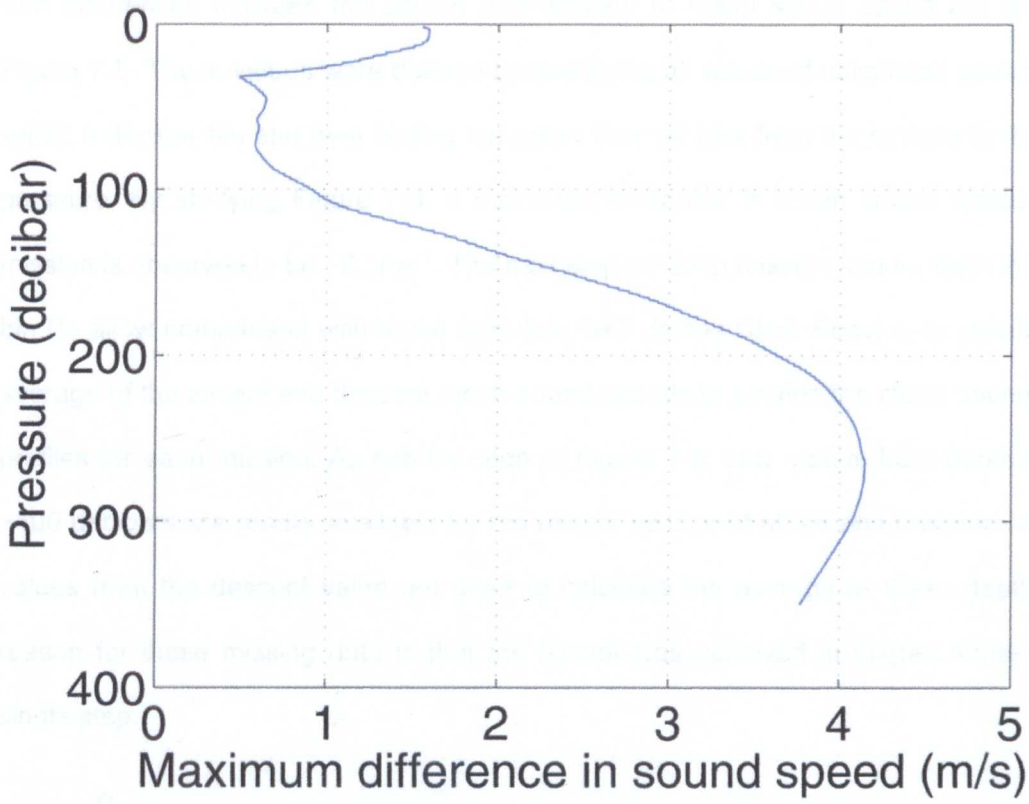

Figure 7-7 Plot of maximum difference in mean sound speed for the three CTD stations from the surface to a pressure of 350 decibars.

7.5.2.2 Sound speed profiles comparison of *RRS James Clark Ross* and Autosub CTD data

There are two sources of temperature and salinity data from each Autosub mission from the vehicle descending to mission depth and the vehicle ascending back to the surface. Therefore, the same procedures used for data from the CTD profiles from *RRS James Clark Ross* (Section 7.5.2.1) can be applied to data measured using Autosub. However, additional care must be taken to minimise the potential problems due to the spatial component (i.e., profiles from diving/surfacing are not at the same location). This latter issue may actually be beneficial as the resulting values of sound speed are calculated

using averaged (over space) values of salinity and temperature rather than from a single location as with the CTD profiles from *RRS James Clark Ross*.

The differences between the ascent and descent of mean sound speed are shown in Figure 7-8. These values were derived by averaging all values of calculated sound speed within a decibar bin and then finding the mean from all bins from the surface to the given pressure. By studying Figure 7-8, a maximum difference in mean sound speed in any mission is observed to be ~0.5ms^{-1}. The next step for each mission and for each 2 decibar bin (to allow comparison with those from the *RRS James Clark Ross*) is to calculate the average of the ascent and descent mean sound speeds to provide the mean sound speed profiles for each mission. As can be seen in Figure 7-8, only values from depths above ~100 decibars are readily available for the ascent section of M324 and therefore only the values from the descent value are used to calculate the average at these depths. The reason for these missing data is that the ascent was achieved in stages rather than a single step.

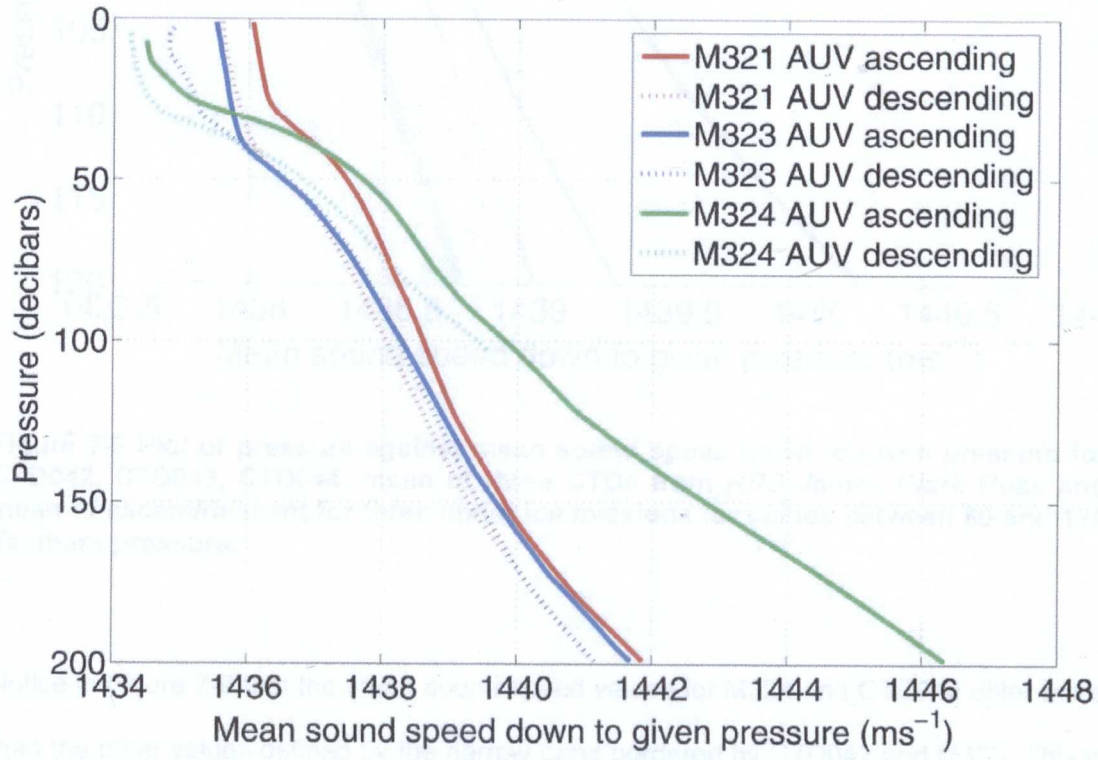

Figure 7-8 Plot of mean sound speed down to given pressure for ascent and descent sections of three under ice missions – M321 (red), M323 (blue) and M324 (green). Ascending sections are solid lines; descending sections are dotted.

Figure 7-9 shows a comparison of the mean sound speeds from the surface down to the given pressure, to a maximum of 200 decibars, for each under ice mission and for the ship-based CTDs. At the typical mission depth of ~100 decibars the maximum discrepancy between any of the mean sound speed profiles is ~1.45 ms^{-1} (1439.7 – 1438.25ms^{-1}) and using these values in Equation (7.5) results in a difference in measured ice draft of ~0.1m if s_1=100m. This discrepancy of 0.1m reflects the maximum difference over the entire study region shown in Figure 7-1 and using the average values from each mission results in a much lower value as discussed in the previous paragraph.

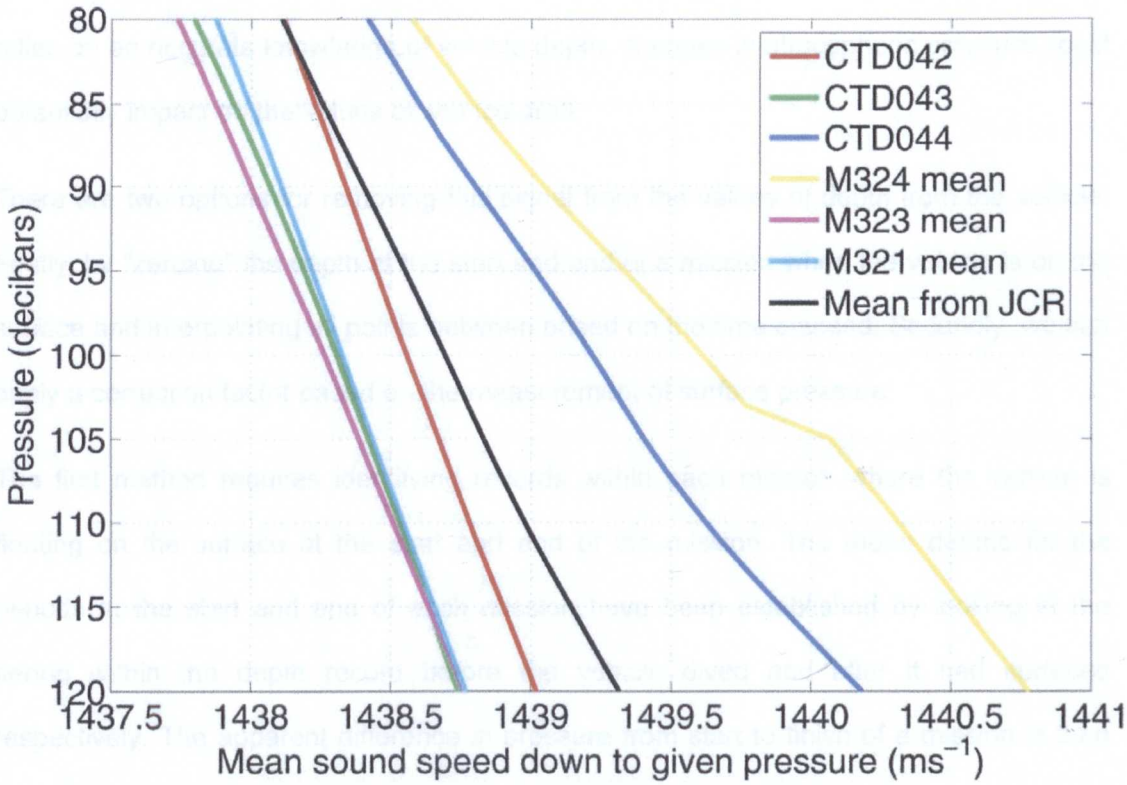

Figure 7-9 Plot of pressure against mean sound speed down to given pressure for CTD042, CTD043, CTD044, mean of three CTDs from *RRS James Clark Ross* and mean of ascent/descent for three under ice missions for values between 80 and 120 decibars pressure.

Notice in Figure 7-9 that the mean sound speed values for M324 and CTD044 differ more than the other values defined by the narrow band bordered by CTD042 and M323. This is perhaps not surprising as study of Figure 7-1 shows that CTD044 and M324 were very close to each other in space and Table 7-3 shows they were at the same time. As a

conclusion, the agreement between the sources is excellent and I have used the values of temperature and salinity for each mission from Autosub to calculate sound speed for all further processing.

7.5.3 Removal of surface pressure changes

As shown in Table 7-2 the length of the under ice missions was of the order of a few hours, during which time the atmospheric pressure may have changed. Changes in atmospheric pressure result in changes in the pressure measured by Autosub's instruments that in turn relates to a different calculated depth. As the methodology here relies on an accurate knowledge of vehicle depth, changes in atmospheric pressure could potentially impact on the values of sea ice draft.

There are two options for removing this signal from the values of depth from the vehicle. Firstly, by "zeroing" the depth at the start and end of a mission when the vehicle is on the surface and interpolating all points between based on the time elapsed. Secondly, we can apply a correction factor based on the measurement of surface pressure.

The first method requires identifying records within each mission where the vehicle is floating on the surface at the start and end of the mission. The mean depths for the periods at the start and end of each mission have been established by looking at the period within the depth record before the vehicle dived and after it had surfaced respectively. The apparent difference in pressure from start to finish of a mission is then simply the difference between the two values of depth. Table 7-4 shows the values of "zero depth" at the start and end of each mission and hence the differences.

Table 7-4 Mean depths at start and end of missions based on apparent *zero* depth.

Mission	Mean depth at start (m)	Mean depth at end (m)	Difference (m)
318	-0.375	-1.124	0.749
321	-0.986	-0.994	0.009
322	-0.972	-0.195	-0.777
323	-0.905	-0.241	-0.664
324	-0.961	-0.125	-0.836

Meteorological data, including atmospheric pressure, were collected on board *RRS James Clark Ross* at a one-second interval and these are averaged over five-second periods. Figure 7-10 shows the pressure values over the length of five missions. If atmospheric pressure rises then the apparent depth of Autosub will be deeper and the ice draft will increase. These pressure changes are significantly less than those found above (Table 7-4). Table 7-5 shows the maximum change in pressure and the corresponding values of depth relating to these changes according to the conversion using Equation (7.1). The values clearly show that the potential difference in ice draft that these pressure variations imply are small especially when considered over the time scale of the missions (e.g., The maximum is in M324 where the change is ~8cm difference in 15 hours). The red line in Figure 7-10 showing the change in atmospheric pressure for M324 includes a long spell at the end of the mission when Autosub was awaiting recovery during deteriorating weather and was too deep to return any useful data (this is indicated in Figure 7-10). The difference in depth of ~8cm is therefore an overestimate of the actual value.

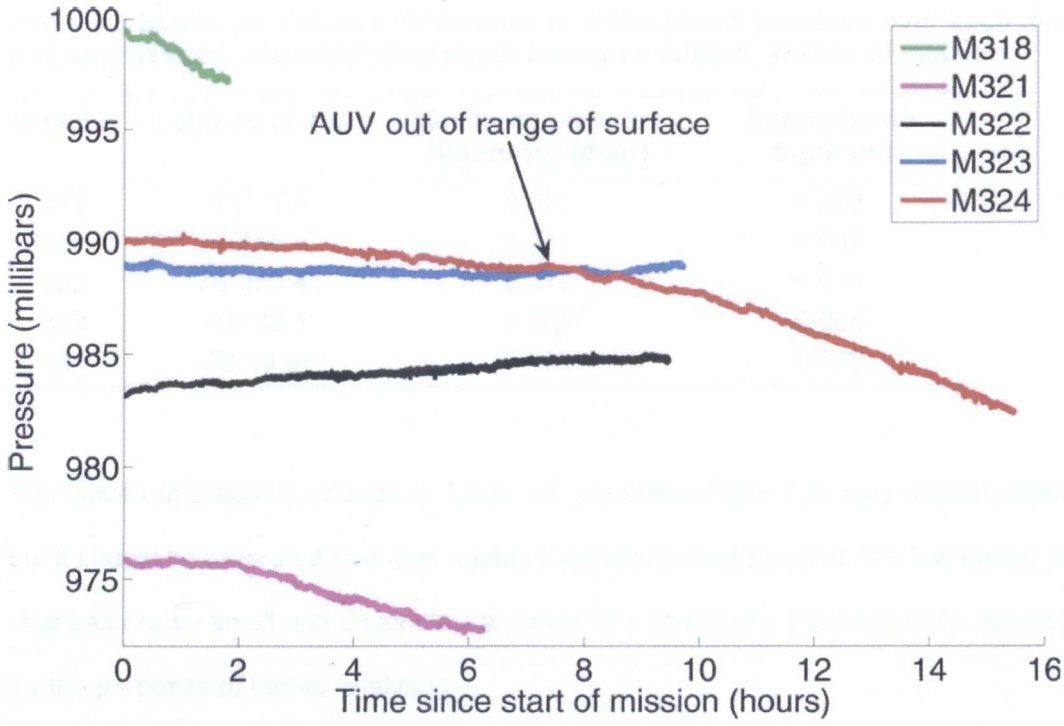

Figure 7-10 Plots of surface pressure as measured from *RRS James Clark Ross* from start to end of mission based on times given in Table 7-2. For M324 only, at times greater than the position of the arrow, Autosub was not collecting any useable data.

Given the actual surface pressure trends shown in Figure 7-10 and Table 7-5 it is likely that the changes measured by Autosub's instruments (Table 7-4) are not a result of changes in depth of Autosub. One possibility was that the vehicle had a different orientation after a mission to depth when different sections of the vehicle become flooded and so the CTD was perhaps at a different depth with respect to the rest of the vehicle. This explanation is supported by the different average values of pitch at the start and end of the missions. Another possibility is that there is some hysteresis in the pressure sensor on Autosub.

Table 7-5 Maximum values of difference in atmospheric pressure over each mission and approximate corresponding depth based on latitude at start of mission.

Mission	Latitude at start	Maximum pressure difference (dbar)	Approximate depth (m)
318	-71°17.4'	0.023	0.023
321	-70°58.5'	0.033	0.033
322	-70°38.841'	0.019	0.018
323	-70°32.1'	0.008	0.008
324	-70°24.95'	0.080	0.079

The values of pressure change in Table 7-5 (and also Table 7-4) may appear significant but it should be reiterated that they relate to variations over a period of a few hours. As the changes are so small and occur over a period of a few hours, I deduce I can ignore them for the purposes of further analyses.

7.5.4 Offset of ADCP and CTD instruments

The ADCP and CTD units had different locations within Autosub; their horizontal separation has been estimated at 4m (Steve McPhail, Personal Communication). Unfortunately, no accurate measurements are available for the separations as at the time of the cruise it was not envisaged that the ADCP would be used for measuring ice draft. Figure 7-11a shows a schematic representation of the locations of the two instruments (A and D) with separation L when the vehicle is horizontal. When the vehicle has a non-zero pitch (of θ) then there is an offset in the depths of the two instruments as shown in Figure 7-11b. The value of Δy can readily be calculated as

$$\Delta y = L \sin \theta \tag{7.6}$$

and hence, the measured depth can be corrected.

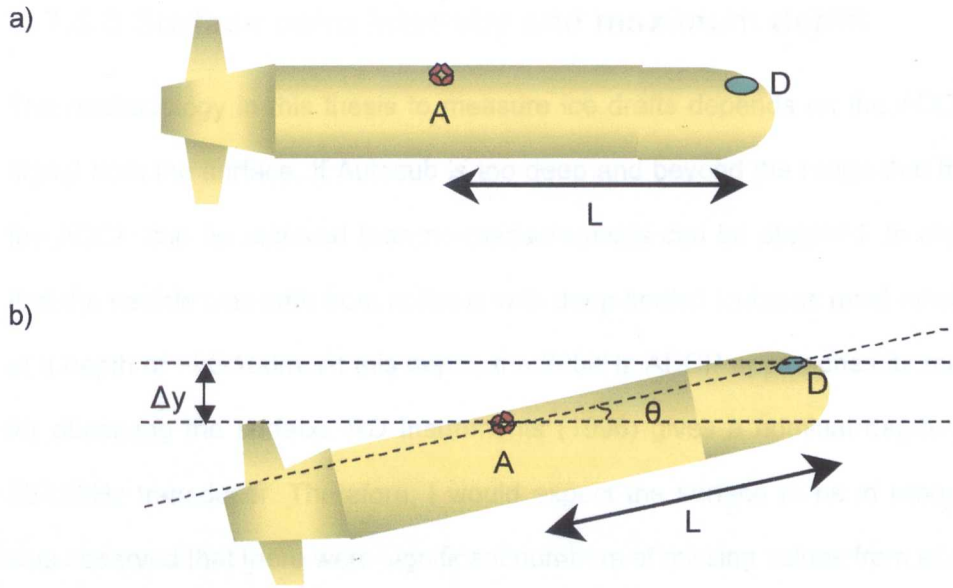

Figure 7-11 Schematic view showing the difference in position (L) of depth sensor (D) and UL-ADCP (A) for a) zero pitch and b) with value of -θ for pitch of the vehicle showing the resulting difference in depth of the two instruments (Δy).

Table 7-6 shows the values of Δy for a variety of values of the horizontal offset (L) with a typical value of pitch of 2°. An estimate of the discrepancy in depth of 0.14m is found when L=4m.

Table 7-6 Values of Δy for various value of L for a pitch of 2°.

L	Δy
4.2	0.15
4.1	0.14
4	0.14
3.9	0.14
3.8	0.13
3.5	0.12
3	0.10
0	0.00

The values of depth for all missions have been adjusted using Equation (7.6) based on the measured values of pitch and L a constant (L= 4m).

7.5.5 Surface echo intensity and maximum depth

The methodology in this thesis to measure ice drafts depends on the ADCP receiving a signal from the surface. If Autosub is too deep and beyond the range that the signal from the ADCP can be received then no measurements can be obtained. In order to be sure that the vehicle was safe from collision with deep-keeled icebergs most missions were run at a depth of ~90-100m. At this depth, the 300kHz ADCP approaches its maximum depth for observing the surface: RD Instruments (1996) gives a nominal depth of 120m for a 307.2kHz transducer. Therefore, I would expect the surface to be in range. However, it was observed that there were significant numbers of missing values from all missions (i.e., that no values for range were returned). This issue is demonstrated in Figure 7-12.

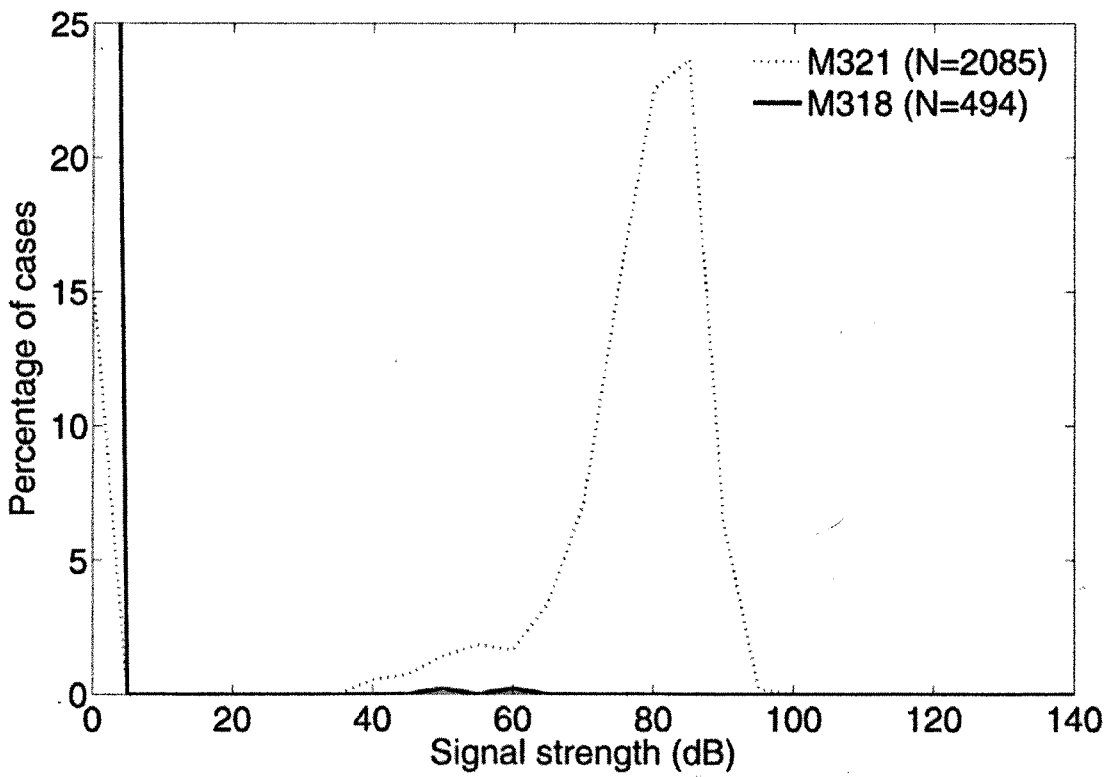

Figure 7-12 Histograms of the percentage of surface returns when the vehicle depth was between 90m and 115m for two missions M318 (open water) and M321 (under ice). N is the number of valid data cycles.

Two missions have been used to produce Figure 7-12, M318 and M321. The first mission, M318, was a test mission down to a depth of 100m and completed under open water.

M321 was at a similar depth to M318 and collected data under sea ice as well as under open water. Both M318 and M321 had the same Autosub instrument setup. In order to allow comparison of the two missions Figure 7-12 only includes data cycles where the depth of the vehicle was in the range 90-115m and also percentages are used rather than the actual number of cases. In M318 (open water) the surface is rarely detected as seen by the low number of non-zero surface returns whereas for M321 (sea ice) there is a bell-shaped distribution of values around 80dB. I conclude from this that the reason for so many non-returns is that the surface condition (i.e., presence of ice) has a significant impact on the number of valid returns. With sea ice there are far more returns from the typical mission depths compared to open water. This implies that it is unlikely that values of range to the open water surface are obtained at these mission depths. Ideally, these values of range to open water would have been used to verify the depth of the vehicle; unfortunately, this was therefore not possible.

As stated above, RD Instruments, the manufacturer of the ADCP, recommend a maximum range to surface of a ~300kHz ADCP system of about 120m due to attenuation of the signal (RD Instruments, 1996). A large number of returns when Autosub was deeper than this value contained implausible values for ice draft and so all values of range in excess of this cut-off (i.e., 120 m) were recoded to be missing values.

7.6 Method

For each of the three under ice missions used (i.e., M321, M323 and M324), Autosub was deployed in open water close to the ice edge and programmed to fly under the sea ice using a *lawnmower pattern*. There are a maximum of four possible values for range to surface (one for each beam) for each data cycle.

These four values are used to calculate values of vertical range to surface using the methodology explained in Section 7.6.1. Subtracting the vertical component of these co-ordinates from the depth of the AUV provides a value of ice draft.

The profiles of ice draft against time elapsed were then studied and the start and finish of the regions of continuous ice were identified for each mission. The definition of the continuous ice zone results in a number of cases being ignored where there were values of ice draft outside of this region but these are limited and I assume they relate to individual floes or icebergs within open water. My aim was to measure the mean draft of the pack and so only records within the continuous ice zone were included for analysis within this thesis.

7.6.1 Rotation matrices

Any rotation in 3-dimenional space can be achieved using the three Euler angles (roll, pitch and yaw/heading). Euler's theorem states that the rotation matrix required to rotate the vehicle through the values of pitch, roll and yaw (P_i, R and Y respectively) is the product of multiplying the rotation matrices required for the individual rotations (M_{Roll}, M_{Pitch} and M_{Yaw} respectively), i.e.,

$$M_{Overall} = M_{Yaw}M_{Pitch}M_{Roll} \qquad (7.7)$$ (Weisstein, 2006)

where

Rotation matrix for roll, R is given by

$$M_{Roll} = \begin{bmatrix} 1 & 0 & 0 \\ 0 & \cos R & \sin R \\ 0 & -\sin R & \cos R \end{bmatrix} \qquad (7.8)$$

Rotation matrix for pitch, P_i is given by

$$M_{Pitch} = \begin{bmatrix} \cos P_i & 0 & \sin P_i \\ 0 & 1 & 0 \\ -\sin P_i & 0 & \cos P_i \end{bmatrix} \qquad (7.9)$$

Rotation matrix for yaw, Y is given by

$$M_{Yaw} = \begin{bmatrix} \cos Y & \sin Y & 0 \\ -\sin Y & \cos Y & 0 \\ 0 & 0 & 1 \end{bmatrix} \quad (7.10)$$

So that substituting (7.8), (7.9) and (7.10) in (7.7) results in

$$M_{Overall} = \begin{bmatrix} \cos P_i \cos Y & \cos R \sin Y - \sin R \sin P_i \cos Y & \sin R \sin Y + \cos R \sin P_i \cos Y \\ -\cos P_i \sin Y & \cos R \cos Y + \sin R \sin P_i \sin Y & \sin R \cos Y - \cos R \sin P_i \sin Y \\ -\sin P_i & -\sin R \cos P_i & \cos R \cos P_i \end{bmatrix} \quad (7.11)$$

In order to calculate the distance from the ADCP/Autosub to the surface there are a number of stages that must be accomplished in order to correct for both the orientation of the four beams with respect to Autosub and the attitude of the AUV. Firstly, the range supplied by the ADCP is the vertical range to surface (see Figure 7-3) so the magnitude of the vector representing the point on the sea/ice surface must be divided through by the cosine of the angle offset from the vertical for each beam (i.e., cos30°).

Next, the vector representing each beam is corrected to Autosub's frame of reference using the rotations required to correct for the four different horizontal orientations (see Figure 7-4) and the offset from the vertical (Kate Stansfield, Personal Communication). The initial values in the x and y directions (as shown in Figure 7-13) are both zero so that the magnitude of the vector is just the vertical range to surface. The vector representing the position of the beam is

$$\mathbf{v}_{beam} = \begin{pmatrix} 0 \\ 0 \\ -range \end{pmatrix} \quad (7.12)$$

where the range is the vertical range from the ADCP to the surface.

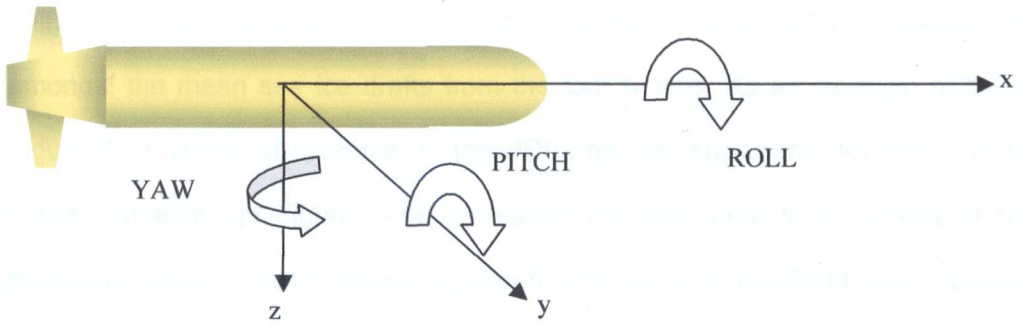

Figure 7-13 Directions of pitch and yaw in Autosub's frame of reference.

Multiplying the vectors given in Equation (7.12) by the matrix in Equation (7.11) and the values for pitch and yaw given in Table 7-7 with a value of roll of zero in all four cases the transformed vectors of the four beams with respect to Autosub can be calculated.

Table 7-7 Values of pitch, roll and yaw to rotate values of the four ranges into a common Autosub frame of reference.

Beam Number	Pitch Value	Yaw Heading
1	-30°	45°
2	-30°	-135°
3	-30°	-45°
4	-30°	135°

For each data cycle, these resulting vectors were rotated once again, using Equation (7.11), to take account of vehicle attitude (i.e., Autosub's pitch, roll and heading). As will be discussed in the next section, a correction is possibly needed to account for the offset in the alignment of the ADCP unit and Autosub's attitude sensors. By adding the relative locations of these final vectors to Autosub's location, the co-ordinates of the beams have been calculated. The revised values of the range to surface (i.e., the z-component) can now be subtracted from the measured vehicle depth to provide a value for ice draft at each location.

7.6.2 Alignment offset of ADCP from vehicle attitude sensors

As stated before (Section 7.3.2), the range values from the ADCP are corrected using the pitch and roll sensor from the vehicle rather than the integrated sensors within the ADCP

unit. Preliminary analyses of the data consistently produced implausible differences amongst the mean sea ice drafts from the four beams. As an example of the problem, Figure 7-14 shows an example of the PDFs for the four beams for M321. It should be noted that although Figure 7-14 represents the data prior to a number of necessary processing steps it clearly shows significant differences in the distributions for the forward looking beams (1 and 3) and the backward looking beams (2 and 4). This pattern was also repeated for the other two missions. The most likely explanation, given that the ADCP instrument is not fixed relative to the attitude sensors, was that there was an offset in the alignment between the ADCP unit and the value of pitch as measured by the vehicle's attitude sensors (i.e., those from the INS). It is therefore likely that there were also offsets in the roll and yaw of the ADCP unit compared to those measured on-board. A methodology was developed to take account of the discrepancies due to offsets in roll and pitch as detailed below. Unfortunately, this methodology could not be developed to identify the possible offset in yaw but the relative locations of all pings on the surface were unaffected.

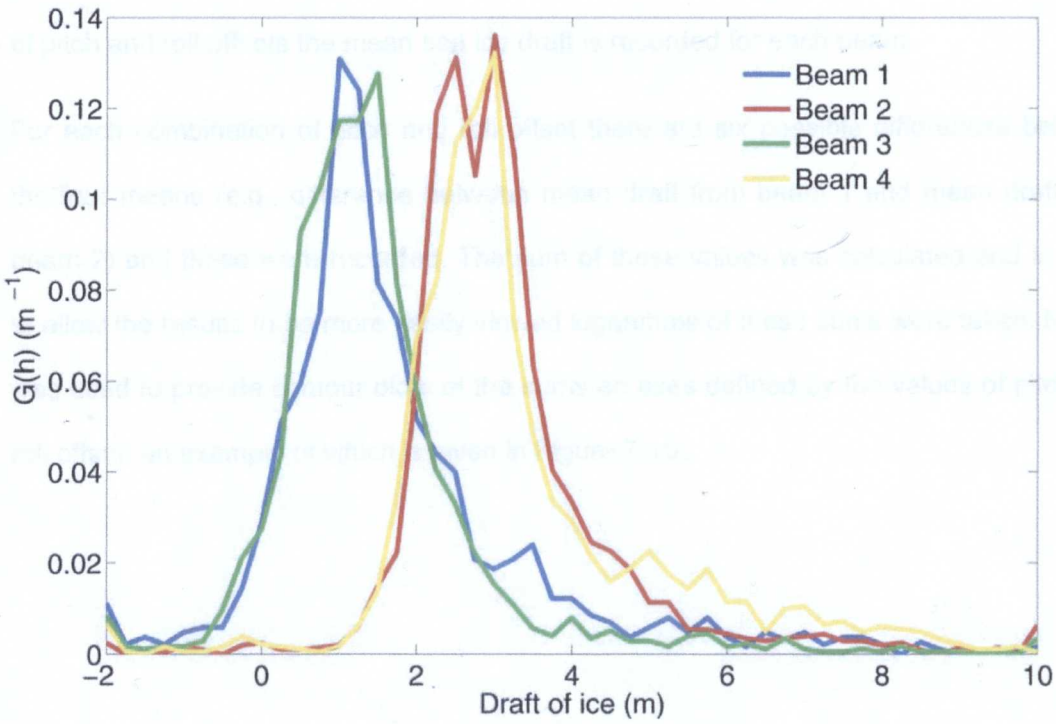

Figure 7-14 M321 Preliminary PDF for sea ice draft from ADCP four beams with no pitch and roll offset corrections. Discrepancies between beams 1 and 3 (blue and green) and beams 2 and 4 (red and yellow) are visible (see text for explanation).

7.6.2.1 Methodology for identifying offset in alignment between ADCP and Autosub attitude sensors

The procedure to identify the offset in pitch and roll was based on assuming that the means of ice draft as determined from each of the four beams were the same. Given the large number of data points within the same region (as will be seen in Figure 7-20) the rearward-looking beams closely follow the locations of the two forward-looking beams. As previously stated, the setup of the vehicle was not changed between the three missions and so the results from M321 were subsequently used for the other two missions.

The same procedures as detailed in the previous sections for obtaining values of sea ice draft were used in addition to an iterative process implemented for different values of the offset in pitch and roll. For each step in the analysis minima and maxima values of pitch and roll offsets were set as well as step increments. The script used iterated through all possible values of roll offset for every possible value of pitch offset. For every combination of pitch and roll offsets the mean sea ice draft is recorded for each beam.

For each combination of pitch and roll offset there are six possible differences between the four means (e.g., difference between mean draft from beam 1 and mean draft from beam 2) and these were recorded. The sum of these values was calculated and in order to allow the results to be more easily viewed logarithms of these sums were taken. Matlab was used to provide contour plots of the sums on axes defined by the values of pitch and roll offset, an example of which is given in Figure 7-15.

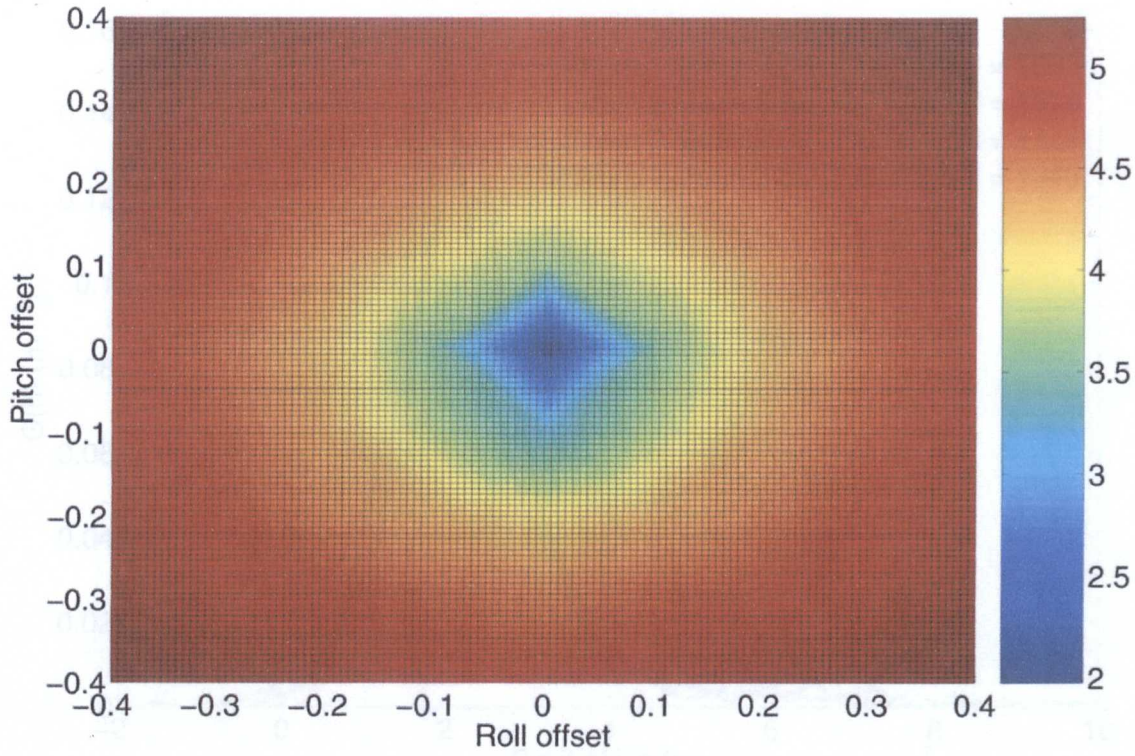

Figure 7-15 Interpolated surface plot of the logarithm of the 6 beam differences for M321 first iteration – pitch and roll offsets vary between –0.4 and 0.4 in steps of 0.1. Units on the axes are radians and of the colour scale are log(metres).

The above process is repeated using smaller and smaller values of pitch and roll offsets and smaller incremental steps until the minimum (optimum) values of pitch and roll offset were established. The value used for pitch offset was –1.15° and the value for roll was a much smaller value of –0.03°. Using these values, the data in Figure 7-14 was reprocessed and the revised distributions of ice draft from M321 are shown in Figure 7-16. As before, these PDFs only represent interim values of ice draft and still require processing further. However, it is clear that the locations of the distributions are, as expected, far more similar.

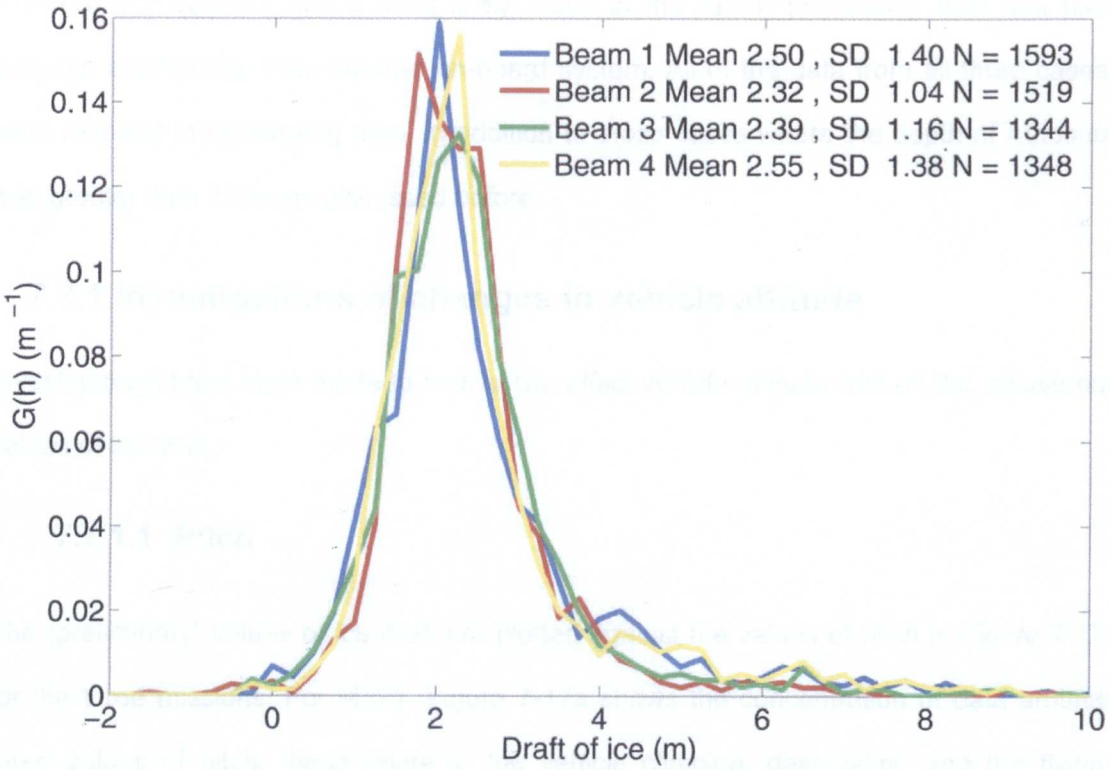

Figure 7-16 Preliminary PDF of ice draft by beam for M321 taking into account offsets between ADCP and attitude sensors. Legend shows mean, SD (standard deviation) of ice draft as well as N (the number of valid measurements for beam 1 (blue), beam 2 (red), beam 3 (green) and beam 4 (yellow).

7.7 Identification and removal of problematic data

This section details the removal of data points from the analysis based on a variety of reasons. Some data were removed because on inspection they were clearly problematic whereas other cases required further investigation. The values that were removed on inspection comprised of the following classes:

1. The value of range from both beam 1 and beam 3 were identical.
2. The value of range from both beam 2 and beam 4 were identical.
3. Single values of range have extreme values that are identified visually (for example, a single value ~tens of metres when all other values are ~2m).

I believe that cases 1 and 2 most likely relate to the ADCP processing data that had acoustic interference from another on-board system. All of the data from all three cases were recoded to be missing data, in addition to those cases where the depth of Autosub was greater than 120m as discussed before.

7.7.1 Investigations of changes in vehicle attitude

Investigations have been made to look at the effect vehicle attitude had on the measured values of ice draft.

7.7.1.1 Pitch

The (preliminary) values of ice draft are plotted against the values of pitch in Figure 7-17 for the three missions. For M321, Figure 7-17a shows the concentration of data around three values of pitch; these relate to the vehicle climbing, descending and the flying attitude of the vehicle. The latter being a small pitch with the nose down to account for Autosub's positive buoyancy. The presence of negative or extreme values of ice draft does not seem to be related to large values of pitch.

For M323 there appear fewer extreme values of draft in Figure 7-17b, although the vertical scale is more exaggerated than for M321. As with M321, I conclude that there is no clear relationship between large values of pitch and estimated values of ice draft.

There are more extreme values of ice draft for M324 in Figure 7-17c and a possible tendency for the two backward-looking beams (2 and 4; red and yellow respectively) to have large negative values of ice draft with a positive pitch. However, as pitch increases this tendency is reduced as the values of negative ice draft become closer to zero. Overall, from this mission, and the other two missions, I conclude that (extreme) pitch does not impact in a regular manner on the values of ice draft. It will not be considered any further. In fact, as will be seen in Section 7.7.1.3, the changes in vehicle depth are far more important and most of the potentially errant values in Figure 7-17 will be removed.

a) M321

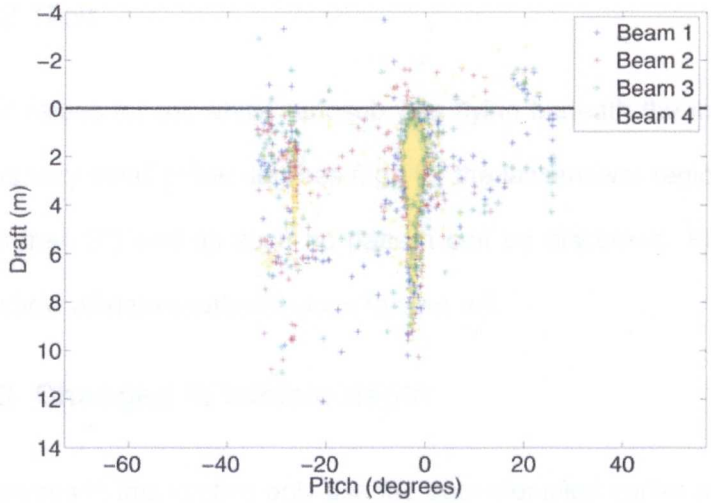

b) M323

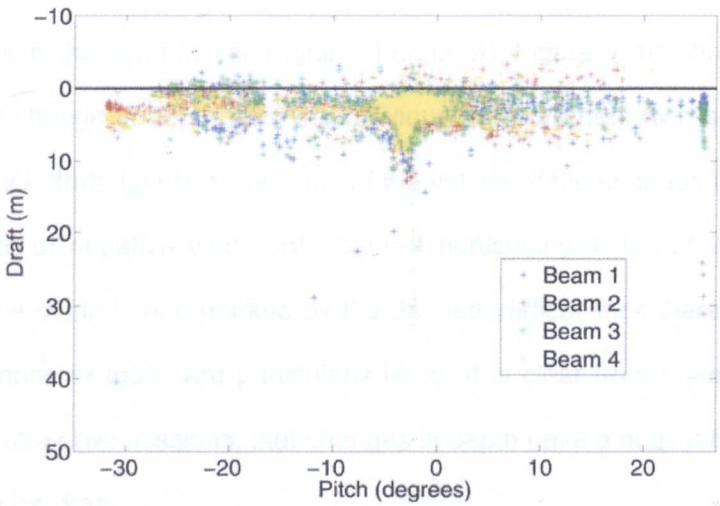

c) M324

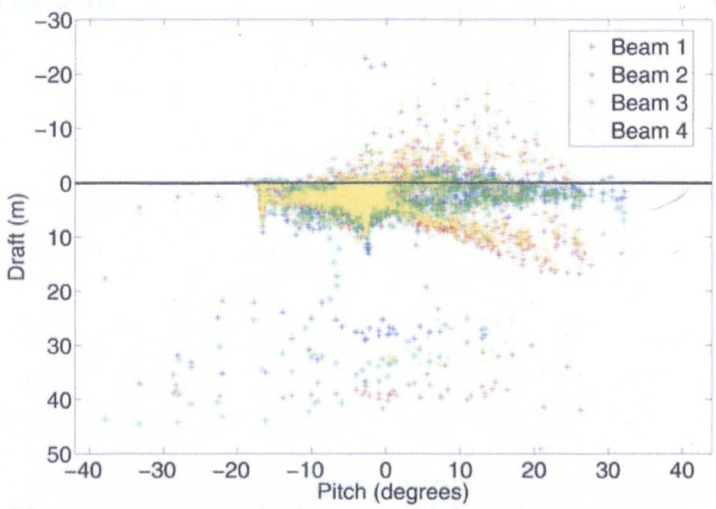

Figure 7-17 Plot showing ice draft (from all four beams) against value of pitch of Autosub (in degrees) from the INS for under ice data cycles for a) M321 b) M323 and c) M324. Note different vertical and horizontal scales.

7.7.1.2 Roll

The range of values for roll whilst Autosub was flying beneath the ice (i.e., the under ice sections) was very small (~few degrees e.g., for the lawnmower region of M321 the mean roll was less than 3°) and as such no pattern can be discerned. Plots similar to Figure 7-17 for roll show all data scattered close to zero roll.

7.7.1.3 Changes in vehicle depth

All of the analyses in this section only use the data identified earlier as being under ice for M321 (i.e., just the lawnmower region). For M321 Figure 7-18 shows the relationship between the change in depth from the previous measurement (two seconds before) and the value of ice draft. Ignoring the signs of the values of the changes in depth, there are a large number of negative values of ice draft particularly at larger values of change in depth. For the central zone marked by the dashed vertical lines there are fewer negative values and none of these are particularly large. It is clear from Figure 7-18, and similar plots for the other two missions, that changes in depth have a noticeable impact on values of measured ice draft.

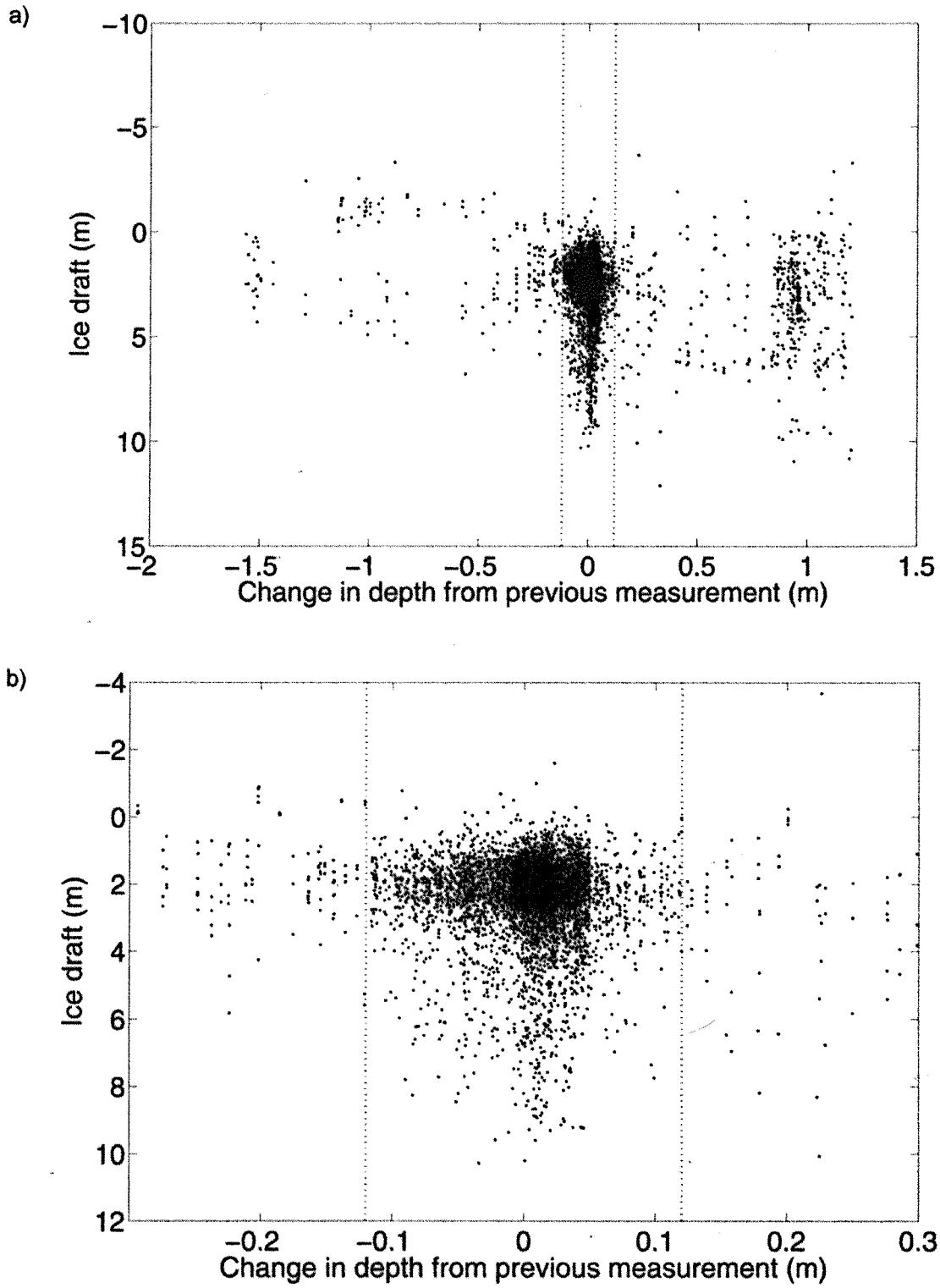

Figure 7-18 Plot of ice draft against the change in depth from the previous measurement for M321 for a) all readings (n=14,096) and b) an enlargement of the values around zero change in depth. The dashed vertical lines show the ±0.12m cut off (see text for further details).

A further plot to help to decide the location of the cut-off values is Figure 7-19, which shows the distributions of depth change (ignoring sign) for all three missions. The break of slope in Figure 7-19 for all three missions is at about 0.12m and this is shown as the dashed vertical lines in Figure 7-18 and Figure 7-19.

For cases where the value of depth was greater or equal to this 0.12m cut-off, all values of ice draft were treated as missing. The number of data values lost is small compared to the total number of observations (from 77% to 87% of data were acceptable depending on mission as detailed in Figure 7-19).

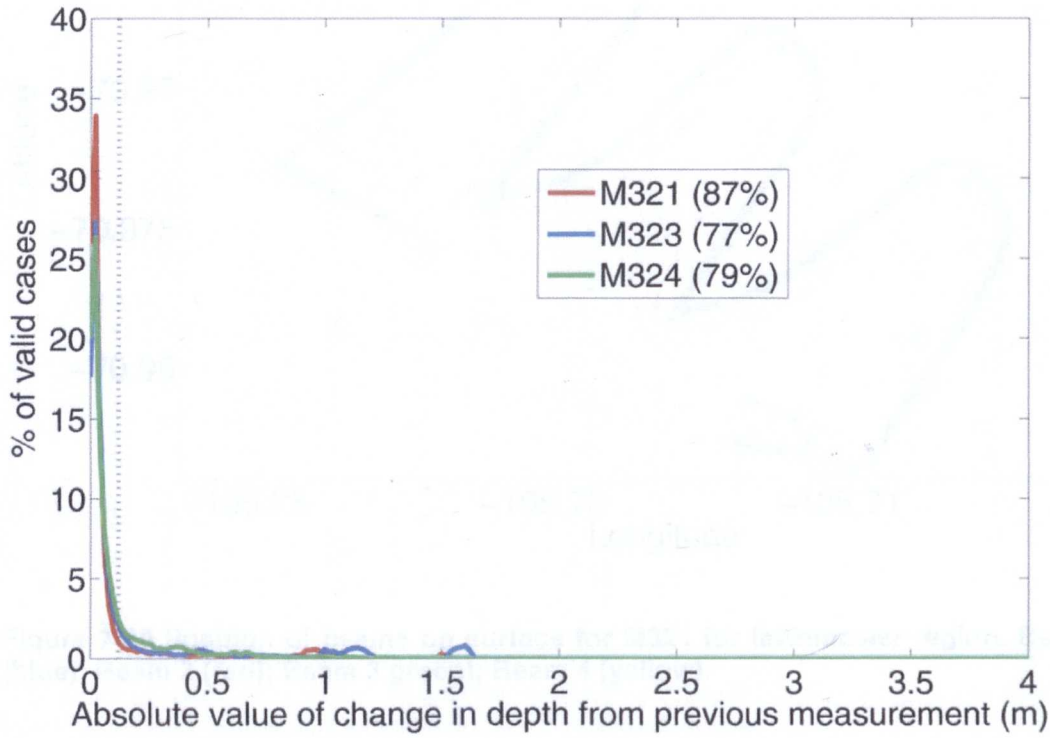

Figure 7-19 Frequency distribution of the absolute change in depth between successive readings for M321, M323 and M324 showing the value of 0.12m as the dotted vertical line (using 2cm bin size). The percentages in parenthesis shows the percentage of cases within the under ice region that have a change in depth ≤0.12m for M321 (red), M323 (blue) and M324 (green).

7.8 Preliminary Results

For all four beams, and for each mission, there are now a series of validated values for ice draft across the three study regions. Figure 7-20 shows the positions of the beams on the

surface of the ocean for M321 and clearly shows how the beams on each side of the vehicle cluster together. The port-beams (2 and 3, red and green respectively) follow a very similar line and the starboard-beams (1 and 4, blue and yellow respectively) follow another track. Only the identified under ice regions are considered in all analyses from now on including Figure 7-20.

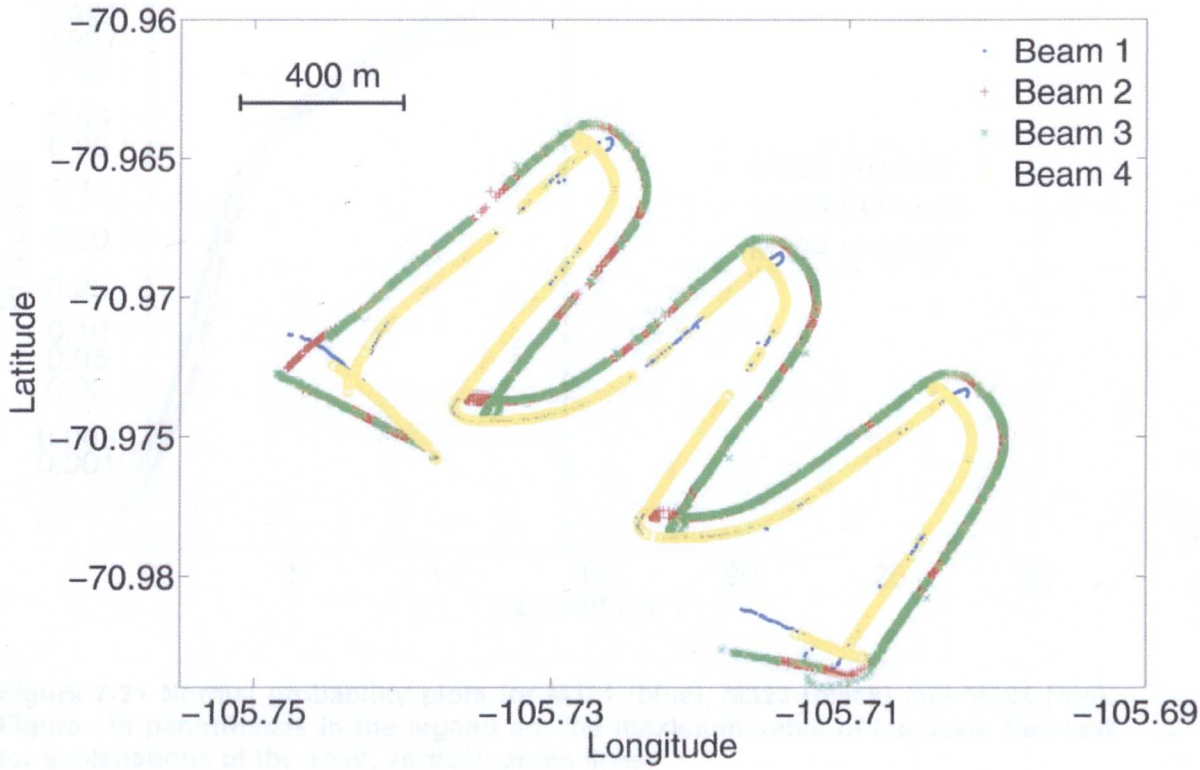

Figure 7-20 Position of beams on surface for M321 for lawnmower region. Beam 1 (blue); Beam 2 (red); Beam 3 green); Beam 4 (yellow).

The descriptive statistics for ice draft for the three missions are given in Table 7-8 below. Two features become apparent when looking at the maxima and minima:

1. a number of values of ice drafts are above the expected value of sea ice draft and these will be considered in Section 7.8.1.

2. there are a number of values with ice draft below zero.

The second case above represents very few cases of ice draft value (~0.1-0.3%) as can be seen in Figure 7-21. In order to produce PDFs for sea ice draft I have used a bin width

of 0.2m with the smallest bin centred on zero and therefore any value of ice draft less than -0.1m has been ignored in the analyses. For this reason, at this stage of the processing all values of ice draft below -0.1m are recoded to missing and this is shown as the left-most, solid, green vertical line in Figure 7-21.

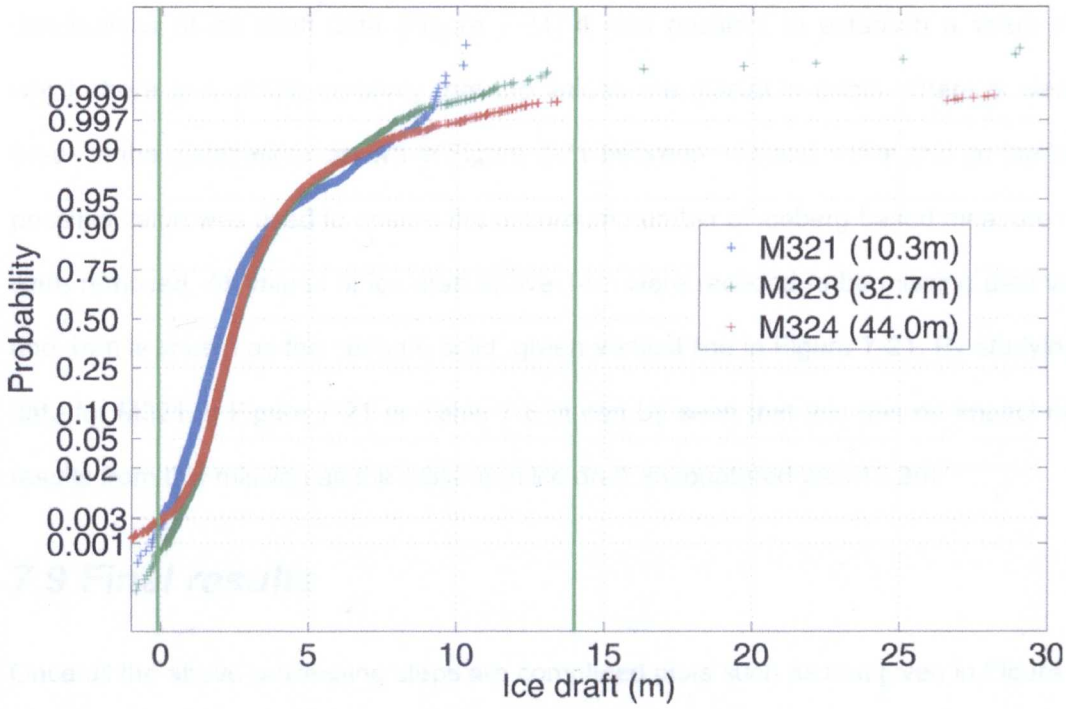

Figure 7-21 Normal probability plots for M321 (blue), M323 (black) and M324 (red). Figures in parentheses in the legend are the maximum value of ice draft. See text for explanations of the solid, vertical, green lines.

Table 7-8 Descriptive statistics for ice draft data including values from icebergs for continuous ice regions. N is the number of observations.

Mission	Mean draft (m)	SD draft (m)	Minimum draft (m)	Maximum draft (m)	N
M321	2.38	1.24	-1.60	10.28	6334
M323	2.77	1.10	-2.89	32.72	26503
M324	2.75	1.56	-22.81	43.99	28700

7.8.1 Removal of iceberg signal

There are a number of records where the ice draft is ~10s of metres and I believe these represent the draft of icebergs. As discussed in Section 2.9, it is not possible to exactly define a cut-off for ice draft to discriminate between sea ice and icebergs. By studying the distributions of ice draft data (Figure 7-21) it was possible to establish a value above which there is a strong certainty that the values are glacial in origin. There is clearly a break in the distributions shown in Figure 7-21 between ~14 and ~16m and so the lowest possible value was used to ensure the maximum number of iceberg based measurements were removed. All values of ice draft above 14m were recoded to be missing data values and 14m is shown as the second, solid, green vertical line in Figure 7-21. By studying the data for M321 in Figure 7-21 or Table 7-8, it can be seen that this has no impact on the results from this mission as the maximum ice draft encountered was 10.3m.

7.9 Final results

Once all the above processing steps are completed plots such as that given in Figure 7-22 can be produced. Figure 7-22 shows a section of 700 data cycles (~23 minutes) from a single beam from M321 and represents the sea ice draft at the start of the continuous sea ice region. Note Figure 7-22 represents the distance that Autosub has travelled and not the location of the beam on the surface.

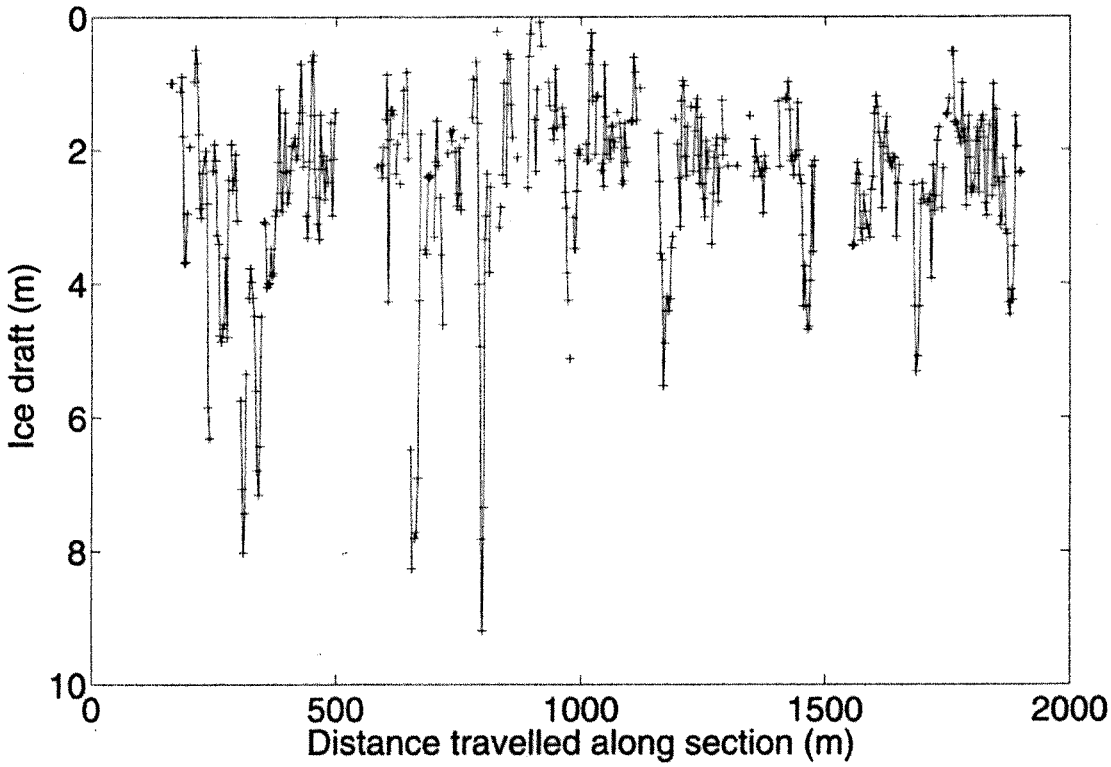

Figure 7-22 Sample profile of sea ice draft from beam 1 (forward/starboard) from start of continuous ice region for M321.

A series of ridges are clearly visible, and drafts are ~9m for the ridge at about 800m along the plotted section. There are also very few values with a draft less than ~1m except for a region ~900m along the profile. The values of ice draft for each mission are summarised in Table 7-9.

Table 7-9 Descriptive statistics for under continuous ice regions of three missions excluding icebergs. N' is the number of cases removed due to draft below –0.1m or above 14m.

Mission	Mean Ice draft (m)	SD of ice draft (m)	Median ice draft (m)	Modal bin of ice draft (m)	Minimum ice draft (m)	Maximum ice draft (m)	Number of observations	N'
M321	2.39	1.23	2.15	1.8	-.07	10.28	6323	11
M323	2.76	1.02	2.58	2.4	-.09	13.04	26478	25
M324	2.72	1.03	2.54	2.4	-.07	13.38	28588	112

Comparing the results of Table 7-8 with Table 7-9 the means for M323 and M324 are lower when data have been removed. The mean for M321 increases slightly as the removed values were all less than -0.1m. Not surprisingly the standard deviations are also smaller for all missions.

The PDFs of ice draft for M321, M323 and M324 are given in Figure 7-23. Only values of ice draft less than 7m are shown, as values above this do not noticeably contribute to the PDFs. All three missions have a single mode suggesting only a single ice type but there is a missing peak for open water (at h=0 m) based on the sea ice observations (Table 7-1). The distributions of M323 and M324 appear very similar, whereas that for M321 has a lower mode and greater spread. These findings can also be seen in the averages (mean, median and mode) and standard deviations in Table 7-9.

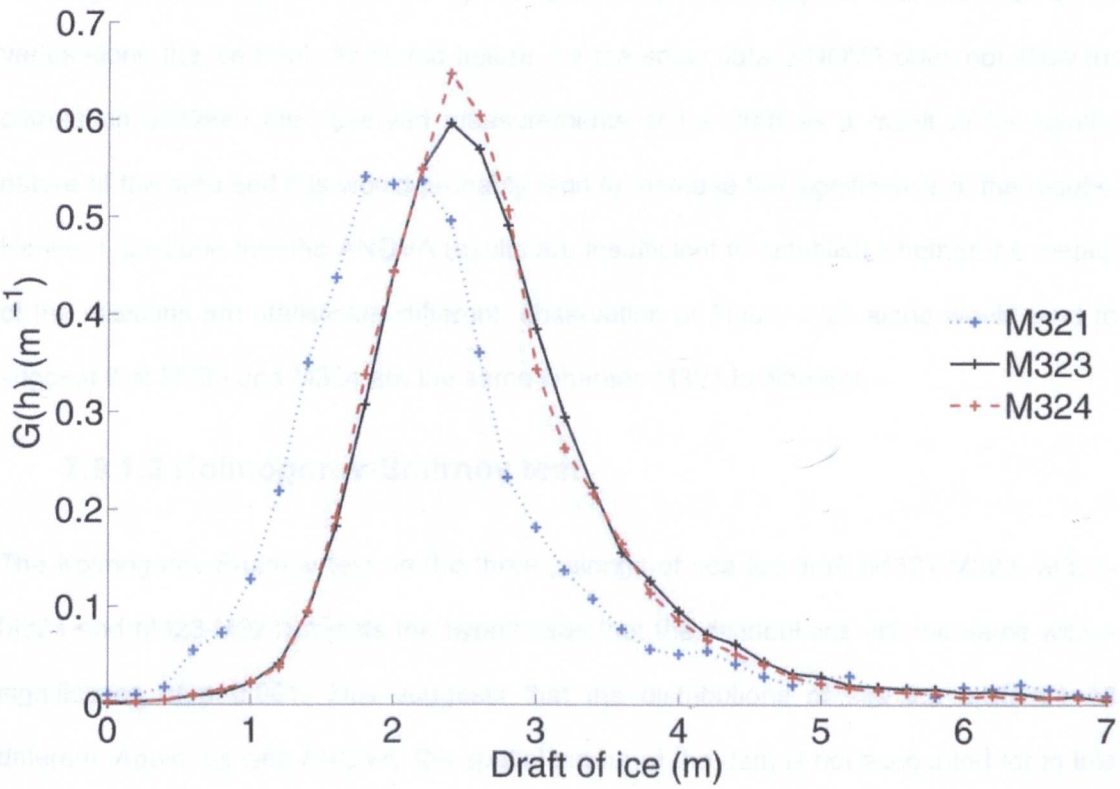

Figure 7-23 PDF of ice draft for M321 (blue), M323 (black) and M324 (red) based on values of draft for under continuous ice regions with icebergs removed.

7.9.1 Comparison of mission distributions

Using the methodology developed in Section 6.5.4 the distributions of the ice draft values from the three missions can be investigated to see if they come from the same population.

7.9.1.1 Analysis of variance

The ANOVA analysis indicates that the values of ice draft for the three missions do not come from a single population ($F=331.1$, sig. < 0.001). Using the *post hoc* tests I have investigated the difference in means between the pairings of the three missions. For both the Scheffé test and the LSD test the significance that the population mean differences are zero are less than 0.001 in all cases. There was only 3 days difference between the periods of data collection and so I assume that the time difference can be considered to be insignificant compared with the spatial difference. This suggests that the draft of ice varies along the ice front. As stated before, for the snow data, ANOVA does not allow for correlation between the observed measurements of ice draft as a result of the spatial nature of the data and this would probably tend to increase the significance of the results. Hence, I conclude that the ANOVA results are insufficient to establish whether the means of the missions are statistically different, observation of Figure 7-23 alone would tend to suggest that M323 and M324 are the same whereas M321 is different.

7.9.1.2 Kolmogorov-Smirnov test

The Kolmogorov-Smirnov test on the three pairings of sea ice draft (M321-M323, M321-M324 and M323-M324) rejects the hypotheses that the distributions are the same with a significance of $p<0.001$. This suggests that the distributions of sea ice draft are all different. Again, as with ANOVA, the spatial nature of the data is not accounted for in this analysis.

7.10 Geostatistical analyses of draft data

As with the snow data in Chapter 6 the sea ice draft data have been analysed using the geostatistical methods described in Section 3.3. In order to readily process the data on a

desktop PC the number of data points has been reduced by only considering the survey grid of parallel transects (the *lawnmower* pattern) and hence comparisons with other distributions are made within this section rather than with the results from the previous sections (i.e., the previous results include all data from the continuous ice zone). Also, cases where the ice draft was less than zero were recoded to missing (this only represents 7 cases across all three missions where the ice draft was between 0m and –0.1m).

As discussed previously (Section 3.3.2), the semi-variograms are more stable when the data have a normal distribution and so the distributions have been tested for normality. Testing the data for normality it became clear that the data were not normally distributed. In order to improve the fit to normality one approach is to remove all extreme values of ice draft. For each mission, all cases where the value of ice draft is greater than 3½ standard deviations above the mean (for that mission) have been deleted. Even after this step all three missions are still non-normal according to the Lilliefors test for normality. However, given the large sample sizes I assume that for the purpose of the geostatistical analyses the distributions approximate to being normal.

7.10.1 Production of KDE based PDFs

As discussed in Section 3.5.6 kernel density estimate (KDE) methods can be used on kriged data using the associated kriging error as the bandwidth. Due to the distributions of the data (i.e., values cannot exist below zero) preliminary studies of the PDFs accounting for the kriging error had a large number of values below zero. To account for this the kriging analyses were re-run transforming the measurements of ice draft (z_d) to y using

$$y = \log_e\left(z_d + 1\right) \tag{7.13}$$

and then transforming the PDF using the Jacobian (Section 3.5.7). All other parameters and setup of the EasyKrig package are kept the same as for the geostatistical analysis of the untransformed measurements. Using an individual value of transformed ice draft (y_i)

and taking the mean kriged value of transformed ice draft and its associated error to be μ_i and σ_i respectively then Equation (3.30) becomes

$$f(y_i) = \frac{1}{\sigma_i \sqrt{2\pi}} \exp\left(-\frac{1}{2} \left(\frac{y_i - \mu_i}{\sigma_i} \right)^2 \right) \quad (7.14).$$

The values of $f(y_i)$ were then calculated for a series of sample values using the kriged, transformed (using Equation (7.13)) sea ice draft data. The PDF of z_d (the untransformed value of ice draft) for a point is given by re-writing Equation 3.35 using Equation (7.14) as

$$f(z_d) = \frac{1}{\sigma_i \sqrt{2\pi}} \exp\left(-\frac{1}{2} \left(\frac{y_i - \mu_i}{\sigma_i} \right)^2 \right) \exp(-y) \quad (7.15).$$

Values of $f(z_d)$ can be calculated using Equation (7.15) and the evaluated sample points of y and $f(y)$ to provide values of the PDF of sea ice data based on the logarithmic transform of the Autosub measurements.

7.10.2 Semi-variograms

7.10.2.1 M321

The semi-variogram model chosen for M321 was a spherical model and is shown with the empirical semi-variogram in Figure 7-24. The model parameters that specify the semi-variogram for M321 are listed in Table 7-10. The resolution for the semi-variogram was the default value of 0.025 and did not require changing to lessen the noise from the data as was required for the snow data in Chapter 6. The modified Cressie goodness of fit test for this semi-variogram for M321 was 0.0005.

Table 7-10 Parameters for spherical semi-variogram model for M321.

Parameter	Value as proportion of total scale (metres in parenthesis)
Sill	0.98 (2674)
Length	0.04 (109)
(Effective) range	0.45 (1228)
Nugget (semi-variance)	0
Resolution	0.025 (68)

The semi-variogram in Figure 7-24 indicates that there is no spatial relationship between points above ~150m apart (i.e., lag >~150m). The effective range was specified to be 0.45 as above this value the semi-variogram has no significant impact (there is essentially no covariance) and the experimental semi-variance above this suggests a possible parabolic effect maybe due to a trend in the data (compare with FS1 in Section 6.5.5.1).

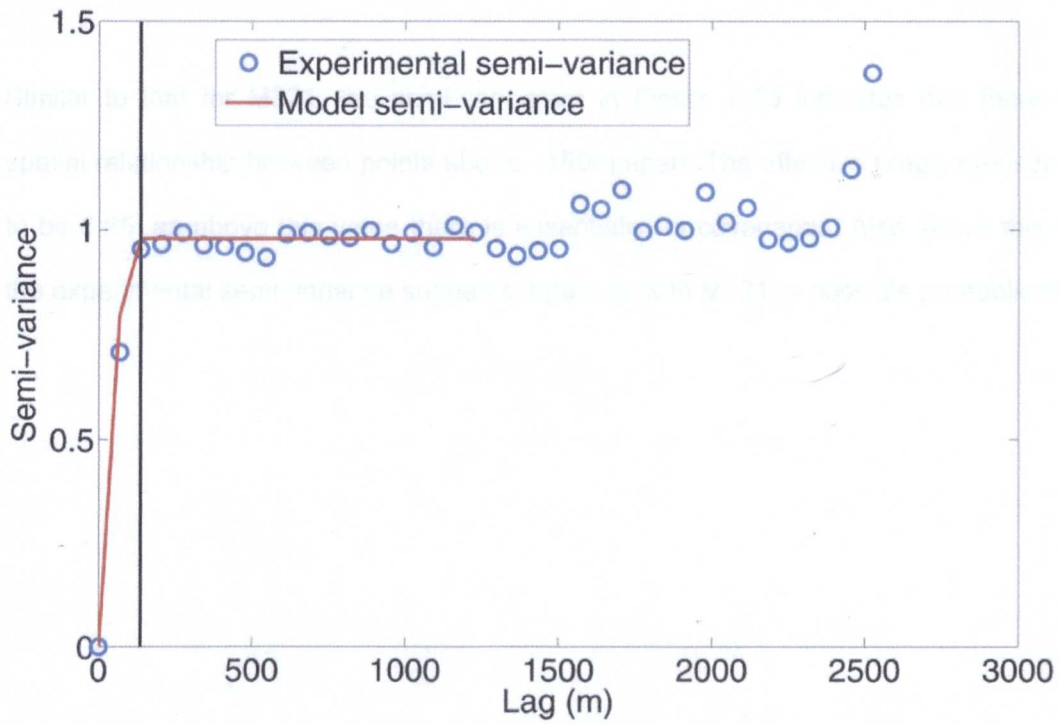

Figure 7-24 Experimental (blue circles) and estimated/modelled (red line) semi-variograms for M321 showing the search radius for kriging as the vertical black line (see Section 7.10.3.2).

7.10.2.2 M323

The model parameters that specify the semi-variogram for M323 are listed in Table 7-11. Unlike M321 the semi-variogram model chosen for M323 was an exponential model and is shown with the empirical semi-variogram in Figure 7-25. The resolution for the semi-variogram was again the default as like M321 this mission did not require changing to lessen the noise from the data. The modified Cressie goodness of fit test for this semi-variogram for M323 was 0.0005.

Table 7-11 Parameters for exponential semi-variogram model for M323.

Parameter	Value as proportion of total scale (metres in parenthesis)
Sill	0.96 (3134)
Length	0.015 (49)
(Effective) range	0.65 (2122)
Nugget (semi-variance)	0
Resolution	0.025 (82)

Similar to that for M321, the semi-variogram in Figure 7-25 indicates that there is no spatial relationship between points above ~150m apart. The effective range was specified to be 0.65, as above this value there is essentially no covariance. Also above this value the experimental semi-variance suggests, again as with M321, a possible parabolic effect.

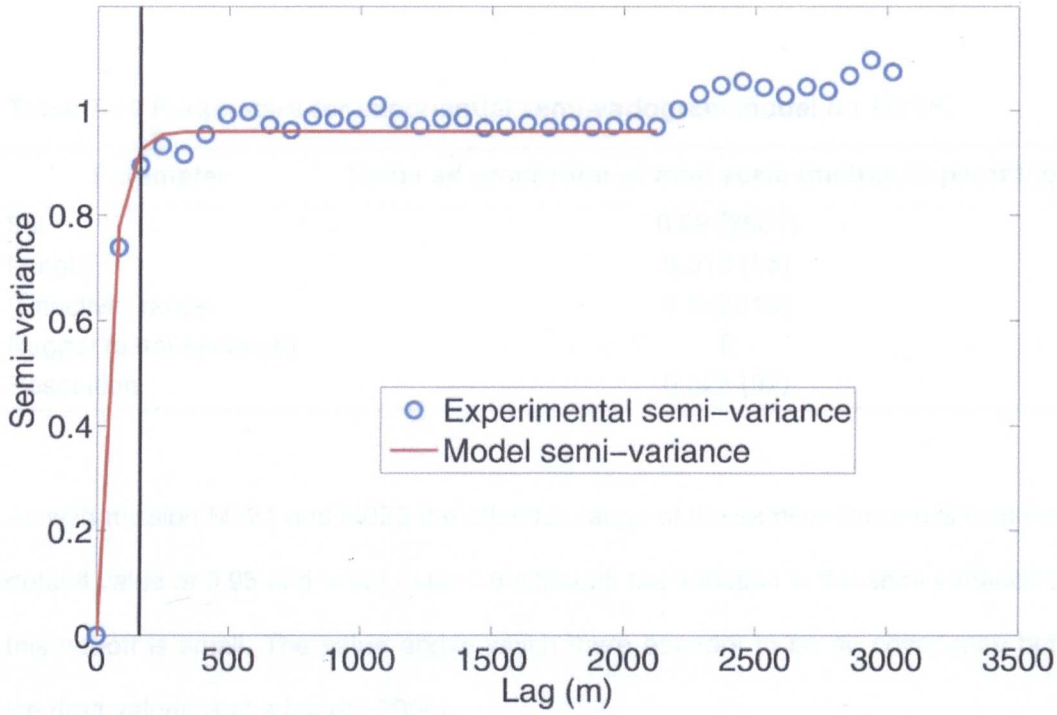

Figure 7-25 Experimental (blue circles) and estimated/modelled (red line) semi-variograms for M323 showing the search radius for kriging as the vertical black line (see Section 7.10.3.2).

7.10.2.3 M324

The semi-variogram model chosen for M324 was again an exponential model and the specifying parameters are listed in Table 7-12. This modelled semi-variogram is plotted, along with the experimental semi-variogram for M324, in Figure 7-26. The modified Cressie goodness of fit test for this semi-variogram for M324 was 0.0002.

Table 7-12 Parameters for exponential semi-variogram model for M324.

Parameter	Value as proportion of total scale (metres in parenthesis)
Sill	0.99 (3661)
Length	0.015 (55)
(Effective) range	0.6 (2219)
Nugget (semi-variance)	0
Resolution	0.025 (92)

As with mission M321 and M323 the effective range of the semi-variogram is less than the default value of 0.95 and is set to be 0.6 although the variation in the semi-variance above this cut-off is small. The value above which there appears to be no covariance between ice draft values is at a lag of ~200m.

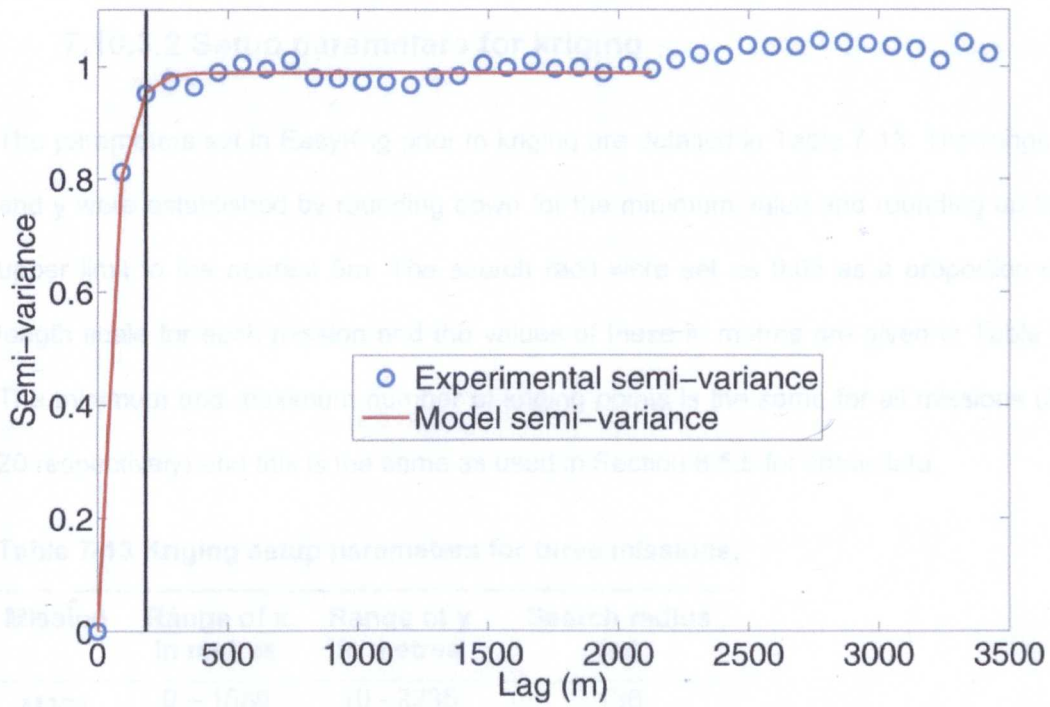

Figure 7-26 Experimental (blue circles) and estimated/modelled (red line) semi-variograms for M324 showing the search radius for kriging as the vertical black line (see Section 7.10.3.2).

7.10.3 Kriged data

7.10.3.1 Impact of grid resolution

A preliminary study of M321 was analysed three times using the same parameters except the resolution of the kriging grid was changed (1m, 2m and 5m). The distributions resulting from these three variations were essentially the same (mean, standard deviation and median the same to 2 decimal places), the only difference being the maximum value decreased slightly as the grid resolution increased (10.82m for 1m resolution to 10.73m for 5m resolution). Given the similarity and the increase in processing time to use a smaller resolution for the kriging grid all the subsequent analyses used a 5m square grid for kriging. For all grids cells EasyKrig calculates a value of ice draft (and error) at every corner (node).

7.10.3.2 Setup parameters for kriging

The parameters set in EasyKrig prior to kriging are detailed in Table 7-13. The range for x and y were established by rounding down for the minimum value and rounding up for the upper limit to the nearest 5m. The search radii were set as 0.05 as a proportion of the length scale for each mission and the values of these in metres are given in Table 7-13. The minimum and maximum number of kriging points is the same for all missions (5 and 20 respectively) and this is the same as used in Section 6.5.5 for snow data.

Table 7-13 Kriging setup parameters for three missions.

Mission	Range of x in metres	Range of y in metres	Search radius (m)
M321	0 – 1580	10 - 2235	136
M323	0 – 1025	0 – 3100	163
M324	605 – 1800	0 - 3500	185

7.10.3.3 Results of kriging

Table 7-14 presents the descriptive statistics for the three missions before and after kriging and shows how the mean ice draft is reduced by the kriging process in all three missions. The same cannot be said of the median values; for M321 the median ice draft of the raw data is 2.13m whereas for the kriged values it is 1.91m. For M323 the ice draft medians of the raw and kriged data are very similar with values of 2.47m and 2.48m respectively. Like M321 the median ice draft for M324 is less for the kriged values than for the raw values (2.50m cf. 2.45m). The ranges of ice draft values encountered are similar for the raw data but this is not surprising as cases below zero have been deleted as have cases more than 3.5 times the standard deviation above the mean. The maximum kriged value of ice draft for M323 is 6.64m (larger than the raw value) and that for M324 is 6.23m (smaller than the raw value). It is surprising that the maximum ice draft value for M321 increase from 6.65m for the raw data to 10m for the kriged value although the number of cases is limited and this is emphasised by the standard deviation remaining unchanged at 1.01m. The standard deviations for M323 and M324 do not remain constant and are both lower for the kriged values than for the original measurements.

Table 7-14 Summary descriptives for pre and post kriging values of sea ice draft for the three missions.

Mission	Mean ice draft (m)		SD of ice draft (m)		Median ice draft (m)		Min ice draft Max ice draft (m)		Modal bin (m)	
	Raw	Kriged	Raw	Kriged	Raw	Kriged	Raw	Kriged	Raw	Kriged
M321	2.30	2.10	1.01	1.01	2.13	1.91	0.03 6.65	0 10	1.8 (1.7–1.9)	1.8 (1.7–1.9)
M323	2.60	2.55	0.84	0.66	2.47	2.48	0.02 6.33	0.33 6.64	2.4 (2.3–2.5)	2.4 (2.3–2.5)
M324	2.62	2.53	0.81	0.58	2.50	2.45	0 6.32	0.47 6.23	2.4 (2.3–2.5)	2.4 (2.3–2.5)

Figure 7-27 shows the PDFs for the M321 lawnmower region both before and after kriging and suggests that the distributions are generally similar in shape. There are a number of

additional peaks in the distribution of kriged values compared to the raw data; probably as a result of the kriging process using the same data points to produce multiple values in regions where measurements were sparse.

Figure 7-28 and Figure 7-29 show the PDFs for M323 and M324 for ice draft values before and after kriging and show similar features for both missions. For M321, M323 and M324 the kriged values of ice draft have a higher central peak (mode) compared to the raw data, to allow for this the extremes represent fewer data. Notice that for both M323 and M324 there are very few cases where the sea ice draft is less than ~1m compared to M321, this will be discussed in Section 7.11.2.

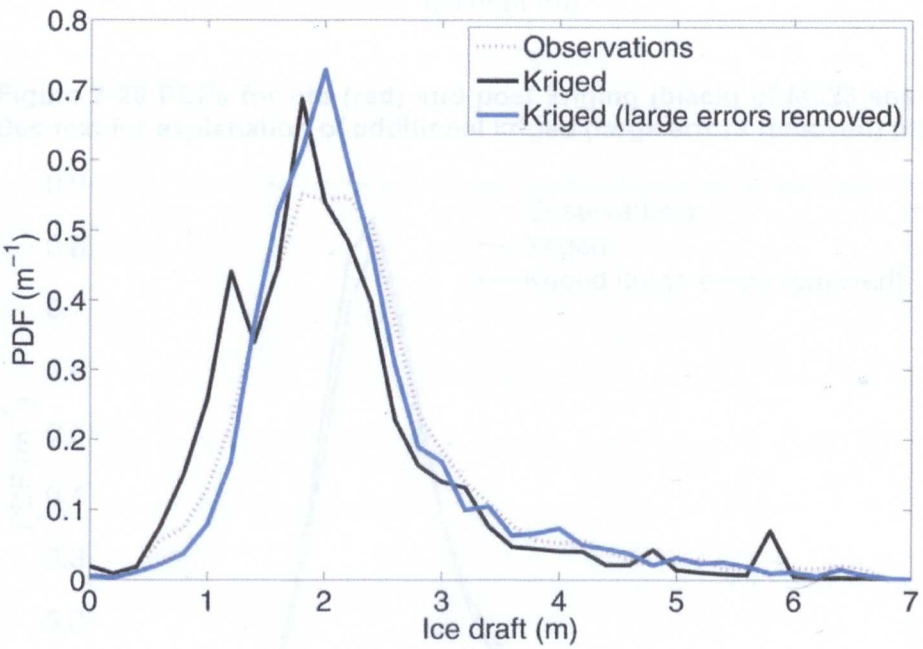

Figure 7-27 PDFs for pre (red) and post kriging (black) of M321 sea ice draft data. See text for explanation of additional kriged (large errors removed) plot.

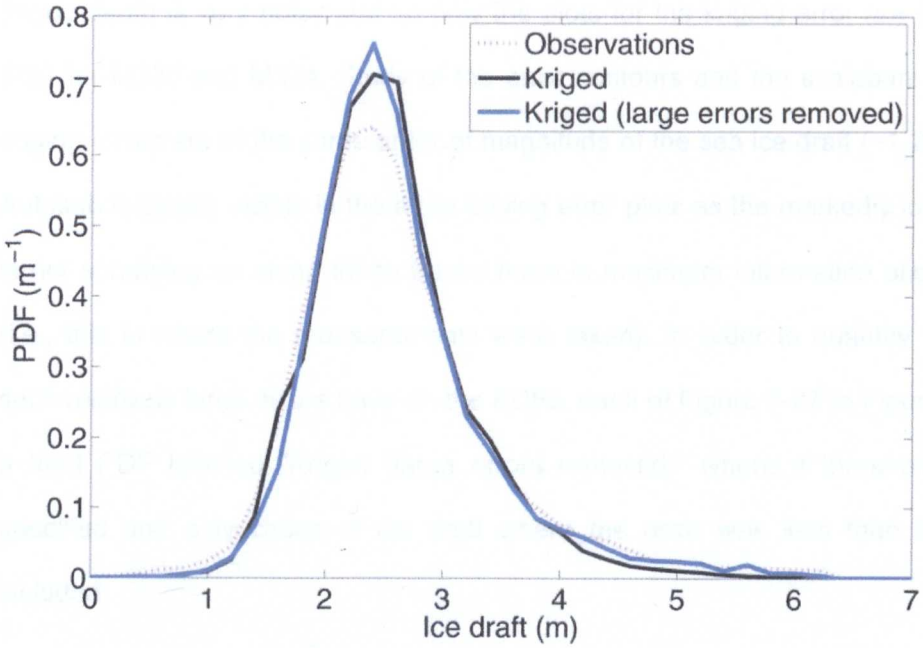

Figure 7-28 PDFs for pre (red) and post kriging (black) of M323 sea ice draft data. See text for explanation of additional kriged (large errors removed) plot.

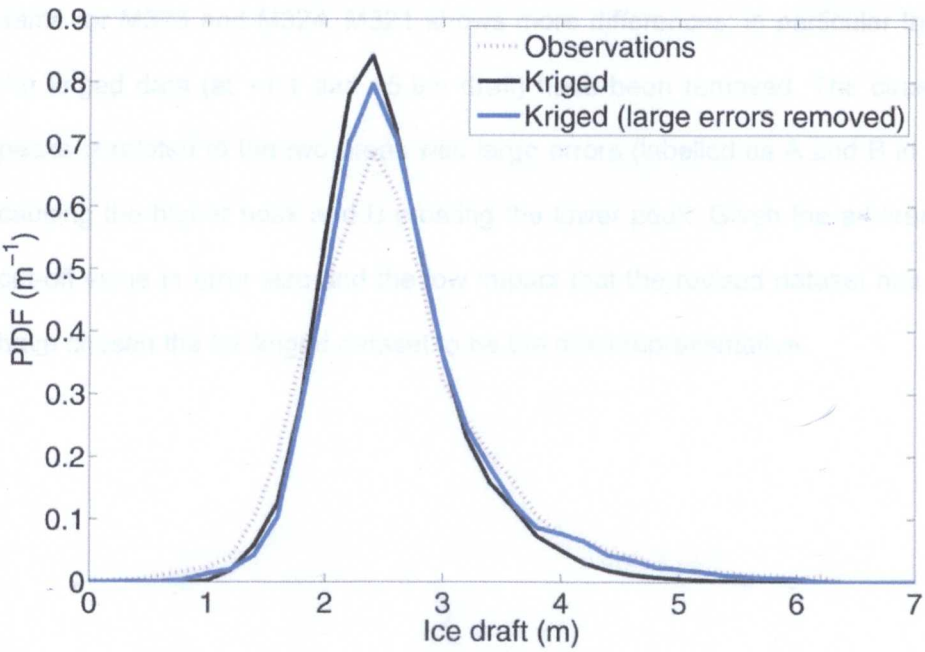

Figure 7-29 PDFs for pre (red) and post kriging (black) of M324 sea ice draft data. See text for explanation of additional kriged (large errors removed) plot.

As discussed in Section 3.3.4 an advantage of using kriging is that with each estimated value of ice draft there is an associated confidence interval. Contour plots of the kriged depth and the associated kriging error for M321 are given in Figure 7-30. The contour of

kriged depth is very noisy and so only the plots for the kriging error are shown in Figure 7-31 for M323 and M324. Study of the error contours and the scalebars shows that the kriging errors are of the same order of magnitude of the sea ice draft (~1-2m). The path of Autosub is clearly visible in the three kriging error plots as the markedly lower values; this is not surprising as along these tracks there is maximum information about the ice draft (i.e., this is where the measurements were taken). In order to quantify the impact that such relatively large errors have on the PDFs, each of Figure 7-27 to Figure 7-29 includes a third PDF labelled "Kriged (large errors removed)" where a threshold of 0.5m was specified and only cases of ice draft where the error was less than this value were included.

The results of the above process are perhaps not surprising in that the results lie between the raw data and the kriged data with the shape of the distributions being essentially the same for M323 and M324. M321 shows more differences; in particular the two spikes in the kriged data (at ~1.1 and ~5.9m draft) have been removed. The cause of these two peaks is related to the two areas with large errors (labelled as A and B in Figure 7-30), A causing the higher peak and B creating the lower peak. Given the arbitrary choice of the cut-off value in error size and the low impact that the revised dataset has on the PDFs, I have chosen the full kriged dataset to be the most representative.

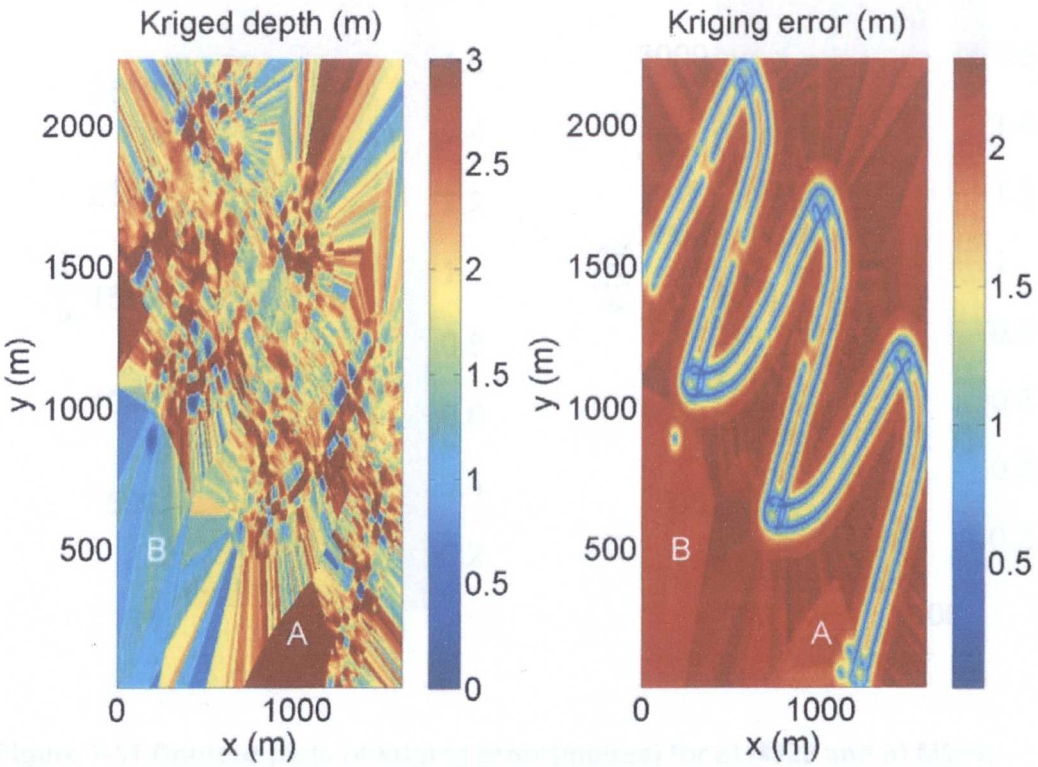

Figure 7-30 Contour plot of kriged ice draft (metres) and associated kriging error (metres) for M321. See text for explanation of regions labelled as 'A' and 'B'.

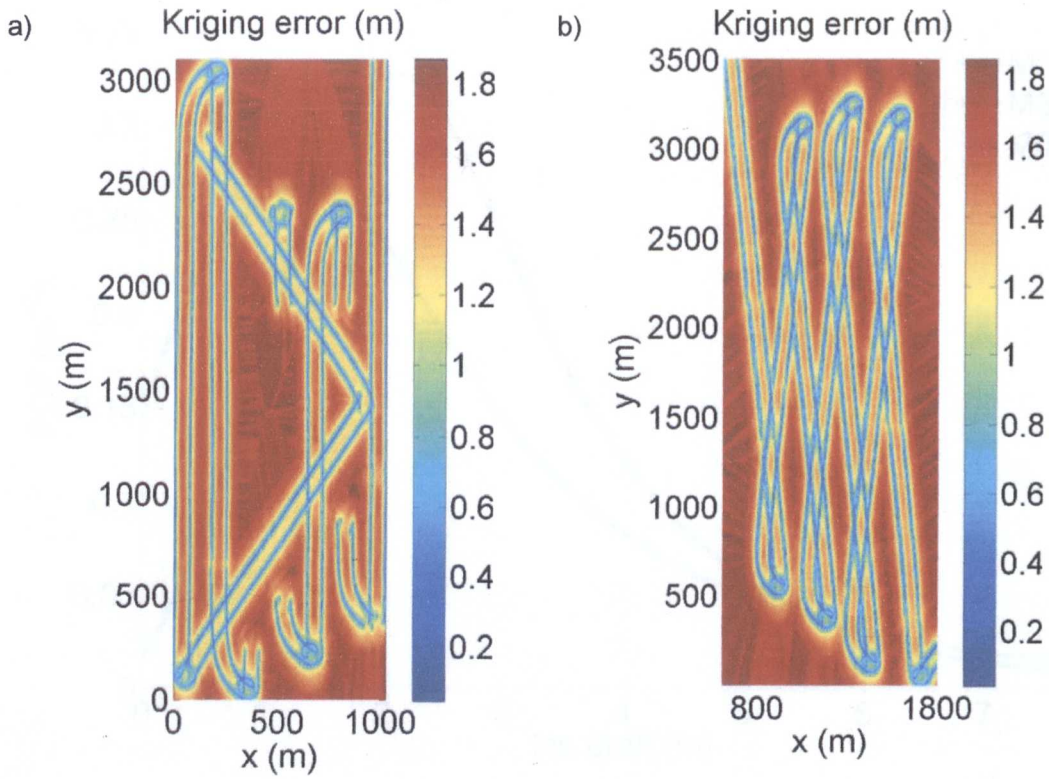

Figure 7-31 Contour plots of kriging error (metres) for a) M323 and b) M324.

7.10.3.4 Comparison of kriged sea ice draft distributions

With the aim of using the kernel density estimation (KDE) technique discussed in Section 7.10.1 and without the large number of negative values (i.e., draft<1m) the kriging for all three missions have been re-run based on the values of $\log_e$(ice draft +1). The PDFs for the sea ice draft, taking into account the kriging error calculated using Equation (7.15), are shown in Figure 7-32.

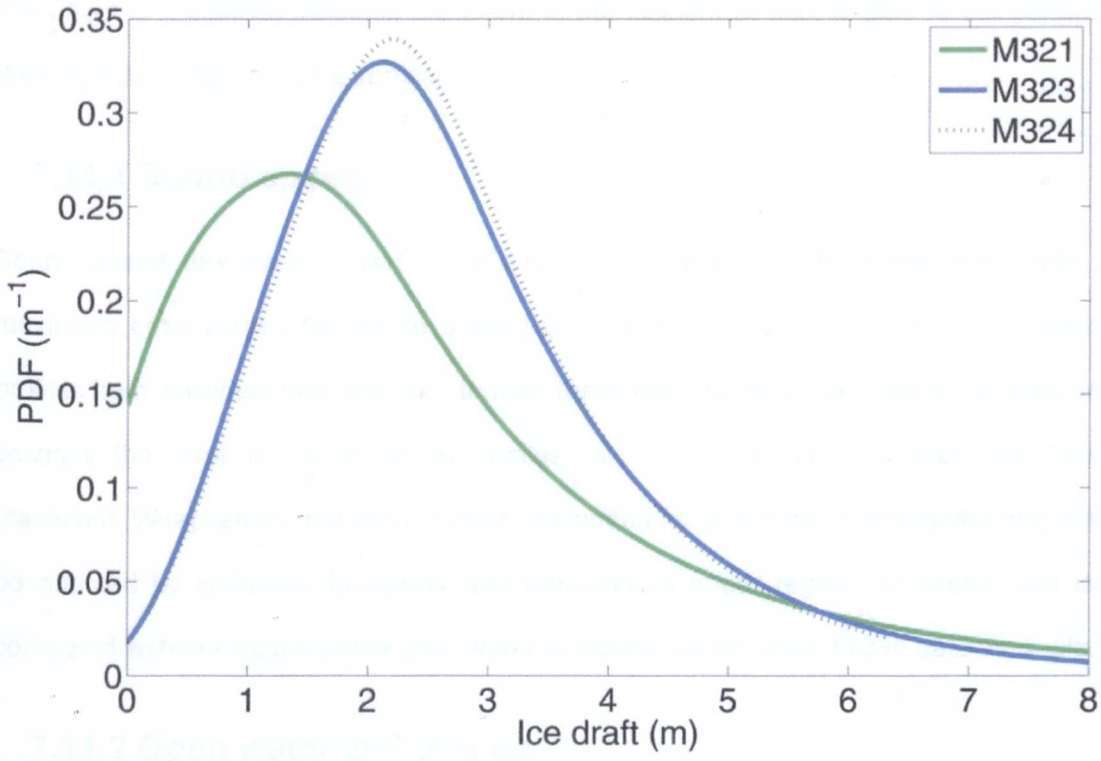

Figure 7-32 KDE of kriged sea ice PDFs for three missions – M321 (green), M323 (blue) and M324 (black).

It is clear from Figure 7-32 that M323 and M324 have the same distribution of sea ice draft; the same cannot be said of M321. The other notable feature of Figure 7-32 is that M321 has a much larger proportion of thinner ice than the other two distributions.

7.11 Summary

The aim of this chapter was to provide PDFs for sea ice draft in the study region based on three Autosub missions. Geostatistical analyses have been performed to ensure that the PDFs incorporate the spatial nature of the sampling (i.e., points close together are more correlated than those further apart). All three PDFs (Figure 7-27 to Figure 7-29) have a single mode suggesting a single ice type although it is likely that the footprint of the ADCP has smoothed out the results to only show the maximum ice draft within the footprint. Depth is a critical factor in the methodology, not just because it impacts on the strength of the returned signal. As depth increases, the area insonified by the beam increases and

this effect is enhanced because the beam is not incident at right-angles to the surface: there is a 30° offset from the vertical.

7.11.1 Sound speed

Sound speed has been shown to be a significant factor on the travel times with a maximum error across the whole study region of ~10cm. By using the sound speed profiles from individual missions and deriving these from the averaged descent and ascent sections the error in sound speed profiles will be significantly less than the 10cm maximum. What cannot and has not been accounted for is that the sound speed may well be affected by variations in salinity and temperature under regions of thicker sea ice compared with the values within open water or thinner ice for which I have data available.

7.11.2 Open water and thin ice

The most significant problem with the current dataset is the lack of returns from open water (see Section 7.5.5). The proportions of open water for each mission can be assessed using the ASPeCt observations and this will be discussed in Section 7.11.5. The PDFs for the three missions shown in Figure 7-32 show a substantial proportion of open water for M321. However, this is as a result of incorporating the kriging errors rather than data from Autosub indicating any open water. In addition there are limited amounts of thin ice in M323/M324 compared to that for M321, which may be because there was less thin ice in the east of the study region or it may be because the ADCP return is based on the thickest ice within the footprint.

The most important reason why the lack of open water is problematic is because it is not possible to verify the vehicle's depth using the range to (open water) surface. In addition, if it were possible to "zero" the readings of range then more accurate values of the ADCP and CTD offsets could be made (both the differences in attitude and location).

7.11.3 Comparison of means

Comparisons of the means and distributions of the three missions have been performed on the raw data. Given the clearly similar distributions of M323 and M324 in Figure 7-32 (see Section 7.11.4.1) and the different distribution of M321, I do not feel this is necessary for the kriged data. I surmise that the differences between M321 and the other missions are spatial and not temporal as there were only 3 days between the timings of all the missions (i.e., the ice draft varies along the ice front).

As with the analysis of the distributions of snow depths in Section 6.5.4, the comparison of the three missions are complicated by the spatial (i.e., correlated) nature of the data within each mission. In addition, the comparison of groups of observations is potentially more difficult if data are skewed as variances differ significantly between groups (Webster and Oliver, 2001).

ANOVA methods indicate that the three missions do not come from the same population ($F=331.1$, significance < 0.001) and *post hoc* tests indicate that all three missions are distinct. These ANOVA results do not take into account the spatial nature of the within group (i.e., mission) variability and so there is insufficient evidence to reject or accept the hypothesis that the means of the three missions are the same. The same conclusions are drawn from the Kolmogorov-Smirnov test that the distributions are not the same but the spatial correlation of the within mission data means that the rejection of the hypothesis that the distributions are the same is complicated.

7.11.4 Kriging issues

It may be more appropriate to use a logarithmic conversion of the measured ice draft and use this transformed values in the kriging process. However, it is not possible to produce unbiased estimates of the (ordinary) kriging variance (and hence kriging error) using logarithms of the observations (Webster and Oliver, 2001). For this reason, the kernel density estimation process does not back-transform the values used but uses the method

from Section 7.10.1 to convert the PDF of transformed ice draft to the PDF of sea ice draft that is desired.

7.11.4.1 KDE values

The PDFs in Figure 7-32 clearly show that the regions of M323 and M324 have the same distribution of sea ice draft as measured from Autosub. These distributions take into account the spatial distribution of the sampling locations. M321 does not have the same distribution with a lower mode and more values at both ends of the distribution, in particular the lower (thinner ice) end, compared to the other two missions, hence a higher standard deviation as can be seen in Table 7-14. Again I conclude that the sea ice PDF for M321 is distinct from those from M323/M324.

7.11.5 Comparison of sea ice observations and Autosub measurements

The ASPeCt sea ice observations (Worby, 1999) allow estimates of the open water proportions for each of the missions. The locations of the sea observations can be seen in Figure 7-1 and a closer examination shows that two of the stations are coincident with the survey areas from Autosub. There is one coincident set from M321 and another for M323, although this is not within the *lawnmower* region of the study area. For this reason only the results from M321 will be considered except for estimates of open water proportions.

For M321 the closest observation was at 70°58' S, 105°44' W and indicated 60% ice cover with open water of type 5 in the ASPeCt terminology (very wide breaks >500m), the summary of these observations are given in Table 7-15. The average ice thickness from this station (for the ice covered area) was estimated to be 1.19m with a snow depth of 40cm giving an overall thickness of 1.59m. The mean combined snow and ice thickness for the ridged area was 2.59m and this will be compared with an estimate from Autosub measurements in Section 8.4. The reason for using this mean is because the Autosub

measurements do not include open water and so is more appropriate than the total area value.

Table 7-15 Results of sea ice observations from the single station within M321 study region output from ASPeCt software (70°58' S, 105°44' W).

Total ice concentration	60.00%
Open water within pack	40.00%
Av level ice thickness (total area) cm	90.00
Av level ice thickness (ice area) cm	150.00
Fraction of surface area ridged	0.20
Av ridged ice thickness (total area) cm	119.15
Av ridged ice thickness (ice area) cm	198.58
Av snow thickness (total area) cm	24.00
Av snow thickness (ice area) cm	40.00
Av snow thickness (snow covered area) cm	60.00
Snow covered ice within pack (total area)	40.00
Snow free ice within pack (total area)	20.00
Percent ice with snow cover	66.67%
Percent ice with no snow	33.33%
Av albedo (total area)	0.48

For M323 and M324 the nearest ship-based observation of ice concentration was 100% ice cover (with only small cracks of open water) whereas for M321 the closest observation was only 60% ice cover. As such the PDFs of sea ice draft for M323 and M324 probably reflect the true PDFs as there is probably no open water present whereas for M321 there is a significant amount of missing data (perhaps 40%).

For the whole region from the observations in Table 7-1, the average ice thickness for the ice covered region was 1.12m with a mean snow covering of 27cm giving an overall thickness of 1.39m. This is thinner than that expected from the Autosub data from M323/M324 where the modes of just ice draft are ~2.5m and for M321 that was ~1.5m. It is worth noting that the mean combined snow and ice thickness for ridged ice was found to be 2.18m from the observations. These values will be considered further in Section 8.4.

Chapter 8 Conclusions and discussion

In this final chapter, I shall review the work detailed in the previous chapters and make comparisons of my results with those from other sources. In addition, I will make recommendations for future work.

The research questions posed as the start of this thesis were as follows:

1. Produce a series of PDFs and descriptive statistics for sea ice draft using measurements from Autosub. This is the key question within this thesis for the reasons above.
2. Provide a geostatistical analysis of the data from 1. This ensures that the spatial nature of the sampling is accounted for and provides revised PDFs.
3. Investigate the variability of snow depth on sampled floes because in order to convert sea ice draft to thickness knowledge of the snow depth is required.
4. Compare the distributions from 1 and 2 above with ship-based observations and direct measurements of snow and ice thickness. This question is concerned with validating the novel methodology described in this thesis.
5. Investigate the likely impact of the spatial distribution of icebergs (whether they cluster or not) on measurements of ice draft from ULS or similar methods (e.g., using Autosub as described in Research Question 1 above). Icebergs generally have a larger draft than sea ice and so a cluster of icebergs would increase the average measured sea ice draft where no other means exist for discriminating between icebergs and sea ice.

The research questions will be discussed individually with reference to the original images and Autosub missions followed by a more general discussion in Section 8.6 onwards.

8.1 Research Question 1

In Chapter 7 I successfully developed a methodology using the Autosub upward-looking ADCP to provide measurements of the ice draft above the vehicle. Using the best estimate of the cut-off between the distributions of sea ice and iceberg drafts (at 14m) M321 has a mean ice draft of 2.39±1.23m (±1 standard deviation) compared to the slightly higher means of 2.76±1.02m and 2.72±1.03m for M323 and M324 respectively. The distributions are unimodal but do not include any measurements of open water. As shown in Chapter 7, the AUV was deeper than the maximum range over which the ADCP system can detect open water.

Using a variety of statistical methods the means and distributions of ice draft from the three missions have been tested to see if they are from the same population. All the statistical tests indicate that the missions do not come from the same population and that the differences are between all the possible mission pairings. However, as discussed in Section 7.9.1, these conclusions do not account for the spatial correlation between measurements within each mission and this may well explain the rejection of the hypothesis that the means of M323 and M324 are the same in spite of their obvious similarity in the PDFs (Figure 7-23).

8.2 Research Question 2

Geostatistical approaches have not been widely used within similar studies of sea ice draft/thickness: previous researchers have assumed using appropriate sample sizes that the mean draft/thickness approaches that of the population mean. I have used the technique of ordinary kriging to investigate the impact of the spatial sampling pattern on the distribution of sea ice draft within the study regions from three Autosub missions. The study regions are different (i.e., smaller) than those discussed in Section 8.1 to ensure there are adequate measurements across the kriging study regions.

For each mission, a model for the observed semi-variance has been used to provide the basis for the kriging analysis. Both M323 and M324 used an exponential semi-variogram model and the associated parameters were similar, suggesting that the ice draft in both regions varies spatially in a similar manner in the two areas. The analysis of M321 relied on a different (spherical) model and as such can be seen to vary differently compared to M323/M324.

The mean (±1 standard deviation) ice drafts for the three missions based on kriging were discussed in Chapter 7. These means and standard deviations were 2.10±1.01m, 2.55±0.66m and 2.53±0.58m for M321, M323 and M324 respectively. These are all smaller than the raw values of sea ice draft for the same regions, which were 2.30±1.01m, 2.60±0.84m and 2.62±0.81m (as noted above these relate to different regions from those described in Section 8.1). The standard deviations of the kriged data are also smaller as I showed in Chapter 7.

For any kriged estimate of sea ice draft there is an associated uncertainty in the value obtained – the so called kriging error. This error has been accounted for in the sea ice draft PDFs shown in Chapter 7, using kernel density estimates (KDE) from each node with the size of the kriging confidence interval as the bandwidth (i.e., a large error would impact over a wider range of ice draft values compared to a smaller error). Using KDE techniques the sea ice draft PDFs from the geostatistical analyses for the three missions have been calculated and are shown again in Figure 8-1. The KDE methodology means that the PDFs are relatively smooth in Figure 8-1.

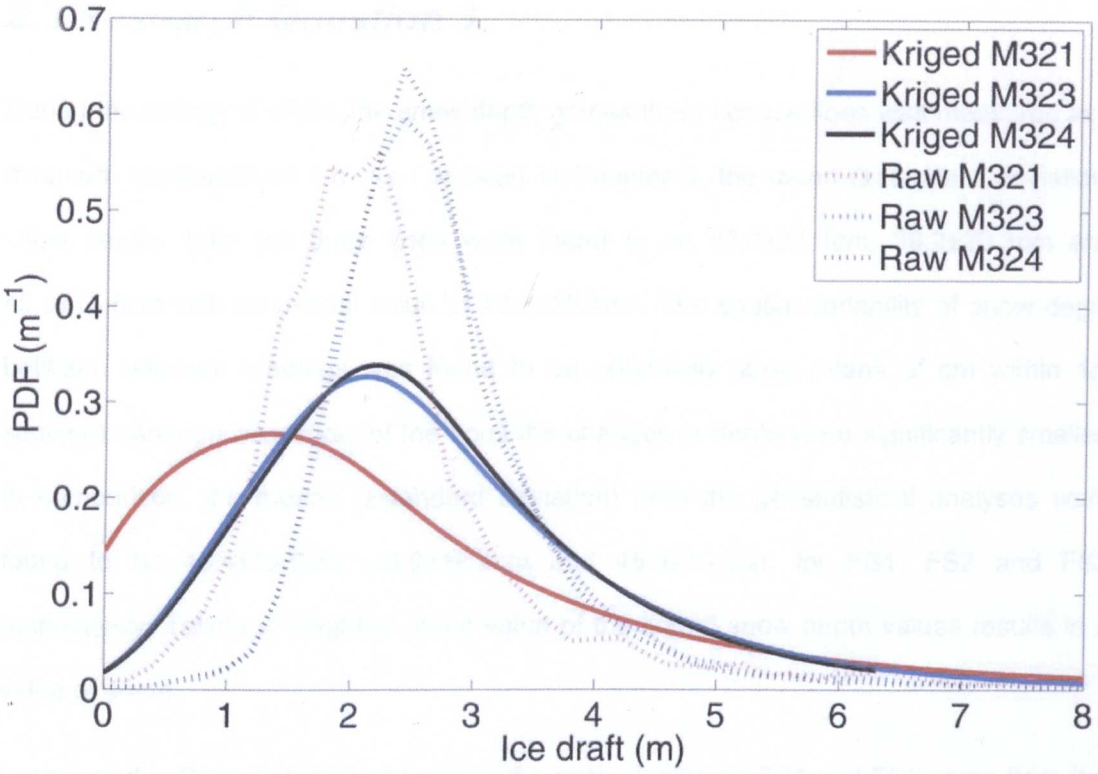

Figure 8-1 Sea ice draft PDFS for three Autosub under ice missions (solid lines) incorporating estimates of kriging error and comparison with PDFs from raw measurements (dotted lines).

It is clear from the kriged data in Figure 8-1 that M323 and M324 have the same distribution of ice draft as the modes and shapes of the PDFs for these two missions are almost identical with modes at ~2.1m. M321 in comparison has a noticeably smaller mode and the distribution is skewed towards zero and includes a substantial proportion of open water. However, this open water is as a result of uncertainties in the kriging process and not from observations.

The PDFs for the unkriged sea ice draft values for the three kriging study regions are also shown in Figure 8-1 to allow for comparison with the results from kriging. Using the kriging errors in the KDE method clearly results in a flatter, wider distribution of ice draft compared to the measurements. The modes for all three missions also decrease following the kriging analysis although the coincidence of the modes for M323 and M324 remains. Overall, it is clear that the region around M321 represents a region of thinner sea ice compared to the region around M323/M324.

8.3 Research Question 3

During the course of JR84, the snow depth across three sea ice floes was measured at a minimum separation of 1m. As I showed in Chapter 6, the mean (±standard deviation) snow depths from the three floes were found to be 47.4±21.1cm, 39.2±20.3cm and 45.3±15.6cm with an overall value of 43.8±19.4cm. The spatial variability of snow depth between adjacent readings was found to be potentially large (~tens of cm within 1m spacing) although over most of the floes the changes in depth were significantly smaller. In comparison, the means (±standard deviation) from the geostatistical analyses were found to be 45.4±12.9cm, 40.9±18.4cm and 45.5±13.0cm for FS1, FS2 and FS3 respectively. Taking a weighted mean value of the kriged snow depth values results in a value of 44cm.

I concluded in Chapter 6 that statistically the snow depths on FS1 and FS3 came from the same population. However, the distribution of snow depths from FS2 is different in a number of ways from the other floes (i.e., significantly different mean and distribution from other two floes and data were not normal). It is not possible using the available dataset to establish whether sampling more floes would result in the identification of two or more snow depth regimes. Also, it is feasible, that a more rigorous sampling of FS2 would have resulted in similar results to the other two floes as the sampling in the x direction of FS2 had a number of spacings that were greater than 1m (see Figure 6-4). I conclude that the most likely explanation for the difference in snow depths on FS2 is due to the underlying difference in the sea ice structure and the best estimate of the mean snow depth is the kriged, weighted mean of 44cm.

8.4 Research Question 4

From Table 7-1 the ship-based observations of sea ice thickness, excluding open water to allow comparison with the values from Autosub, suggest a mean ice thickness of 1.12m covered with an average 27cm of snow (i.e., total thickness of 1.39m). The mean thickness of snow and ice of the ridged regions was found to be 2.18m. These results

cover the entire JR84 sea ice study region (as defined in Figure 7-1) with 14 observations. Only one observation station overlaps with an Autosub mission and that is for M321, as detailed in Table 7-15. This had a mean ice thickness of 1.19m and combined snow and ice thickness of 1.59m. For the ridged regions the combined snow and ice thickness was found to be 2.59m.

The thickness of sea ice for each of the sampled floes has been estimated from the thickness of snow using the approximation in Equation (6.1). I calculated a weighted mean of the combined ice and snow thickness for all three floes using this equation as 1.90m. However, this value is based on the raw observations and it is more appropriate to use the kriged values of snow depth because these take account of the spatial nature of the sampling. The values of total sea ice and snow thickness estimated from the kriged snow depth values are 1.96m, 1.77m and 1.98m for FS1, FS2 and FS3 respectively. I have used the 44cm value of weighted snow depth to calculate a combined ice and snow thickness of 1.92m. These values are very close to the 2.18m combined sea ice and snow thickness obtained by the observational technique.

It should be noted that, as can be seen in Figure 7-1, the floe stations are located between M321 and M323. In fact, the closest mission to the floe stations was M322 (located southwards from CTD042 in Figure 7-1) from which no data on ice draft could be obtained, as Autosub was operating at too great a depth.

The sea ice drilling programme on JR84 was very limited and produced too few data to be useful. On all three floes drillsites were chosen to be representative of what appeared to be level ice although, as can be seen above, whilst the top snow surface may be level, the ice surface certainly is not. On FS1, sea ice was found to be in excess of 1m thick whilst on FS2 sea ice was measured at 1.91m. FS3 had sea ice thicknesses of 2.43m and 2.66m (with snow depths of 27cm and 34cm) with a third site >2.7m.

8.4.1 Converting draft values to thickness

Equation (2.3) gives the thickness of sea ice (z_i) in metres

$$z_i \approx \frac{1027z_d - 351z_s}{920}, \quad (2.3)$$

where z_d is the measured ice draft (m) and z_s is the measured snow thickness (m). Using the kriged means of the ice draft from the three missions (2.10m, 2.55m and 2.53m) along with the overall kriged snow depth mean (44cm) in Equation (2.3), I have calculated estimates of sea ice thicknesses of 2.18m, 2.68m and 2.66m for M321, M323 and M324 respectively. Hence, the mean combined snow and ice thicknesses for the three missions were found to be 2.62m, 3.12m and 3.10m for M321, M323 and M324.

A summary of various ice thickness values is given in Table 8-1 as well as the combined ice and snow thickness values. It should be noted that many of the values of ice and snow thicknesses are approximations as they are calculated using many assumptions including proportions of ice types, the homogeneity of ice and snow in terms of density, composition, and whether pores are fluid or air filled. In a study in the Arctic, it was found that the ratio of ice draft to total ice and snow thickness was not constant even on a length scale of 235m, suggesting structural inhomogeneity (Melling *et al.*, 1993). However, the mean ice drafts used to calculate thickness are based on longer scales than 235m as they represent the entire kriged study regions.

Table 8-1 Summary of sea ice thickness (and combined with snow thickness). Values from JR84 M321, M323 and M324 are estimated from the kriged values as measured from Autosub and the mean kriged snow depth. FS1, FS2 and FS3 are based on the kriged values of mean snow depth from the three sampled floes. Profiles 054 and 055 are taken from Haas (1998) and these do not include open water or thinner ice on ice edges. Sea ice observations are reported for the sea ice regions and exclude open water.

Source	z_i Mean ice thickness (m)	$(z_i + z_s)$ Mean ice and snow thickness (m)
M321	2.18	2.62
M323	2.68	3.12
M324	2.66	3.10
FS1	1.51	1.96
FS2	1.36	1.77
FS3	1.52	1.98
From mean raw snow depth all three floes	1.46	1.90
Mean from kriged FS1, FS2 and FS3 snow depths	1.47	1.92
Sea ice observations (all in Table 7-1)	1.69	2.18
Sea ice observation concurrent with M321 (see Table 7-15)	1.99	2.59
Completed drillsites on FS3	2.43/2.66	2.70/3.00
Profile 054	-	3.12
Profile 055	-	2.31

The results of the three Autosub missions are in general agreement with the results from Haas (1998) and this will be discussed further in Section 8.6.1.

The results from the sea ice observations are lower than those from Autosub. Using all sea ice observations the mean ice thickness was between ~40cm and 100cm less than the values from Autosub. However, it should be noted that the sea ice observations relate to the values of ice thickness from the ice edge to the Autosub study regions. Worby *et al.* (1996) suggested that the ice thickness increases into the ice from the ice edge and so this could explain the difference between the two techniques. The difference in sea ice thickness between M321 and the concurrent sea ice observation was much lower at 19cm.

8.5 Research Question 5

Chapter 4 and Chapter 5 presented work on trying to establish whether icebergs cluster. The first of these chapters used data from the Autosub USIPS cruise and the second chapter extended the study to two-dimensions using satellite images.

As shown in Figure 5-3, the relative motion of sea ice and icebergs causes patches of open water or "wakes". Open water is critical to the exchange of heat and matter between the ocean and atmosphere (as discussed in Section 2.6) and therefore, any additional regions of open water have a significant impact. Using methodologies such as that discussed in Chapter 7 and submarine/moored buoy ULS methods, the clustering of icebergs would result not only in more values of larger (than expected) ice draft but also more open water.

The conclusion from the one-dimensional study in Chapter 4 is that icebergs were not randomly distributed along Autosub mission tracks. In addition, the number of icebergs encountered in any mission was not the same as would be expected from assuming that icebergs were randomly distributed along the entire track-length of all missions. As such, I concluded that icebergs must be considered when producing a PDF of sea ice draft. Hence, in Chapter 7, I removed all values of ice draft greater than 14m. However, this does not remove the possibility of bergy bits with a shallower draft.

From the work reported in Chapter 5, I concluded that icebergs are not randomly located within open water, i.e., they are not completely spatially random. For the image within the sea ice zone, I conclude that icebergs can be considered completely spatially random on scales up to 3.75km (this is the maximum length that the study regions support). Factors for which I cannot correct within this study include the potential impact of bathymetry within the study regions and, related to this, the differences in size of the icebergs. In addition, the study regions were geographically removed from each other and hence, overall, the representativeness of the study regions can be questioned.

Overall, from both studies it is clear that studies of sea ice draft should account for the spatial distribution of icebergs within the study regions. For some ULS studies, this is achieved by using the signal backscatter/strength (Mark Brandon, Personal Communication). For other methodologies additional data are required.

8.6 Other concurrent estimates of sea ice cover

In order to verify the results of the sea ice draft values from Autosub, a review was made of available sources of concurrent results. The first source identified was the Antarctic ice chart for the region issued by the US National Ice Center for the period 24-28 March 2003 (see Figure 8-2). These charts are derived from remotely sensed and, where available, in-situ data using a standardised methodology. As can be seen in Figure 8-2, M321 is on the boundary between region G and region K whereas M323 and M324 are within region K. This supports the observation that the region around M321 has a lower concentration of sea ice than that around M323/M324 (~70 to 90% for region G compared with 90 to 100% for region K).

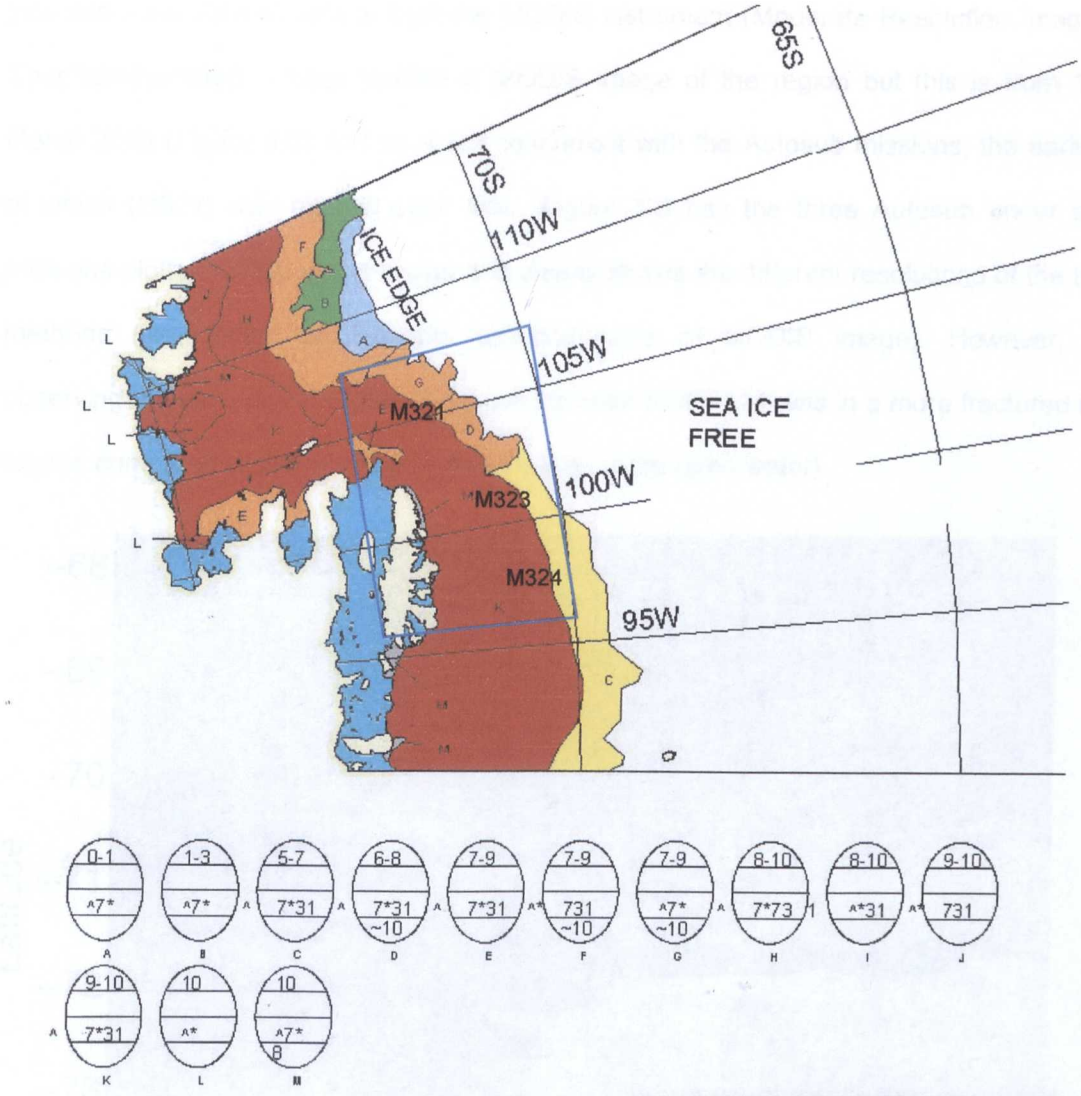

Figure 8-2 National Ice Center ice chart for study region for week of under ice missions* showing the approximate area of the Autosub study region as defined in Figure 7-1 (—) as well as locations of the three under sea ice missions.

* http://www.natice.noaa.gov/pub/antarctica/amundsen_east/2003/amune030324color.jpg

The second source of data is from the MODIS instrument (Moderate Resolution Imaging Spectroradiometer). I have located a MODIS image of the region but this is from 16th March 2003 (Figure 8-3) and so is not concurrent with the Autosub missions, the earliest of which (M321) was over a week later. Figure 8-3 has the three Autosub under sea missions plotted on top of the image and clearly shows the different resolutions of the two methods (i.e., length of Autosub missions<<size of MODIS image). However, by observing the ice types in Figure 8-3 it can be seen that M321 was in a more fractured ice regime compared to the other two missions (i.e., more open water).

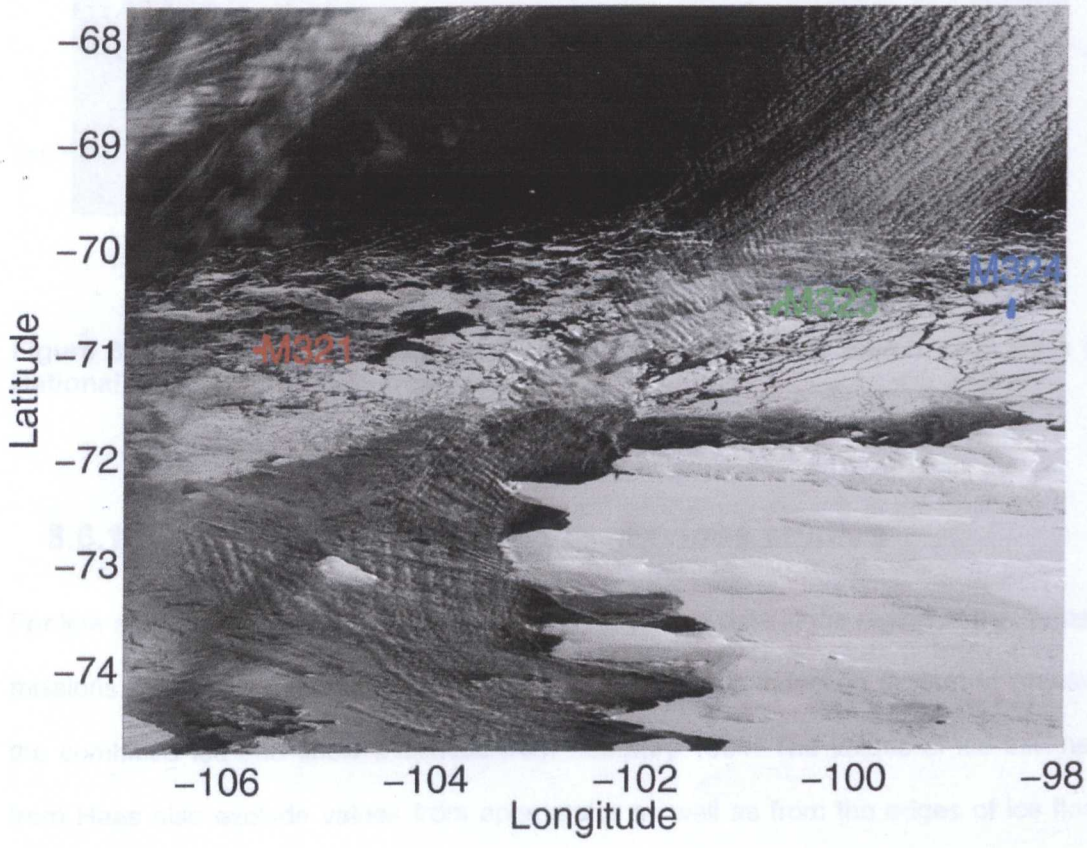

Figure 8-3 MODIS image of study region taken on 16 March 2003 showing location of under ice missions (M321 – red, M323 – green, M324 – blue).

The only other readily available MODIS image from the same period (acquired 14th March 2003) does not fully show the study region and is shown in Figure 8-4. Studying the sea ice to the north of Thurston Island in Figure 8-4, there is a trend that the further west, the more fractured the ice appears. If this is extended northwards to the study region, then it

supports the hypothesis of thinner ice with more open water in M321 compared to the thicker, less open water nature of sea ice in M323 and M324.

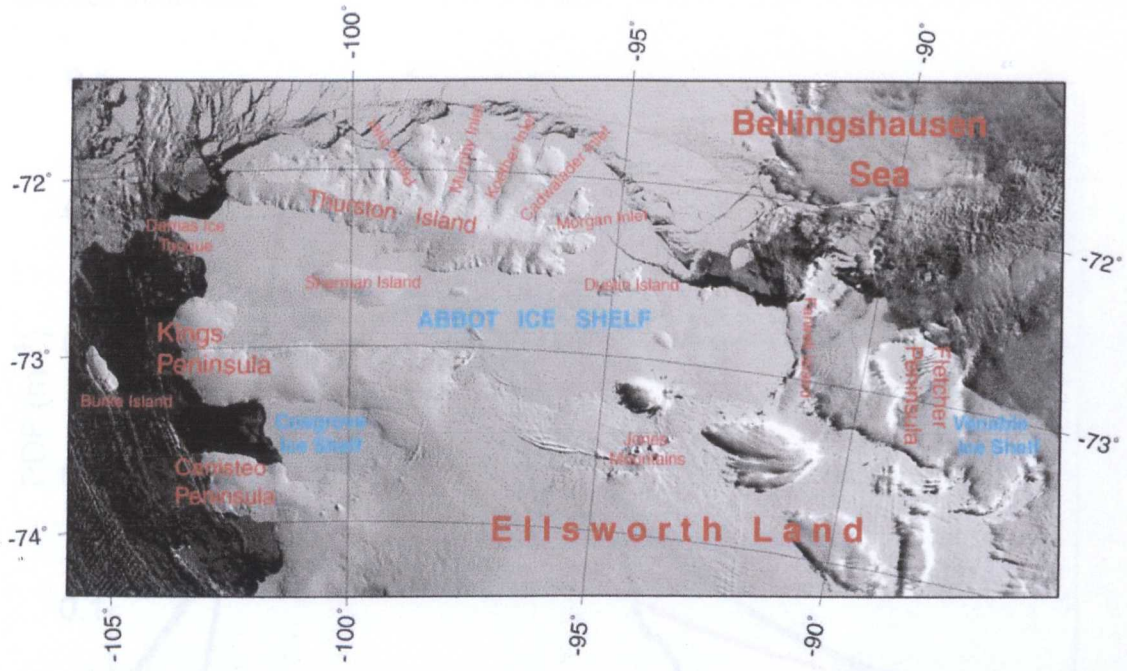

Figure 8-4 MODIS visible image with overlay grid from 14th March 2003 from US National Snow and Ice Data Center*.

8.6.1 Ice draft PDFs compared to previous studies

For late summer, there are limited sea ice draft/thickness data in the region of the Autosub missions. Haas (1998) used a ship-based electromagnetic induction system to measure the combined ice and snow thickness from February 1994. The values of ice thickness from Haas also exclude values from open water as well as from the edges of ice floes. The values from the two profiles from Haas closest to the current study (054 and 055 from the eastern Amundsen Sea) are shown in Table 8-1 and have means of 3.12m and 2.31m. These are comparable to the range of results from Autosub for the three missions; in fact, the means from M323 and M324 are within 2cm of the mean from Profile 054. Figure 8-5 shows the best estimates of the ice thickness PDFs for the three Autosub

* http://nsidc.org/

missions based on Figure 7-32 and converting the x-axis using Equation (2.3). The value of snow depth is the 44cm mean. In addition, Figure 8-5 shows the PDFs for profiles 054 and 055 from Haas.

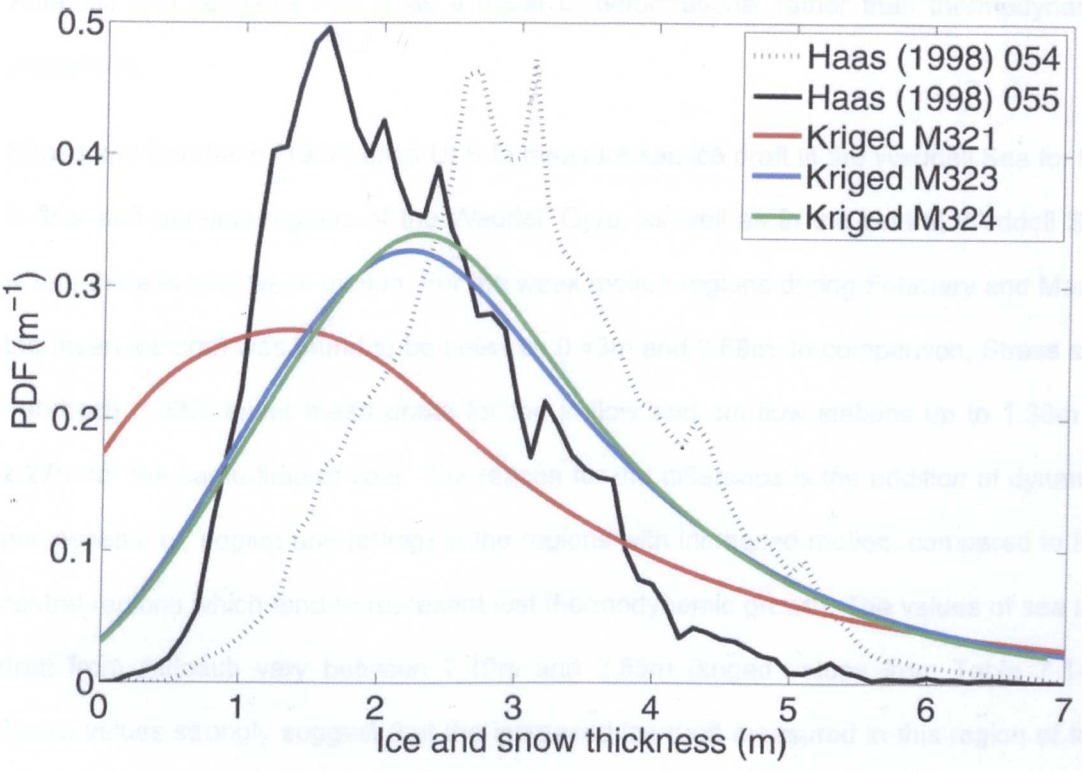

Figure 8-5 Comparison of Autosub results (see text for derivation of snow and ice thickness) for M321 (red), M323 (blue) and M324 (green). Also shown are two closest profiles from Haas (1998).

The PDF for the combined thickness of ice and snow reported in Haas indicates that most values are between zero and 6 m, which is similar to the values reported here and this can be seen in Figure 8-5. Haas also suggests that the lower values of ice draft within 055 compared to 054 is because off its closer proximity of the ice edge. For M321 and M323, Autosub was programmed to initially fly down to a depth of ~200m and the surface was then out of range of the ADCP. Hence, no information is available on the start of the ice edge so Haas' hypothesis cannot be verified. Based on the work in this thesis and that in Haas (1998), it is apparent that there is variability in the thickness of sea ice within this region. Haas suggests this is related to the distance from the ice edge. I hypothesise that the ice thickness also varies along the ice front, decreasing to the west.

I conclude that overall the results from Autosub show good agreement with the results from Haas (1998), which relate to the same time of year and location. As Haas (1998) notes the thickness of sea ice in this region is some of the thickest observed in the Antarctic and suggests that is as a result of deformational rather than thermodynamic processes.

Strass and Fahrbach (1998) used ULS to measure sea ice draft in the Weddell Sea for the in-flow and out-flow regions of the Weddell Gyre, as well as in the central Weddell Sea where there is only weak motion. For the weak motion regions during February and March the mean ice draft was found to be between 0.43m and 0.68m. In comparison, Strass and Fahrbach (1998) found mean drafts for the in-flow and out-flow stations up to 1.36m to 2.27m for the same time of year. The reason for the difference is the addition of dynamic processes (i.e., ridging and rafting) in the regions with increased motion, compared to the central regions which tend to represent just thermodynamic growth. The values of sea ice draft from Autosub vary between 2.10m and 2.55m (kriged values from Table 7-14). These values strongly suggest that the increased ice draft measured in this region of the Amundsen Sea is due to dynamic processes.

8.7 Suggestions for future work

My results leave many unanswered questions and opportunities for future work. Among these questions, the key ones are identified below for future work using both the data already described within this thesis and new data sources. Additional explanations and comments are given as necessary. Suggestions for the setup of the instrumentation on Autosub and the associated operating depth are not included, as these have already been covered in the relevant sections.

1. **Compare results of ADCP with results from other Autosub based ULS data**

There are two options for this issue. First, use the USIPS ADCP data and compare this with the results from the single beam echo-sounder reported in Brandon *et al.* (Submitted). Second, compare the results of the ADCP methodology with those from the

successful use of the multi-beam echo-sounder reported in Wadhams *et al.* (2006). Ideally, any further work to compare results should also comprise an extensive groundtruthing exercise using sea ice drilling, observations and sampling.

2. **Analyse EM2000 data for M321 to provide ice draft images/drafts**

As discussed in Section 7.1.1, M321 provided data on ice draft using the swath bathymetry system: these data have not been analysed, as the other missions did not provide any data from this instrument. If there is substantial agreement between the results from the ADCP methodology and the swath system, then a correlation should be found for points where data are co-located from both approaches.

3. **Develop a method for comparing the distributions of the sea ice draft from the three missions (or snow depths from three sampled floes) to take into account the spatial nature of the data.**

The statistical methods used for comparing the means/distributions of the sea ice draft/snow thickness between missions/floes assume there is no correlation between values, which is not correct because this ignores the spatial element of the sampling. For example, it would then be possible to test such variability whilst including this spatial variability in a mixed model.

4. **Comparison of Autosub sea ice draft measurements with satellite measurements**

As was discussed in Chapter 2, satellite methods have successfully been used to measure sea ice thickness. Comparison of the PDFs from this thesis cannot be made with data from ICESat, as this platform was not operational until February 2004. However, it would be possible to compare the results from either ERS2 or ENVISAT and a potential methodology is presented in Laxon *et al.* (2003).

5. **Provide PDFs for the depth of snow based on the same logarithmic transformation as used for sea ice draft (see Section 7.10.1)**

In order to account for the non-normality of the sea ice draft data a logarithmic transformation was used and the PDFs were obtained using a combination of kernel density estimate techniques and the Jacobian. This approach could also be used to produce PDFs for the snow data presented in Chapter 6. The advantage of this approach is that the non-normality of the snow depth data could also be taken into account for the geostatistical analysis.

6. **Use Autosub to investigate the change of mean ice thickness with respect to distance from ice edge**

Worby *et al.* (1996) found that during late winter the ice thickness increased with distance from the ice edge in the Bellingshausen/Amundsen Seas. In addition to collecting further data, Autosub would be an ideal tool for verifying whether this is a general phenomenon, if there is a preferential axis along which this increase occurs (e.g., perpendicular to the ice edge) and whether after a given distance there is a plateau effect and the mean thickness of the ice remains fairly constant. This is important, as satellite measurements do not use results from the ice edge (~ 100km) to avoid open water contamination (Seymour Laxon, Personal Communication). The data from the USIPS project could potentially be used to answer this question.

7. **Investigate the footprint of the ADCP and develop a model for explaining whether an average or maximum ice draft is retuned**

Drilling of floes shows that there are significant differences in sea ice thickness over relatively short distances (for example drilling on FS3 resulted in sea ice thicknesses of 2.43m, 2.66m and a third hole >2.7m). The area over which these measurements were made could, conceivably, have been insonified by a single beam (footprint is ~10m x ~10m). For example, Figure 8-6 shows a view of FS3 and the surrounding ice, the red line in the figure represents ~10m. The area encompassed by such a footprint could clearly

incorporate ice from the thinner, broken ice region as well as the more consolidated FS3, but what ice draft would be returned by the ADCP is not clear – it could be an averaged draft or may just be biased towards thicker ice as this would represent the first strong return.

Figure 8-6 View from *RRS James Clark Ross* of members of the scientific party on floe station FS3 on 9th March 2003. The red line indicates the approximate scale of 10m ADCP footprint (Photograph courtesy of Prof David Vaughan).

8. Investigate the distribution of (possible) icebergs within the survey regions.

The data based on the ADCP measurements can be used to identify the location of icebergs, determined by the large draft. Similar procedures to those in Chapter 5 could be used to analyse whether the icebergs can be considered as CSR. It should be noted that icebergs falling between measurements may actually have been omitted and cannot be accounted for within the kriging analyses.

9. **Analysis of contiguous region of sea ice and open water to compare iceberg CSR and provide information on iceberg CSR over a longer scale length than that in Chapter 4 or Chapter 5**

The two images used in Chapter 5 are a considerable distance apart and it would be beneficial to identify a single image (or set of images) where there are icebergs throughout and regions of sea ice and open water are adjacent. This could be achieved using the methodology I developed in Chapter 5 and could incorporate investigations of the iceberg sizes with respect to the bathymetry.

In addition, greater processing power could allow larger images to be analysed following the methodology in this thesis where the processing power was a desktop PC. This would allow the study of iceberg clustering on scales above 3.75km.

8.8 Summary

In this thesis, I have shown how measurements of sea ice draft can be made from the Autosub vehicle using an ADCP. The importance of such measurements to understanding global climate has been discussed, in particular given the limited number of data for the Antarctic. I have described the methodology developed and have shown how the results are in agreement with previous studies.

In addition, I have investigated the spatial distribution of icebergs in sea ice and open water. This work has shown that icebergs should be accounted for in deriving PDFs of sea ice thickness.

Finally, I have suggested further work to build on the methodologies I have developed in this thesis.

References

Abrams, M., S. Hook, and B. Ramachandran, *ASTER User Handbook*, Pasadena, CA, USA, 2002.

Ackley, S.F., Mass-balance aspects of Weddell Sea pack ice, *Journal of Glaciology, 24* (90), 391-405, 1979.

Ainley, D.G., C.T. Tynan, and I. Stirling, Sea ice: A critical habitat for Polar marine mammals and birds, in *Sea ice: An introduction to its physics, chemistry, biology and geology*, edited by D.N. Thomas, and G.S. Dieckmann, pp. 240-266, Blackwell Science Ltd, Oxford, 2003.

Andreas, E.L., and K.J. Claffey, Air-Ice Drag Coefficients in the Western Weddell Sea .1. Values Deduced from Profile Measurements, *Journal of Geophysical Research-Oceans, 100* (C3), 4821-4831, 1995.

Andreas, E.L., M.A. Lange, S.F. Ackley, and P. Wadhams, Roughness of Weddell Sea-Ice and Estimates of the Air-Ice Drag Coefficient, *Journal of Geophysical Research-Oceans, 98* (C7), 12439-12452, 1993.

Apel, J.R., *Principles of Ocean Physics*, Academic Press, London, 1987.

Badgley, F.I., Heat balance at the surface of the Arctic Ocean, Proceedings of the Symposium on the Arctic Heat Budget and Atmospheric Circulation, in *Symposium on the Arctic Heat Budget and Atmospheric Circulation*, edited by J.O. Fletcher, pp. 267-278, Rand Corp, 1966.

Belliveau, D.J., G.L. Bugden, B.M. Eid, and C.J. Calnan, Sea Ice Velocity-Measurements by Upward-Looking Doppler Current Profilers, *Journal of Atmospheric and Oceanic Technology, 7* (4), 596-602, 1990.

Bivand, R., and A. Gebhardt, Implementing functions for spatial statistical analysis using the R language, *Journal of Geographical Systems, 2* (3), 307-317, 2000.

Bowen, R.G., and D.R. Topham, A study of the morphology of a discontinuous section of a first year arctic pressure ridge, *Cold Regions Science and Technology*, *24* (1), 83-100, 1996.

Brandon, M.A., A.S. Brierley, P.G. Fernandes, F. Armstrong, N.W. Millard, S.D. McPhail, P. Stevenson, M. Pebody, J. Perrett, and M. Squires, The ice thickness distribution in the north-west Weddell Sea measured by an autonomous underwater vehicle., *Geophysical Research Letters*, Submitted.

Brandon, M.A., M. Naganobu, D.A. Demer, P. Chernyshkov, P.N. Trathan, S.E. Thorpe, T. Kameda, O.A. Berezhinskiy, E.J. Hawker, and S. Grant, Physical oceanography in the Scotia Sea during the CCAMLR 2000 survey, austral summer 2000, *Deep-Sea Research Part Ii-Topical Studies in Oceanography*, *51* (12-13), 1301-1321, 2004.

Brandon, M.A., Z. Pozzi-Walker, D. Hayes, and A. Jenkins, Physical Oceanography, in *JR84 Cruise Report: Autosub Under Ice Cruise to the Amundsen Sea*, edited by A. Jenkins, pp. 30-49, British Antarctic Survey, Cambridge, UK, 2003.

Brierley, A.S., P.G. Fernandes, M.A. Brandon, F. Armstrong, N.W. Millard, S.D. McPhail, P. Stevenson, M. Pebody, J. Perrett, M. Squires, D.G. Bone, and G. Griffiths, Antarctic krill under sea ice: Elevated abundance in a narrow band just south of ice edge, *Science*, *295* (5561), 1890-1892, 2002.

Brierley, A.S., P.G. Fernandes, M.A. Brandon, F. Armstrong, N.W. Millard, S.D. McPhail, P. Stevenson, M. Pebody, J. Perrett, M. Squires, D.G. Bone, and G. Griffiths, An investigation of avoidance by Antarctic krill of RRS James Clark Ross using the Autosub-2 autonomous underwater vehicle, *Fisheries Research*, *60* (2-3), 569-576, 2003.

Budd, W.F., Antarctica and Global Change, *Climatic Change*, *18* (2-3), 271-299, 1991.

Calvert, J., *Surface at the Pole: The extraordinary voyages of the USS Skate*, McGraw-Hill Book Company, Inc., New York, USA, 1960.

Chu, D., The GLOBEC Kriging Software Package - EasyKrig, Woods Hole. MA, USA, 2004.

Clark, I., and W.H. Harper, *Practical Geostatistics 2000*, Geostokos, 2000.

Comiso, J.C., Large-scale characteristics and variability of the global sea ice cover, in *Sea ice: An introduction to its physics, chemistry, biology and geology*, edited by D.N. Thomas, and G.S. Dieckmann, pp. 112-142, Blackwell Science Ltd, Oxford, 2003.

Comiso, J.C., J. Yang, S. Honjo, and R.A. Krishfield, Detection of change in the Arctic using satellite and in situ data, *Journal of Geophysical Research*, *108* (C12), 14-1 - 14-24, 2003.

Cressie, N.A.C., *Statistics for spatial data*, 928 pp., John Wiley and Sons, Inc, New York, 1991.

Curran, M.A.J., T.D. van Ommen, V.I. Morgan, K.L. Phillips, and A.S. Palmer, Ice core evidence for Antarctic sea ice decline since the 1950s, *Science*, *302* (5648), 1203-1206, 2003.

Daly, F., D.J. Hand, M.C. Jones, A.D. Lunn, and K.J. McConway, *Elements of Statistics*, The Open University, Milton Keynes, UK, 1995.

Dieckmann, G.S., and H.H. Hellmer, The importance of sea ice: An overview, in *Sea ice: An introduction to its physics, chemistry, biology and geology*, edited by D.N. Thomas, and G.S. Dieckmann, pp. 1-21, Blackwell Science Ltd, Oxford, 2003.

Diggle, P.J., *Statistical Analysis of Spatial Point Patterns*, 159 pp., Arnold, London, UK, 2003.

Eicken, H., From the microscopic to the macroscopic to the regional scale: Growth, microstructure and properties of sea ice, in *Sea Ice - An introduction to its physics, biology, chemistry and geology*, edited by D. Thomas, and G.S. Dieckmann, Blackwell Science, London, UK, 2003.

Eicken, H., M.A. Lange, H.W. Hubberten, and P. Wadhams, Characteristics and Distribution Patterns of Snow and Meteoric Ice in the Weddell Sea and Their Contribution to the Mass-Balance of Sea-Ice, *12* (1), 80-93, 1994.

Fahrbach, E., G. Rohardt, M. Schroder, and V. Strass, Transport and Structure of the Weddell Gyre, *Annales Geophysicae-Atmospheres Hydrospheres and Space Sciences*, *12* (9), 840-855, 1994.

Fetterer, F., and K. Knowles, Sea ice index, National Snow and Ice Data Center, Boulder, CO, USA, 2002 (updated 2004).

Gill, A.E., Circulation and bottom water production in the Weddell Sea, *Deep-Sea Research*, 20, 111-140, 1973.

Gladstone, R., and G.R. Bigg, Satellite tracking of icebergs in the Weddell Sea, *Antarctic Science*, *14* (3), 278-287, 2002.

Gladstone, R.M., G.R. Bigg, and K.W. Nicholls, Iceberg trajectory modeling and meltwater injection in the Southern Ocean, *Journal of Geophysical Research*, *106* (C9), 19903-19915, 2001.

Gloersen, P., W.J. Campbell, D.J. Cavalieri, J.C. Comiso, C. Parkinson, and H.J. Zwally, *Arctic and Antarctic Sea Ice, 1978-1987: Satellite Passive-microwave observations and analysis*, NASA, Washington, D.C., 1992.

Gloersen, P., C.L. Parkinson, D.J. Cavalieri, J.C. Comiso, and H.J. Zwally, Spatial distribution of trends and seasonality in the hemispheric sea ice covers: 1978-1996, *Journal of Geophysical Research-Oceans*, *104* (C9), 20827-20835, 1999.

Haas, C., Evaluation of ship-based electromagnetic-inductive thickness measurements of summer sea-ice in the Bellingshausen and Amundsen Seas, Antarctica, *Cold Regions Science and Technology*, *27* (1), 1-16, 1998.

Haas, C., S. Gerland, H. Eicken, and H. Miller, Comparison of sea-ice thickness measurements under summer and winter conditions in the Arctic using a small electromagnetic induction device, *Geophysics*, *62* (3), 749-757, 1997.

Haas, C., H. Rebhan, D.N. Thomas, and T. Viehoff, Sea ice, in *The Expedition ANTARKTIS-XI/3 of RV Polarstern in 1994.*, edited by H. Miller, and H. Grobe, pp. 29-43, Alfred Wegener Institute for Polar and Marine Research, Bremerhaven, 1996.

Hogg, R.V., and E.A. Tanis, *Probability and statistical inference*, Macmillan Publishing Co., Inc., New York, 1977.

Hopkins, M.A., On the Ridging of Intact Lead Ice, *Journal of Geophysical Research*, *99* (C8), 16351-16360, 1994.

Huppert, H.E., and E.G. Josberger, The melting of ice in cold stratified water, *Journal of Physical Oceanography*, 10, 953-960, 1980.

Jeffries, M.O., S. Li, R.A. Jaña, H.R. Krouse, and B. Hurst-Cushing, Late winter first-year ice floe thickness variability, seawater flooding and snow ice formation in the Amundsen and Ross Seas, in *Antarctic Sea Ice: Physical processes, interactions and variability*, edited by M.O. Jeffries, pp. 69-87, American Geophysical Union, Washington, 1998.

Jones, M.C., and K.J. McConway, The Sinh-Arcsinh and Related Transformations, In preparation.

Kanji, G.K., *100 Statistical Tests*, 216 pp., SAGE Publications Ltd, London, 1993.

Kovacs, A., D. Diemand, and J.J. Bayer Jnr, Electromagnetic Induction Sounding of Sea Ice Thickness, pp. 16, CRREL, Hanover, New Hampshire, USA, 1996.

Kovacs, A., and J.S. Holladay, Sea-ice thickness measurement using a small airborne electromagnetic sounding system, *Geophysics*, *55* (10), 1327-1337, 1990.

Kovacs, A., and R.M. Morey, Sounding sea ice thickness using a portable electromagnetic induction instrument, *Geophysics*, *56* (12), 1992-1998, 1991.

Kwok, R., H.J. Zwally, and D.H. Yi, ICESat observations of Arctic sea ice: A first look, *Geophysical Research Letters*, *31* (16), art. no.-L16401, 2004.

Lange, M.A., S.F. Ackley, P. Wadhams, G.S. Dieckmann, and H. Eicken, Development of sea ice in the Weddell Sea, *Annals of Glaciology*, *12*, 92-96, 1989.

Lange, M.A., and H. Eicken, The Sea Ice Thickness Distribution in the Northwestern Weddell Sea, *Journal of Geophysical Research*, *96* (C3), 4821-4837, 1991.

Lange, M.A., P. Schlosser, S.F. Ackley, P. Wadhams, and G.S. Dieckmann, O-18 Concentrations in Sea Ice of the Weddell Sea, Antarctica, *Journal of Glaciology*, *36* (124), 315-323, 1990.

Laxon, S., N. Peacock, and D. Smith, High interannual variability of sea ice thickness in the Arctic region, *Nature*, *425* (6961), 947-950, 2003.

Leroy, C.C., Development of simple equations for accurate and more realistic calculation of speed of sound in seawater, *Journal of the Acoustical Society of America*, *46*, 216-226, 1969.

Leroy, C.C., and F. Parthiot, Depth-pressure relationships in the oceans and seas, *Journal of the Acoustical Society of America*, *103* (3), 1346-1352, 1998.

Lewis, T., *Unit 3: Patterns in Space*, The Open University Press, Milton Keynes, UK, 1988.

Madejski, P., and S. Rakusa-Suszczewski, Icebergs as Tracers of Water-Movement in the Bransfield Strait, *Antarctic Science*, *2* (3), 259-263, 1990.

Massom, R.A., H. Eicken, C. Haas, M.O. Jeffries, M.R. Drinkwater, M. Sturm, A.P. Worby, X.R. Wu, V.I. Lytle, S. Ushio, K. Morris, P.A. Reid, S.G. Warren, and I. Allison, Snow on Antarctic Sea ice, *Reviews of Geophysics*, *39* (3), 413-445, 2001.

McLaren, A.S., P. Wadhams, and R. Weintraub, The Sea Ice Topography of McLure Strait in Winter and Summer of 1960 from Submarine Profiles, *Arctic*, *37* (2), 110-120, 1984.

McPhail, S., ADCPs and Navigation, in *JR84 Cruise Report: Autosub Under Ice Cruise to the Amundsen Sea*, edited by A. Jenkins, pp. 83-84, British Antarctic Survey, Cambridge, UK, 2003a.

McPhail, S., Connector problems, in *JR84 Cruise Report: Autosub Under Ice Cruise to the Amundsen Sea*, edited by A. Jenkins, pp. 88, British Antarctic Survey, Cambridge, UK, 2003b.

Melling, H., D.R. Topham, and D. Riedel, Topography of the Upper and Lower Surfaces of 10 Hectares of Deformed Sea-Ice, *Cold Regions Science and Technology*, *21* (4), 349-369, 1993.

Millard, N.W., G. Griffiths, G. Finegan, S.D. McPhail, D.T. Meldrum, M. Pebody, J.R. Perrett, P. Stevenson, and A.T. Webb, Versatile autonomous submersibles - the realising and testing of a practical vehicle, *Underwater Technology*, *23* (1), 7-17, 1998.

Perovich, D.K., The Optical Properties of Sea Ice, U.S. Army Cold Regions Research and Engineering Laboratory, Hanover, New Hampshire., 1996.

RD Instruments, *Acoustic Doppler Current Profiler, Principles of Operation, A Practical Primer*, 51 pp., RD Instruments, San Diego, CA, USA, 1996.

RD Instruments, ADCP Coordinate Transformation, RD Instruments, San Diego, California, USA, 1998.

Rothrock, D.A., Y. Yu, and G.A. Maykut, Thinning of the Arctic sea-ice cover, *Geophysical Research Letters*, *26* (23), 3469-3472, 1999.

Shcherbina, A.Y., D.L. Rudnick, and L.D. Talley, Ice-draft profiling from bottom-mounted ADCP data, *Journal of Atmospheric and Oceanic Technology*, *22* (8), 1249-1266, 2005.

Squire, V.A., and S.C. Moore, Direct measurement of the attenuation of ocean waves by pack ice, *Nature*, *283*, 365-368, 1980.

Steele, M., Sea Ice Melting and Floe Geometry in a Simple Ice-Ocean Model, *Journal of Geophysical Research*, *97* (C11), 17729-17738, 1992.

Strass, V.H., Measuring sea ice draft and coverage with moored upward looking sonars, *Deep Sea Research Part I: Oceanographic Research Papers, 45* (4-5), 795-818, 1998.

Strass, V.H., and E. Fahrbach, Temporal and regional variations of sea ice draft and coverage in the Weddell Sea obtained from upward looking sonars, in *Antarctic Sea Ice: Physical processes, interactions and variability*, edited by M.O. Jeffries, pp. 123-139, American Geophysical Union, Washington, 1998.

Sturm, M., K. Morris, and R. Massom, The Winter snow cover of the West Antarctic pack ice: its spatial and temporal variability, in *Antarctic Sea Ice: Physical processes, interactions and variability*, edited by M.O. Jeffries, pp. 1-18, American Geophysical Union, Washington, 1998.

Tchernia, P., and P.F. Jeannin, Circulation in Antarctic Waters as Revealed by Iceberg Tracks 1972-1983, *Polar Record*, *22* (138), 263-260, 1984.

Telford, W.M., L.P. Geldart, and R.E. Sheriff, *Applied Geophysics*, 770 pp., Cambridge University Press, Cambridge, UK, 1990.

The Mathworks, I., Matlab, Natick, MA, 2004.

Thorndike, A., Sea ice thickness as a stochastic process, *Journal of Geophysical Research*, *105* (C1), 1311-1313, 2000.

Thorndike, A.S., D.A. Rothrock, G.A. Maykut, and R. Colony, The thickness distribution of sea ice, *Journal of Geophysical Research*, *80* (33), 4501-4513, 1975.

Tin, T., and M.O. Jeffries, Morphology of deformed first-year sea ice features in the Southern Ocean, *Cold Regions Science and Technology*, *36* (1-3), 141-163, 2003.

Visbeck, M., and J. Fischer, Sea Surface Conditions Remotely Sensed by Upward-Looking ADCPs, *Journal of Atmospheric and Oceanic Technology*, *12* (1), 141-149, 1995.

Wadhams, P., *Ice in the ocean*, OPA, Amsterdam, 2000.

Wadhams, P., M.A. Lange, and S.F. Ackley, The ice thickness distribution across the Atlantic Sector of the Antarctic Ocean in Midwinter, *Journal of Geophysical Research*, *92* (C13), 14535-14552, 1987.

Wadhams, P., J.P. Wilkinson, and S.D. McPhail, A new view of the underside of Arctic sea ice, *Geophysical Research Letters*, *33* (4), 2006.

Webster, R., and M.A. Oliver, *Geostatistics for Environmental Scientists*, John Wiley & Sons, Ltd., Chichester, 2001.

Weeks, W.F., S.F. Ackley, and J. Govoni, Sea ice ridging in the Ross Sea, Antarctica as compared with sites in the Arctic, *Journal of Geophysical Research*, *94* (C4), 4984-4988, 1989.

Weeks, W.F., and M. Mellor, Some elements of iceberg technology, in *Iceberg Utilization*, edited by A.A. Husseiny, pp. 45-98, Pergamon Press, New York, 1978.

Weisstein, E.W., Euler Angles. From *MathWorld*--A Wolfram Web Resource. http://mathworld.wolfram.com/EulerAngles.html, 2006.

WMO, Sea-Ice Nomenclature, World Metrological Organization, 1970.

Worby, A.P., Observing Antarctic sea ice: A practical guide for conducting sea ice observations from vessels operating in the Antarctic pack ice. A CD-ROM produced for the Antarctic Sea Ice Processes and Climate (ASPeCt) program of the Scientific Committee for Antarctic Research (SCAR) Global Change and the Antarctic (GLOCHANT) program, Hobart, Australia, 1999.

Worby, A.P., and I. Allison, *A Technique for Making Ship-Based Observations of Antarctic Sea Ice Thickness and Characteristics: PART I Observational Technique and Results*, pp. 1-23, Antarctic CRC and Australian Antarctic Division, Hobart, Tasmania, 1999.

Worby, A.P., G.M. Bush, and I. Allison, Seasonal development of the sea-ice thickness distribution in East Antarctica: measurements from upward-looking sonar, *Annals of Glaciology*, *33*, 177-180, 2001.

Worby, A.P., P.W. Griffin, V.I. Lytle, and R.A. Massom, On the use of electromagnetic induction sounding to determine winter and spring sea ice thickness in the Antarctic, *Cold Regions Science and Technology*, *29* (1), 49-58, 1999.

Worby, A.P., M.O. Jeffries, W.F. Weeks, K. Morris, and R. Jana, The thickness distribution of sea ice and snow cover during late winter in the Bellingshausen and Amundsen Seas, Antarctica, *Journal of Geophysical Research*, *101* (C12), 28441-28455, 1996.

Worby, A.P., and R.A. Massom, The structure and properties of sea ice and snow cover in East Antarctic pack ice, Cooperative Research Centre for the Antarctic and Southern Ocean Environment, Hobart, Australia, 1995.

Zwally, H.J., J.C. Comiso, C.L. Parkinson, D.J. Cavalieri, and P. Gloersen, Variability of Antarctic sea ice 1979-1998, *Journal of Geophysical Research*, *107* (C5), 1029-1047, 2002a.

Zwally, H.J., B. Schutz, W. Abdalati, J. Abshire, C. Bentley, A. Brenner, J. Bufton, J. Dezio, D. Hancock, D. Harding, T. Herring, B. Minster, K. Quinn, S. Palm, J. Spinhirne, and R. Thomas, ICESat's laser measurements of polar ice, atmosphere, ocean, and land, *Journal of Geodynamics*, *34* (3-4), 405-445, 2002b.